Effects of Heavy-Ion Irradiation on the Phase Stability of Several Copper-Base Alloys

Robert W. Knoll

August 1981

UWFDM-436

Ph.D. thesis.

FUSION TECHNOLOGY INSTITUTE

UNIVERSITY OF WISCONSIN

MADISON WISCONSIN

Effects of Heavy-Ion Irradiation on the Phase Stability of Several Copper-Base Alloys

Robert W. Knoll

Fusion Technology Institute
University of Wisconsin
1500 Engineering Drive
Madison, WI 53706

http://fti.neep.wisc.edu

August 1981

UWFDM-436

Ph.D. thesis.

EFFECTS OF HEAVY-ION IRRADIATION ON THE PHASE STABILITY OF SEVERAL COPPER-BASE ALLOYS

BY

ROBERT WALTER KNOLL

A thesis submitted in partial fulfillment of the requirements for the degree of

DOCTOR OF PHILOSOPHY

(Nuclear Engineering)

at the

UNIVERSITY OF WISCONSIN-MADISON

1981

TABLE OF CONTENTS

ABSTRACT

EFFECTS OF HEAVY-ION IRRADIATION ON THE PHASE STABILITY OF SEVERAL COPPER-BASE ALLOYS

Robert Walter Knoll

Under the supervision of Professor G.L. Kulcinski and Dr. P. Wilkes.

The mechanical and physical properties of an alloy are dependent on the nature of the phases that comprise that alloy. Previous studies have shown that the microstructural defects produced by intense, energetic irradiation, such as that within fast-fission reactors or proposed nuclear fusion reactors, can directly and indirectly alter the characteristics (e.g., the structure, size distribution, or volume fraction) of an alloy phase. Therefore, prediction of the long-term integrity of structural alloys in an irradiation environment requires a thorough understanding of the effects of irradiation on alloy phase stability. The primary subject of this thesis is the characterization of radiation-induced precipitation in a binary Cu-3.4 at% Be alloy, under various irradiation conditions. More limited investigations were conducted regarding the phase stability of two other simple alloys: Cu-1% Co and Cu-1% Fe.

The alloy specimens were irradiated with 14 MeV Cu ions, which produced depth dependent displacement damage within a layer extending ~3000nm from the specimen surface. At a depth of 1000nm, displacement damage ranged from 0.25 to 10 dpa, at a damage rate of $\sim 10^{-3}$dpa/sec. Irradiation temperatures ranged from 300-525°C. Cu-Be specimens and some Cu-Co and Cu-Fe specimens were irradiated in the solution-annealed and quenched condition. Other Cu-Co and Cu-Fe specimens were aged prior to irradiation to produce a distribution of coherent precipitates. The microstructure

of irradiated specimens and unirradiated controls was examined using transmission electron microscopy (TEM). Two different TEM specimen preparation techniques were employed: (a) conventional backthinning, and (b) cross sectional thinning, whereby the specimen was thinned in a plane normal to the specimen surface, allowing the microstructure throughout the ion range to be examined. Prior to TEM specimen preparation, the near-surface alloy composition-vs.-depth profiles were measured using Auger electron spectroscopy (AES), to investigate the role of radiation-induced solute segregation in the phase stability of these alloys.

Irradiation of supersaturated Cu-3.4 at% Be solid solution, at temperatures of 300-400°C to damage levels as low as 0.1 dpa, induced continuous precipitation of CuBe platelets, whose morphology was similar to γ' platelets observed during thermal aging of more concentrated Cu-Be alloys. No precipitation was observed in unirradiated control samples. The undersaturated solid solution decomposed during irradiation at 430° and 475°C, although the dose required to induce precipitation increased with temperature. Overall, precipitate size increased with increasing temperature, increasing dose and decreasing dose-rate. Precipitate number density increased with increasing dose-rate and decreasing temperature. In cross sectioned samples, precipitate morphology was not strongly depth dependent, except near the surface and near the end of ion range.

The continuous CuBe precipitation dissolved during post-irradiation annealing, even at a temperature (400°C) within the two-phase region on the equilibrium phase diagram. Instead , prolonged thermal aging near this temperature produced coarse discontinuous precipitation at grain boundaries and in clusters within the grains.

The radiation-induced precipitate morphology was attributed to the segregation of Be solute to dislocation loops formed early during irradiation, although the existence of this mechanism could not be confirmed directly. The AES measurements detected enhanced Be enrichment at the irradiated surface, however this Be was oxidized, and it was established that the observed enrichment was due mainly to enhanced BeO formation under irradiation.

The principal effect of irradiation at 350°C~500°C on the Cu-Co and Cu-Fe alloys was loss of precipitate coherency. In cross sectioned samples, coherency loss was observed well beyond the end of the ion range, and this was attributed to the long-range migration of interstitial defects originating in the irradiated zone. Precipitate size did not change measurably during irradiation, and no significant radiation-induced solute segregation (at the specimen surface) was detected by AES measurements, so it was concluded that the Fe and Co solutes did not interact strongly with the irradiation-induced defects. Void formation was never observed, except in one Cu-Fe specimen.

CHAPTER I

INTRODUCTION

Structural materials within proposed nuclear fusion or fast-fission reactors will be exposed at high temperatures to intense radiation from energetic neutrons or charged particles. In crystalline materials under such conditions, atomic collisions displace atoms from their lattice sites and cause localized disruptions in the microstructure of the material. Mobile point defects - vacancies and interstitials - are created. These defects are responsible for a variety of processes which, by altering the microstructure and the microcomposition, change the engineering properties of the material. Radiation induced changes in the physical properties of pure metals result from excess concentrations of point defects, and from the formation of defect clusters such as voids and dislocation loops. Reactor structural materials, however, will generally not be pure metals, but multicomponent, multiphase alloys, in which the radiation effects are more complex. In addition to defect cluster formation, point defects may interact with alloying elements and alter the stability of an alloy phase. For instance, the growth rate of a precipitate, the relative volume fraction of an alloy phase, or the structure of a phase may be different under irradiation than under exposure to high temperatures alone.[1,2] To predict the long term behavior of an alloy under irradiation, it is therefore necessary to understand the various mechanisms by which irradiation can affect phase transformations in alloys.

Methods and Objectives

The objective of this study was to characterize, by experimental methods, the precipitation process in a simple alloy under irradiation, to try to improve upon the understanding of the solute/point-defect interactions responsible for such phase changes. For reasons outlined below, several Cu-base binary alloys were chosen as the subjects of this research: Cu-3.4 at% Be, Cu-1 at% Co, and Cu-1 at% Fe. When this investigation was begun several years ago, few systematic studies of alloy phase stability under irradiation had been performed. In light of the complexity of the subject, relatively little experimental data was available in the literature, particularly with regard to Cu-base alloys. To determine the best path to follow, preliminary irradiation experiments were performed on each of the above alloys. Irradiation was found to greatly accelerate the rate of decomposition of the Cu-3.4 at% Be solid solution. In contrast, the precipitation process was found to be very sluggish during thermal aging of the supersaturated solution in the absence of irradiation, and the resulting equilibrium precipitation had a very different morphology than the radiation-induced precipitation. The characterization of radiation-induced precipitation in the Cu-3.4 at% Be alloy was the primary subject of this study. Also, an attempt was made to determine whether radiation-induced point-defect fluxes cause segregation of the Be solute at defect sinks. This work involved the measurement of solute concentration vs. depth profiles near the surface of the irradiated specimens. Since the surface is an

unsaturable point defect sink, it was assumed such measurements might provide insight with respect to compositonal changes at internal sinks, which might aid in the explanation of the radiation-induced precipitation. The nature of the defect clusters that formed in the irradiated alloys was also of interest in this study. In connection with this, a brief, preliminary investigation of radiation-induced defect-cluster formation in high purity Cu was performed.

Displacement damage was produced in the specimens by irradiation with 14 MeV Cu ions, using the University of Wisconsin tandem Van de Graaff accelerator. Heavy ion irradiation produces a large concentration of displaced atoms in a relatively short time, although the damage is confined to the near-surface region (~ 3 microns) of the specimen. Temperatures during irradiation ranged from 300°C to 525°C, corresponding to 0.4-0.6 of the melting point of the alloys, a possible operating temperature range for reactor materials. Ion fluences ranged from about 9×10^{14} to 3.5×10^{16} ion/cm^2 at a flux of about 3.5×10^{12} ions/cm^2-sec. These fluences produced maximum damage doses of 1 to 42 displacements per atom (dpa). Depending on the experiment, the alloy specimens were either irradiated in the solution annealed and quenched state, or else were aged before irradiation to produce a desired precipitate distribution. Following irradiation, the alloy specimens were analyzed by Auger electron spectroscopy, to measure the near surface alloy composition. Specimens were then thinned for analysis in the electron microscope, to study the microstructural changes produced by irradiation. Some

specimens were electroplated with Cu, then were thinned in a plane perpendicular to the specimen surface, allowing examination of the microstructure along the entire path of the incident ions. To the author's knowledge, this study represents the first application of the cross sectioning technique to the study of precipitation phenomena in ion-bombarded alloys.

Copper Base Alloys

Dilute copper base alloys were used in this study for several reasons:

a) The effects of irradiation on the base metal - high purity copper - have been well characterized, and the metallurgical and physical properties of copper and its alloys have been widely studied, so a good data base exists on these materials.

b) No previous systematic studies of the irradiation phase stability of Cu base alloys have been performed. Most other phase stability studies have centered on Ni-base alloys, stainless steels, or refractory metals.[1,2]

c) From a practical standpoint, Cu alloys are easy to work with; e.g., the cross-sectional thinning technique for electron microscopy analysis can be used on these alloys because the specimens can be easily electroplated with copper.

d) The Cu-Be, Cu-Co and Cu-Fe systems have interesting characteristics for the study of irradiation phase stability. The Cu-Be system is complex, containing several intermetallic compounds.[3] The Be solute atom is undersize, and is expected to interact

strongly with point defects. In Cu-Co and Cu-Fe the solutes are similar in atomic size to Cu, and the equilibrium phase diagrams of the system are simple.[3] The relative atomic size of the solute is of interest because it plays an important role in several theories of irradiation phase stability.

The Organization of This Paper

Before the experimental methods and results of this study are presented, a brief literature review is given of the theory of radiation damage and of previous experiments that pertain to this work. Radiation induced phase changes in alloys have their origins in the displacement events produced by irradiation. Therefore, Chapter II summarizes the theories of point defect formation under irradiation, the agglomeration of point defects into voids and dislocation loops, and the effects of alloying elements on defect cluster formation. Theoretical models of alloy phase stability under irradiation are then reviewed in Chapter III. An attempt is made in these chapters to give a unified account of the origins of, and the inter-relationships among the various types of microstructural changes and localized compositional changes that have been observed in irradiated metals and alloys. In Chapter IV, the metallurgy of the Cu-Be, Cu-Co and Cu-Fe alloy systems is discussed. The equlibrium phase diagrams of these systems are described, and studies of phase changes in the dilute Cu-base alloys, caused by conventional driving forces such as thermal activation and deformation, are reviewed. The reason for this metallurgical review is that, to understand the effect of radi-

ation on phase transformations in a particular alloy, it is necessary to thoroughly understand the behavior of the alloy under the conventional driving forces that are also acting on the material as it is irradiated. Finally, in Chapter V, some previous experiments on alloy phase stability under irradiation are reviewed.

References for Chapter I

1. Radiation Effects in Breeder Reactor Structural Materials, M. L. Bleiberg and J. W. Bennett (eds.), The Metallurgical Society of AIME, 1977.

2. Irradiation Effects on Phase Stability, (Proceedings of the Irradiation Phase Stability Session of the 1980 Fall Meeting of the TMS-AIME), D. I. Potter (ed.), The Metallurgical Society of AIME, 1981, (to be published).

3. M. Hansen, Constitution of Binary Alloys, McGraw-Hill Book Co., 1958.

CHAPTER II

THEORY OF POINT DEFECT PRODUCTION AND DEFECT CLUSTER FORMATION UNDER IRRADIATION

A. Primary Defect Production

The primary defect produced in a metal by energetic radiation is the Frenkel (vacancy-interstitial) pair, which forms when the incident radiation transfers sufficient energy to a lattice atom to displace it from its lattice site. For particulate radiation, both the number of Frenkel pairs and their spatial distribution along the path of the incident particle depend strongly on the nature and energy of the particle. Fast neutrons, for instance, have relatively small elastic and inelastic collision cross sections, so neutron-lattice atom interactions energetic enough to produce primary knock-on atoms (PKA's) are relatively widely spaced. Typically, a fast neutron dissipates its energy over a path length that is on the order of centimeters. A PKA produced by these collisions may receive much more energy than that necessary to displace it, in which case it initiates displacement sequences of its own. The PKA becomes immediately ionized as it collides with other lattice atoms, dissipating its energy both through electronic collisions that do not result in further displacements, and through elastic nuclear collisions, which may produce higher order knock-on atoms. The collision cross section is large for these knock-on atoms, so the entire PKA energy is dissipated in a very localized region. These concentrated pockets of vacancy and

interstitial defects are termed collision cascades or displacement spikes, and will be discussed in detail later.

If the metal is irradiated with ions rather than neutrons, as in this study, the primary defects are likewise generated within displacement cascades, but the spatial distribution of the cascades themselves is compressed. The incident ion interacts much more strongly than the neutron with the lattice atoms, so the initial ion energy is dissipated over a path length of microns rather than centimeters. Displacement damage therefore occurs only in the near-surface region. The displacement cascades are closely spaced and in fact may overlap. Another characteristic of ion radiation is that the concentration of displacements increases along the path of the incident ion, because the nuclear collision cross section increases as the ion velocity decreases. The displacement rate near the end of the range of the ion may be an order of magnitude greater than at the surface. In contrast to neutrons or ions, high energy electrons (.5 - 5 MeV) produce only one or two displacements per nuclear collision, so isolated point defects rather than displacement cascades are formed. The range of such electrons is on the order of millimeters.

The radiation effects that ultimately occur in the metal depend in part on the total number of Frenkel pairs produced during irradiation. For this reason, and to provide a basis of comparison between radiation damage experiments, the dpa (displacements per atom) is commonly used as the basic measure of radiation damage. A dose of 1 dpa administered to a certain volume of atoms indicates, on the

average, each atom in that volume has been displaced from its lattice site once during irradiation. In addition to dpa level, there are several qualitative criteria, regarding primary defect production, which must be considered in interpreting the radiation effects and in correlating the results of different experiments; a) the initial spatial distribution of the vacancies and interstitials, which affects their probability of recombination; b) impurities that are introduced co-incidentally with the defect production; and c) the damage rate. Damage rate effects will be discussed later, since they influence the behavior of defect cluster formation. This section describes the method by which the dpa profile is calculated for an ion-bombarded metal, and also discusses the effect of the initial spatial distribution of the displaced atoms on primary defect survival.

Dpa calculation

The distribution of the displacement damage in a material bombarded with monoenergetic ions is determined as follows: a) The energy loss due to electronic excitation and to nuclear collisions of an average ion is calculated as a function of depth, x, into the metal; from this calculation the range of the ion is also found. b) Energy dissipated through nuclear scattering at a depth x is then converted into atomic displacements at x, using a suitable formula. The most widely accepted model for determining energy loss of an ion is based on the theoretical work of Lindhard, Scharff, Schiott (LSS), and others.[1-6]

Application of this theory to radiation damage calculations has been discussed previously (e.g., see Kulcinski et al.[7]), but is outlined here. LSS theory separates the scattering into a quasi-elastic part that describes particle deflection or ion-atom scattering, and an electron-excitation part that contributes only to the energy loss. The theory is based on a universal nuclear-stopping cross section calculated from a Thomas-Fermi statistical model of the atom. It is applicable to many ion-target combinations over a wide energy range, using only a small number of parameters. The target is assumed to be amorphous.

LSS[5] uses a screened-coulomb potential to describe the ion-target atom interaction, with a screening radius $a = 0.8853\ a_o\ (Z_1^{2/3} + Z_2^{2/3})^{-1/2}$, where a_o is the Bohr radius. For the case of ions colliding with atoms at rest, this leads to the use of dimensionless parameters for the ion range, R, and initial ion energy, E, respectively:

$$\rho = RNM_2\ 4\pi a^2 M_1/(M_1 + M_2)^2 \qquad (2.1)$$

$$\varepsilon = EaM_2/Z_1Z_2e^2(M_1 + M_2) \quad . \qquad (2.2)$$

In the expressions for a, ρ and ε, the subscripts 1, 2 denote the incident ion and target atom, respectively; M is the atomic mass; Z is the atomic charge; and N is the target atom density. Using an extrapolated perturbation method for scattering in the screened Coulomb potential, Lindard obtains a universal differential scattering cross section for the nuclear collisions:

$$d\sigma = \pi a^2 \frac{dt}{2t^{3/2}} f(t^{1/2}) \tag{2.3}$$

where $t^{1/2} = \varepsilon \sin(\theta/2)$, and is the center-of-mass scattering angle. The function $f(t^{1/2})$, which depends on the screening function, was calculated numerically by Lindhard.[5] Winterbon et al.[8] later obtained an analytical approximation for this function:

$$f(t^{1/2}) = 1.309\ t^{1/6}\ (1 + 1.9t^{4/9})^{-3/2} \quad . \tag{2.4}$$

In dimensionless form the nuclear stopping cross section is given by

$$(d\varepsilon/d\rho)_n = \int_0^{\varepsilon} dx\ f(x)/\varepsilon \quad , \quad \text{where } x = t^{1/2} \quad . \tag{2.5}$$

LSS theory assumes the electronic stopping is proportional to ion velocity[1-3], i.e. in reduced form,

$$(d\varepsilon/d\rho)_e = k\sqrt{\varepsilon} \tag{2.6}$$

where k is a constant that varies slowly with Z_1 and Z_2 (usually $0.1 < k < .2$). For self ion irradiation[5] $k = 0.133\ Z^{2/3}\ A^{-1/2}$; for Cu on Cu, $k = .157$. Equation (2.6) is valid only if the incident ion energy is less than $25\ Z_1^{4/3}\ A_1$ (KeV); therefore, for Cu on Cu the ion energy must be less than 141 MeV. There is experimental evidence that Eq. (2.6) overestimates the electronic stopping for heavy ions incident on copper. Narayan et al.[9-11] bombarded copper specimens with 1 MeV protons and alpha particles, and with high energy Ni and Cu ions (4 MeV - 58 MeV), then studied the damage regions in cross section to compare the range of the observed displacement damage with the range predicted by LSS theory.

In the 1 MeV proton-irradiated specimens, the range of the ions as indicated by the cutoff in the defect clusters, and the overall profile of the damage distribution, was in good agreement with that predicted by LSS theory. The agreement with theory was not as good for the Cu and Ni ion bombarded specimens. The experimental damage profiles were compared with calculated E-DEP-1 damage energy profiles, using various forms for the electronic stopping. From this the correct electronic stopping powers as a function of energy were deduced. LSS theory, with the LSS predicted values of the proportionality constant k, consistently underestimated the peak damage position for Cu and Ni ions incident on copper. Disagreement was greatest (~ 25%) for low energy ions, but improved to with a few percent of the observed results for the highest energy ions. Agreement with LSS calculations was obtained by reducing the value of the proportionality constant k in the electronic stopping formula. For the higher energies it was necessary to use an electronic stopping power of the form $d\varepsilon/d\rho = k_2\ \varepsilon^{1/2} - C$ to obtain agreement. Hence, the electronic stopping of the Cu and Ni ions in copper is not proportional to the ion velocity as predicted by LSS theory.

The total stopping cross section is simply the sum of Eqs. (2.5) and (2.6), so the average path length of the ion is

$$\rho = \int_0^{\varepsilon} d\varepsilon[(d\varepsilon/d\rho)_n + (d\varepsilon/d\rho)_e]^{-1} \quad . \tag{2.7}$$

Lindhard, Scharff and Schiott[5] calculated the variation of ρ with ε, for various values of k. From these curves, and using Eqs. (2.1)

and (2.2), the range-energy relationships for most ion-target combinations (within the valid energy range) can be estimated. In practice the projected range is usually of more interest than the path length, although for heavy ion irradiation these quantities are very similar. It should be noted that Eq. (2.7) represents only the range of an average particle, while in reality there is a distribution of ranges due to straggling. The spatial distribution of the injected atoms is often represented as a normal Gaussian distribution.

The displacement rate in a region dx at depth x in the target can now be determined if the total energy loss through nuclear elastic collisions in dx is known. The average energy, E'(x) dissipated (to a PKA) by the incident ion x is found by the methods just discussed. However, only a portion of E'(x) results in displacements, the remainder being lost through electronic excitation as the PKA slows down. Lindhard et al.[4] derived a relatively simple expression relating E'(x) to the energy available for displacements, $S_D(x)$:

$$S_D(x) = E'(x)/[1 + kg(\varepsilon)] \tag{2.8}$$

where $g(\varepsilon)$ is a universal function that $\to 0$ as $\varepsilon \to 0$, and $g(\varepsilon) \to \varepsilon$ for $\varepsilon \gtrsim 100$. A numerical approximation to $g(\varepsilon)$ was derived by Robinson[12]:

$$g(\varepsilon) = 3.4008\ \varepsilon^{1/6} + 0.40244\ \varepsilon^{3/4} + \varepsilon \quad . \tag{2.9}$$

Several models have been proposed[13] for calculating the number of displacements from the deposited nuclear energy. Using the modified Kinchin-Pease model of Torrens and Robinson[14] the displacement rate (dpa/sec) at x, for an incident particle flux ϕ cm^{-2} sec^{-1} on a target of atomic density N, is

$$N_d(x)(dpa/sec) = (\phi/N)(\beta S_D(x)/2E_d) \quad . \tag{2.10}$$

The factor β is the displacement efficiency, which depends on the form of the interatomic potential. Computer simulations[14] of displacement cascades in cubic metals have indicated that $\beta \sim 0.8$. The effective displacement energy, E_d, is the average energy that must be transferred to an atom to displace it from its lattice site. E_d varies by a factor of 2-3 with crystallographic direction. The value used in Eq. (2.10) is obtained by multiplying the minimum displacement threshold energy, E_d', by a factor of 5/3 to compensate for the directional dependence. In copper, Makin[15] found E_d' to be 20-25 eV, therefore E_d is about 33 to 40 eV. The value of E_d is not critical in high energy ion bombardment because most displacements occur at energies much greater than E_d.

Manning and Mueller[16] have incorporated the Lindhard slowing down theory into a computer code, E-DEP-1, which calculates the energy deposition and the injected ion distribution as a function of depth. Brice[17] has also developed a code based on LSS theory, which is more sophisticated than E-DEP-1 in that the energy transported by recoil atoms is calculated. The electronic stopping can be

calculated by a semi-empirical three-factor formula, therefore calculations involving light-ion irradiation (e.g., C or N) can be performed at much higher energies than allowed by LSS theory. The Brice code is used in this work to calculate the damage-energy deposition profile, and the distribution of implanted ions, for 14 MeV Cu ions incident on a copper target.

Spatial Distribution of the Damage

The dpa level alone is not an accurate measure of radiation damage, since long-term radiation effects are caused by the residual defects that remain in the lattice after the annealing of the displacement event. The number of surviving defects depends strongly on the initial spatial distribution of the displacements. It was explained earlier that neutron and ion irradiation produce displacements in the form of highly localized displacement cascades. Since the cascade forms and anneals too quickly for experimental observation, most information on the interstitial and vacancy behavior within the cascade has come from computer simulation studies (e.g., summarized in Olander[18]). These studies indicate that immediately after formation, the displacement cascade probably exists as a vacancy rich core surrounded by an interstitial rich shell. This highly unstable configuration remains for $\sim 10^{-13}$ sec, followed by an annealing period of about a microsecond, during which relative stability is achieved. The proximity of vacancies and interstitials within the cascade leads to spontaneous recombination of a large fraction of the initial displacements. The remaining defects either

escape, or, if the temperature is not too high[19], remain behind as immobile clusters (residual vacancy clusters are much more likely to remain than interstitial clusters). Cluster formation further reduces the number of free defects, and also provides nuclei for secondary defects such as voids and dislocation loops. In a Monte Carlo simulation of a 20 KeV cascade at 525°C, Doran[20] found that only about 20% of the defects did not recombine during the anneal; only 7% of the vacancies survived as monovacancies while the remaining 13% existed as immobile clusters of three or more.

It is possible to measure the number of free defects that escape to the matrix, and the number of defects that become incorporated into observable clusters. Blewitt et al.[21] measured resistivity changes in fast neutron irradiated, disordered Cu_3Au specimens to determine the fraction of vacancies that escaped the cascades. Compared to Kinchin-Pease model estimates, only ~ 2% escaped, while ~ 8% escaped if compared to experimental estimates of the number of initial defects in the cascades. Narayan et al.[9-11] measured cluster size distributions in copper following room temperature irradiation with 1 MeV H^+ and He^{++}, and with 5-58 MeV Cu or Ni ions. Only ~ 1% of the displaced atoms theoretically produced by the light ions were retained as visible defect clusters, while 4-6% were retained after the heavy ion irradiations. Some defects, of course, are lost through recombination and through capture at sinks, so those retained as clusters represent only a fraction of those that escape the cascades.

B. Defect Cluster Formation

At sufficiently high temperatures ($\gtrsim 0.3\ T_{mp}$) where both vacancies and interstitials are mobile, defects that escape recombination within the displacement cascades diffuse throughout the matrix. During steady-state irradiation, a dynamic balance is quickly established between the defect generation rate, and the rate at which defects are lost through mutual recombination in the matrix and absorption at sinks (e.g., free surfaces, grain boundaries, dislocations, and defect clusters). The theoretical steady-state concentrations of vacancies and interstitials, C_v and C_i, respectively, are usually found by solving a pair of simultaneous equations that describe the production and loss of the defects in terms of chemical-reaction rate theory. Since the rate theory formalism is also used to model the growth of defect clusters, the determination of C_v and C_i is deferred until then. The point to be made here is that the vacancy and interstial concentrations under irradiation are always greater than the thermal equilibrium concentrations, $C_{i,v}^{eq}$, so the material is supersaturated by an amount

$$S_{i,v} = C_{i,v}/C_{i,v}^{eq} \tag{2.11}$$

where the subscripts i, v refer to the interstitials and vacancies, respectively. Under certain conditions a fraction of the defects precipitate into clusters -- vacancies into dislocation loops or voids, and interstitials into dislocation loops -- which alter the physical properties of the material. The type and concentration of

clusters that form and their growth characteristics depend on many factors — temperature, irradiation variables, microstructure of the material, applied stress, etc. One property change of particular interest is macroscopic swelling caused by void formation. If interstitial atoms condense into dislocation loops or are incorporated into dislocation networks, while vacancies condense into dislocation loops, then the macroscopic volume of the material remains unchanged. However, if vacancies condense into three-dimensional voids rather than planar loops, net swelling of the material occurs. The technological importance of swelling has caused much of the theory of defect cluster formation to center on void formation. This section summarizes the accepted theoretical models of void and dislocation loop formation under steady-state irradiation, with the aim of identifying the many physical processes involved in these phenomena.

The evolution of a void or dislocation loop can be separated into two phases — nucleation and growth. The former refers to the statistical process of the agglomeration of point defects into clusters that are unstable below some critical size. The growth phase, which is better understood than nucleation, refers simply to the growth of stable clusters with time. Although both nucleation of new clusters and growth of stable clusters often occur simultaneously during irradiation of a material, for modeling purposes it is necessary to treat cluster formation as a sequential process of nucleation followed by growth.

Nucleation of defect clusters under irradiation is fundamentally different than traditional nucleation, such as precipitation of a second phase in an alloy, because the impingement of defects of opposite types can cause either growth or shrinkage of a cluster.[22] Therefore, classical nucleation theory cannot be directly applied to void or dislocation loop formation. In the classical case, the precipitate cluster grows by the addition of a single atom, and shrinks by the emission of an atom.[23] During irradiation, however, when large concentrations of both vacancies and interstitials are present, a vacancy cluster, for example, grows by the addition of a vacancy or by the emission of an interstitial (which is rather unlikely), and shrinks by the opposite process. Experiment has shown that the presence of gas atoms and other impurities can greatly influence the nucleation rate, so three or more species must often be taken into account when modeling the nucleation process. Also, classical nuclei draw from a population of atomic species that is initially fixed, while irradiation induced defect clusters form from defects that are created continuously.

Void Nucleation

The nucleation of stable vacancy clusters in general requires that three conditions be satisfied simultaneously: a) a substantial vacancy supersaturation must exist; b) the vacancies must be highly mobile; and c) either a net excess flux of vacancies must impinge upon the cluster, or the clusters must be structured so that vacancies rather than interstitials are preferentially absorbed. The

supersaturation and mobility requirements are satisfied during irradiation between ~ 0.3-0.6 of the melting point of the metal, provided that high concentrations of defect trapping sites do not exist. The third requirement depends strongly on the microstructure of the material. There are a number of possible mechanisms by which nucleation may occur[24]: a) homogeneous nucleation of vacancies and interstitials only; b) heterogeneous nucleation on an immobile gas atom or gas atom cluster; c) nucleation in which mobile gas atoms precipitate simultaneously with vacancies and interstitials; d) development of a vacancy cluster directly from the vacancy rich core of a displacement cascade; and e) nucleation in the presence of surface active impurities. In homogeneous nucleation, clusters form as the result of random encounters of vacancies and interstitials that are migrating throughout the matrix. Small clusters of one defect type that happen to form are easily annihilated when opposite-type defects impinge on them, or when defects of the same type are emitted. Only a small fraction of all embryonic clusters will absorb enough defects of the same type to grow beyond some critical size, x. This size is dependent on energy considerations and other parameters; beyond it, growth rather than annihilation of the cluster is likely. Heterogeneous nucleation occurs in a similar manner, except the clusters form on impurities or structural defects where cluster formation is favored relative to that in the matrix. Nucleation theory, then, is aimed at determining the rate (clusters/cm^3 sec) at which clusters surpass the critical size.

Similar theories of homogeneous nucleation of voids in the absence of gas or impurity atoms were developed simultaneously and independently by Katz and Wiedersich[22,25] and by Russell[26]. They extended and generalized the ideas of classical nucleation theory by considering void formation in the presence of arbitrary supersaturations of vacancies and interstitials, where the void distribution is not in equilibrium with either defect, as is the case during irradiation. The nucleation rate is expressed as a flux of clusters between adjacent size classes in a one-dimensional phase-space, where the size of a cluster is characterized by its vacancy content.[26] The flux between clusters containing n and (n + 1) vacancies, respectively, is:

$$J_n = \beta_v(n)\rho(n) - \alpha_v(n+1)\rho(n+1) - \beta_i(n+1)\rho(n+1) \quad (2.12)$$

where $\rho(n)$ and $\rho(n+1)$ are the numbers of clusters containing n and (n + 1) vacancies respectively. $\beta_v(n)$ is the rate of vacancy capture by a cluster of size n, $\beta_i(n+1)$ the rate of interstitial capture by a cluster of size (n + 1), and $\alpha_v(n+1)$ is the rate of vacancy emission by that cluster. The interstitial emission rate is small enough to be neglected. The vacancy emission rate, α_v, is obtained by applying detailed balancing[27] principles to voids that are in equilibrium with each other. This implies that the supersaturated vacancies are in equilibrium with the voids and with the interstitial populations, so the interstitial concentration, C_i, is very low. At equilibrium the voids are found to exist in a Maxwell-Boltzmann

distribution, given by the function

$$\rho^{o}(n) = N_{o} \exp(- \Delta G_{n}^{o}/kT) \tag{2.13}$$

where ΔG_{n}^{o} is the free energy of formation of a void of size n and N_{o} is the atomic site concentration. ΔG_{n}^{o} depends on the void size, the void-matrix surface energy, and on the vacancy supersaturation. Detailed balancing yields the following expression for $\alpha_{v}(n + 1)$, which is then inserted into Eq. (2.12):

$$\alpha_{v}(n + 1) = \beta_{v}(n)\rho^{o}(n)/\rho^{o}(n + 1) \quad . \tag{2.14}$$

The defect capture rates β_{i} and β_{v} are derived from diffusion theory, assuming the clusters are neutral, spherical sinks.

An expression is obtained for the steady-state void nucleation rate, J_{k}, which is superficially similar to the classical equation. According to Russell,[26,28]

$$J_{k} = Z'\beta_{k}N_{o} \exp(-\Delta G_{k}'/kT) \tag{2.15}$$

where β_{k} is the rate at which vancancies impinge on the critical nucleus. The factor $\Delta G_{k}'$ is the activation barrier for nucleation, which depends on the defect arrival ratio β_{i}/β_{v}, and on ΔG_{n}^{o}. Z' is analogous to the Zeldovich factor, and is a function of the second derivative of $\Delta G_{n}'$ evaluated at the critical nucleus size. Another factor of interest in the theory is the incubation time, $\tau = (2Z'^{2}\beta_{k})^{-1}$, the time necessary for steady-state nucleation to become established.

Powell and Russell,[28] and Katz and Wiedersich[25] evaluated the nucleation rate and the incubation time using parameters typical of nickel or stainless steel in a breeder reactor environment. The capillarity model[26] was invoked in estimating ΔG_n^o, which was then used in determining the activation barrier ΔG_n^* for the nonequilibrium case. Both J_k and τ were found to be extremely sensitive to the defect arrival rate ratio, β_i/β_v, and to the vacancy supersaturation, S_v. At 500°C, increasing β_i/β_v from 0 to 0.99 greatly broadened the activation barrier, decreased J_k by several orders of magnitude, and increased τ by a factor of $\sim 10^4$ at constant supersaturation.[28] The critical cluster size also increased sharply as $\beta_i/\beta_v \to 1$, although the increase became less dramatic as S_v increased. At $\beta_i = \beta_v$, nucleation could not occur since each incoming vacancy was matched by an incoming interstial. When the defect arrival rate was held constant but S_v was increased by a factor of 10, the nucleation rate increased by at least several orders of magnitude. However, the incubation time τ decreased by only the amount that S_v was increased, indicating that τ is much more dependent on the interstitial involvement than on the vacancy supersaturation. The behavior of the void nucleation rate with respect to β_i/β_v implies that in a real material, voids form only if mechanisms exist that ensure $\beta_i/\beta_v < 1$. It is well known[27] that one such mechanism is the bias of dislocation sinks for interstitials; i.e. the effective capture-radius of a dislocation for an interstitial atom is somewhat larger than for a vacancy, therefore more interstitials than vacancies are captured.

This reduces the interstitial concentration in the matrix, so a net excess number of vacancies flows to voids. Although most nucleation theories[22-33] have assumed that voids are neutral sinks, calculations by Mansur and Wolfer[34], and by Wolfer et al.[35,36] have shown that small, bare voids possess a strong interstitial bias due to an image force interaction. This would keep $\beta_i/\beta_v > 1$ and prohibit void nucleation and growth. Because segregation of impurity atoms to voids has been observed experimentally and predicted theoretically, these authors suggested that an impurity surface coating may be necessary for a void to nucleate. Calculations[34] have indicated that a void coating greatly reduces the interstitial capture efficiency of a void. Furthermore, the impurities lower the activation barrier to nucleation by reducing the void-matrix surface energy.

Subsequent void nucleation theories focussed on nucleation in the presence of gas atoms or other impurities. Inert gases, particularly helium that is ion implanted or generated by transmutation reactions, are known to enhance void formation. The theoretical treatment depends on the mobility of the gas atoms relative to the mobility of the vacancies.[27,30] Katz and Wiedersich[31,37] developed a model that viewed the nucleation process as the sum of independent, parallel nucleation processes, i.e. homogeneous nucleation as described above, and heterogeneous nucleation on a pre-existing distribution of single immobile He atoms or He atom clusters. Assuming the He to be immobile allows the growth of the cluster to be determined

only by the number of vacancies it contains, since the cluster retains the number of gas atoms it started with. When insoluble gas atoms are incorporated into a vacancy cluster, the formation energy of the cluster must be described in terms of both the number of gas atoms, x, and vacancies, n, that the cluster contains. Therefore, the activation barrier to nucleation is described by a surface in (n,x) space, and the critical nucleus size corresponds to the saddle point on that surface. Insoluble gas atoms contained within a vacancy cluster stablize the cluster against annihilation by interstitials, because the addition of a interstitial requires work to compress the gas. The void nucleation rate can thereby be greatly enhanced. One calculation[23] showed a 10^2 to 10^4-fold increase in the nucleation rate, relative to homogeneous nucleation, for 10 ppm He in stainless steel at 500°C, where $\beta_I/\beta_V = 0.98$ and $S_V = 10^3$ to 10^4.

In reality, even gases such as helium are not completely immobile in a metal in the temperature range where voids form. Complete immobility would in fact preclude the existence of gas clusters as assumed in the above model. If the gas or impurity atoms have limited mobility -- on the order of that of a vacancy -- the nucleation process consists of a simultaneous precipitation of vacancies, interstitials and foreign atoms. Russell[29] found that under such conditions an analytical expression for the nucleation rate cannot be obtained and numerical methods must be used. An analytical solution exists only if the impurity is very immobile, or if it is so mobile that the cluster reaches equilibrium between vacancy captures. An

attempt was made by Wiedersich, Burton and Katz[32] to numerically determine nucleation rates in the case of intermediate helium mobility. However, their results greatly overestimated the nucleation rate because of a mathematical error[33] that was made in deriving the helium arrival rate.

Russell[24,33] has recently developed a comprehensive theory describing void nucleation via a critical point/nodal line formalism. The most probable behavior of a void containing n vacancies and x impurity atoms is given by a velocity in the (n,x) plane, which equals the sums of jump frequencies times unit jump vectors. The jump vectors (Fig. 2.4) represent the physical processes involved in nucleation and have the same meaning as in previous theories. Radiation resolution of an impurity or gas atom in the void is included in this theory, represented by the resolution parameter K_x^c. The velocities of a cluster in the (n,x) plane are

$$\dot{n} = \beta_v^o n^{1/3} - \alpha_v - \beta_i^o n^{1/3} \tag{2.16}$$

$$\dot{x} = \beta_x^o n^{1/3} - \alpha_x - xK_x^c \tag{2.17}$$

where the $n^{1/3}$ factor accounts for the dependence of the defect capture rate on the void size. The impingement frequencies β and the emmission rates α are derived as in previous theories[22,25,26] (Eqs. 2.13, 2.14). Hence, the velocities (Eq. 2.16) and (Eq. 2.17) become dependent on $\Delta G^o(n,x)$, the free energy of forming an (n,x) cluster in the metal.

Russell proceeds by inserting the appropriate value of $\Delta G^{o}(n,x)$ into the velocity equations, thereby obtaining equations for the nodal lines where $\dot{n}$ and $\dot{x}$ are equal to zero. The nodal lines divide the (n,x) plane into various regions, and intersect at so-called critical points. A qualitative understanding of void nucleation trends as a function of vacancy content and impurity atom content is obtained by examining the location of the critical points and the direction of the velocity vectors that characterize each region. The nucleation rate is calculated using the equations that were derived in previous theories.

Several interesting results of Russell's analysis are: a) under conditions that may exist during neutron irradiation, or during heavy ion irradiations of He doped samples, spontaneous void nucleation may occur. Voids may develop from elementary point defects without passing over a nucleation barrier; b) under certain conditions, metastable gas-containing embryos may exist that cannot grow spontaneously, but which may serve as heterogeneous void nucleation sites, or which may contribute strongly to the overall sink density of the material; c) dissolved gases may greatly enhance void formation by reducing the void-matrix surface energy, but they cannot lead to spontaneous nucleation; d) synergetic effects between inert gases and surface active solutes may greatly enhance the nucleation rate.

Still another approach to nucleation is a unified formulation developed by Wolfer et al.[36], which describes both nucleation and growth. The void size variable, x, is assumed to be continuous (for

$x \gg 1$), which leads to a Fokker-Planck equation for the evolution of the void size distribution

$$\partial f(x,t)/\partial t = -\partial/\partial x \{F(x) - \partial/\partial x\, D(x)\}\, f(x,t) \qquad (2.18)$$

where $f(x,t)$ is the size distribution function, $F(x)$ is the drift force, and $D(x)$ is a space dependent diffusion coefficient. Here the critical void size x^* is defined by $F(x) = 0$, and void growth occurs when $F(x) > 0$.

Void and Loop Growth

A vacancy cluster that surpasses the critical size will continue to grow if the conditions prevail that allowed void nucleation in the first place, i.e. vacancy mobility and supersaturation, and net absorption of vacancies by the void. Void growth generally occurs at irradiation temperatures between about 0.3 to 0.5 T_{mp}, and is heavily dependent on the purity and microstructure of the material. The most successful and widely used model of void growth or dislocation loop growth is based on the formalism of chemical reaction rate theory, where physical processes that are actually discrete in space and time are modeled as if they occur continuously and homogeneously throughout the material. In this theory, the rate of change of the point defect concentrations or the growth of a defect cluster is expressed through conservation equations, which describe each relevant physical processes in terms of an appropriate reaction rate coefficient. The basic rate equations for void and loop growth are presented in this section. Recent reviews of the application of rate theory to void

swelling, by Mansur[38] and by Brailsford and Bullough[31], have been used as a guide.

The rate theory approach was first applied by Harkness and Li[40] in 1971, and was further developed by Wiedersich[41] and by Brailsford and Bullough[42]. The growth rate of a void of radius r_v is determined by the net flux of vacances per unit void are per unit time,[38]

$$dr_v/dt = (\Omega/r_v)\{Z_v^v(r_v)D_vC_v - Z_v^v(r_v)D_vC_v^e(r_v) - Z_i^v(r_v)D_iC_i\} \quad (2.19)$$

where $D_{v,i}$ are the vacancy and the interstitial diffusion coefficients, respectively, $Z_{v,i}^v$ are the capture efficiencies of voids for vacancies and interstitials, respectively, and Ω is the atomic volume. The term containing $C_v^e(r_v)$ is the thermal vacancy emission rate of the void. $C_v^e(r_v)$ is the thermal vacancy concentration at a void of radius r_v, $C_v^e(r_v) = C_v^e \exp(-(P_g - 2\gamma/r_v)\Omega/kt)$, where C_v^e is the bulk thermal vacancy density, P_g is the gas pressure in the void, and γ is the void-matrix surface tension. The vacancy and interstitial concentrations $C_{v,i}$ respectively, are found by solving two coupled conservation equations for the defects. For a homogenized medium under irradiation, where defect trapping is not important, the point defect concentrations at steady-state are given by

$$dC_v/dt = G_v - RC_vC_i - K_vC_v = 0 \quad (2.20)$$

$$dC_i/dt = G_i - RC_vC_i - K_iC_i = 0 \quad . \quad (2.21)$$

The effective vacancy generation rate is $G_v = G + G^e$, where G

accounts for vacancies produced directly by irradiation, and G^e accounts for vacancies re-entering the matrix due to thermal re-emission by the sinks. Since thermal emission of interstitials is negligible, the interstitial generation rate is just G. R, the recombination coefficient, can be expressed as $4\pi r_o(D_i + D_v)$, where r_o is the radius of the point defect recombination volume.(38)

Most of the physics of the rate theory model lies in the reaction rate constants K_v and K_i, which describe the loss of vacancies and interstitials, respectively, to sinks. There are j types of sinks, such as voids, dislocations, etc., which are modeled as distributed throughout the continuum, so $K_v = \sum_j K_v^j$, and $K_i = \sum_j K_i^j$. The rate constant for a specific type of sink, j, is expressed as $K_{i,v}^j = S_{i,v}^j D_{i,v}$, where $S_{i,v}^j$, the sink strength, is itself composed of three multiplicative constants.(38) The sink strength is expressed as the product of a geometric parameter g^j, a sink capture efficiency Z^j, and a multiple sink correction factor m^j. Here g^j describes that property of a sink that defect absorption is proportional to, such as dislocation line length; Z^j is the ratio of the point defect current of the real sink to that which would occur if the sink was a perfect absorber of point defects and created no stress field that interacted with defects; finally, m^j accounts for interactions thay may occur between sinks. The strength of a particular type of sink for a given type of point defect is determined by solving a diffusion problem for a discrete sink in an effective sink-containing medium.(39,42,43) To accurately model a material under

irradiation the time evolution of the microstructure must be considered. The overall sink strength of the material changes with dose because new sinks form (e.g., the voids and dislocation loops themselves) and because saturable sinks (e.g., sessile dislocations, coherent precipitates, solute atoms) can accommodate only a finite number of defects.

Interstitial dislocation loops form over a much wider temperature range and at lower doses than voids. In general, they precede voids and help provide the bias necessary for void formation, and they are more stable than voids at high temperature. The growth of an interstitial loop of radius r_l is given by[38]

$$dr_l/dt = a^2 \{Z_i^l(r_l)D_iC_i + Z_v^l(r_l)D_vC_v^e(r_l) - Z_v^l(r_l)D_vC_v\} \quad (2.22)$$

where $C_v^e(r_l) = C_v^e \exp(-(\gamma_f + E_l - \sigma a)/kT)$ is the thermal equilibrium vacancy concentration at the loop, γ_f denotes stacking fault energy, σ is the hydrostatic stress and a is the lattice parameter. The first and second terms in Eq. (2.22) indicate that the loop grows both by interstitial capture and by thermal vacancy emission, respectively, while the third term denotes loop shrinkage by vacancy capture. Wolfer and Yoo[44] have shown that for small ($r_l \lesssim 50$ Å) dislocation loops the bias factor for interstitials, Z_i^l, is significantly greater than that for vacancies, Z_v^l; therefore, the interstitial dislocation loop is an inherently stable structure. This theoretical prediction is borne out by numerous experimental observations of

continuous interstitial loop growth during irradiation, as discussed in the following section.

The growth of a vacancy dislocation loop is given by an expression similar to Eq. (2.22), except the sign of each term is reversed. Thus, the vacancy loop shrinks by interstitial capture and by vacancy emission, and since $Z_i^l > Z_v^l$ for small loops, the vacancy loop is inherently very unstable. Under equal point defect generation rates the vacancy loop cannot nucleate and grow unless a mechanism exists to relieve the interstitial bias. However, there is extensive evidence[45] that vacancy loops, which are observed in irradiated metals, skip the nucleation step and form directly from the collapse of the vacancy-rich center of the displacement cascade. At about room temperature and below, where vacancies are immobile, this is the only way vacancy loops can be created. At temperatures above the onset of void formation vacancy loops anneal quickly after forming, due to thermal vacancy emission.

C. Effects of Alloying Elements on the Nucleation and Growth of Defect Clusters

Alloying elements affect the delicate balance that exists between the processes of point defect generation, annihilation at sinks, and cluster formation. The complicated nature of these processes coupled with the unique properties of a given alloy system prohibits the formulation of a general theory. However, specific effects can be modeled and then incorporated into the theoretical framework that has been presented in the previous sections. This

discussion is restricted to materials whose total impurity concentrations are less than several atomic percent, e.g., a dilute binary alloy.

There are three general ways that solute or impurity atoms can influence the formation of voids and dislocation loops. First, foreign atoms may interact directly with defect clusters to change their nucleation and growth characteristics. The effects of surface active impurities in reducing the free energy of void nucleation, gaseous impurities in stabilizing void nuclei, or a solute shell in changing the bias of small voids or loops, have been discussed in the previous section. The influence of such impurities on the growth rates of voids or dislocation loops is found through the growth Eqs. (2.19) and (2.22). An impurity-induced change in the void surface energy, γ, or in the loop stacking fault energy, γ_{sf}, alters the growth rates through the thermal vacancy emission terms in these equations. Another phenomenon in which impurity atoms interact directly with the defect clusters is the enrichment of the solute concentration (not necessarily formation of a precipitate shell) around a void or loop due to solute segregation.[46-57] The mechanisms responsible for solute segregation are discussed in detail in the next chapter. Anthony[49] was the first to hypothesize that the presence of an enriched solute shell could alter the growth rate of a void by changing the vacancy diffusion coefficient and the vacancy chemical potential in the zone around the void. Alteration of the surface energy of the growing void could change the vacancy

concentration in equilibrium with the void, thereby inhibiting void growth. In addition, solute-solvent size differences that generate stresses near the solute shell could influence the magnitude of the vacancy current impinging on the void. Brailsford[51], and Mansur and Wolfer[38,52] found that a solute shell around a void could change the void capture efficiency, $Z^v_{v,i}$, for a vacancy or interstitial. Brailsford assumed the diffusion coefficient for vacancies in the shell, D^s_v, was different from that in the matrix D_v. Therefore, for a shell of thickness δ, the capture efficiency of a void of radius r_v for a vacancy becomes $Z^v_v(r_v) = (1 + \delta/r_v)/(1 + D_v\delta/D^s_v r_v)$, where $Z^v_v(r_v)$ equals unity for an uncoated void.

Mansur and Wolfer[52] found that differences between the elastic constants of the solute shell and the matrix produce an energy barrier to the incorporation of point defects. This results in a capture efficiency given approximately by $Z^v_{i,v}(r_v) = ((r_v/r_c) + r_v D_{i,v}/(r_c + \delta)^2 w_{i,v})$, where $r_c \approx r_v$. Here $w_{i,v}$ is the transfer velocity of the defect at the void, given by $w_{i,v} = (D_{i,v}/a) \exp(-E_{i,v}/kT)$, a is the lattice parameter, and $E_{i,v}$ is the largest positive value of the repulsive interaction energy. Since E is proportional to the square root of the point defect relaxation volume, the larger repulsion of the interstitial makes Z^v_i much smaller than Z^v_v; i.e. interstitial capture is inhibited so void growth is enhanced.

The second general mechanism by which foreign atoms may influence void and loop growth is by changing the concentrations of free vacancies and interstitials in the matrix. For instance, if the

impurity atoms sufficiently disrupt the crystallographic perfection of the metal, the initial configuration of the displacement cascades, and hence the number of free defects that escape the cascades may be changed.[38] In this process, focussing sequences that help transport interstitials away from the vacancy rich core of the cascade are disrupted, thereby enhancing point defect recombination within the cascade. Another direct means of reducing the point defect concentration in the matrix is point defect trapping, which is discussed below in detail.

A third, indirect, mechanism of solute atom influence is solute interaction with other structures or impurities within the crystal that play a role in point defect cluster formation. For instance, solutes may tie-up active impurities such as oxygen or hydrogen that would influence void or loop formation. Solute atoms may interact with defect sinks, such as dislocations, and change their bias or capture efficiency, which in turn alters the concentration of free defects available for cluster formation. Since the cluster growth rate is proportional to the difference between the impinging vacancy and interstitial fluxes, small changes in these flux levels may result in large changes in the cluster growth rate.

Point defect trapping is considered an important mechanism for influencing the irradiation behavior of an alloy by reducing the vacancy and interstitial populations.[47,48,58-60] The trapping is the result of an affinity (which can be described by a binding energy) between a point defect and a solute atom, a solute atom

cluster, or a coherent precipitate. These structures often have different specific volumes or different electronic properties than the matrix, which produce localized strain fields or electrostatic fields that can interact with, and enhance the recombination of, point defects. By increasing the fraction of point defects that recombine in the matrix relative to those captured at sinks, the free defect concentrations available for other processes, such as void nucleation and growth, are reduced. Large reductions in void swelling following impurity additions to pure metals have often been attributed to point defect trapping (e.g., Refs. 44, 62); however, there have been relatively few direct observations of trapping, or direct measurements of binding energies. Blewitt[61] has shown, through measurements of the annealing kinetics of dilute copper alloys irradiated at low temperatures, that a strong interaction exists between interstitial copper atoms and certain types of solute atoms. In alloys containing 1 at% of the undersized solutes Be or Si, interstitials remained trapped at temperatures more than 100°K above the normal Stage I annealing temperatures. Similar concentrations of the oversized solutes Au or Zn affected Stage I annealing in a less drastic manner than Be or Si, while Ni impurities, which are similar in size and electronic structure to the Cu atoms, did not affect the annealing kinetics.

Several theoretical models have accounted for the effect of trapping on void growth either by modifying the recombination term[62] in the point defect conservation equations (Eqs. 2.20 and

2.21), or by deriving an effective vacancy diffusion coefficient[60] that accounts for the delay in diffusion when vacancies are trapped for a time. In the former case Harkness and Li[62] found that a concentration of 0.1% solute having a high interstitial binding energy, could increase recombination by a factor of $\sim 10^5$, and reduce void swelling by about 40%. In the latter case Schilling and Schroeder[60] found that by impeding diffusion, vacancy trapping increased the threshold temperature for the onset of swelling, with the amount of increase dependent on the defect-solute binding energy. In more sophisticated trapping models[38,39,47,48,59] the free-defect conservation equations have been modified to include trapping, and additional conservation equations are written for each trapped defect. The model discussed here, due to Monsur and Yoo[47], assumes solute-defect complexes are immobile, and describes a given type of trap by its concentration C_t, trapping radius, capture radius for a free-defect of the opposite type, and by its binding energy for point defects, E_i^b or E_v^b. With appropriate corrections this theory is valid for solute concentrations up to several percent.

If one type of vacancy and interstitial trap is assumed to exist in the material, then the quasi-steady state rate theory equations describing the conservation of free vacancies, free interstitials, trapped vacancies or trapped interstitials are respectively:

$$\frac{dC_v}{dt} = 0 = G_v - RC_iC_v - K_vC_v + \tau_v^{-1}C_v^1 - C_vR_iC_i^1 - C_vk_v(C^t - C_v^1 - C_i^1) \tag{2.23}$$

$$\frac{dC_i}{dt} = 0 = G_i - RC_iC_v - K_iC_i + \tau_i^{-1}C_i^1 - C_iR_vC_v^1 - C_ik_i(C^t - C_v^1 - C_i^1) \tag{2.24}$$

$$\frac{dC_v}{dt} = 0 = C_vk_v(C^t - C_v^1 - C_i^1) - \tau_v^{-1}C_v^1 - C_iR_vC_v^1 \tag{2.25}$$

$$\frac{dC_i^1}{dt} = 0 = C_ik_i(C^t - C_v^1 - C_i^1) - \tau_i^{-1}C_i^1 - C_vR_iC_i^1 \tag{2.26}$$

In Eqs. (2.23) and (2.24) the first three terms describe free defect production, loss through recombination of free-defects in the matrix, and loss through annihilation at sinks, respectively (see Eqs. 2.20 and 2.21). The fourth terms describe release of point defects from traps, where $\tau_{v,i}$ denote the mean time a defect is trapped, and $C_{v,i}^1$ are the trapped vacancy or interstitial concentrations, respectively. The fifth terms describe recombination of a given free defect with the opposite type of trapped defect, where $R_{i,v}$ are the recombination coefficients. The final terms describe loss of free defects due to

trapping of impurities, where C^t is the trap concentration and $k_{v,i}$ the capture coefficients. The concentration difference ($C^t - C_v^1 - C_i^1$) accounts for the fact that a fraction of the traps are occupied by vacancies and interstitials, and hence are unable to capture free defects. The size of a trap is included in the recombination coefficient $R_{i,v}$, and trap-defect binding energies are contained in the mean trapping times, $\tau_{i,v}$.

Mansur and Yoo solved the above equations to examine the effects of trapping by individual solute atoms on the fraction of defects recombining the matrix (i.e. not being removed at sinks), and ultimately on the void nucleation and growth rates. They used parameters appropriate to nickel, and established reasonable upper and lower limits of the effects of trapping (E_v^b = .5 eV, E_i^b = 1.7 eV) versus no trapping ($E_v^b = E_i^b = 0$). In general, the fraction recombining decreased with temperature, but increased with dose rate and solute concentration. However, at a given temperature the importance of recombination vs. loss to sinks was very dependent on the magnitude of the total sink strength. For a sink strength of 10^{10} cm^{-2}, recombination was dominant over most of the temperature range, but it was dominant only below ~ 430°C for a sink strength of 5 x 10^{11} cm^{-2}. The difference between the strong-trapping and no-trapping cases was greatest at low temperatures (300-400°C), at high solute concentrations, and at low dose rates. This last point is important in correlations between reactor irradiations and ion-simulation work, since the results show trapping to be more important during reactor ir-

radiations. Trapping has a drastic effect on the void nucleation rate, since it both increases the height of the free energy barrier to nucleation, and increases the size of the critical nucleus. Increasing E_v^b from 0 to .5 eV decreased the nucleation rate by 6 orders of magnitude. The effect of trapping on the void growth rate, dr/dt, is to reduce the magnitude of dr/dt and also to compress the temperature range over which dr/dt is positive. These void nucleation and growth calculations illustrated an asymmetry between the effects of vacancy and interstitial trapping. Whereas a vacancy binding energy E_v^b of 0.1 eV noticeably reduced nucleation of growth rates, interstitial binding energies had an effect only when $E_i^b > 1.25$ eV. The theory shows that interstitial trapping is effective only when E_i^b is greater than the difference between the vacancy and interstitial migration energies, which is $\sim$ 1.2 eV in Ni. Further work by Brailsford[48] has shown this asymmentry to be dependent on the size of the trap; while it exists for individual solute atom traps, it does not exist for large coherent-precipitate traps.

Recently workers[54-56] have examined the effect of point-defect trapping on void growth in alloys where solute segregation also occurs; that is, in alloys where the solute-defect complexes are mobile and therefore the alloy composition does not remain spatially uniform during irradiation. The main result was than any suppression of swelling that results from trapping is reduced when solutes are swept from the matrix by segregation mechanisms. Lam et al[55] have shown that when strong solute-interstitial binding exists, solute

trap depletion from the matrix is greatest at temperatures below the peak swelling temperature, while at higher temperatures segregation is reduced. Therefore, swelling will remain suppressed at higher temperatures but not at lower temperatures, so the swelling peak will shift to lower temperatures. When solute-vacancy binding is dominant, whether the matrix becomes enriched or depleted of traps depends on the magnitude of the binding energy, therefore the swelling behavior depends on the binding energy.

References for Chapter II

1. J. Lindhard and M. Scharff, Dan. Mat. Fys. Medd. 27, No. 15 (1953).

2. N. Bohr and J. Lindhard, Dan. Mat. Fys. Medd. 28, No. 7 (1954).

3. J. Lindhard and M. Scharff, Phys. Rev. 124, No. 1, 128-130 (1961).

4. J. Lindhard, V. Nielsen, M. Scharff, and P. V. Thomsen, Mat. Fys. Medd. Dan. Vid. Selsk. 33, No. 10 (1963).

5. J. Lindhard, M. Scharff, and H. E. Schiott, Mat. Fys. Medd. Dan. Vid. Selsk. 33, No. 14 (1963).

6. J. Lindhard, Phys. Letters 12, No. 2, 126-128 (1964).

7. G L. Kulcinski, J. J. Laidler, and D. G. Doran, Radiation Effects 7, 195-202 (1971).

8. K. B. Winterbon, P. Sigmund, and J. B. Sanders, Mat. Fys. Medd. Dan. Vid. Selsk. 37, No. 14 (1970).

9. O. S. Oen, J. Narayan, and T. S. Noggle, in Applications of Ion Beams to Metals, ed. by S. T. Picraux, E. P. Eernisse, and F. L. Vook, 639-650, 1974.

10. J. B. Roberto and J. Narayan, in CONF-751006-P1, Fundamental Aspects of Radiation Damage, 120-126 (1975).

11. J. Narayan, O. S. Oen, and T. S. Noggle, J. Nucl. Mat. 71, 160-170 (1977).

12. M. T. Robinson, in Nuclear Fusion Reactors, British Nuclear Energy Soc., London, 364 (1970).

13. M. J. Norgett, M. T. Robinson, and I. M. Torrens, Nuclear Engineering and Design 33, 50-54 (1975).

14. I. M. Torrens and M. T. Robinson, in Radiation Induced Voids in Metals, AEC Symposium Series No. 26, J. W. Corbett and L. C. Ianniello, eds., 739 (1972).

15. M. J. Makin, Phil. Mag. 18, No. 152, 637-653 (1968).

16. I. Manning and G. P. Mueller, Computer Physics Comm. 7, 85-94 (1974).

17. D. K. Brice, SAND75-0622, Sandia Laboratories, Albuquerque, NM, July 1977.

18. D. R. Olander, Fundamental Aspects of Nuclear Reactor Fuel Elements, Ch. 17, ERDA Technical Info. Center Document TID-26711-P1, 1976.

19. D. G. Doran, Nuclear Engineering and Design 33, 55-62 (1975).

20. D. G. Doran, Rad. Effects 2, 249 (1970).

21. T. H. Blewitt, A. C. Klank, T. Scott, W. Weber, in Rad. Induced Voids in Metals, AEC Symposium Series No. 26, J. W. Corbett and L. C. Ianniello, eds., 757 (1972).

22. J. L. Katz and H. Wiedersich, in Rad. Induced Voids in Metals, J. W. Corbett and L. C. Ianniello, eds., (1972).

23. K. C. Russell, "Nucleation in Solids," Ch. 6 of Phase Transformations, American Soc. for Metals, 1970.

24. K. C. Russell, Acta Met. 26, 1615-1629 (1978).

25. J. L. Katz and H. Wiedersich, J. Chem. Phys. 55, No. 3, 1414-1425 (1971).

26. K. C. Russell, Acta Met. 19, 753-758 (1971).

27. D. R. Olander, ERDA Doc. TID-26711-P1, Chapter 19, (1976).

28. R. W. Powell and K. C. Russell, Rad. Effects 12, 127-131 (1972).

29. K. C. Russell, Scripta Met. 6, 209-214 (1972).

30. K. C. Russell, Scripta Met. 7, 755-760 (1973).

31. J. L. Katz and H. Wiedersich, J. Nucl. Mat. 46, 41-45 (1973).

32. H. Wiedersich, J. J. Burton, and J. L. Katz, J. Nucl. Mat. 51, 287-301 (1974).

33. K. C. Russell, J. Nucl. Mat. 61, 330-333 (1976).

34. L. K. Mansur and W. G. Wolfer, J. Nucl. Mat. 69 & 70, 825-829 (1978).

35. W. G. Wolfer and M. H. Yoo, ORNL/TM-5398, Oak Ridge National Lab., May 1976.

36. W. G. Wolfer, L. K. Mansur, and J. A. Sprague, in Radiation Effects in Breeder Reactor Structural Materials, 841 (1977).

37. J. L. Katz and H. Wiedersich, in Defects and Defect Clusters in bcc Metals and Their Alloys, R. J. Arsenault, ed., Nat. Bureau Standards, 530 (1973).

38. L. K. Mansur, "Void Swelling in Metals and Alloys Under Irradiation: An Assessment of the Theory," Oak Ridge Nat. Lab., (1978).

39. A. D. Brailsford and R. Bullough, J. Nucl. Mat. 69 & 70, 434-435 (1978).

40. S. D. Harkness and C. Y. Li, Met. Trans. 2, 1457-1470 (1971).

41. H. Wiedersich, Rad. Effects 12, 111-125 (1972).

42. A. D. Brailsford and R. Bullough, J. Nucl. Mat. 44, 121-135 (1972).

43. A. D. Brailsford, R. Bullough and M. R. Haynes, J. Nucl. Mat. 60, 246-256 (1976).

44. W. G. Wolfer and M. H. Yoo, Intl. Conf. on Rad. Effects and Tritium Technology for Fusion Reactors, Vol. II, Gatlinburg, TN, 458-474 (1975).

45. B. L. Eyre, J. Phys. F: Metal Physics 3, 422 (1973).

46. H. Wiedersich, P. R. Okamoto, and N. Q. Lam, in Rad. Effects in Breeder Reactor Structural Materials, Bleiberg and Bennett, eds., AIME, 801-819 (1977).

47. L. K. Mansur and M. H. Yoo, J. Nucl. Mat. 74, 228-241 (1978).

48. A. D. Brailsford, J. Nucl. Mat. 78, 354-361 (1978).

49. T. R. Anthony, Radiation Induced Voids in Metals, J. W. Corbett and L. C. Ianniello, eds., 630-646 (1972).

50. P. R. Okamoto, S. D. Harkness, and J. J. Laidler, Trans. ANS 16, 70 (1973).

51. A. D. Brailsford, J. Nucl. Mat. 56, 7-17 (1975).

52. L. K. Mansur and W. G. Wolfer, Proc. Intl. Conf. on Properties of Atomic Defects in Metals, Argonne Nat. Lab., Oct. 18-22, 1976.

53. R. A. Johnson and N. Q. Lam, Phys. Rev. B 15, No. 4, 1794-1800 (1977).

54. P. R. Okamoto, N. Q. Lam, H. Wiedersich, and R. A. Johnson, J. Nucl. Mat. 69 & 70, 821-824 (1978).

55. N. Lam, P. R. Okamoto, H. Wiedersich, J. Nucl. Mat. 74, 101-113 (1978).

56. L. K. Mansur, J. Nucl. Mat. 83, 109-127 (1979).

57. M. Baron, J. Nucl. Mat. 83, 128-138 (1979).

58. R. Bullough and R. C. Perrin, Voids Formed by Irrad. of Reactor Materials, S. F. Pugh, ed., Reading, U.K., BNES, 79 (1971).

59. F. A. Smidt, Jr. and J. A. Sprague, Scripta Met. 7, 495-502 (1973).

60. W. Schilling and K. Schroeder, Consultant Symposium on the Physics of Irradiation Produced Voids, Harwell, England, 1974, AERE-R 7934, 212-229.

61. T. H. Blewitt, in Radiation Damage in Solids, D. S. Billington, ed., 630-716 (1962).

62. S. D. Harkness and C. Y. Li, Radiation Induced Voids in Metals, J. W. Corbett and L. C. Ianniello, eds., 798-824 (1972).

CHAPTER III

THEORETICAL MODELS OF ALLOY PHASE STABILITY UNDER IRRADIATION

Numerous experiments[1-6] utilizing analytical techniques such as transmission electron microscopy have shown that energetic irradiation can alter the size distribution and structure of second phase particles, enhance their nucleation rate, or cause their complete dissolution. Irradiation can also cause enhanced ordering or disordering of ordered phase and can even lead to the formation of non-equilibrium phases that are stable only under irradiation. In general, the microstructural changes produced by radiation can be classed as either "radiation-enhanced" changes where the approach to equilibrium is accelerated, or "radiation-induced" changes that revert to equilibrium when the radiation ceases.[7] From the viewpoint of the basic radiation damage processes described previously, the sources of these changes are: the collisions of primary knock-on themselves, including the "mixing" processes occurring within the collision cascades; the defect currents that result from the flow of point defects to sinks; and the presence of excess defect concentrations in the matrix, i.e., vacancies and interstitials that escape from the cascades, and anti-structure defects in ordered phases. Various phase stability effects arising from these processes can be categorized roughly as follows:

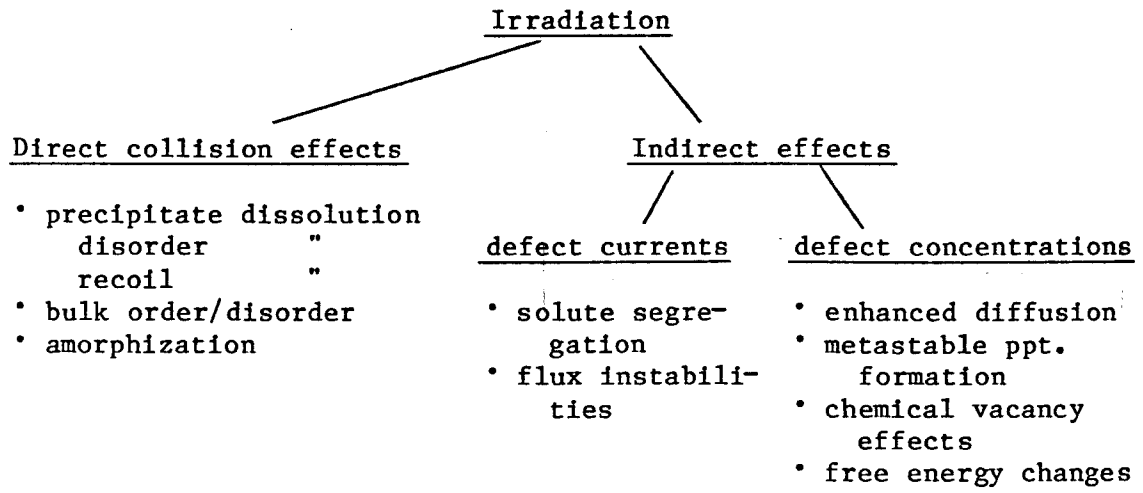

During the past 5 years, a number of theoretical models have been developed to describe alloy phase changes under irradiation. As of now, no general theory exists because of the complexity of the problem. Instead, each model applies to a specific situation, incorporating one or more of the atomistic mechanisms listed above. The models emphasized in this chapter describe two important processes: i) the radiation induced transport and redistribution of solute atoms, which can cause decomposition of undersatruated or supersaturated solid solutions; and ii) changes in the size distribution or the structure of second phase particles. These models attribute the radiation induced changes to kinetic processes. Another point of view discussed briefly in this chapter argues that phase changes can be caused by the effect of the point defect supersaturations on the thermodynamic free energy of the alloy. Finally, a model concerning the stability of ordered phases under irradiation is discussed. This is important because many intermetallic phases (e.g., CuBe) are

ordered. A more complete overview of theoretical and experimental attempts to understand irradiation phase stability is given in recent review articles.[1-4,7-10]

A. Solute Transport and Redistribution Under Irradiation

1. Radiation Enhanced Diffusion

An increase in atomic diffusion rates due to irradiation-produced point defect supersaturations is a basic effect of irradiation.[11-14] Radiation enhanced diffusion can accelerate any process that depends on diffusion, such as the growth of second phase particles. Experiments with irradiated alloys[2,11-13] have shown that radiation enhanced diffusion can increase the precipitation rate, the ordering rate in ordered alloys, or the clustering rate of solute atoms. Since the approach to equilibrium is accelerated, many complex commercial alloys with non-equlibrium microstructures could evolve under irradiation to equilibrium microstructures having unknown or undesirable properties. Radiation enhanced diffusion often occurs simultaneously with other radiation damage processes, therefore many of the phase stability models discussed in this chapter incorporate radiation enhanced diffusion.

In substitutional alloys, the predominant diffusion mechanism is vacancy migration. The diffusion coefficients of solute and solvent atoms are of the form

$$D_v = C_v V_v d^2 \tag{4.1}$$

where C_v is the vacancy concentrations, V_v the effective jump fre-

quency, and d the jump distance.[11] The increase in C_v that occurs during irradiation therefore results in a proportional increase in the diffusion coefficient. The enhanced diffusion coefficient is $D' = D_r + D_v^o$, the sum of the irradiation and thermal diffusion coefficients, respectively. The behavior of D_r depends on the irradiation flux and on whether defects are lost mainly through mutual recombination or annihilation at sinks, which in turn depends on temperature and sink strength. Dienes and Damask[11] developed a simple model of radiation enhanced diffusion by substituting into Eq. (4.1) the value of C_v obtained from the point defect conservation equations (2.20 and 2.21). The dependence of D' on temperature and sink strength divides D' into several regimes:

i) At high temperatures ($> 0.5\ T_m$), thermal diffusion dominates; thus, even for high dose rates ($\sim 10^{-2}$ dpa/sec) D' is unaltered by irradiation.

ii) At intermediate temperatures where defect loss is dominated by annihilation at sinks, the rate equations yield $C_v = G/K_v$, where G is the point defect generation rate and K_v is the sink strength. Hence, $D' = G/K_v + D_v^o$, so the diffusion coefficient is independent of temperature (provided $G/K_v >> D_v^o$) and is linearly dependent on the radiation flux. Measurements of the ordering rate vs. temperature in reactor irradiated α-brass[11] agreed with this theoretical prediction.

iii) At lower temperatures and/or for low sink strengths, defect loss is predominantly through mutual recombination. Hence, D' is

proportional to the square root of G_v, and D' decreases with inverse temperature. If mutual recombination and loss to sinks both contribute to defect loss, D' is still proportional to $G_v^{1/2}$, but the decrease in D' with 1/T occurs with a different activation energy.

Thus, depending on the displacement rate, irradiation can greatly enhance the diffusion coefficient of an atom. The temperature at which enhanced diffusion becomes important depends on the materials parameters and on the displacement rate.

2. Solute Transport Due to Interactions With Defect Currents

A coupling between solute atoms and irradiation-produced defects migrating to sinks provides a mechanism for the transport, or redistribution, of solute atoms, resulting in the enrichment or depletion of solutes in the vicinity of a sink. Solute segregation at defect sinks can cause precipitation at the sink, when the solute concentration exceeds the equilibrium solubility limit. In addition to inducing precipitation, solute segregation can alter the surface properties of a material, affect the mechanical properties because of segregation to grain boundaries and dislocations,[15] and affect the formation of point defect clusters through the mechanisms described in the previous chapter.

The segregation of solutes due to vacancy currents or current-gradients generated near voids and other sinks was first postulated by Anthony[16] in 1972, and was observed experimentally by Okamoto et al.[17] in 1973. Since then, a good deal of theoretical[18-26] and

experimental work[27-40] has been devoted to understanding the mechanisms of solute segregation, and to determining the role it plays in the irradiation behavior of metals. It should be noted here that radiation induced segregation is a non-equilibrium process, which is unrelated to so-called equilibrium segregation.[54] The latter occurs only at surfaces and interfaces, and is dependent on thermodynamic properties such as the relative heats of vaporization of the solvent and solute. Whereas equilibrium segregation produces solute concentration gradients in only the first few atomic layers of a surface or interface, radiation induced segregation can produce solute concentration gradients within the bulk.

Current theoretical models link radiation induced solute segregation to the formation of mobile defect-solute complexes[20,22,41], and/or to so-called inverse Kirkendall effects[15,25,26], arising from differences in the diffusion rates of solute and solvent atoms when migrating via a vacancy or interstitial mechanism. Anthony[16] suggested two mechanisms for kinetic segregation due to vacancy flow. The first was a preferential exchange of a substitutional alloying element with vacancies, leading to a preferential flow of this element opposite to the vacancy flow, thereby depleting this element near the defect sink. The second mechanism was the dragging of an alloying element toward a sink due to a strong binding between a vacancy and the alloying element. Johnson and Lam[20] developed a detailed phenomenological theory of solute segregation in dilute alloys based on a similar solute drag concept. However, they

considered the transport of solutes by both vacancy and interstitial mechanisms, through the formation of stable, mobile i-s (interstitial-solute) or v-s (vacancy-solute) complexes. Vacancies are assumed to bind to nearest neighbor impurities only, with a binding energy H^b_{vs}, and migrate via nearest neighbor jumps. Interstitial transport is much more complicated. The self interstitials are assumed to exist as <100> dumbbells that migrate via 90° rotation steps. Johnson and Lam postulate that two types of i-s complexes form an "a" type and a "b" type, which have different configurations within the fcc unit cell, and therefore different binding and migration energies. The "b" complex is effectively immobile (it only migrates around the impurity), so interstitial-solute transport occurs by migration of the "a" complex. For the interstitial transport mechanism to work, solute atoms must replace interstitial solvent atoms by thermal activation, to form so-called mixed dumbbell complexes. This is likely only if the solute is undersize with respect to the solvent. The binding energies of both v-s and i-s complexes are dependent on the solute-solvent size differences.

The reactions that can occur between the various species are described in terms of chemical reaction rate theory, with each reaction assigned a forward, and (if appropriate) a reverse reaction rate constant, K_j. Each rate constant is characterized by one or more activation energies, i.e., point-defect migration energies, or binding and migration energies of defect-solute complexes. The binding energies of the defect-solute complexes are, in general, not

well known, so the exponential dependence of the rate constants on the binding energies could cause large uncertainties in the behavior predicted by the theory.

The Johnson-Lam model produced a set of coupled, space and time dependent rate equations describing the conservation of solute atoms, vacancies, interstitials, and v-s and i-s complexes. To study the dependence of solute segregation on various irradiation and materials parameters, these equations were solved numerically[20] for a thin foil geometry subjected to a uniform point defect generation rate. The materials constants used were appropriate for a dilute (.1%) solution of Zn in Ag. At a dose rate of 10^{-3} dpa/sec, segregation of Zn to the foil surface occurred in the temperature range of ~ .2 to .6 T_{mp}, with a maximum near the middle of this range. At low temperatures, reduced vacancy mobility leads to enhanced reombination, thus reducing the defect flux gradients necessary for solute transport. At high temperatures, solute-defect binding is weak, and large diffusion coefficients prevent the build-up of solute concentration gradients.

Other predictions of this model included solute redistribution even at very low doses (10^{-3} dpa), and dose rate effects. Reducing the defect production rate from 10^{-3} dpa/sec to 10^{-6} dpa/sec increased the magnitude of the steady state segregation and shifted the maximum about 150°C downwards. This behavior was attributed to the increased probability of long range migration of point defects to sinks as the dose rate decreased. Finally, segregation was studied

as a function of the binding energies of the v-s and i-s complexes. The value of the interstitial binding energy was dominant in determining whether solute enrichment or depletion occurred at a surface. If the interstitial binding energy was positive, enrichment occurred, while depletion occurred for negative binding energies.

The Johnson-Lam model was extended to study segregation to spherical sinks (voids) by solving the rate equations for spherical geometry.[41] These calculations indicated that surface enrichment is dependent on the curvature of the void surface. Enrichment at the void surface was negligible for very small voids, rose to a maximum for larger voids ($\sim$ 200 Å), then decreased slowly to an infinite-radius limit. Solute depletion in the matrix, however, rose monotonically with void radius. Steady-state void surface enrichment was greatest when the i-s migration energy equaled the migration energy of the vacancy.

Spatially varying defect production rates, due to ion bombardment, have also been shown to cause segregation.[23] During ion bombardment, the driving force for segregation is the gradient in the defect flux, due to the spatially varying damage rate and the flow to sinks. The ion bombarded surface becomes enriched in solute when i-s interactions dominate, or when v-s interactions dominate and the v-s binding energy is $\gtrsim$ .1 eV. Surface depletion occurs if v-s interactions dominate and v-s binding energies are $\lesssim$ .05 eV.

Theories of solute redistribution in concentrated binary alloys have been developed by Marwick[26] and by Wiedersich et al.[25] In

concentrated alloys (i.e. at concentrations where a solute atom tends to have other solute atoms as nearest neighbors), the vacancy is, on the average, surrounded by one or more solute atoms, so the concept of v-s binding becomes meaningless. A different approach must be used. Marwick has ascribed the segregation of major alloying elements to an inverse Kirkendall effect, based on a vacancy diffusion mechanism. This approach allows the concept of defect-solute binding to be neglected. The normal Kirkendall effect occurs in an alloy where composition gradients initially exist. A net vacancy flux through a "marker plane" is established if the two desegregating components have different partial diffusion coeffecients. Under irradiation the reverse process occurs; in an initially homogeneous alloy, a vacancy flux imposed by irradiation establishes an atomic flux, causing segregation of the alloy components. The behavior of a given solute is governed by its relative partial diffusion coefficient; faster diffusing components become depleted at sinks while slower diffusing components become enriched. If the effect of interstitials is assumed to be neutral, the inverse Kirkendall mechanism can qualitatively explain the surface enrichment of slower diffusing elements such as Ni in ion-bombarded Fe-Cr-Ni alloys.

The theory of Wiedersich et al.[25] of segregation in a concentrated binary A-B alloy allows transport of the constitutent atoms by either vacancy or interstitial mechanisms and the concept of v-s binding is abandoned. However, the idea of strong attraction between interstitials and undersized solute atoms is retained, based on

experimental evidence. Segregation behavior is expressed in terms of the partial diffusion coefficients of the defects and alloy components. The relation between the vacancy concentration gradient and the steady state concentration gradient of component A is[15]

$$\nabla C_A = \frac{D_I^B \, D_I^A}{\alpha\left(D_I^B \, D_A^{irr} + D_I^A \, D_B^{irr}\right)} \left(\frac{D_A^v}{D_B^v} - \frac{D_A^I}{D_B^I}\right) \nabla C_v \qquad (3.1)$$

where $D_I^{A,B}$ are the partial diffusion coefficients of an interstial diffusing via A and B atom exchanges, respectively; $D_{A,B}^{irr}$ are the radiation enhanced diffusion coefficients for the A and B atoms, and α is a thermodynamic factor. The direction of segregation of component A therefore depends on the difference between the ratios of the partial diffusion coefficients of A and B via the vacancy and interstitial mechanisms respectively.

Precipitation due to solute segregation is of particular interest in the present study. The Johnson-Lam model simply predicts that precipitation of a second phase will occur at a defect sink when the solute enrichment surpasses the equilibrium solubility limit.[23,24] According to Russell,[10] such precipitates must represent a phase that appears on the equilibrium phase diagram at that temperature. That is, solute segregation can only shift the phase diagram laterally, but cannot create phases not normally appearing in the alloy system in the absence of irradiation at that temperature.

Martin[42] has recently derived a simplified model for radiation induced precipitation based on the Johnson-Lam concept. Using the vacancy and interstitial balance equations and an equation for the flux of undersize solute to a sink, Martin obtains an expression for the steady-state solute enrichment at the sink. Several conclusions from this model are: a) for a given temperature and solute content, the steady-state enrichment increases with dose rate. Hence, a solid solution stable at low dose may decompose at high dose; b) the solubility limit under irradiation is a function of the sink density, which changes during the course of irradiation; c) solute segregation can increase but cannot decrease the composition range over which a given phase exists. It can produce precipitation in a single phase region, but cannot dissolve precipitates to revert a normally two-phase alloy to a single phase.

Cauvin and Martin[43] have utilized the defect-solute-coupling idea to account for the homogeneous nucleation of precipitates in solid solutions under irradiation. As in solute segregation theory, solute-defect interactions are assumed to cause localized solute enrichment and precipitation; however, defect sinks need not be present for precipitation to occur. Because of long range interaction between solute atoms and point defects, local heterogeneities in the solute concentration can produce potential wells for the defects. An analysis of the point defect continuity equations in the presence of an attractive potential shows that defects drift down the potential and recombine at the bottom of the well. A coupling

between the defect current and the solute atoms would cause either growth or decay of the initial heterogeneity. If solute atoms are dragged with the defect current into the well, the solute concentration would be enhanced and precipitation would occur; but if solute atoms are transported against the defect current, the initial solute concentration would disappear. A repulsive defect-solute interaction would lead to the opposite behavior. Although the mathematical details remain to be worked out, this theory could, in principle, be applied to either coherent or incoherent precipitation.

Evidence for this mode of homogeneous nucleation was found in an Al-1.9% Zn solid solution irradiated with 1 MeV electrons at temperatures well above the solvus temperature. There was no spatial correlation between the precipitate and the defect sinks, as solute segregation theory[20] requires. Also, the incoherent Zn precipitates were undersize with respect to the matrix ($\delta < 0$), so they would be unstable according to the theory of Maydet and Russell.[49]

B. Precipitate Size and Structure Changes Under Irradiation

Nelson, Hudson, and Mazey[5] (NMH) carried out extensive heavy ion irradiation and transmission electron microscopy of Ni-Al alloys and Ni-base PE16 alloys, which normally contain γ' precipitates. During room temperature irradiations these coherent precipitates disappeared after doses of ~ .1 dpa, while at elevated temperatures the precipitates either dissolved completely or became finer in size and more numerous. NHM developed a model describing precipitate size change as a competition between growth aided by radiation enhanced

diffusion, and shrinkage due to either recoil dissolution or disorder dissolution. Recoil dissolution occurs when a collision cascade intersects the precipitate-matrix interface, causing some atoms to be ejected from the precipitate surface into the matrix. This is analogous to ejection of atoms at external surfaces due to sputtering, hence the flux of recoil atoms can be estimated using sputtering theory.[44] Since the energy spectrum of sputtered atoms is strongly peaked at low energies (< 100 eV),[45] ejected atoms would be deposited very close to the precipitate surface, and a significant fraction would diffuse back to the precipitate. NHM estimated the flux of recoil atoms from a precipitate to be $\phi \sim 10^{14}$ G atoms/cm^{2}sec, where G is the displacement rate (atoms/sec). The recoil-dissolution rate of a spherical precipitate of radius r is then

$$dV/dt = -(1/N)\ 4\pi r^2 \phi \qquad (3.2)$$

where N is the atomic concentration.

An alternative mode of precipitate shrinkage, disorder dissolution, is pertinent to ordered coherent precipitates and is a much more efficient means of dissolution than recoil-dissolution. Here, the disordering effect of the collision cascade destroys the ordered precipitate lattice, creating localized regions of high free-energy and hence high solubility. At sufficiently high temperatures, diffusion allows small disordered regions within the particle to reorder, but regions near the particle surface lose solute by diffusion to the

matrix. NHM assumed that only displacements in a shell of thickness L at the coherent particle surface results in loss of solute atoms, where L ~ 100 Å is the cascade size. Only a fraction, f, of such solute atoms escape to the matrix, hence the disorder dissolution rate of a spherical precipitate is

$$dV/dt = -4\pi r^2 LfG \quad . \tag{3.3}$$

According to NHM, ordered incoherent precipitates would not undergo disorder dissolution because diffusion across the interface is unlikely.

The precipitate growth rate from a supersaturated solution is taken as

$$dV/dt = 3D'c_s r/p \tag{3.4}$$

where D' is the enhanced diffusivity, c_s the solute concentration in solution, and p the atomic fraction of solute atoms in the precipitate. The net precipitate growth rate is found by combining Eq. (3.4) with either Eq. (3.2) or (3.3), using the solute conservation condition $c_t = (4/3)\pi r^3 pn + c_s$, where c_t is the total solute concentration and n the precipitate number density. The result is

$$dr/dt = -yG + (3D'c_t/4pr) - D'r^2 n \tag{3.5}$$

where y is ~ $10^{14}/N$ for recoil dissolution or Lf for disorder dissolution. NHM argue that Eq. (3.5) shows that all precipitates reach an equilibrium size dictated by dr/dt = 0, in contrast to thermally

activated precipitate behavior where there is no maximum precipitate size because of coarsening.

Although the NHM model is based on sound physical concepts, it neglects the increased solubility of small precipitates[8,10] (which could cause complete dissolution of small precipitates), and it fails to predict the correct thermal behavior (coarsening) when the displacement rate, G, is set to zero.[7,46] Wilkes[7] shows that the assumptions made by NHM in deriving Eq. (3.5) allow the equation to predict only that precipitates shrink under irradiation until a steady-state matrix solute concentration is attained. The steady-state precipitate size will, in general, not be uniform, instead the final size distribution will reflect the initial distribution before irradiation, which fixes the size of the diffusion cell surrounding each precipitate. The final particle size distribution cannot be predicted from the analysis of NHM.

A theory of precipitate size redistribution during irradiation, which is based on the physical ideas of the NHM model and on a statistical theory of precipitate coarsening by Lifshitz, Slyozov and Wagner, has recently been proposed by Baron et al.[46,48] The theory derives an expression for the precipitate size distribution function, f(R,t), during irradiation. It shows that the steady-state size distribution under irradiation, f_∞, is characterized by a maximum particle size R_{max}, and by a solute supersaturation in the matrix, Δ_∞. Both R_{max} and Δ_∞ are related to the irradiation conditions through the NHM[5] concept that at steady-state, the rate at which

solute diffuses to a precipitate equals the rate at which solute is lost from the precipitate by irradiation dissolution. Once $f_\infty(R)$, Δ_∞, and R_{max} are known, other quantities such as the steady-state precipitate volume fraction and the precipitate concentation can be easily found. The theory shows that regardless of the starting conditions, the same steady state values of R_{max}, Δ_∞, etc., are obtained; hence the solute supersaturation in solution and the maximum particle size can increase or decrease during irradiation, depending on the initial state of the alloy. However, irradiation always leads to a supersaturation of solute in the matrix. When the displacement rate is set to zero, this theory, unlike the NHM model, predicts coarsening (where a maximum particle size does not exist). Factors such as solute segregation that may affect phase stability are not taken into account in Baron's theory.

In a precipitate stability theory developed by Russell et al.[49-51] the strain energy created when an incoherent precipitate absorbs excess vacancies is a major factor in determining whether the precipitate grows or dissolves under irradiaton. The interfaces of incoherent precipitates act as efficient sinks for point defects, allowing the defects to enter into the precipitation reaction. Key quantities in this theory, which determine whether particles are stabilized or destabilized under irradiation, are β_i/β_v, the relative arrival rate of interstitials and vacancies to the particle, and δ, the volumetric misfit of the particle relative to the matrix. As discussed previously, in a material where dislocations act as

significant defect sinks, the bias of dislocations for interstitial defects causes neutral sinks, such as incoherent precipitates, to be subjected to a net excess vacancy flux ($\beta_i/\alpha_v < 1$). If the precipitate phase is undersized ($\delta < 0$) with respect to the matrix, elastic strain energy will prevent the precipitate from growing unless it can emit vacancies into the matrix to relieve strain.[10] However, the excess vacancy flux under irradiation will force the particle to absorb vacancies, creating strain that is relieved if the particle emits solute atoms. If the precipitate is oversize ($\delta > 0$) with respect to the matrix, the opposite behavior occurs, so growth of the precipitate is enhanced. To determine the conditions that govern precipitate stability, Maydet and Russell[49] used a nodal line/critical point analysis like that used by Russell[52] in analyzing void nucleation. The matrix and precipitate are assumed to be substitutional solid solutions dilute in solute and solvent, respectively. A spherical incoherent precipitate is then characterized by the number of solute atoms (x) and excess vacancies (n) it contains. An oversized precipitate needs $n > 0$ to relieve strain energy, while an undersized precipitate needs $n < 0$. The particle's behavior under irradiation is found by analyzing a pair of equations describing the particle's motion in the (n,x) phase space, which is the result of five different mechanisms acting on the particle (Fig. 4.1). The particle moves in the x-direction by capturing or emitting solute atoms, and moves in the n-direction by emitting or capturing vacancies, or by capturing interstitials. Its motion in the (n,x) plane

is given by

$$dx/dt = \beta_x(n,x) - \alpha_x(n,x) \tag{3.6}$$

$$dn/dt = \beta_v(n,x) - \alpha_v(n,x) - \beta_i(n,x) \tag{3.7}$$

where the emission and capture rate notation is explained in Fig. III.1.

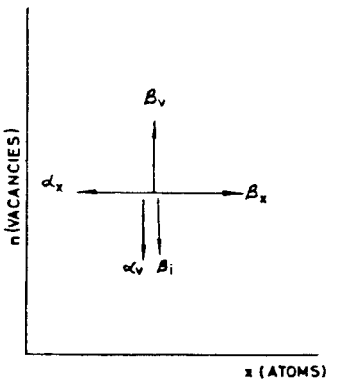

Figure III.1. Phase space for particle trajectories, showing capture and emission processes. β_x=solute capture rate, α_x=solute emission rate, β_v=vacancy capture rate, α_v=vacancy emission rate, β_i=self interstitial capture rate (from Ref. 49).

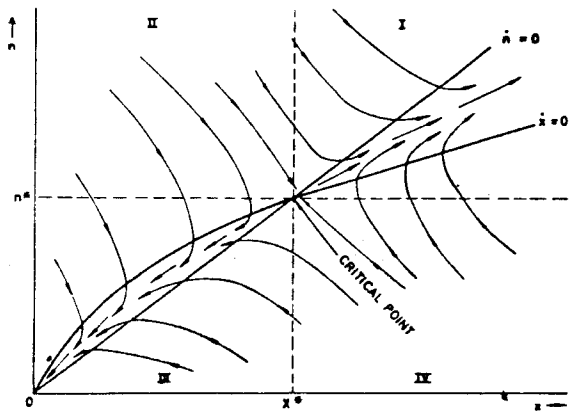

Figure III.2. Schematic illustration of nodal lines, critical point, and particle trajectories (from Ref.49).

The stability of a precipitate can be determined once the emission and capture rates are known and the initial conditions have been specified. Application of the principle of detailed balancing to a system of equilibrium precipitates, in the absence of interstitials, allows the emission rate to be expressed as

$$\alpha_{v,x}(n,x) = \beta_{v,x}(nx,)\ \exp\left((1/kT)(\partial\Delta G^{o}(n,x)/\partial x)\right) \quad . \qquad (3.8)$$

Here $\Delta G^{o}(n,x)$ is the free energy change on forming a precipitate particle from a solid solution supersaturated with vacancies and solute atoms:

$$\Delta G^{o}(n,x) = -xkT\ \ln S_x - nkT\ \ln S_v + (36\pi\Omega^2)^{1/3}\gamma x^{2/3} + \Omega E x(\delta - n/x)^2/9(1 - v) \quad . \qquad (3.9)$$

This equation was derived by Russell[50] using the capillarity model, and links the kinetic parameters (β_v,β_x) with thermodynamic parameters. The first two terms reflect the solute and vacancy supersaturation, S_x, S_v, the third accounts for surface energy, γ, and the fourth is due to the strain energy associated with a particle having either more or fewer vacancies than necessary to make it strain free. In the last term, Ω is the atomic volume of a precipitate atom, $\delta = (\Omega - \Omega_m)/\Omega_m$ is the volumetric misfit of the precipitate where Ω_m is the atomic volume of a matrix atom; E is Young's modulus and v is the Poisson's ratio.

Use of Eqs. (3.6-3.9), and calculation of the capture rates β_i, β_v, and β_x via kinetic considerations allows particle motion in (n,x) space to be determined. Although individual trajectories could be calculated, Maydet and Russell used nodal line analysis (solving Eqs. 3.6, 3.7 for $\dot{n} = 0$, $\dot{x} = 0$) to observe trends in the precipitate behavior over the entire (n,x) plane. Critical points, where the nodal lines intersect, separate regions where particles grow from regions where particles are unstable (Fig. 3.2). The solute content and

radius of a critical size precipitate are respectively

$$x^* = -32\pi\gamma^3\Omega^2/2(\Delta\phi)^3 \tag{3.10}$$

$$r^* = -2\gamma\Omega/\Delta\phi \tag{3.11}$$

where

$$\Delta\phi = -kT \ln S_x (S_v(1 - \beta_i/\beta_v))^\delta - (kT \ln S_v(1 - \beta_i/\beta_v))^2/4B \quad . \tag{3.12}$$

The quantity $\Delta\phi$ is an irradiation-modified potential function that predicts whether or not incoherent precipitates of a particular phase will be stable under irradiation in a particular matrix. If $\Delta\phi < 0$, then a critical size, x^*, exists, above which precipitates grow and below which they shrink. If $\Delta\phi > 0$, the precipitate is always unstable. The former condition usually applies for oversize particles, while the latter usually applies for undersize precipitates. Regarding phase stability, $\Delta\phi$ effectively shifts the thermal free energy up or down, which may cause the dissolution of phases seen normally in the absence of radiation, or it may bring about phases that would not normally be seen.

One limitation of Maydet and Russell's model is that it does not normally apply to coherent precipitates, although it may partially apply to semi-coherent particles, depending on their ability to capture point defects. The theory does not include solute segregation effects, which could either reinforce or cancel point defect

effects. The direct effect of cascades (recoil dissolution) was not included in the model because it was assumed to be unimportant for incoherent precipitates. Also, it has been noted[7] that the volume misfit strain surrounding a precipitate can be accommodated by prismatic dislocation loop punching, which requires much less energy than the dissolution of an existing precipitate. Dislocation loop punching has been observed, for instance, around incoherent precipitates in several copper base alloys.[53]

C. Thermodynamic Theories of Phase Stability

Several workers[55-57] have taken a purely thermodynamic rather than a kinetic approach to radiation induced phase stability, by considering the change in free energy of an alloy due to the supersaturated point defect concentrations. Wilkes et al.[55] suggested that the potential energy introduced by these defects could shift the free energy curve of one phase relative to another, and hence alter the composition of the phases. However, the contribution to the free energy from the defect supersaturations has been shown to be only ~ 1 J/mole at best, which is normally several orders of magnitude less than the free energy differences between various alloy phases.[7,10] Indeed, Kaufman et al.[56] have performed detailed caluclations of the free energy changes needed to eliminate the sigma phase in M316 stainless steel and in W-75% Re under irradiation at high temperatures, and found these changes to be between 10^3 and 10^4 J/mole. In another detailed calculation, Bocquet and Martin[57] have treated a binary (A,B) alloy under irradiation as a ternary (A,B,defect) alloy

in constrained equilibrium. They used a variational method to calculate free energy surfaces. The analysis produced specific requirements that radiation induced precipitation must follow if the source of the precipitation is the supersaturated point defect concentrations. However, actual alloys in which irradiation induced precipitation has been observed experimentally do not adhere to these requirements; therefore it was concluded kinetic processes rather than static thermodynamic processes are responsible for irradiation induced precipitation.

D. Stability of Ordered Phases

In an ordered alloy phase, irradiation-produced defects include the usual vacancies and interstitials, and also anti-structure defects produced mainly be replacement reactions (due to the mixing effect of the cascades and to focussed collision sequences). Anti-structure defects ae atoms that sit on the wrong sublattice of an ordered compound, destroying local order and thereby increasing the internal energy of the alloy. Because replacements may outnumber displacements by up to three orders of magnitude,[58] the potential energy associated with the presence of large numbers of anti-structure defects may be sufficient to destabilize an ordered equilibrium phase. This idea is the basis of a model by Wilkes et al.[7,58,59] of the effects of irradiation on the stability of ordered alloy phases. In this model, the ordered state is characterized by the Bragg-Williams long range order parameter, S, which equals unity for a completely ordered lattice and zero for a

completely random lattice. Steady-state irradiation displaces the alloy from an equilibrium state with an order parameter S_e, to a steady state with order parameter S, where the free energy is higher than at equilibrium. The stability of the ordered phase is determined by: a) calculating the value of S as a function of S_e, for a given radiation dose rate. Here the instantaneous ordering rate, dS/dt, is viewed as a competition between irradiation disordering due to replacements, and thermal reordering, which is accelerated by radiation enhanced diffusion; b) determining S_e, using one of the established theories; and c) calculating the resulting increase in the free energy of the partially disordered phase. By knowing the free energy curves for neighboring equilibrium phases, and using tangent-line analysis, one can then determine whether the ordered phase is stable with respect to the neighboring phases at a specific temperature and dose rate.

This model has been applied to the binary alloy systems Ti-Co, Nb-Rh, and Ti-Ru[59], which contain an ordered intermetallic phase, and to the ordered compound Cu_3Au.[58] In the case of the first two systems, irradiation rates up to 10^{-3} dpa/sec altered the solid solution solvus line somewhat but did not destabilize the ordered phase. However, in Ti-Ru the strongly ordered TiRu phase was completely eliminated at steady-state dose rates of 10^{-7} dpa/sec, for low and intermediate temperatures. In general, it was concluded that ordered phases having very high ordering energies, free energies similar to

adjacent phases, and approximately equi-atomic compositions were most likely to undergo radiation induced destabilization.

References for Chapter III

1. O. Hauser and M. Schenk, AERE-Trans-1008, translated by O. S. Whitston (1964), from Kernenergie 6, No. 12, 655-667 (1963).

2. J. A. Hudson, J. Br. Nucl. Energy Soc. 14, No. 2, 127-136 (1975).

3. R. S. Nelson, in Application of Ion Beams to Meatls, S. T. Picraux, E. P. Eernisse, and F. L. Vook, eds., 221-239 (1974).

4. G. Martin, J. L. Bocquet, A. Barbu, and Y. Adda, in Rad. Effects in Breeder Reactor Structural Materials, AIME, 899-915 (1977).

5. R. S. Nelson, J. A. Hudson, and D. J. Mazey, J. Nucl. Mat. 44, 318-330 (1972).

6. D. I. Potter, J. Nucl. Mat. 83, 208-213 (1979).

7. P. Wilkes, J. Nucl. Mat. 83, 166-175 (1979).

8. R. C. Russell, in Radiation Effects in Breeder Reactor Structural Materials, AIME, 821-839 (1977).

9. J. A. Hudson, in Precipitation Processes in Solids, K. C. Russell and H. I. Aaronson, eds., AIME, 284-313 (1978).

10. K. C. Russell, J. Nucl. Mat. 83, 176-185 (1979).

11. G. J. Dienes and A. C. Damask, J. Appl. Phys. 29, No. 12, 1713-1721 (1958).

12. A. C. Damask, in Radiation Damage in Solids, D. S. Billington, ed., 763-776 (1962).

13. Y. Adda, M. Beyeler, and G. Brebec, Thin Solids Films 25, 107-156 (1975).

14. R. Sizmann, J. Nucl. Mat. 69&70, 386-412 (1968).

15. P. R. Okamoto and L. E. Rehn, J. Nucl. Mat. 83, 2-23 (1979).

16. T. R. Anthony, Radiation Induced Voids in Metals, J. W. Corbett and L. C. Ianniello, eds., 630-646 (1972).

17. P. R. Okamoto, S. D. Harkness, and J. J. Laidler, Trans. ANS 16, 70 (1973).

18. P. R. Okamoto and H. Wiedersich, J. Nucl. Mat. 53, 336-345 (1974).

19. P. R. Okamoto and H. Wiedersich, Consultant Sumposium on the Physics of Irradiation Produced Voids, Harwell, England, Sept. 1974, pp. 231-238.

20. R. A. Johnson and N. Q. Lam, Phys. Rev. B13, No. 10, 4364-4375 (1976).

21. H. Wiedersich, P. R. Okamoto, and N. Q. Lam, in Radiation Effects in Breeder Reactor Structural Materials, Bleiberg and Bennett, eds., AIME, 801-819 (1977).

22. R. A. Johnson and N. Q. Lam, J. Nucl. Mat. 69&70, 424-433 (1978).

23. N. Q. Lam, P. R. Okamoto, and R. A. Johnson, J. Nucl. Mat. 78, 408-418 (1978).

24. N. Q. Lam, P. R. Okamoto, H. Wiedersich, and A. Taylor, Met. Trans. A9A, 1707-1714 (1978).

25. H. Wiedersich, P. R. Okamoto, and N. Q. Lam, (1979), to be published.

26. A. D. Marwich, J. Phys. F: Metal Phys. 8, No. 9, 1849-1861 (1978).

27. P. R. Okamoto, A. T. Santhanam, H. Wiedersich, A. Taylor, Nucl. Tech. 22, 45-51 (1974).

28. K. Farrell, J. Bentley, and D. N. Braski, Scripta Met. 11, 243-248 (1977).

29. R. A. Erck, D. I. Potter, and H. Wiedersich, J. Nucl. Mat. 80, 120-125 (1979).

30. A. D. Marwick, W. A. D. Kennedy, D. J. Mazey, and J. A. Hudson, Scripta Met. 12, 1015-1020 (1978).

31. E. A. Kenik, Script Met. 10, 733-738 (1976).

32. A. Bartels, F. Dworschak, H. P. Meurer, C. Abromeit, and H. Wollenberger, J. Nucl. Mat. 83, 24-34 (1979).

33. D. I. Potter, L. E. Rehn, P. R. Okamoto, and H. Wiedersich, Scripta Met. 11, 1095-1099 (1977).

34. A. D. Marwick and R. C. Piller, Rad. Effects 33, 245-250 (1977).

35. R. C. Piller and A. D. Marwick, J. Nucl. Mat. 71, 309-313 (1978).

36. L. E. Rehn, P. R. Okamoto, D. I. Potter, and H. Wiedersich, J. Nucl. Mat. 74, 242-251 (1978).

37. P. P. Pronko, P. R. Okamoto, and H. Wiedersich, Nucl. Inst. and Methods 149, 77-82 (1978).

38. L. E. Rehn, P. R. Okamoto, and H. Wiedersich, J. Nucl. Mat. 80, 172-179 (1979).

39. A. D. Marwick, R. C. Piller, and P. M. Sivell, J. Nucl. Mat. 83, 35-41 (1979).

40. R. C. Piller and A. D. Marwick, J. Nucl. Mat. 83, 42-47 (1979).

41. R. A. Johnson and N. Q. Lam, Phys. Rev. B 15, No. 4, 1794-1800 (1977).

42. G. Martin, Phil. Mag. A38, 131 (1978).

43. R. Cauvin and G. Martin, J. Nucl. Mat. 83, 67-78 (1979).

44. P. Sigmund, Phys. Rev. 184, No. 2, 383-416 (1969).

45. H. H. Anderson, Proc. Seventh Yugoslav Conf. on Physics of Ionized Gases, (1974).

46. M. Baron, A. Chang, and M. L. Bleiburg, in Radiation Effects in Breeder Reactor Structural Materials, M. L. Bleiberg and J. W. Bennet, eds., AIME, 395-404 (1977).

47. I. M. Lifshitz and V. V. Slyozov, J. Phys. Chem. Solids 19, Nos. 1-2, 35-50 (1961).

48. M. Baron, A. Chang, and M. L. Bleiberg, WARD-AD-3045-5, (1977).

49. S. I. Maydet and K. C. Russell, J. Nucl. Mat. 64, 101-114 (1977).

50. K. C. Russell, Scripta Met. 3, 313 (1969).

51. M. R. Mruzik and K. C. Russell, J. Nucl. Mat. 78, 343-353 (1978).

52. K. C. Russell, Acta Met. 19, 753-758 (1971).

53. L. M. Brown and G. R. Woolhouse, Phil. Mag. 21, 329-345 (1970).

54. E. D. Hondros and M. P. Seah, "Segregation to Interfaces," Intl. Metals Review, Dec. 1977, pp. 262-301.

55. P. Wilkes, K. Y. Liou, and R. G. Lott, Radiation Effects 29, 249-251 (1976).

56. L. Kaufman, J. Watkin, J. Gittus, A. Miodownik, Calphad 1, No. 3, 281-290 (1977).

57. J. L. Bocquet and G. Martin, J. Nucl. Mat. 83, 186-199 (1979).

58. R. Zee and P. Wilkes, UWFDM-314, Sept. 1979.

59. K. Y. Liou and P. Wilkes, UWFDM-292, Feb. 1979.

CHAPTER IV

METALLURGY OF THE CU-BE, CU-CO AND CU-FE SYSTEMS

To identify phase changes that are caused by irradiation, and to understand the mechanisms responsible for such changes, familiarity with the behavior of the alloy in the absence of irradiation is essential. The equilibrium phase diagram of an alloy system defines the conditions of temperature and composition under which a particular phase is stable. Often, an equilibrium phase is preceded in its formation by one or more metastable phases, which do not appear on the equilibrium diagram. In this chapter, the phase diagrams of the Cu-Be, Cu-Co and Cu-Fe systems are presented, and previous experimental studies of the precipitation reactions that have been observed in these Cu-base alloys are reviewed.

A. Copper-Beryllium

Phase transformations in Cu-Be alloys containing 0.5 to 2.5 wt% Be (3.4 to 16 at% Be) have interested many workers in the past[1-14], who studied the precipitation reactions using x-ray diffraction, optical metallography, electrical resistivity techniques and transmission electron microscopy (TEM). The Be atom is undersize and is quite insoluble in Cu, having a volumetric misfit of -26.5%.[15] The Cu-Be equilibrium phase diagram (Fig. IV-1) indicates that a supersaturated copper base Cu-Be solution eventually decomposes into a mixture of α-Cu solid solution and intermetallic compound, γ-CuBe. Early x-ray studies by Guinier and Jacquet[1] and by Guy et al.[2] determined the equilibrium structure of the CuBe precipitate, while

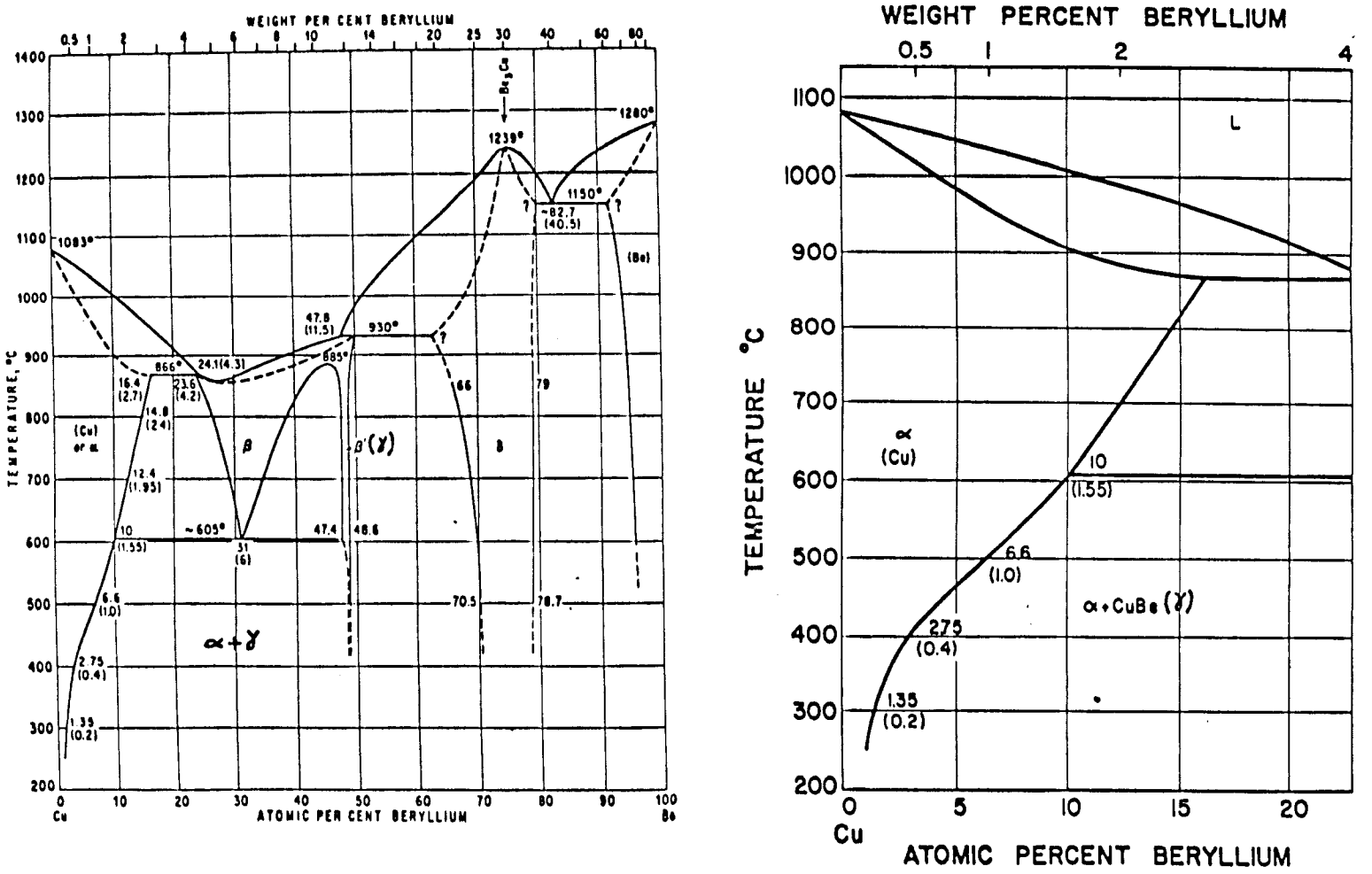

Figure IV.1. The equilibrium phase diagram of the copper-beryllium system (left, from Hansen, Ref. 28). Enlargement of the copper-rich end of the diagram (right).

subsequent studies[3,4] revealed that the equilibrium phase does not form directly, but is preceded by a series of metastable transition structures.

Many details of the structures and transformation mechanisms of the metastable phases and the γ phase have been elucidated by transmission electron microscopy studies.[6-14]. The subject of most of these studies has been Cu-Be containing approximately 2 wt% Be (~ 12 at% Be), which is a commercially important, high strength alloy. Precipitation processes in less concentrated Cu-Be alloys have not been extensively explored. Because of the relative complexity of the CuBe precipitation sequence, there is considerable disagreement among several of the TEM studies. However, comprehensive papers by Bonfield and Edwards[12,13], and most recently by Rioja and Laughin[14], have clearly documented the precipitation process.

In Cu-2 wt% Be that has been solution annealed and quenched, thermal aging produces continuous precipitation in the matrix and discontinuous precipitation at grain boundaries. The relative reaction rates of the discontinuous and continuous modes of precipitation, as well as other details of the phase transformations, depend on the aging temperature, the aging time, and the quenching method (i.e., downquenching directly to the aging temperature, vs. quenching to room temperature then reheating to the aging temperature). The decomposition of the 2 wt% Be supersaturated matrix proceeds via the following sequence of metastable precipitates:

supersaturated solution → equiaxed Be clusters

→ G.P. zones → γ'' → γ' .

The superlattice structure, habit plane, and orientation relationship with the matrix of these precipitates were determined by analysis of selected area diffraction patterns, and by dark field and weak beam imaging.

The first phase of the continuous precipitation sequence, equiaxed Be clusters, was observed by Roija and Laughlin[14] after aging the quenched alloy at room temperature for 10 minutes. Further aging at temperatures above about 175°C produced G.P. (Guinier-Preston) zones, which are disc-shaped monolayers of Be atoms, ~ 100 Å in diameter, lying on {100} planes.[6,8-10,14] The G.P. zones give rise to continuous streaks in <100> directions in the electron diffraction patterns, and their geometric arrangement causes the "tweed" pattern observed in TEM images of mildly aged Cù-2 wt% Be alloys.[8] Wilkes[8,9] reported an apparent G.P. zone solvus at ~ 320°C, since G.P. zones were not found when the alloy was directly quenched to temperatures above 320°C. However, Bonfield and Edwards[12] did observe G.P. zones in alloys directly quenched and then aged at temperatures ranging to 425°C. In a study of the Cu-1/2 wt% Be alloy used in the present work, Wilkes[8,9] observed only scattered G.P. zones surrounded by dislocation tangles, in contrast to the dense array of zones found in higher concentration alloys.

Formation of the metastable γ" phase has been reported only under certain conditions, otherwise the G.P. zones evolve directly into the γ' phase. Roija and Laughlin[14] postulated that the γ" phase forms only if the G.P. zones have grown to a maximum size. The phase is detected by the formation of diffuse spots near ±2/3{200} reciprocal lattice positions on the electron diffraction pattern. Geisler et al.[4] proposed that the γ" structure is bc monoclinic with a = b = 0.254 nm, c = 0.324 nm and β = 85°25'; while Shimizu et al.[10] proposed a bc tetragonal structure with a = 0.253 nm, c = 0.29 nm.

The γ' precipitate that forms in the matrix is a semi-coherent platelet whose structure and habit plane vary. At early stages the habit plane of the γ' is the {112} family of matrix planes, and its structure is bc tetragonal, with a = 0.27 nm and c = 0.256 nm.[4,14] As the γ' grows, its c axis expands to the value c = 0.27 nm, its habit plane evolves to the {113} matrix planes, and it has an ordered bcc CsCl-type structure.[10,12,14] During its growth, the relationship of the γ' with the matrix changes from:

$$(\bar{1}\bar{1}2)_{\alpha} \parallel (\bar{1}20)_{\gamma'} \quad , \quad [\bar{1}10]_{\alpha} \parallel [001]_{\gamma'}$$

to $(\bar{1}\bar{1}3)_{\alpha} \parallel (130)_{\gamma'}$, $[110]_{\alpha} \parallel [001]_{\gamma'}$.

The continuous γ' precipitation in the matrix has not been observed to transform directly into the equilibrium γ phase. Instead, the equilibrium phase forms only after the cellular precipitation that originates at the grain boundaries has swept through the grain.

Bonfield and Edwards[13] have studied the discontinuous precipitation, termed γI, that forms at grain boundaries. Low temperature aging (200°C) produces blocky nodules ~ 150 nm in length at the grain boundaries, and at somewhat higher temperature lamellar γI grows into adjoining grains. The γI is a metastable phase having the same structure and orientation as mature γ' precipitates (CsCl structure with a = 0.27 nm, and habit plane close to $\{113\}_\alpha$). At temperatures above about 425°C, the discontinuous cells grow quickly and soon engulf the grains, consuming the γ' precipitates. Prolonged aging (e.g., 800 hrs. at 425°C) was required to transform the metastable γI into the equilibrium γ phase. The equilibrium precipitate has the same structure and lattice parameter as the γ', but can have two different crystallographic orientations. According to Rioja and Laughlin[14], γ platelets that form after the γ' phase have the Bain orientation:

$$(110)_\alpha \parallel (100)_\gamma \quad , \quad [100]_\alpha \parallel [100]_\gamma$$

while γ phase that forms directly from the supersaturated α matrix (at high aging temperatures such as 500°C) has a Kurdjumov-Sachs orientation:

$$(111)_\alpha \parallel (101)_\gamma \quad , \quad [1\bar{1}0]_\alpha \parallel [11\bar{1}]_\gamma \quad .$$

B. Copper-Cobalt

Unlike the Cu-Be system, the Cu-Co system contains no stable intermetallic phase (Fig. IV-2). The solubility of Co in Cu is

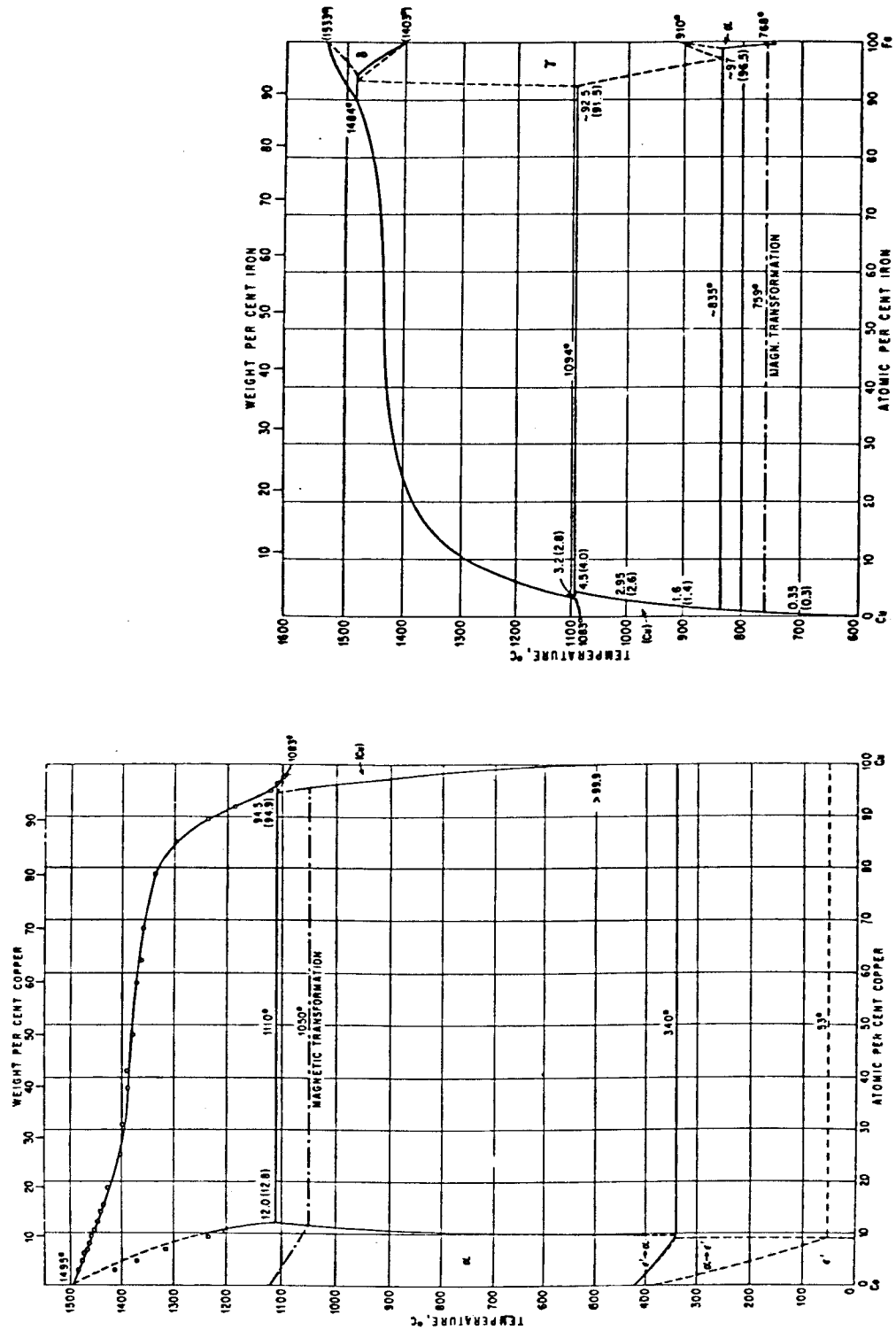

Figure IV.2. The equilibrium phase diagrams of the copper-cobalt system (left) and the copper-iron system (right). (Hansen, Ref. 28)

small, falling from 5.6 at% at 1110°C to less than .1% at 500°C. A coherent, cobalt-rich (~ 90% Co) spherical precipitate forms initally in the copper-rich alloy. The equilibrium structure of this precipitate is fcc above 340°C and hcp below, although the fcc structure is usually retained at temperatures below 340°C. Because the cobalt atom is slightly smaller than the copper atom (it has a volumetric misfit of -3.8%)[15] the elastic strain field around the coherent precipitate increases as the particle grows, so eventually coherency is lost.

Workers using electron microscopy[16-19] and magnetic techniques[20] have measured various properties (size distributions, shape, coherency state, etc.) of the Co precipitate after aging treatments. In a TEM study of 3.1% Co alloys aged at 600 to 700°C, Phillips[16] showed that the coherency loss is a gradual process. In the microscope, the strain field-contrast of the spherical coherent precipitate produced a circular image crossed by a line of no contrast which became striated as interfacial dislocations nucleated during aging (to compensate for lattice mismatch as the particle grew). Particles reached diameters of 500-600 Å before full coherency was lost.[16,17] Fully incoherent particles tended to develop {111} faces and become octahedral in shape. Phillips also noted that, although most of the precipitation occurred within the matrix, discontinuous precipitation was observed at some grain boundaries in all specimens examined.

Servi and Turnbull[21] studied the precipitation kinetics of alloys containing 1-2.7% Co and successfully interpreted their results in terms of classical nucleation theory. They quenched solution-treated specimens directly to temperatures below the equilibrium solvus, then measured the degree of precipitation as a function of time. One result of interest here is that the precipitation kinetics of dilute Cu-Co alloys are very rapid; in many cases the equilibrium precipitate concentrations and volume fractions were attained within minutes.

C. Copper-Iron

The copper-iron system is analogous to the copper-cobalt system: the Cu-Fe system is amenable to the use of magnetic techniques to measure precipitation properties; the phase diagram shows no stable intermetallic phases; the solute, Fe, is quite insoluble (less than .1%) in copper below ~ 500°C; and there is only a slight mismatch between the copper lattice and the fcc iron lattice, so precipitates are initially coherent. Coherency is lost as the particles grow to diameters greater than 500 to 600 Å[22] Although electron microscopy[23] has shown these particles to be spherical, x-ray evidence has indicated that the precipitate initially forms as coherent platelets on the {111} and {100} matrix planes.[24]

According to the Cu-Fe phase diagram, the Fe precipitate is stable in the fcc paramagnetic form above ~ 835°C, while the bcc ferromagnetic form is stable at lower temperatures. This allotropic transformation has been the subject of much of the previous research

on Cu-Fe alloys.[22-27] In alloys that were quenched from solution temperatures to approximately room temperature, then aged, the resulting fcc precipitate remained stable even at cryogenic temperatures.[24] Denney[24] found that no amount of thermal aging in the range 550-800°C produced the bcc precipitate in a quenched 2.4% alloy. Mechanical deformation was necessary to produce the ferromagnetic bcc structure[24,26], which transformed by a martensitic reaction. However, Boltax[25] noted that some bcc ferromagnetic precipitates formed in 3.25% Fe alloys that were cooled slowly from 1050°C. Two distinct stages in the precipitation sequence were detected. Above 850°C a coarse, fcc precipitate formed that transformed spontaneously to the bcc state below 850°C. Precipitation continued below 850°C with the formation of fine fcc coherent particles that were stable at room temperature.

Boltax[25] studied the precipitation kinetics for quenched alloys between 200-700°C. The kinetics of Fe precipitation appear to be several orders of magnitude slower than for Co in copper. There was evidence for stress assisted nucleation of precipitates on dislocation loops that formed during quenching, rather than homogeneous nucleation as observed in Cu-Co.

The degree of misfit of a solute in a solid solution is an important parameter in several theories of alloy phase stability under irradiation. However, for Fe dissolved in Cu, a review of the literature reveals disagreement over whether Fe is oversize or undersize in Cu solid solution. Several x-ray studies[29,30] and a simple

calculation[31] indicated Fe is slightly undersize, while other precision x-ray measurements[32,33] showed that the addition of Fe to pure Cu increased the lattice parameter of the solution.

References for Chapter IV

1. A Guinier and P. Jacquet, Revue De Metallurgie 1, 1-16 (1944).

2. A. G. Guy, C. S. Barrett, and R. F. Mehl, Trans. AIME 175, 216-239 (1948).

3. W. Gruhl and G. Wassermann, Metall. 5, 93-98 (1951).

4. A. H. Geisler, J. H. Mallery and F. E. Steigert, J. Metals, 307-316 (March 1952).

5. A. R. Entwisle and J. K. Wynn, J. Inst. Metals 89, 24-29 (1960-61).

6. M. Nakagawa, Jap. J. Applied Phys. 4, No. 10, 760-766 (1965).

7. L. E. Tanner, Phil. Mag. 14, No. 127, 111-130 (1966).

8. P. Wilkes and M. M. Jackson, Metal Sci. J. 3, 130-133 (1969).

9. P. Wilkes, Ph.D. Thesis, Univ. of Manchester, England, (1967).

10. K. Shimizu, Y. Mikami, H. Mitani, and K. Otsuka, Trans. Japan Inst. Metals 12, 206-213 (1971).

11. T. Kainuma and R. Watanabe, J. Japan Inst. Metals 35, No. 12, 1126-1133 (1971).

12. W. Bonfield and B. C. Edwards, J. Mat. Sci. 9, 398-408 (1974).

13. W. Bonfield and B. C. Edwards, J. Mat. Sci. 9, 409-414 (1974).

14. R. J. Rioja and D. E. Laughlin, Acta Met. 28, 1301-1313 (1980).

15. H. W. King, J. Materials Sci. 1, 79-90 (1966).

16. V. A. Phillips, Trans. AIME 230, 967-976 (1964).

17. L. E. Tanner and I. S. Servi, Acta Met. 14, 231-234 (1966).

18. V. A. Phillips, Acta Met. 14, 271-278 (1966).

19. V. A. Phillips and J. D. Livingston, Phil Mag. 7, 969-980 (1962).

20. J. J. Becker, Trans. Aime 212, 138-144 (1958).

21. I. S. Servi and D. Turnbull, Acta Met. 14, 161-169 (1966).

22. K. E. Easterling and P. R. Swann, Acta Met. 19, 117 (1971).

23. W. Scharfenberger, G. Wagner, and H. Borchers, Z. Metallkde. 60, H.2., 100-105 (1969).

24. J. M. Denney, Acta Met. 4, 586-592 (1956).

25. A. Boltax, Trans. AIME 218, 812-821 (1960).

26. K. E. Easterling and H. M. Miekk-Oja, Acta Met. 15, 1113 (1967).

27. J. B. Newkirk, J. Metals, 1214-1220 (Oct. 1957).

28. M. Hansen, Constitution of Binary Alloys, McGraw-Hill, London, 1958.

29. A. J. Bradley and H. J. Goldschmidt, J. Inst. Metals 2, 389-401 (1939).

30. T. S. Hutchison and J. Reekie, Phys. Rev. 83, 854-855 (1951).

31. E. T. Teatum et al., LA-4003, (1968).

32. A. G. H. Anderson and A. W. Kingsbury, Trans. AIME 152, 38-47 (1943).

33. W. Klement, Trans. AIME 233, 1180-1182 (1965).

CHAPTER V

REVIEW OF PREVIOUS EXPERIMENTS

A. Dislocation Loop and Void Formation in Copper

In copper, as in other metals, the characteristics of void and dislocation loop nucleation and growth are governed by many factors: the nature and energy of the incident radiation; the fluence and the flux; the specimen temperature during irradiation; and the specimen purity and original microstructure. A thorough summary of previous studies of void and loop formation in copper has been published elsewhere by the author[1], and only a brief summary is given here.

High Purity Copper

Void swelling has been observed in high purity copper irradiated with neutrons[2-4,13], ions[2,9-12], and electrons[19-22], at temperatures in the range of 220°C-550°C. Within and below this temperature range, interstitial and vacancy dislocation loops formed on {111} planes.[5-8] In heavy-ion bombarded copper, Glowinski and coworkers[9-12] observed void swelling over a relatively narrow temperature range (400°C-550°C), at dose rates of 10^{-3} - 10^{-4} dpa/sec. Void formation was sensitive to the concentration and type of gas in the copper. Voids nucleated and grew in annealed, non-degassed Cu irradiated with 500 KeV self ions at a dose rate of 2 x 10^{-4} dpa/sec, and temperatures of 400 to 500°C. A relatively sharp peak in the swelling vs. temperature curve occurred at 450°C.[10] Void size increased with temperature, from a mean diameter of 300 Å at 400°C to 900 Å at 450°C, while void density remained about the same. Below

the temperature of the onset of swelling, only vacancy loops and black spots were observed. Above the maximum temperature for swelling no radiation effects were observed.

The effect of an increase in dose-rate was to shift the temperature range of swelling to higher temperatures. Compared with neutron irradiations[4] that occurred at a dose-rate of 2×10^{-7} dpa/sec, the peak swelling temperature for the ion bombarded specimens (at 2×10^{-4} dpa/sec) was increased by about 115°C. An order-of-magnitude increase in the ion bombardment rate to 2×10^{-3} dpa sec shifted the swelling range upward by 50°C; that is, the onset of swelling occurred at 450°C and peak swelling was observed at 500°C. In this higher dose-rate case, void size increased while void density dropped by a factor of 10, as temperature increased from 450°C to 530°C.

If the Cu was completely outgassed prior to ion bombardment, voids did not form. In one study[11], specimens outgassed at 700°C in high vacuum, then irradiated at 450°C to a maximum dose of 30 dpa, contained some black spots and vacancy loops, but no voids, interstitial loops, or dislocation networks. It was assumed that the high vacuum annealing removed residual gases necessary for void nucleation. To precisely determine the effect of gases on void formation, Glowinski et al.[10,12] implanted vacuum degassed Cu with various concentrations of oxygen, helium, or hydrogen, then irradiated the samples at 450-550°C to 30 dpa. Voids did form in Cu implanted with oxygen or helium, in contrast to Cu that had been degassed but not

implanted with O and He. (It was assumed that O and He enhanced void nucleation by stabilizng small vacancy clusters.) Swelling did not occur in specimens pre-implanted with hydrogen, and the hydrogen appeared to have no effect at all on the irradiated microstructure.

The importance of dislocations in void nucleation and growth was verified in both neutron and charged particle irradiation experiments. A minimum dislocation density was necessary for void nucleation[11,13], and there was a direct correlation between void number density and dislocation density.[11] Voids were almost always nucleated near interstitial loops or dislocation lines, on the compression side of the dislocation, and void growth was influenced by the proximity of a dislocation.[9-11] These observations contribute to the evidence that dislocations act as biased sinks absorbing interstitials in preference to vacancies, thereby creating an excess of vacancies that precipitate into voids.

Copper Alloys

Defect-cluster formation in binary Cu-base alloys is dependent on the type of alloying element, and on the concentration of this element in solution vs. the concentration tied up in precipitates. If precipitates exist in the specimen during irradiation, the precipitate structure (e.g., coherent vs. incoherent) can influence the fate of migrating point defects, and therefore determine whether defect cluster formation is enhanced or suppressed. Since the precipitate structure, size, and concentration (and hence the concentration of solute) can evolve during irradiation, the effect of the alloying

element on void and loop formation depends strongly on the experimental conditions. In view of the complexity of this situation, relatively few studies of defect cluster formation in Cu alloys have been performed.

Several studies of radiation damage in Cu-Be alloys have been reported, but voids have not been observed. Makin[14] irradiated Cu-1.2 at% Be at 250°C, up to a dose of 100 dpa in the high-voltage electron microscope (HVEM), but did not observe voids. Kinoshita and Mitchell[15,16] irradiated Cu-1.3 at% Be and Cu-6 at% Be, at 280-430°C, to various doses in the HVEM, and no voids were observed, although precipitates formed under irradiation (discussed in the next section). In a low temperature, low dose (40°C, 5 x 10^7 n/cm^2) reactor irradiation of Cu-Be alloys (10^{-4} % Be to 1% Be) Ipohorski and Brown[17] noted only that the addition of Be decreased the concentration of interstitial loops.

No studies of void formation in Cu-Co alloys have been reported in the literature, although one study of void formation in HVEM irradiated Cu-1.5 wt% Fe has been reported recently. Takeyama et al.[18] aged the Cu-Fe alloy for various lengths of time, to produce specimens containing coherent, semi-coherent, or incoherent precipitates, then irradiated the specimens at 250°C to a maximum dose of 10 dpa. At a given dose, swelling was greatest in the samples aged for the longest time (containing incoherent precipitates), and swelling was lowest in as-quenched samples or in samples aged for only a short time to produce a high concentration of coherent precipitates. In

as-quenched samples swelling was zero until radiation-induced precipitates formed, at which time void swelling began to increase linearly with dose. Voids nucleated at the site of coherent or semi-coherent interfaces only after an interstitial dislocation loop had grown around the precipitate. In samples sufficiently aged to contain incoherent precipitates, voids formed on dislocations near the particle or in the matrix. The experiment indicated that the suppression of void swelling decreased (because of decreased point defect trapping) as the Fe solute concentration decreased, or as the concentration of coherent precipitates decreased.

Other studies of the effect of nongaseous impurities on defect cluster formation in Cu produced the following results: the addition of 30 ppm carbon to Cu that had been doped with helium or oxygen suppressed the formation of both voids and dislocation networks.[12] (Carbon, like beryllium, is an undersize solute in Cu and is expected to trap interstitials). The addition of 1% Cd[14] or 1% Ag[14,20] (oversize solutes) either had no effect, or increased void swelling in HVEM irradiated Cu, depending on the irradiation temperature. In reactor irradiated Cu, solutes that lowered the stocking fault energy (1-5% Ge or Al) suppressed void formed, relative to high purity Cu.[4] Finally, Ni solute concentrations of a few percent reduced void swelling, while Ni concentrations of 10-20% completely eliminated swelling.[20-23] There is almost no atomic-size misfit between Ni and Cu, and Ni and Cu are completely soluble in one another at equilibrium. It was suggested, however,[22] that the suppression of

void growth in Cu-Ni is caused by the formation of non-equilibrium Ni clusters during irradiation, which trap interstitials.

B. Phase Stability of Copper-Base Alloys Under Irradiation.

Among the earliest studies of the effects of irradiation on solids were those concerned with the phase stability of copper-base alloys.[24-28,36-38] Since that time, a number of researchers have studied the effects of irradiation on precipitation in copper-base alloys containing Be[27-34,15,16], Fe[35-40], or Co[35,41-44]. Many of these irradiations, however, were performed at temperatures below 100°C, instead of at temperatures above about 200°C, where both vacancies and interstitials are mobile. Damage was produced using fission spectrum neutrons or high energy electrons; no heavy ion experiments have been performed. Since electron microscopy was not available to the early workers, the radiation effects in those studies were characterized by measuring changes in physical and mechanical properties of the samples (electrical resistivity, tensile strength, hardness, magnetic properties), which were sometimes difficult to interpret in terms of microstructural changes within the sample. Details of previous studies in Cu-Be, Cu-Co and Cu-Fe are summarized in Table V-1.

Copper-Beryllium

Early studies by Billington and Siegel[27] and by Murray and Taylor[28] reported large increases in the resistivity and hardness of supersaturated Cu-Be alloys (~ 13 at% Be) after neutron irradiation at ambient temperatures. These increases were much greater

than those observed in pure metals or stable alloys irradiated under similar conditions. Samples were irradiated either in the as-quenched state, or after various aging treatments. Changes were greatest in the quenched alloys, i.e. those containing the greatest initial Be concentration in solution. The changes were similar to those observed in Cu-Be aged for many hours at 100°C, suggesting that radiation enhanced the formation of Be particles or clusters. Later experiments by Yoshida et al.[29-32] showed indirectly that such resistivity increases were due to enhanced formation of G.P. zones (Be atom platelets). In two cases[31,32], the intermediate precipitate, γ', also formed during irradiation. Radiation enhanced diffusion was thought to have been responsible for these effects. Post-irradiation aging[30,31] of these alloys at about 250°C (5 to 2000 min.) dissolved some G.P. zones and enhanced precipitation of the γ' phase.

Kinoshita and Mitchell[15,16] have recently reported on precipitation produced during HVEM irradiation of a Cu-6.1 at% Be supersaturated solid solution and a Cu-1.3 at% Be undersaturated solid solution. Irradiation at 350°C and 430°C enhanced the precipitation kinetics of the supersaturated alloy, as γ-CuBe precipitates formed heterogeneously at dislocation sites and homogeneously within the matrix. The undersaturated alloy was irradiated at 340-410°C, well above its solid-solution solvus temperature of 280°C, yet CuBe precipitates also formed within the matrix and at dislocations. While precipitation at dislocations in the undersaturated alloy was assumed

to result from radiation-induced segregation of Be interstitials, the cause of the homogeneous precipitation within the matrix was not clear. In both of the alloys, the crystal structures of the precipitates were the same as commonly observed in aged Cu-13 wt% Be, however the morphology of the precipitates was different.

Copper-Iron

In copper-base Cu-Fe alloys a metastable, coherent precipitate (fcc Fe, spherical) forms initially upon aging. This precipitate is paramagnetic. The equilibrium precipitate is a non-coherent, ferromagnetic structure (bcc Fe), whose concentration in the alloy can be measured using saturation magnetization techniques. Denney[36] first used such techniques to study the effect of 0.5 MeV electron irradiation on a 2.4% Fe alloy that had been aged to contain large precipitates. He reported that irradiation caused an fcc-to-bcc allotropic transformation in some precipitates. Denney[37] also measured a decrease in the ferromagnetic precipitate concentration following 9 MeV H^+ bombardment at room temperature, and concluded that some particles dissolved due to recoil dissolution. In a more comprehensive study of this alloy, Boltax[38,39] measured electrical resistivity and magnetization changes in fast-neutron irradiated specimens. The specimens had been aged at 300°C to 700°C for intervals up to 10^4 minutes, to grow coherent precipitates of various concentrations and size distributions. In those specimens aged at the lower end of this temperature range (which contained a high concentration of small precipitates), a significant resistivity increase was observed

following irradiation. This was thought to have resulted from precipitate dissolution by action of the displacement cascades. Magnetic saturation measurements of many of Boltax's specimens suggested that some coherent, paramagnetic precipitates had been transformed into incoherent, ferromagnetic precipitates during irradiation.

In a later study, Gould and Vincent[40] used a sensitive Mössbauer spectroscopy technique to measure changes in the clustering and precipitation behavior of Fe atoms, as a function of heat treatment and fast neutron exposure. Competing processes - irradiation aging vs. precipitate dissolution - were observed during irradiation, the exact behavior being strongly dependent on the initial particle size distribution. Small Fe atom clusters that formed in as-quenched samples, and very large precipitates in aged samples, were particularly subject to enhanced aging during irradiation. However, intermediate size particles were more subject to dissolution, which increased with particle size up to a critical diameter, whereupon irradiation aging began to predominate. This behavior suggested that medium size particles were broken into small Fe clusters by displacement spikes.

Copper-Cobalt

Like the Fe precipitate in copper, the Co precipitate is magnetic, so precipitate concentrations and size distributions can be measured by magnetic saturation techniques. Piercy[41] irradiated a number of Cu-2% Co samples, each of which were aged under different conditions to produce different initial precipitate size

TABLE V.1. SUMMARY OF PREVIOUS PHASE-STABILITY STUDIES IN IRRADIATED Cu-Be, Cu-Co, AND Cu-Fe.

Solute, at %	Preirrad. treatment	Energy, incident particle	Dose n/cm^2	Dose rate $n/cm^2 \cdot sec^{-1}$	Irradiation temperature °C	Physical property measured	Comments	Ref.
13.4% Be	1	a	.2-4E19	-	~ 60	Resistivity, hardness increase		27
13.5% Be	1	a	to 3E19	1E12	40	Resistivity, hardness increase	Formation of ppt. nuclei due to enhanced diffusion; irradiation has same effect as low T aging.	28
9.5% Be	1	a	4E17	9E11	80	Resistivity increase	G.P. zone formation; post-irr. aging→enhanced formation of γ' ppt.	29
12.6% Be	1	a	to 2E19	-	20	Increased flow stress, decreased elongation	G.P. zones; partially coherent γ' forms.	30
12.6% Be	1	>1Mev,a	1-4E17	2E13	80	Increased tensile prop. & hardness during aging	Enhanced G.P. zone and γ' ppt. formation during post-irrad. aging compared to non-irrad. specimens.	31
9.7% Be	2	>1Mev,a	to1E16	1.5E11	100-160	Resistivity increase		
13% Be	2							31
.0017-.018% Be	-	b, 3 MeV	to 1 E20	-	7-137	Resistivity change.	Be solute concentration decreases during irradiation due to solute segregation to internal sinks.	33, 34
1.3% Be	-	.65 MeV b	to 5 E21	1.5E18	280-430	Precipitation (TEM)	Precipitation occurs in saturated and undersaturated solid solutions during irradiation.	15, 16
6.1% Be	-			1.5E19				
2.2% Co	2	",b	3.4E19	1.5E13	50	Superparamagnetic effects	Dissolution of Co ppts. smaller than 25 Å due to displacement spikes.	41
1% Co	1	",b	~1E19	-	42-210	"	Ppt. of Co greatly increased by irradiation; dist. of particle sizes different from specimen aged at same temp.	42
1% Co	3	.45Mev,b		1μA	20	Ppt. contrast change (TEM)	Dislocation loops produced by HVEM irrad. interact with coherent Co ppt., causing them to lose coherency.	43

TABLE V.1. continued

Solute, at %	Preirrad. treatment	Energy, incident particle	Dose cm^{-2}	Dose rate $cm^{-2}sec^{-1}$	Irradiation temperature °C	Physical property measured	Comments	Ref.
3% Co	4	a	2E17	-	~ 20	Ppt. contrast change (TEM)	Ppts. larger than 300 Å became incoherent due to irrad. after after brief post irrad. anneal.	44
15% Co ? % Fe	2	a .45Mev,b	~E17- ~E22	- 3 E19	65-100 20	" "	Coherency loss appears to be due to absorption of free interstitials produced by irrad.	35
.7% Fe	1	a	.4-9E19	-	55	Mossbauer spec. change	Irrad. formation of very small Fe clusters by enhanced diffusion.	
"	2	a	"	-	"	" " "	Irrad. disperses some existing clusters and ppts.	40
2.7% Fe	2	>.5Mev,b	-	-	20?	Paramagnetic to ferromagnetic transition	Irrad. with e^- > 500 Kev induces fcc to bcc transition in Fe ppts.	40
2.7% Fe	2	9 Mev H^+	-	-	"	?	Evidence for dissolution of Fe ppt. dinplacement spikes.	36
.3 to	2	a	5E17-	-	"	Resistivity; saturation induction	Neutron irrad. induces fcc → bcc transition particularly in larger ppts; radiation aging or ppt. dissolution occurs depending on pre-irrad. treatment.	38
5.4% Fe	2	a	2E20		70	" "		39

1. Solution treated then quenched to ~ room temperature.
2. Specimens aged at various temperatures for various time intervals.
3. Aged 625°C, 100 hr. to produce 100-500 Å diameter precipitates.
4. Aged 600°C, 200 hr. to produce 60-340 Å diameter precipitates.

a. Fission spectrum neutrons (> .1 MeV)
b. Electrons

distributions. Measurements of the precipitate size and concentration before and after irradiation indicated that precipitate density decreased in those specimens containing particles smaller than ~ 25 Å in diameter. Precipitate density increased, but size decreased, in samples containing larger particles. No explanation for this behavior was given. Blaise[42] observed the competing processes of enhanced precipitation and precipitate dissolution in supersaturated Cu-1% Co solutions irradiated at 40 to 210°C. Compared to specimens subjected to identical thermal conditions, more precipitation occurred in the irradiated alloys, and partcle size distributions were different.

Several workers[35,43,44] used transmission electron microscopy to investigate radiation-induced coherency loss in Co precipitates in aged, dilute Cu-Co alloys. In an HVEM study, Woolhouse[43] observed that dislocation loops migrated to metastable coherent precipitates (100-560 Å diameter), causing them to become incoherent. Later it was suggested that this coherency loss resulted from strain-relief provided by free interstitials produced by irradiation.

C. Solute Segregation

Radiation-induced segregation of alloying elements can alter the properties of surfaces, interfaces, and other point defect sinks, and can cause precipitation of a second phase at these features. Solute segregation has been observed at external surfaces[45-52], and near internal sinks such as voids[53-57], grain boundaries[55] and dislocation loops.[58] A variety of techniques were used to detect and

measure the segregation: transmission electron microscopy (TEM) to observe strain fields around voids caused by precipitate shells[53,59]; auger electron spectroscopy (AES) combined with sputtering[45,48,50], secondary ion mass spectrometry[46,47] (SIMS), and nuclear reaction techniques[49] to measure solute concentration profiles near external surfaces; and energy dispersive x-ray analysis (EDAX) to measure concentration gradients near internal sinks.[54,56-58]

In copper base alloys, little data on solute segregation is available. Bartels and co-workers[33,34] detected a decrease in the bulk solute concentration in very dilute Cu-Be alloys (17-180 ppm Be), following irradiation with 3 MeV electrons at 7°C to 137°C, and they attributed this decrease to the segregation of Be interstitials at point defect sinks. Their analysis indicated that the mechanism of segregation was the diffusion of tightly bound mixed-dumbbell, solute-interstitial complexes. Takayama et al.[57], using EDAX, measured solute profiles around voids and grain boundaries in Cu-2 at% Fe and Cu-2 at% Ag, which has been irradiated in the HVEM at 250°C. The oversize Ag solute appeared to be depleted at grain boundaries and void surfaces, while the Fe solute (approximately the same size as Cu) was enriched. This behavior was attributed to solute segregation, although there were also unexplained spatial variations in their concentration profiles.

Because measurements of solute concentration gradients near internal sinks are relatively difficult to perform, measurements at

ion-bombarded external surfaces have provided much of the current data on solute segregation behavior. This data, most of which was obtained from Ni-base solid solutions, is summarized in Table V-2. It is clear from these studies that the solute-solvent atomic size difference plays an important role in determining whether a solute becomes enriched or depleted near a sink. Solutes that are oversize in Ni-base solid solutions (Al, Ti, Mo, Mn, Au) became depleted near the irradiated surface, while undersize solutes (Be, Si) became enriched. Rehn et al.[48] used AES combined with sputtering to measure the concentration profiles of Al, Ti, or Mo solutes (1% bulk concentration) in Ni foils. The foils had been irradiated with 3.5 MeV Ni^+ ions to ~ 11 dpa at 510 to 620°C. In each case, the solute concentration was markedly depleted in the near-surface region (0-50 nm), while at greater depths it was slightly enriched. Marwick and Piller[46], using SIMS analysis, observed surface depletion of the oversize solute Mn in a .15 at% alloy irradiated with 75 KeV Ni^+ ions at 500°C. Strong solute depletion also existed well beyond the end of range of the ions (40 nm), but a sharp Mn peak was measured near the peak damage region. Low temperature irradiation (-8.5°C to 23°C) caused enrichment of the oversize Al, Cr, Mn, and Ti solutes at the surface, but depletion ~ 20 nm below the surface. The surface depletion following high temperature irradiations was linked to a vacancy transport mechanism, while the low temperature surface depletion was ascribed to a weak interstitial-solute attraction. Vacancies are

immobile at the lower temperatures, so only interstitial atoms could participate in solute redistribution.

In contrast to oversize solutes, Be and Si became enriched at ion-bombarded surfaces[45,47-50] and depleted in the matrix. Rehn et al.[48] irradiated Ni-1 at% Si at 385°C to 660°C to determine the temperature dependence of segregation. Segregation was most pronounced between ~ 530°C to 600°C, where a surface film of the γ' precipitate Ni_3Si formed. At the maximum segregation temperature (~ 560°C) the Ni_3Si layer was more than 10 nm thick; the Si concentration then dropped abruptly to almost zero between depths of 50-175 nm, then returned slowly to the bulk value. Piller and Marwick[47] also observed strong surface enrichment of Si in Ni following Ni ion irradiation at 500°C and room temperature. Since vacancies are immobile at room temperature, this segregation indicated a strong Si-interstitial interaction that resulted in a fast-diffusing Si-interstitial complex.

Rehn et al.[48] attempted to measure Be depth profiles in ion irradiated Ni-1 at% Be, using AES analysis, but overlap of the Auger transition lines of Be and Ni prevented this measurement. Using low energy proton-Be nuclear reactions however, Pronko et al.[49] measured Be profiles in Ni-.7% Be foils that had been irradiated at 625°C with 3.2 MeV Ni ions. The Be concentration was doubled within 50 nm of the surface, and was depleted within the next 300 nm interval. (Thermal-equilibrium segregation was detected in non-irradiated regions of the foil.)

The dose dependence of radiation induced segregation was investigated by Rehn et al.[50] in Ni-1% Si irradiated at 525°C and 600°C. The most striking finding was pronounced Si enrichment at the surface after an ion dose of only .05 dpa. As dose increased the rate of segregation rapidly decreased; e.g., the Si surface concentration increased to 11 at% after a dose of .05 dpa, but rose to only 20% after a dose of 1 dpa.

TABLE V.2. Previous Studies of Radiation-Induced Surface Segregation in Binary Nickel Base Alloys.

at % solute	Ni ion energy (mev)	Peak dose (dpa)	Peak dose rate (10^{-3} dpa/s)	Temperature °C	Depth of peak damage rate (nm)	Method of analysis	Direction of segregation*	Solute misfit (fractional)	Comments	Ref.
1% Si	3.5	4	2.5	385, 480	600	AES	t	-.025	Slight segregation	
1% Si	3.5	4-8	2.5	530-600	600	AES	t	-.025	Strong segregation; Ni_3Si surface film	45
1% Si	3.5	4-10	2.5	620-660	600	AES	t	-.025	Strong segregation, but no surface film	48
2% Si	3.5	11.4	2.5	600	600	AES	t	-.025	Strong segregation, but no surface film	
.06% Si	.075	46	46	500	14	SIMS	t	-.025	Strong segregation; Si enrichment well beyond end of ion range	
.06% Si	.075	46	46	16	14	SIMS	t	-.025	Strong segregation, but less than at 500°C; strong interstitial interaction	47
.15% Mn	.075	46	46	500	14	SIMS	a	+	Sharp Mn peak at 19 nm; Mn depletion 40-120 nm	
.15% Mn	.075	46	46	23	14	SIMS	t	+	No depletion at surface, but at 5-40 nm	46
.7% Be	3.2	23	-	625	580	**nr	t	-	Be conc. doubled within 50 nm of surface	49
1% Al	3.5	10.7	2.5	620	600	AES	a	+.05	Al conc.~ zero at 0-25 nm	
1% Al	3.5	10.3	2.5	510	600	AES	a	+.05	Less segregation than at 620°C	48
1% Ti	3.5	8.5	2.5	575	600	AES	a	+.10		
1% Ti	3.5	11.2	2.5	515	600	AES	a	+.10		
1% Mo	3.5	11.2	2.5	615	600	AES	a	+.12	Mo conc.~ zero at 0-10 nm depth	
1% Mo	3.5	11.6	2.5	530	600	AES	a	+.12	Mo conc.~ zero at 0-10 nm depth	
1% Si	3	.05-6.5	2.5	525, 600	540	AES	t	-.025	Pronounced segregation even at .05 dpa; seg. rate decreases rapidly with increasing dose	50

* a,t = away from, toward irradiated surface ** nuclear reaction

References for Chapter V

1. R. W. Knoll, "A Literature Review of Radiation Damage Data for Copper," University of Wisconsin Fusion Design Memo UWFDM-384, Nuclear Engineering Department, University of Wisconsin, Madison, 1980.

2. Y. Adda, in Radiation Induced Voids in Metals, J. W. Corbett and L. C. Ianniello, eds., AEC Symposium Series No. 26, 1972, 31-81.

3. V. Levy, J. Mathie, A. Risbet, R. Levy, and J. P. Poirier, in Voids Formed by Irrad. of Reactor Materials, S. F. Pugh, ed., British Nuclear Energy Society, 1971, 64-68.

4. M. Labbe and J. P. Poirier, J. Nucl Mat. 46, 86-98 (1973).

5. M. Ruhle, F. Haussermann, and M. Rapp, Phys. Stat. Sol. 39, 609-620 (1970).

6. J. B. Mitchell, C. M. Logan, and C. J. Echer, J. Nucl. Mat. 48, 139-142 (1973).

7. D. E. Barry and B. L. Eyre, Phil. Mag. 22, 717-737 (1970).

8. L. M. Howe and M. Rainville, Rad. Effects 16, 203-209 (1972).

9. J. M. Lanore, L. Glowinski, A. Risbet, P. Regnier, J. L. Flament, V. Levy, and Y. Adda, Fundamental Aspects of Rad. Damage in Metals, 1169-1180 (1975).

10. L. Glowinski, C. Fiche, and M. Lott, J. Nucl. Mat. 47, 295-310 (1973).

11. L. D. Glowinski and C. Fiche, J. Nucl. Mat. 61, 22-28 (1976).

12. L. D. Glowinski and C. Fiche, J. Nucl. Mat. 61, 29-40 (1976).

13. J. L. Brimhall and B. Mastel, J. Nucl. Mat. 29, 123-125 (1969).

14. M. J. Makin, in Voids Formed by Irrad. of Reactor Materials, S. F. Pugh, ed., British Nucl. Energy Soc., 269-274 (1971).

15. C. Kinoshita and T. E. Mitchell, 38th Annual Proc. Electron Microscopy Soc. America, San Francisco, CA, G. W. Bailey (ed.), 148-149 (1980).

16. C. Kinoshita and T. E. Mitchell, Electron Microscopy 1980 4, 236-239 (1980).

17. M. Ipohorski and L. M. Brown, Phil. Mag. 22, 931 (1970).

18. T. Takeyama, S. Ohnuki, and H. Takahashi, J. Nucl. Mat. 89, 253-262 (1980).

19. L. D. Glowinski, J. Nucl. Mat. 61, 8-21 (1976).

20. P. Barlow, Radiation Damage in Pure FCC Metals and Alloys in HVEM, Ph.D. Thesis, 1977, Univ. of Sussex, England.

21. T. Leffers, B. N. Singh, and P. Barlow, Riso-M-1937, Research Establishment Riso, Roskilde, Denmark, May 1977.

22. P. Barlow, T. Leffers, and B. N. Singh, Riso-M-2129, Research Establishment Riso, Roskilde, Denmark, August 1978.

23. J. L. Brimhall and H. E. Kissinger, Rad. Effects 15, 259-272 (1972).

24. S. Siegel, Phys. Rev. 75, No. 12, 1823-1824 (1949).

25. T. H. Blewitt and R. R. Coltman, Phys. Rev. 85, No. 2, 384 (1952).

26. Nature 168, No. 4275, 581-583 (1951).

27. D. S. Billington and S. Siegel, Metal Progress, 847-52 (Dec. 1950).

28. G. T. Murray and W. E. Taylor, Acta Met. 2, 52-62 (1954).

29. H. Yoshida, Phil. Mag. 19, 987-991 (1969).

30. H. Yoshida, H. Kodaka, and K. Miyata, Reactor Res. Inst. Ann. Report 4, Kyoto Univ., 119-122 (1971).

31. H. Yoshida, S. Yamamoto, Y. Murakami, and H. Kodaka, Trans. Jap. Inst. Metals 12, No. 4, 229-237 (1971).

32. H. Yoshida and T. Sagane, J. Nucl. Sci. Tech. 9, 1-6 (1972).

33. W. Lensa, A. Bartels, F. Dworschak, and H. Wollenberger, J. Nucl. Mat. 71, 78-81 (1977).

34. A. Bartels, F. Dworschak, H. P. Meurer, C. Abromeit and H. Wollenberger J. Nucl. Mat. 83, 24-34 (1979).

35. G. R.. Woolhouse and M. Ipohorski, Proc. R. Soc. London A324, 415-431 (1971).

36. J. M. Denney, Phys. Rev. 92, No. 2, 531 (1953).

37. J. M. Denney, Phys. Rev. 94, No. 5, 1417-18 (1954).

38. A. Boltax, ASTM Special Tech. Pub. 208, Rad. Effects on Materials, Vol. 1, 183-190 (1956).

39. A. Boltax, Nucl. Appl. 1, 337-347 (1965).

40. T. H. Gould and D. H. Vincent, J. de Physique C6, No. 12, 315-319 (1974).

41. G. R. Piercy, J. Phys. Chem. Solids 23, 361-365 (1962).

42. A. Blaise, J. de Physique 26, 361-365 (1965).

43. G. R. Woolhouse, Nature 220, 573-74 (1968).

44. L. M. Brown, G. R. Woolhouse, and U. Valdré Phil. Mag. 18, 781-789 (1968).

45. D. I. Potter, L. E. Rehn, P. R. Okamoto, and H. Wiedersich, Scripta Met. 11, 1095-1099 (1977).

46. A. D. Marwick and R. C. Piller, Rad. Effects 33, 245-250 (1977).

47. R. C. Piller and A. D. Marwick, J. Nucl. Mat. 71, 309-313 (1978).

48. L. E. Rehn, P. R. Okamoto, D. I. Potter, and H. Wiedersich, J. Nucl. Mat. 74, 242-251 (1978).

49. P. P. Pronko, P. R. Okamoto, and H. Wiedersich, Nucl. Inst. and Methods 149, 77-82 (1978).

50. L. E. Rehn, P. R. Okamoto, and H. Wiedersich, J. Nucl. Mat. 80, 172-179 (1979).

51. A. D. Marwick, R. C. Piller, and P. M. Sivell, J. Nucl. Mat. 83, 35-41 (1979).

52. R. C. Piller and A. D. Marwick, J. Nucl. Mat. 83, 42-47 (1979).

53. P. R. Okamoto, A. T. Santhanam, H. Wiedersich, and A. Taylor, Nucl. Tech. 22, 45-51 (1974).

54. K. Farrell, J. Bentley, D. N. Braski, Scripta Met. 11, 243-248 (1977).

55. R. A. Erck, D. I. Potter, and H. Wiedersich, J. Nucl. Mat. 80, 120-125 (1979).

56. A. D. Marwick, W. A. D. Kennedy, D. J. Mazey, and J. A. Hudson, Scripta Met. 12, 1015-1020 (1978).

57. T. Takeyama, S. Ohnuki, and H. Takahashi, Electron Microscopy 1980 4, 208-211 (1980).

58. E. A. Kenik, Scripta Met. 10, 733-738 (1976).

59. P. R. Okamoto, S. D. Harkness, and J. J. Laidler, Trans. ANS 16, 70 (1973).

CHAPTER VI

EXPERIMENTAL METHODS AND APPARATUS

A. Specimen Preparation

Four different specimen materials were irradiated in this study: Cu-3.4 at% Be, Cu-1 at% Co, Cu-1 at% Fe, and high purity Cu. The impurities contained in these materials were determined by the suppliers and are listed in Table VI-1. The Cu-Be alloy, which was from the same stock used by Wilkes[1,2] in studies of precipitation kinetics, was in the form of a billet, from which 0.3 mm foils were cut using a diamond saw. The Cu-Co and Cu-Fe alloys were prepared by Materials Research Corporation using high purity (MARZ grade) stock, and were received in the form of cold-rolled strips about 1 mm thick. Portions of these strips were annealed at 840°C in a hydrogen atmosphere, quenched into water, then were cold-rolled to a final thickness of about 0.3 mm. The high purity Cu was also obtained from Materials Research Corporation, as MARZ grade, 0.25 mm sheetstock. Irradiation specimens were cut from the stock materials to a size of either 10 mm x 6 mm or 10 mm x 12 mm, depending on the specimen holder that was used for irradiation.

The pre-irradiation heat treatment of a specimen depended on the type of specimen, and on the objectives of the irradiation experiment. Before heat treating, all specimens were cleaned by electropolishing in a solution of 67% CH_3OH-33% HNO_3 at -30°C. Specimens were then solution annealed at 800°C-900°C for about 1-1/2 hours, in an H_2 atmoshpere. The annealing was carried out in a vertical,

TABLE VI-1. Impurity Analysis of the Specimen Stock Material[#]

Element	High Purity Cu	Cu-1 wt% Co	Cu-1 wt% Fe	Cu-.5 wt% Be
C	6	6	6.1	**
H	< 1.0	< 1	< 1	**
O	< 5.0	5.1	5.3	6
N	< 1.0	< 1	1.1	**
Ag	.50	.5	.5	8
Al	1.0	1.0	1.0	20
Ca	.40	.40	.4	-
Co	< .10	9900.	.13	-
Cr	.30	.36	.31	1
Fe	.80	.96	9800.	100
Pb	.70	.70	.7	20
S	.50	.51	.52	-
Si	.30	.33	.3	100
Zn	1.50	1.5	1.5	-
Mg	*	*	*	200
Sn	*	*	*	80
Mn	*	*	*	20
Ni	*	*	*	3
Cd	*	*	*	1

parts per million, weight
* < .10 ppm
** not analyzed

stainless steel tube, through which high purity H_2 gas flowed, and which was heated within an electric furnace. The specimens were suspended at the center of the furnace tube, within a stainless steal-mesh cage that was released into a distilled water quenching-bath at the end of the anneal. Annealing temperatures were monitored with a chromel-alumel thermocouple that was positioned inside the specimen cage.

Thermal aging of alloy specimens, and outgassing of some of the high purity Cu foils, were performed in an ultra-high vacuum furnace, at pressures in the 10^{-8} - 10^{-9} torr range. The specimens rested in a tantalum holder, which was heated by thermal radiation and by electron bombardment. Specimen temperatures were monitored by chromel-alumel thermocouples spot-welded to the tantalum holder. The input line voltage to the furnace power supplies was precisely regulated, which prevented the aging temperature from fluctuating more than ± 2°C after steady state was attained. A gas analyzer (Varian Associates, Model VGA-100) mounted on the furnace allowed residual gases in the system to be identified. Details of the ultra high vacuum furnace have been described previously by W. J. Weber.[3]

Because of the importance of clean specimen surfaces, the specimens were again polished after heat treatment, before being loaded into the irradiation target chamber. During quenching of the Cu-Be foils after annealing in the vertical furnace, a thin BeO film formed on the foils, which was removed by mechanical polishing. The annealed Cu-Be specimens were mounted on polished steel blocks using

double-sided adhesive tape, then were ground on abrasive paper (#240-#600), and were finally polished in a vibratory metallographic polisher using a 3 μm alumina slurry. Following the mechanical polish, a mirror-like surface was obtained by electropolishing each specimen in the 33% HNO_3-67% CH_3OH electrolyte at -30°C. Approximately 0.025-0.05 mm were removed from each Cu-Be specimen surface by this polishing procedure. The Cu, Cu-Co and Cu-Fe specimens were also electropolished in this manner, but they were not mechanically polished. Clean specimens were stored in a dry argon atmosphere before and after irradiation.

B. Irradiation Facility

All specimens in this study were irradiated with 14 MeV copper ions in the University of Wisconsin Heavy-Ion Irradiation Facility. This facility was used successfully for several previous radiation-effects studies[3-6] and has been described in detail elsewhere.[7] The main contribution of the author to this facility (in addition to minor improvements) has been a redesign of the specimen holder and specimen heater within the target chamber, as described below.

The energetic heavy-ions that produce damage in the specimens are accelerated by a tandem Van de Graaff electrostatic accelerator (High Voltage Engineering Corporation, Model EN). A schematic of the accelerator facility is presented in Fig. VI-1. In this study, the Cu negative ions that were injected into the accelerator were produced within a negative ion source (SNICS type) developed by Billen and Richards.[8,9] This source is simple in design, and was found to

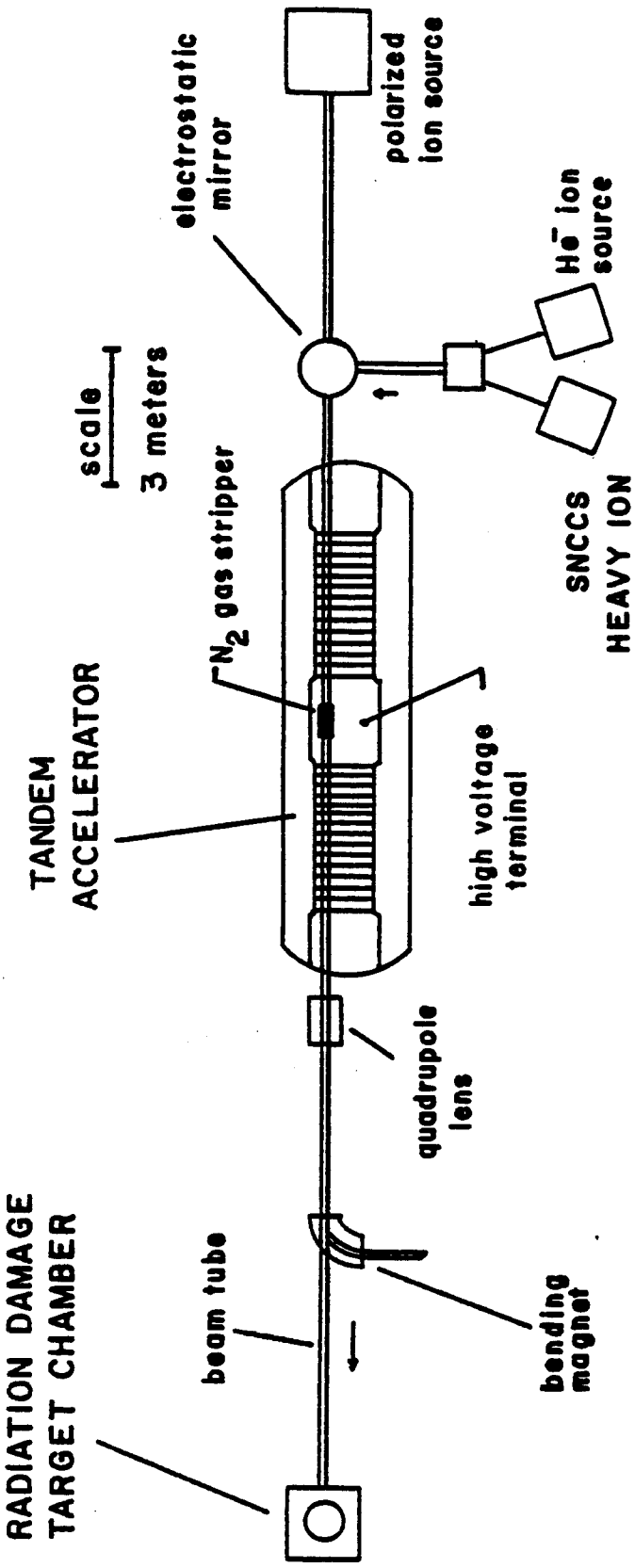

Figure VI. 1. SCHEMATIC OF UNIVERSITY OF WISCONSIN TANDEM ACCELERATOR FACILITY. NEGATIVE COPPER IONS ARE PRODUCED IN THE SNCCS SOURCE AND INJECTED INTO THE ACCELERATOR. IN THIS STUDY, 14 MeV Cu^{+3} IONS IRRADIATE SPECIMENS IN THE TARGET CHAMBER.

be extremely reliable. Basic components within the source are a negatively biased cylindrical cathode (copper), a helical tungsten filament coaxial with the cathode, and a Cs reservoir. Cs atoms that are surface ionized on the hot filament bombard the cathode and create Cu ions by sputtering. Negative Cu^- ions, which form within the source by charge-exchange reactions with Cs atoms, are extracted from the source, pass through a selecting magnet, then are deflected 90° (by an electrostatic mirror) into the tandem accelerator. The ions are accelerated into the high voltage terminal, which is operated at a positive potential V. Collisions with N_2 gas molecules in a gas-stripper canal within the terminal convert the energetic negative ions into positive ions of charge nq, where n is an integer and q is the electronic charge. Because of the random nature of the stripping process, the beam of positive ions emerging from the high voltage terminal contains a mixture of charge states (n has several values). Therefore, an ion of charge state nq exiting the accelerator has acquired an energy of

$$E = qV(1 + n) \quad . \tag{6-1}$$

In this study, the accelerator terminal was operated at a potential of 3.5 MV, and 14 MeV Cu^{+3} ions were directed into the target section. Copper ions of other charge states and energies were also produced, but were prevented from entering the target chamber. The charge state selection was accomplished mainly with a quadrupole lens that is positioned on the high energy beam line.

The target chamber and its vacuum system were originally designed and built by Smith and Lott.[4,7] Figure VI-2 shows in detail the components comprising the target section. This entire section lies ~ 1/2° off the tandem accelerator axis, to prevent neutral atoms and low z ions from impinging upon the target. The heavy ion beam is deflected into the target section using a large analyzing magnet. A three-stage vacuum system on the target section provides a high vacuum within the target chamber (pressures in the 10^{-9} torr range can be achieved), even though the vacuum in the accelerator beam line is several orders of magnitude poorer. The first and intermediate pumping stages incorporate a 200 ℓ/sec diffusion pump and a 400 ℓ/sec orbitron pump, respectively. The target chamber is separated from the intermediate stage by a low-conductance series of 6.5 mm Ta aperatures, and is pumped by a large orb-ion pump. The composition of residual gases in the target chamber can be determined with a gas analyzer (Varian, Model, VGA-100) that is mounted on the chamber.

Several diagnostic devices are mounted on the target section to measure the intensity and the charge state composition (energy spectrum) of the beam. Faraday cups for measuring total beam current are located at the entrance to the target section, at the entrance to the specimen chamber and behind the specimens at the rear of the target section. During irradiations in this study, total beam current at the target chamber entrance has been typically 100 to 130 nA. The size of the beam that strikes the specimen is defined by a Ta mask containing a mm dia. hole centered on the beam-tube axis. To measure

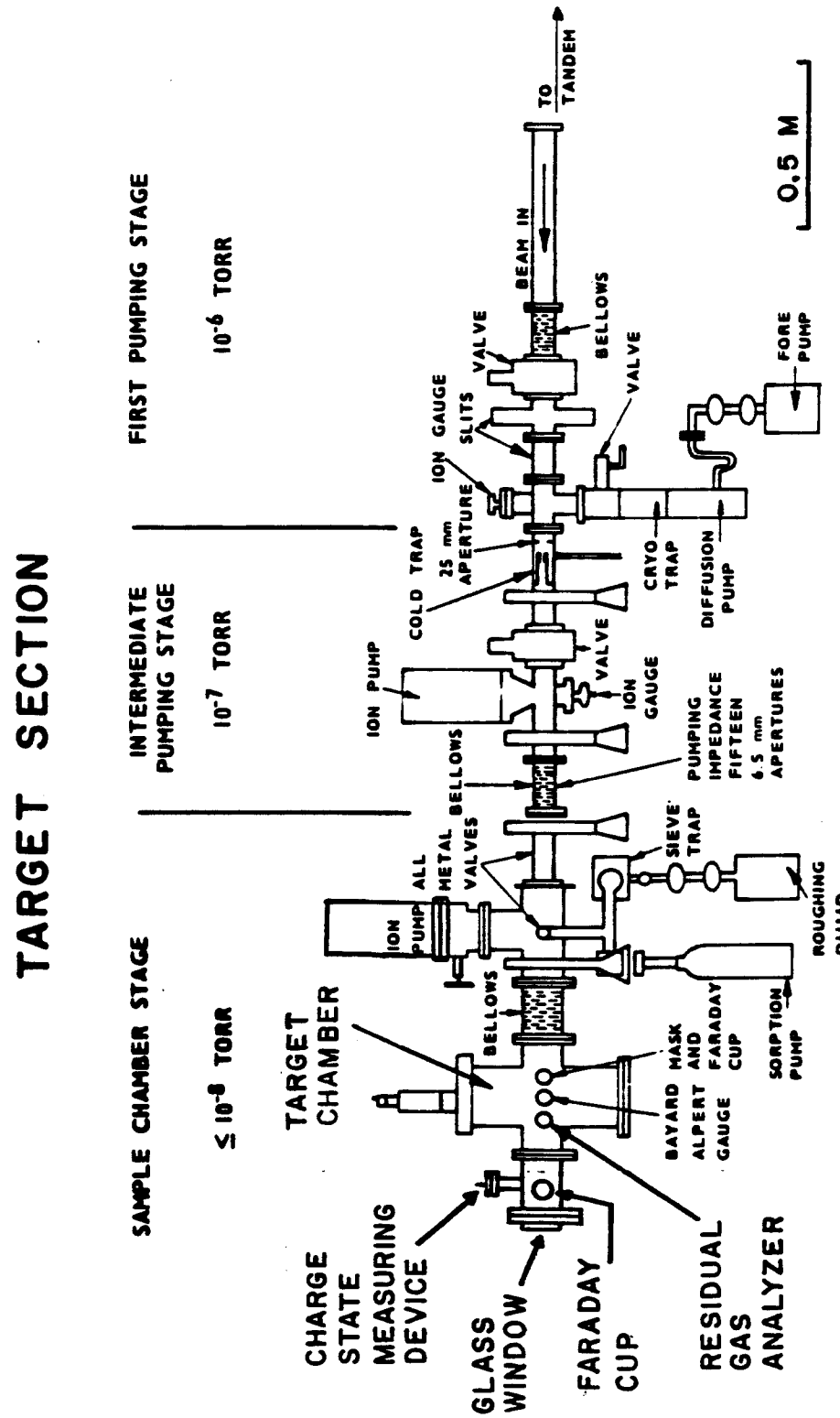

Figure VI.2. Target section of the U.W. Heavy Ion Irradiation Facility.

the charge-state distribution a gold film is inserted into the beam path; the energy of particles scattered 90° from the beam axis is measured with a solid state detector, then converted into the initial particle energy using the Rutherford scattering formula. Energy spectra produced by the technique have shown that when the Cu^{+3} state is selected using appropriate lens and magnet settings, over 99% of the total beam consists of Cu^{+3} ions.

The target chamber is a vertical, stainless steel tube (14.6 cm I.D.), containing side ports for the diagnostic devices and for entry and exit of the heavy-ion beam. A specimen holder assembly is mounted through the top flange of the target chamber, and a furnace, for heating specimens during irradiation, is mounted through the bottom flange. In this study, the specimen holder and the heater were redesigned, such that a sample was heated only during the irradiation, while other samples in the holder remained at lower temperatures to prevent thermal aging and annealing. For practical reasons, eight specimens were loaded into the target chamber at one time, and these could be irradiated in a one-day run. In the old design of the specimen holder[7], all eight of the samples were mounted in a row on a single 2 cm x 8 cm tantalum plate, which was attached to a vertical-motion feedthrough that allowed samples to be moved successively into the path of the heavy-ion beam. The furnace in that design was constructed of 0.025 mm Ta foil, which was rolled into the shape of a tube 4 cm in diameter by 13 cm, and which was heated by passing an electrical current through it. The furnace was

mounted vertically, concentric with the target chamber, and it contained a pair of 1 cm diameter holes for passage of the ion beam. During irradiation the specimen holder was suspended within the furnace and was heated by thermal radiation. The disadvantage of this design was that the specimens were heated en masse, therefore the temperature history of an individual specimen could not be controlled. At an irradiation temperature of 500°C, the temperatures of the hottest and coolest samples in the holder differed by only about 40°C. Since the irradiation of an entire set of 8 samples typically required 10 to 20 hours, an individual sample was often exposed to high temperature for many hours before and after its irradiation. Such pre-irradiation heating could cause significant thermal aging, while post-irradiation heating could alter or anneal out any irradiation induced changes in the alloy microstructure. Because of the time required to design, construct and test the new system, however, the old system was used for the irradiation of the first three sets of specimens in this study (the high purity Cu; the Cu-Co; and the first set of Cu-Be specimens).

The specimen holder assembly and the furnace that were designed for this study are shown in Figs. VI-3 to VI-6. The heating elements of the furnace are a pair of 0.025 mm tantalum sheets (4 cm wide by 10 cm long), which sit parallel to each other, but are separated by a gap of 1.3 cm (Figs. VI-4 and VI-5). The tantalum sheets are ohmically heated, and they each contain a 0.7 cm hole for passage of the ion beam. During ion bombardment, an individual specimen is

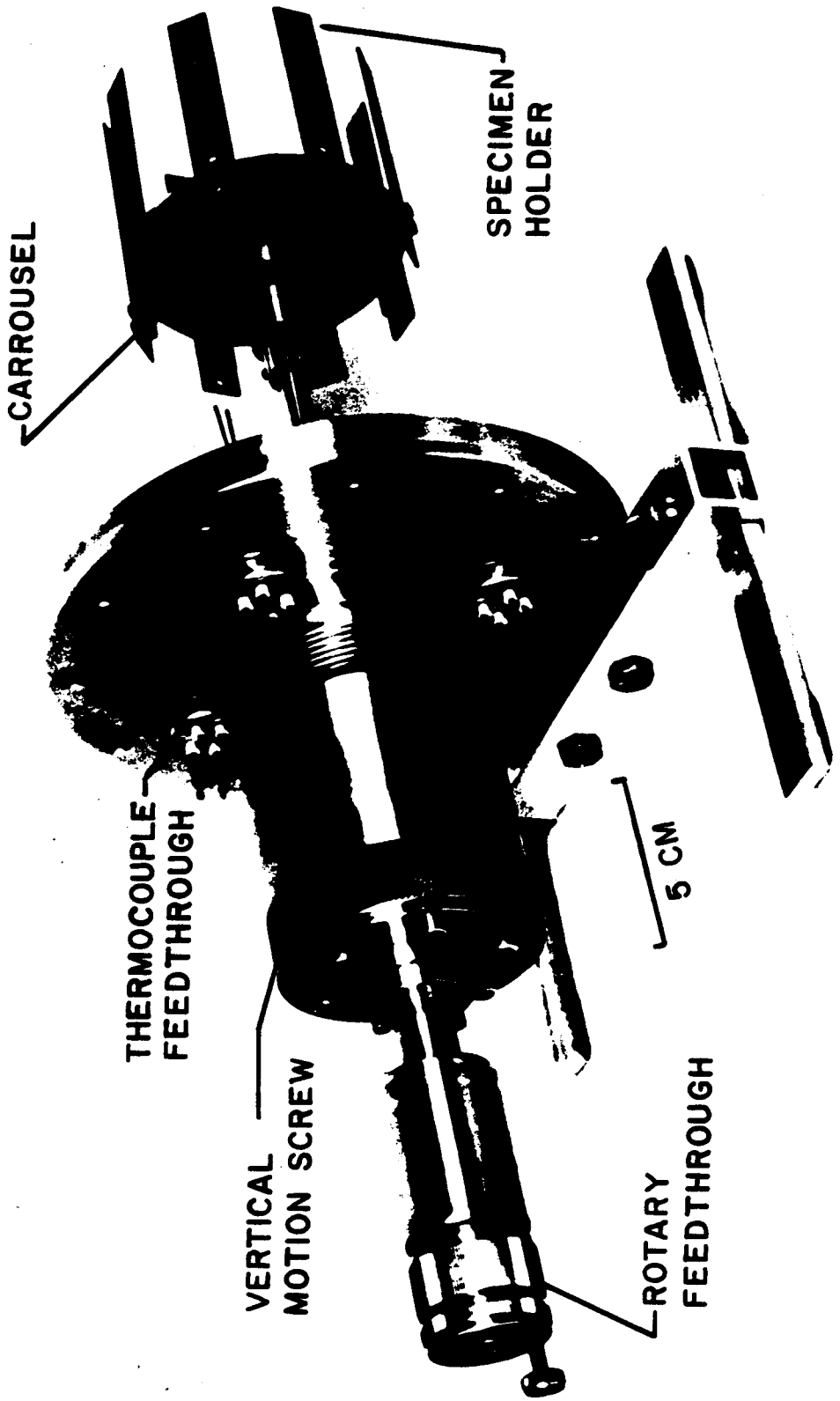

Figure VI.3. Carrousel specimen holder assembly.

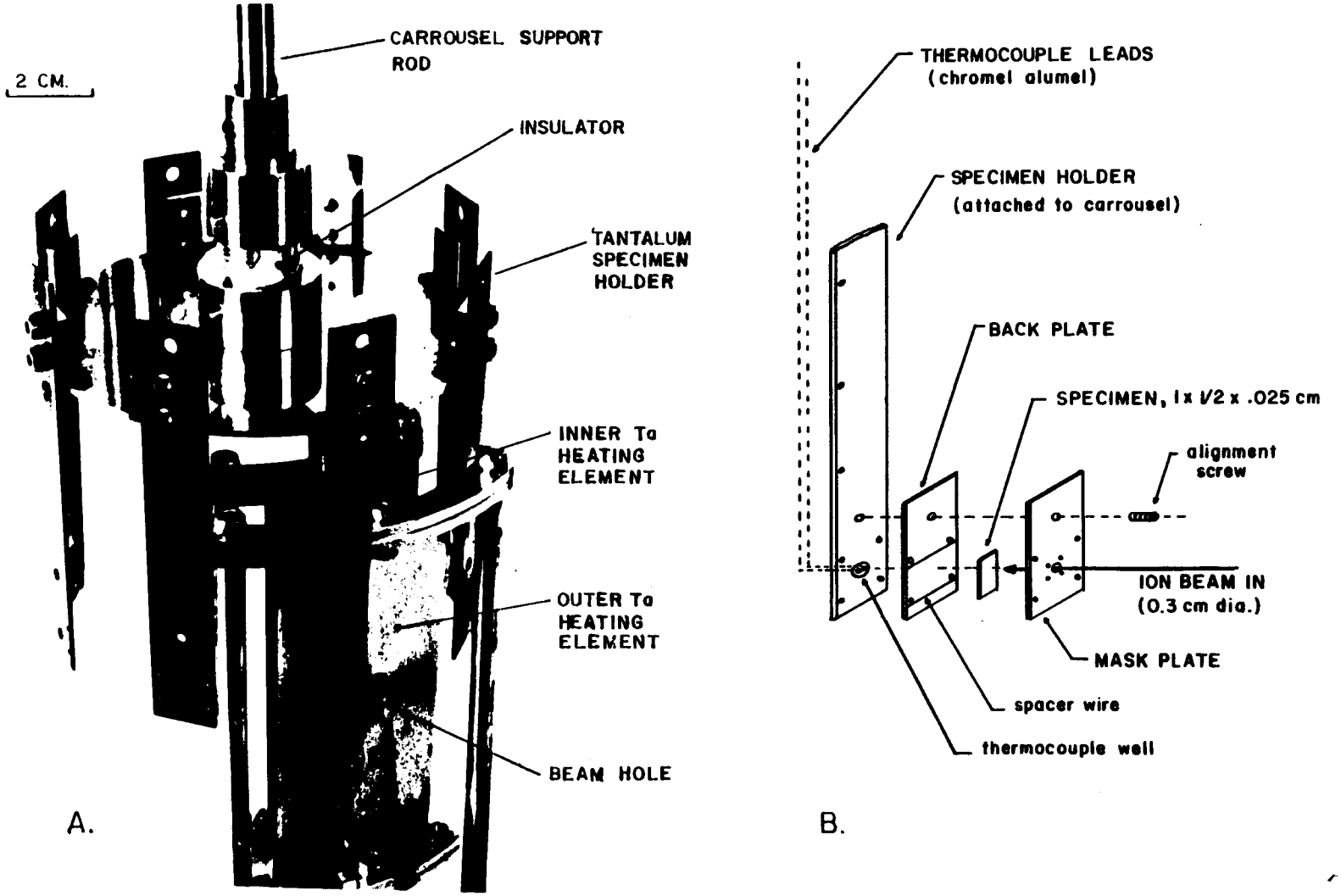

Figure VI.4. (a) Specimen holder in the irradiation position within the heater.
(b) Exploded view of a specimen holder.

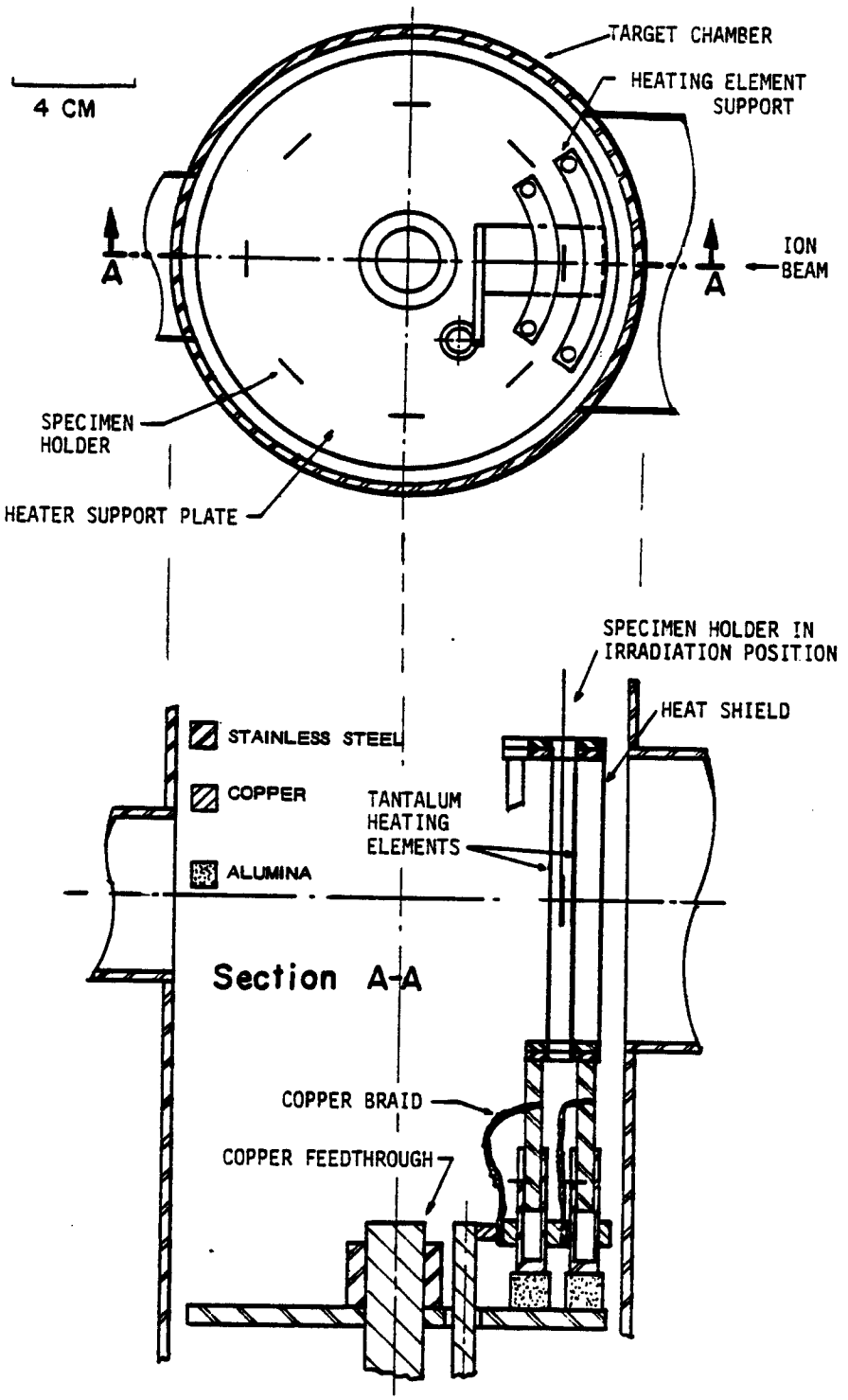

Figure VI. 5. Drawing showing top and cross sectional views of the specimen heater.

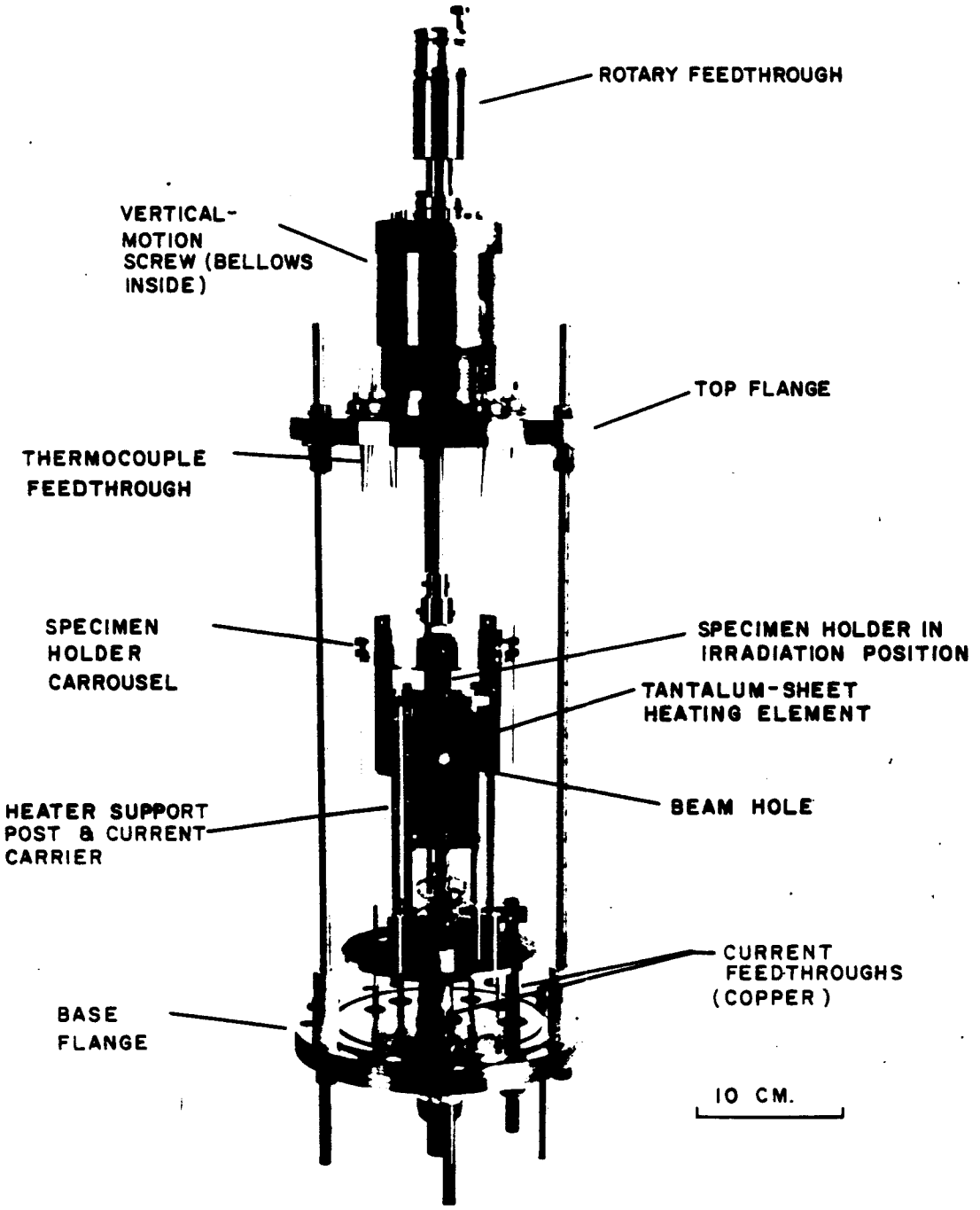

Figure VI.6. Specimen holder and heater assembly.

positioned in the gap between the Ta sheets, and is heated by thermal radiation as it is bombarded with Cu ions.

The construction of the furnace is as follows: each end of each heating element is clamped between a pair of stainless steel arcs, which constrain the heating elements into cylindrical-sections that are concentric with the target chamber, and which subtend an angle of 40°. The positon of the top end of each element is fixed by stainless steel posts, which support the steel arcs and which serve as electrical current leads. However, the bottom ends of the Ta elements are not fixed, to prevent buckling of the thin sheets because of thermal expansion. Electrical current is carried to the lower end of each element by flexible Cu braid. Heat shields constructed of 0.025 mm Ta sheet (not shown in the the figures) are affixed to the stainless steel support posts to decrease thermal radiation loss. The entire heater assembly is supported on a 14 cm diameter steel baseplate, which is mounted on a 1.9 cm diameter Cu electrical feedthrough that penetrates the bottom flange of the target chamber.

Each specimen is mounted on an individual tantalum holder (Fig. VI-4(b)), which is suspended between the heating elements during irradiation. The specimen is covered by a Ta mask containing a 3 mm hole, which defines the area on the specimen exposed to the ion beam. (Small marks were inscribed on the samples to record the location of the beam spot.) The mask-specimen-back plate assembly is clamped tightly to the holder to provide good thermal contact, and specimen

temperature is monitored with a chromel-alumel thermocouple that is located in a well, directly behind the irradiated area of the sample.

Each of the eight individual specimen holders is attached (at 45° intervals) to a 10 cm diameter stainless steel plate, creating a carousel arrangement (Fig. VI-3), which is suspended above the heater (Fig. VI-6). This specimen holder assembly is attached to a feed-through that allows both rotational and vertical positioning of the holders. Rotational motion is provided by a commercial rotary, high vacuum feedthrough (Varian), while vertical motion is provided by a 9 cm O.D. brass screw assembly, which surrounds a stainless steel bellows. Vertical motion is necessary because opposing specimen holders differ in length, to allow visual alignment of the holder in the irradiation position. A specimen is aligned with respect to the ion beam by sighting on the back of the thermocouple well, using a alignment telescope that is mounted rigidly behind the target chamber, on the beam axis.

The new specimen holder design performed well with respect to temperature measurement and control. The relatively small angle subtended by the furnace, combined with the thermal radiation shields, prevented excessive heating of specimens not in the irradiation position. Listed below are typical steady-state temperatures of all specimens in the carousel, T_1 through T_8, when the temperature of the specimen in the irradiation position was 500°C (T_3) and 300°C (T_7), respectively:

Specimen Holder:	T_1	T_2	T_3	T_4	T_5	T_6	T_7	T_8
Temperature °C:	177	259	500	239	165	166	159	165
	103	99	96	100	105	151	300	139

At high irradiation temperature (500°C) even the specimens adjacent to the heater (T_2 and T_4) remained at least 240°C below the temperature of the specimen in the furnace (T_3). The estimated accuracy of the absolute temperature measurement was ±5°C.

Instantaneous measurement of the beam current striking the sample during irradiation is obtained from a picoammeter connected between one of the thermocouple feedthroughs (which are in electrical contact with the specimens) and ground. The carousel is isolated from ground by a ceramic coupling. Beam current was integrated electronically throughout the irradiation to obtain the total ion fluence. There were problems in measuring the absolute beam current on target in this study, at temperatures greater than about 400°C. Poor suppression of secondary electrons emitted from the beam spot contributed to this problem, but extraneous currents also were measured, which were temperature dependent and (to a lesser extent) time dependent, and which were not well understood. Therefore, the actual intensity of the ion beam passing through the 3 mm mask aperture into the target chamber was periodically measured using the rear Faraday cup, and this value was correlated with the apparent beam current measured directly off the thermocouple leads. The estimated error in the absolute fluence measurement is ±20%.

C. Post-Irradiation Analysis

Irradiated specimens were analyzed using two techniques -- transmission electron microscopy (TEM) and Auger electron spectroscopy (AES), each of which had different objectives. Transmission electron microscopy, the primary technique, was used to examine and to characterize the microstructure within all of the irradiated specimens. Auger electron spectroscopy, combined with ion-sputtering, was used to profile the elemental composition of the near-surface region of many of the alloy specimens, to determine whether radiation-induced solute segregation occurred. In addition, unirradiated portions of many of the alloy specimens were examined with these techniques. The unirradiated regions served as a control specimens, since they experienced the same temperature history as the irradiated region.

C-1. Transmission Electron Microscopy

Because of the shallow depth of the damaged region, and the non-uniformity of the displacement damage within this region (with respect to depth), special techniques are required to prepare heavy-ion irradiated specimens for TEM analysis. Transmission electron microscopy requires thin, electron-transparent foils, therefore irradiated specimens must be prepared such that thin-sections (< 500 nm) are obtained from the damage zone. Also, the nonuniformity of the displacement damage with depth requires that the location of the thin section, relative to the original specimen surface, be known. In this study, two different speciment preparation methods were used -

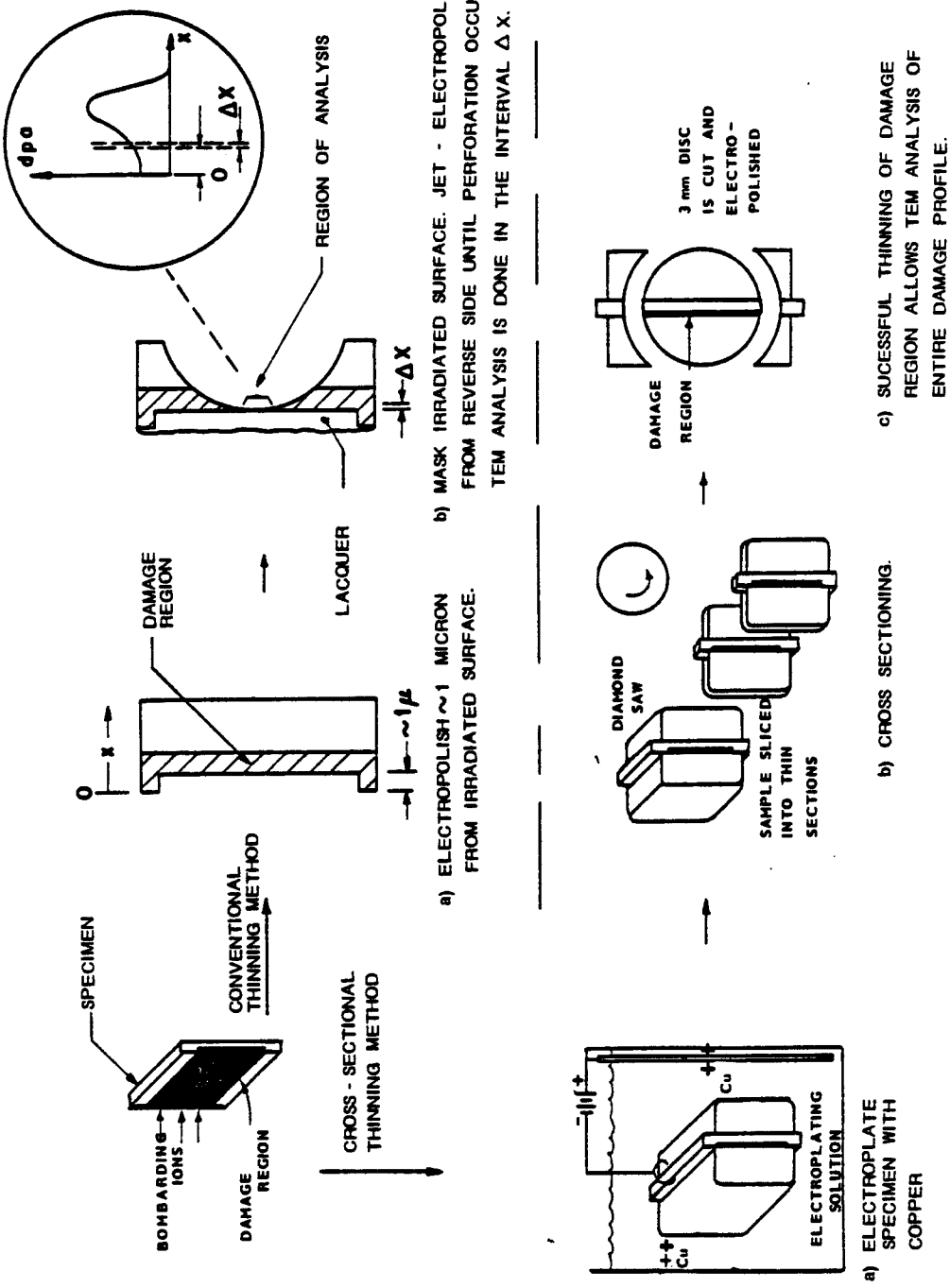

Figure VI. 7. Schematic explanation of the two procedures used in this study to prepare irradiated specimens for analysis in the electron microscope.

backthinning and cross sectioning - as explained schematically in Fig. VI-7. The backthinning, or conventional, method allows the examination of only a narrow depth interval (Δx) in the damage zone, and the remainder of the zone is destroyed. The cross sectioning method is more complicated, because the irradiated foil is first electroplated and wafered, then a thin section is obtained in a plane parallel to the path of the incident ions. Using the cross sectioning method, the entire depth of the irradiated region can be imaged, however, providing data over an entire range of displacement levels and displacement rates.

Backthinning Method

In backthinned, or conventionally thinned samples, a thin section was obtained at a depth of about 1000 nm into the damage zone. This was accomplished in three steps: (a) the irradiated sample was first electropolished in an electrolyte composed of 67% CH_3OH-33% HNO_3 at -42°C, to remove a nominal thickness of 1000 nm. The actual depth removed was determined using an optical interference microscope, which measured the step height between electropolished areas of the specimens and areas that were masked from electrochemical attack; (b) a 3 mm diameter disc, centered on the 3 mm diameter irradiated region, was punched from the oversize specimen (with the irradiated surface face-down to protect it from the impact of the punch); and (c) the irradiated side of the 3 mm disc was masked with a commercial protective lacquer, and the disc was thinned from the reverse (unirradiated) side in a commercial, twin-jet

electropolishing machine (E. A. Fischione, Model 120) until perforation occurred. The very thin foil bordering the perforation was then suitable for TEM analysis. The electrolyte used in the jet polisher consisted of 25% H_3PO_4-25% C_2H_5OH-50% H_2O at a temperature of -10°C to -15°C. The thickness of 1000 nm nominally removed in step (a) was chosen because the displacement vs. depth profile is relatively flat near this depth, minimizing the effect of errors in the step-height measurement. This measurement error was estimated at ±300 nm, yielding an uncertainty of ±25% in the displacement dose assigned to the thin section. (The displacement profile for 14 MeV Cu on Cu is shown in Fig. VII-1.)

Cross Sectioning Method

The cross sectioning method of TEM specimen preparation was first applied to ion-bombarded specimens by Spurling and Rhodes[10], who studied proton irradiated stainless steel. This method has since been used by Narayan and his co-workers[11-13] in the study of pure copper irradiated at room temperature, and by Whitley[5] in a study of void formation in heavy-ion bombarded nickel. In the present study, all of the pure Cu samples were cross sectioned, as were about 40% of the Cu-Be, Cu-Co and Cu-Fe samples. A good deal of experimentation, mainly by trial and error, was required to develop a TEM specimen preparation procedure that yielded usable thin specimens, i.e. specimens that were uniformly thinned throughout the irradiated region. The procedure that evolved is outlined here:

(a) Immediately before electroplating, the irradiated specimen was electropolished very briefly in the CH_3OH-HNO_3 electrolyte at -44°C, which dissolved 50 nm ± 20 nm from the surface. This removed the surface oxide and carbon contamination (which was several monolayers thick, according to AES measurements) that inhibited strong bonding between the specimen and the electrodeposited copper.

(b) A thick layer of Cu (2-3 mm) was electrodeposited onto both sides of the clean specimen, encapsulating the irradiated region. The electroplating was done in an aqueous solution containing 55 grams/liter H_2SO_4 and 178 grams/liter $CuSO_4$, at a current density of approximately 100 mA/cm^2 (see Fig. VI-8). When the specimen was first immersed in the plating bath, the plating current was reversed for several seconds, which removed 50 nm ± 20 nm from the foil surface. This procedure, combined with the electropolishing in (a), resulted in the dissolution of 100 ± 30 nm from the irradiated zone.

(c) The electroplated specimen was mounted in an epoxy resin and cross sectioned into 0.25 mm wafers using a low-speed diamond saw. A 3 mm diameter disc, centered on the interface between the plating and the irradiated region of the sample, was then punched from each wafer.

(d) The 3 mm disc was thinned until perforation occurred, in the twin-jet electropolishing machine. A successfully thinned specimen perforated at the plating/specimen interface, and a

portion of thin foil surrounding the perforation intersected the damage zone.

Successful thining required that the specimen be centered with the electrolyte jets, that the plating adhere completely to the specimen, and that the copper plating, the damage zone of the specimen, and the annealed specimen material beyond the damage zone electropolish at equal rates. The main problem encountered was the tendency of different regions of the 3 mm cross sectioned disc to electropolish at different rates (because of differences in the microstructure of these regions), producing the perforation away from the interface, or causing nonuniform thinning of the interface region. In an effort to obtain uniformly thinned cross sectioned specimens, several different electrolytes were tested under a variety of electropolishing conditions. The most successful procedure was to first dish the specimen by jet-polishing for ~ 45 sec in 20% HNO_3-80% CH_3OH at -30°C and 45 volts, then continue thinning until perforation occurred, in a solution of 25% C_2H_5OH-25% H_3PO_4-50% H_2O at -14°C. Occasionally, an ion milling device (which eroded a specimen by sputtering with 6 KeV Ar ions) was used to extend the thin area in specimens where the perforation did not form initially at the interface. A TEM micrograph of a cross sectioned, annealed, unirradiated Cu specimen is presented in Fig. VI-9, which shows that the electoplating itself did not significantly alter the near-surface region of the specimen.

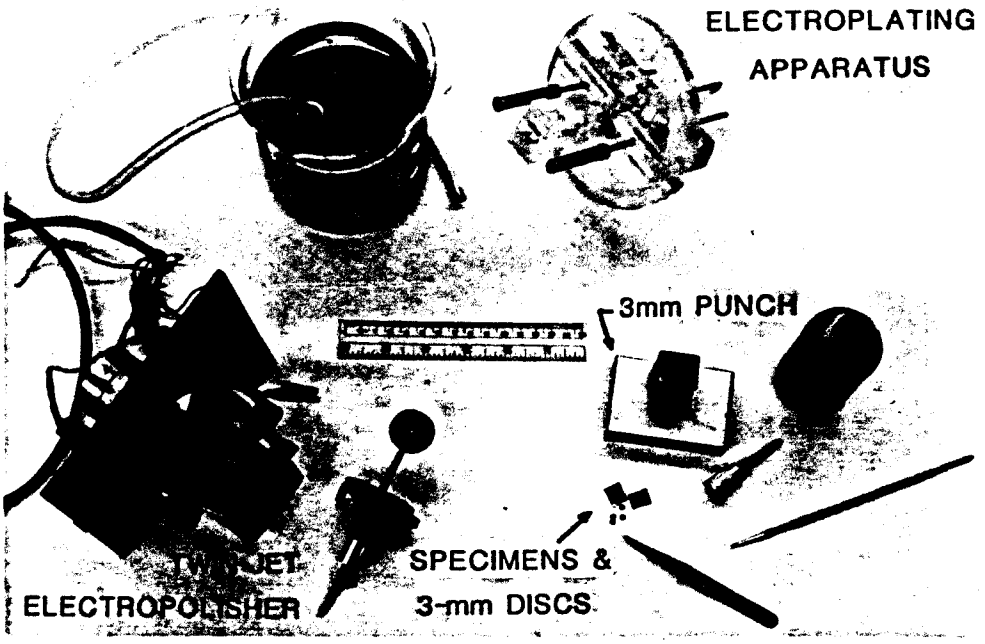

Figure VI.8. Apparatus for preparation of transmission electron microscopy specimens.

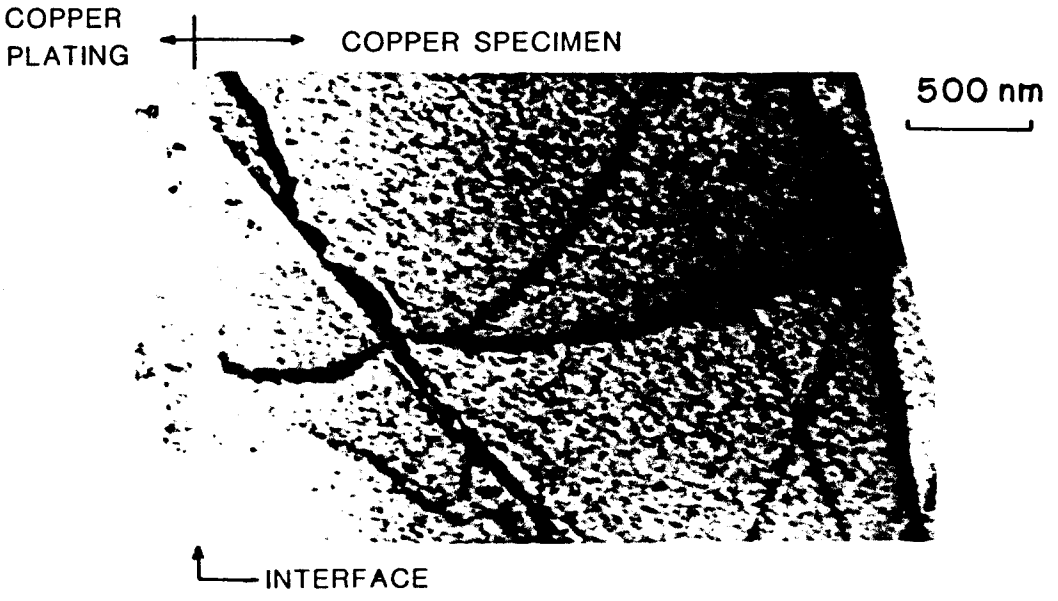

Figure VI.9. A transmission electron micrograph showing the microstructure of a cross sectioned, unirradiated, annealed Cu specimen. The mottled background results from slight surface etching.

Thinned specimens were examined, using conventional TEM imaging technqiues, in a JEOL 100B transmission electron microscope modified to operate at 120 KeV, which was equipped with a double-tilt specimen holder. Dynamical two-beam diffraction conditions, with $s \gtrsim 0$, were usually used when in the bright field mode. Selected area diffraction, along with centered dark-field imaging, were employed for identification and characterization of precipitates. Specimen thicknesses were measured by depositing small, superimposed carbon contamination spots on both surfaces of the foil, using the microscope in the scanning-transmission (STEM) mode. The specimen was then tilted about one axis to an angle of $\theta = 35°$ to $45°$, and the displacement between the centers of the contamination spots was obtained as $t = d/\sin\theta$. The uncertainty in the thickness measurement was estimated at ±20%. Precipitate and void sizes and concentrations were measured from TEM micrographs using a Zeiss particle size analyzer.

C-2. Auger Electron Spectroscopy

Following irradiation, but prior to TEM specimen preparation, many of the alloy samples were analyzed using Auger electron spectroscopy (AES). Since AES is a surface analysis technique, depth profiles of the elemental composition of the near-surface regions of alloy specimens were obtained by combining AES analysis with sputter etching. The energy spectra of the Auger electrons were recorded in the conventional manner, as $dN(E)/dE$ vs. E, where E is the Auger electron energy and N(E) is the number of electrons detected at that

energy. The concentration of an element was correlated with the measured amplitude of the differential peak of a characteristic Auger transition, for that element.

The measurements were performed on a commercial Auger/ESCA system (Physical Electronics Industries, Model 548), using a 3 KeV primary electron beam to excite Auger transitions. The beam diameter was 0.2 mm, beam current was 30 μA, and a peak-to-peak modulation energy of 3 eV was used. In the usual procedure, two specimens at a time were mounted on an aluminum pedestal, which was introduced into the high vacuum chamber on a vacuum-feedthrough probe. (The Cu-Be specimens from Run #5 were mounted on the carousel holder to allow degassing before analysis.) In either case, each specimen was covered with a tantalum or stainless steel mask, containing a 3 mm diameter hole that was centered on the region to be anlayzed.

Sputter etching was accomplished with a beam of either 5 KeV Ar^+, 2 KeV Ar^+ or 2 KeV Xe^+. After introduction of the high purity Ar or Xe, the pressure in the chamber was 5×10^{-5} torr (otherwise it was $\sim 5 \times 10^{-9}$ torr). The sputtering rate under a given set of conditions, close to the point of contact of the primary electron beam, was determined by masking off part of the specimen, and then measuring the resulting step-height in an interference microscope. The resolution of interference fringes limited this method to step heights $\gtrsim$ 100 nm. Absolute sputtering rates (for several different Ar ion energies and beam focus conditions) were also measured by recording the time required to sputter through a 250 nm Ni film

deposited on a Cu foil, while the Auger spectrum of the target was recorded in the multiplex mode. From the measured values of the Ni sputtering rates, the Cu sputtering rates were obtained using published values of the Cu/Ni sputtering-yield ratio[14] (Y_{Cu}/Y_{Ni} = 0.67 for low energy Ar^+ bombardment). The estimated uncertainty in the abslute sputtering rate was ±25%, although the estimated uncertainty in the relative sputtering rate (from sample-to-sample) was ±5%.

References for Chapter VI

1. P. Wilkes, Ph.D. Thesis, University of Manchester, England, 1967.

2. P. Wilkes, Acta Met. 16, 153 (1968).

3. W. J. Weber, Ph.D. Thesis, University of Wisconsin, Madison, Wisconsin, 1977.

4. R. G. Lott, Ph.D. Thesis, University of Wisconsin, Madison, Wisconsin, 1979.

5. J. B. Whitley, Ph.D. Thesis, University of Wisconsin, Madison, Wisconsin, 1978.

6. K. Y. Liou, Ph.D. Thesis, University of Wisconsin, Madison, Wisconsin, 1979.

7. H. V. Smith and R. G. Lott, Nucl. Inst. Methods 143, 125-132 (1977).

8. J. H. Billen and H. T. Richards, Proc. of Symp. of Northeastern Accelerator Personnel, Oak Ridge National Laboratory, Oak Ridge, TN, p. 137, Oct. 1978.

9. J. H. Billen, "A Radio Frequency He^- Source and a Source of Negative Ions by Cesium Sputtering," Presented at 6th Conf. on Application of Accelerators in Research and Industry, Denton, TX, Nov. 1980. Also published as UWFDM-368.

10. R. A. Spurling and C. Rhodes, J. Nucl. Mat. 44, 341 (1972).

11. O. S. Oen, J. Narayan, and T. S. Noggle, in Applications of Ion Beams to Metals, ed. by S. T. Picraux, E. P. Eer Nisse, and F. L. Vook, 639-650 (1974).

12. J. B. Roberto and J. Narayan, CONF-751006-P1, Fundamental Aspects of Radiation Damage, 120-126 (1975).

13. J. Narayan, O. S. Oen, and T. S. Noggle, J. Nucl. Mat. 71, 160-170 (1977).

14. L. Maissel and R. Glang, Handbook of Thin Film Technology, McGraw-Hill, 1970.

CHAPTER VII

RESULTS OF EXPERIMENTS ON THE Cu-3.4 AT% Be ALLOY

The experiments that constitute this thesis were performed in two stages. First, a set of each type of material -- pure Cu, Cu-3.4 at% Be, Cu-1% Co, and Cu-1% Fe -- was irradiated, and the effect of irradiation on the microstructure of each material was surveyed. Based on the results of these experiments, radiation-induced precipitation and Be surface-segregation in the Cu-Be alloy were studied in detail. All results of the Cu-Be experiments are reported in this chapter, while results of the survey irradiations of the other materials are reported in the following chapter.

The preliminary experiments on Cu-3.4 at% Be revealed that the principal effect of irradiation was to induce continuous precipitation of CuBe platelets within the damage zone (the region traversed by the high energy ions) under certain conditions. In contrast, no precipitation of any kind was observed in regions of the specimens masked from the heavy ion beam. The experiments described here were designed primarily to define the temperature range over which radiation-induced precipitation occurred, and to explore how the microstructure evolved with increasing damage dose. In addition, experiments were designed to compare the precipitation process under irradiation with the precipitation process in unirradiated, thermally aged Cu-3.4 at% Be.

In part A of this chapter, the results of transmission electron microscopy (TEM) analysis of the radiation induced precipitation are

reported. First, measurements of the variation of precipitate size and density with temperature are presented, and the effect of irradiation temperature on precipitate morphology is described. The radiation induced CuBe precipitation in cross sectioned specimens is then characterized with respect to depth in the damage zone, and the effects of damage dose and dose-rate on precipitate size and density are described. Following this, results of post-irradiation heating experiments are reported. These experiments proved that the radiation induced precipitation was unstable at an aging temperature somewhat below the equilibrium solvus temperature. Finally, results of thermal aging studies of unirradiated Cu-3.4 at% Be samples are given, and the precipitate morphology produced by aging is compared with that produced during irradiation.

A second radiation effect reported here is the enhanced enrichment of Be (and the formation of BeO) near the irradiated surface of the Cu-Be specimens. Using Auger electron spectroscopy (AES) combined with sputter-etching, the near-surface composition of specimens irradiated under various conditions was profiled. These results are reported in part B of this chapter.

In the Cu-Be studies, twenty-eight Cu-3.4 at% Be specimens were irradiated with 14 MeV Cu ions, at temperatures ranging from 300°C to 525°C, and at ion fluences of $8.8 \times 10^{14}/cm^2$ to $3.5 \times 10^{16}/cm^2$ (corresponding to 0.25 to 10 dpa damage at 1 micron depth). The irradiation parameters and methods of post-irradiation analysis for each of the Cu-Be specimens are indicated in Table VII-1. All

TABLE VII.1. Irradiation Parameters and Methods of Post-irradiation Analysis for Cu-3.4 at% Be Samples

Run Number	Specimen Code Number	Irradiation Temperature °C	Nominal Dose, dpa @ 1 μm	Nominal Fluence, 10^{16} ions/cm^2	Particle Flux, 10^{12}/cm^{2}sec	TEM		Auger analysis
						back-thinned	cross-sectioned	
2	T51-00-1	475	9.2	3.2	4.4	x		x
2	T51-00-2	475	0.92	0.32	2.8		x	x
2	T51-00-3	430	4.6	1.6	2.6	x		x
2	T51-00-4	430	0.92	0.32	3.1		x	x
2	T51-00-5	400	4.6	1.6	2.4	x		
2	T51-00-6	400	0.92	0.32	2.3		x	
2	T51-00-7	350	4.6	1.6	2.6	x		x
2	T51-00-8	350	0.92	0.32	2.3	x		x
5	T51-00-9	475	5	1.75	3.1	x		x
5	T51-00-10	430	0.5	0.175	4.1	x		x
5	T51-00-11	430	0.25	0.088	4.1		x	x
5	T51-00-12	400	0.5	0.175	4.3	x		x
5	T51-00-13	400	0.25	0.088	4.3		x	x
5	T51-00-14	375	5	1.75	4.3		x	x
5	T51-00-15	375	1	0.35	4.2	x		x
5	T51-00-16	350	10	3.5	4.4		x	x
6	T51-00-17	430	3	1.05	3.2	x		
6	T51-00-18	475	8	2.8	4.0	x		x
6	T51-00-19	475	8	2.8	4.3	x		x
6	T51-00-20	400	2	0.70	4.1	-	-	x
7	T51-00-21	525	10	3.5	3.1	x		x
7	T51-00-22	525	2	0.70	3.4		x	x
7	T51-00-23	500	5	1.75	3.5	x		x
7	T51-00-24	400	5	1.75	3.9	x		x
7	T51-00-25	350	2	0.70	3.7		x	
7	T51-00-26	300	10	3.5	3.7		x	
7	T51-00-27	300	5	1.75	4.0	x		
7	T51-00-28	300	2	0.70	3.9		x	

specimens were solution annealed prior to being mounted in the target chamber of the accelerator. Specimens 1 to 8, however, were irradiated in the old (linear) specimen holder and were therefore subjected to some thermal aging both before and after irradiation, the effects of which are discussed later. The average ion flux for specimens 1-8 was $2.8 \times 10^{12}/cm^2 sec$, corresponding to an average dose-rate of 7.4×10^{-4} dpa/sec at a depth of 1000 nm into the damage zone. Specimens 9-28 were irradiated in the carousel specimen holder at an average dose-rate of 1.1×10^{-3} dpa/sec at 1000 nm, and were heated only during irradiation.

The calculated displacement damage vs. depth profile that is used as a reference in this work is shown in Fig. VII-1. This profile, which applies to 14 MeV Cu ions incident on a pure Cu target, was generated from ion energy-deposition data calculated with the Brice codes COREL, RASE4, and DAMG2.[1] The energy deposition data was converted to the dpa profile using the modified Kinchin-Pease model[2] with a displacement energy of 34 eV, as discussed in the first section of Chapter II. The maximum displacement damage occurs at a depth of about 2300 nm from the target surface, and the total depth of the damage zone is about 3200 nm. The degree of displacement damage at the peak-damage depth is about 16 times greater than at the specimen surface, and about 4.4 times greater than at a depth of 1000 nm. Effects of alloying elements were not included in the calculations, since impurity effects (in dilute alloys) were considered insignificant compared to experimental uncertainties.

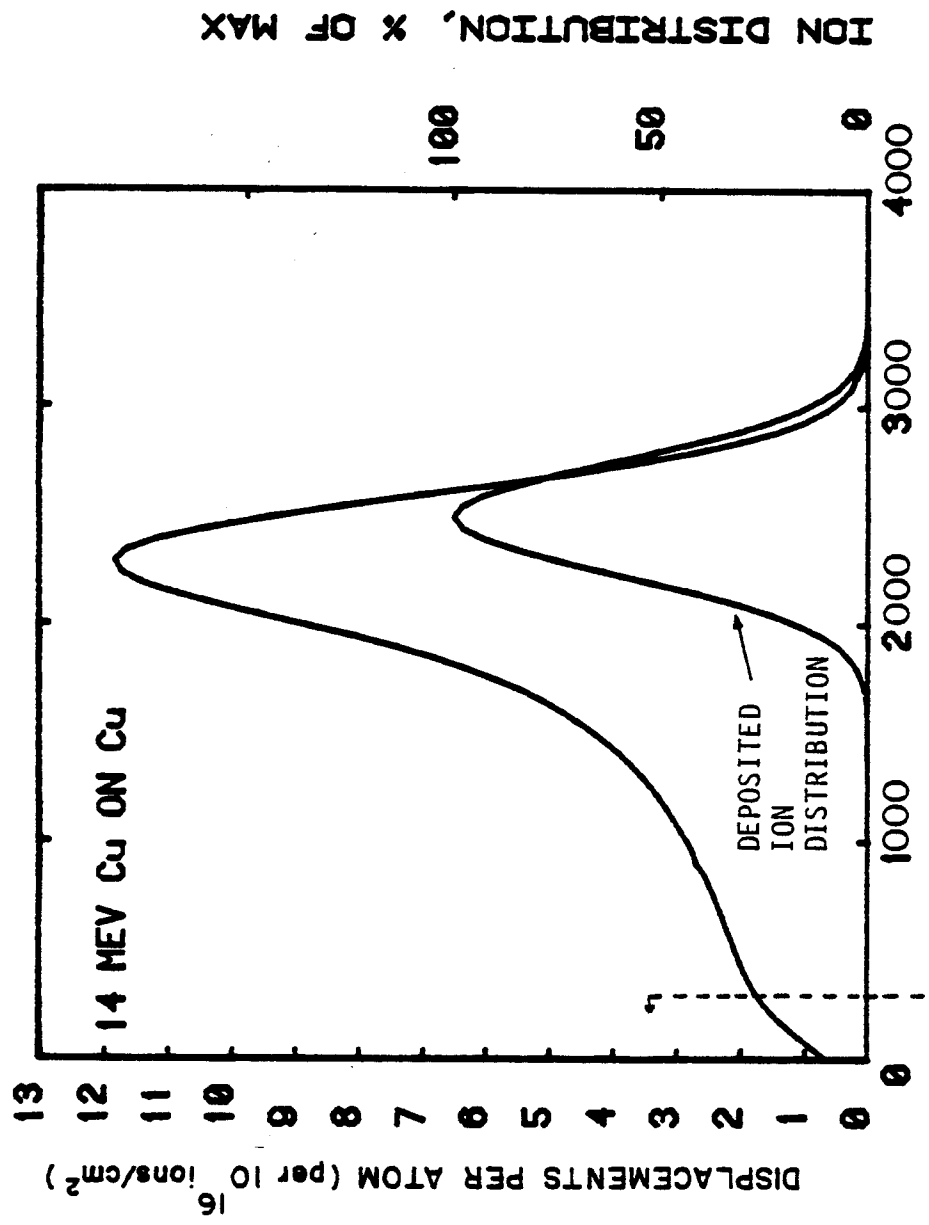

Figure VII.1. Displacement damage vs. depth curve for 14 MeV Cu ions incident on Cu, normallized for 10^{16} ions/cm^2, and calculated using the Brice code. The distribution of deposited ions is also shown (right axis). The vertical dotted line at 300 nm indicates the maximum depth to which depth profiling was done using Auger analysis.

A. Radiation Induced Precipitation in Cu-3.4 at% Be

A-1. Precipitate Morphology and the Effect of Irradiation Temperature

Specimens of the Cu-3.4 at% Be alloy, initially solution annealed and quenched, were irradiated at temperatures of 300, 350, 375, 400, 430, 475, and 525°C, with the ion fluences listed in Table VII-1. These irradiation temperatures are plotted in Fig. VII-2 on a segment of the equilibrium phase diagram of the Cu-Be system, which indicates that the Cu-3.4 at% Be solid solution is undersaturated above ~ 420°C and supersaturated below this temperature. Transmission electron micrographs* in Fig. VII-3 illustrate the typical microstructure of (supersaturated) specimens irradiated at 300, 350, 375, and 400°C, to doses of 5-10 dpa.** In all specimens irradiated at these temperatures, the supersaturated solid solution decomposed into a mixture of α_{Cu} solid solution, and platelets of the intermetallic compound CuBe. The precipitate structure was identified using standard electron diffraction analysis and dark-field imaging techniques,[4] as described in detail later. The displacement

*Unless otherwise indicated, TEM micrographs shown in this chapter were obtained in the bright field mode, using two-beam diffraction conditions with $s \gtrsim 0$, where s is the deviation from the Bragg angle. The principal diffraction vector, $\vec{g}$, and the nearest zone axis (in square brackets) are drawn on or near each micrograph. Specimen thicknesses were typically 300-450 nm.

**In the present section, results in two groups of specimens are described: high dose specimens irradiated to 5-12 dpa, and low dose specimens irradiated to 1/2-1 dpa. This approach is justified because the precipitation process was much less dependent on dose than on temperature.

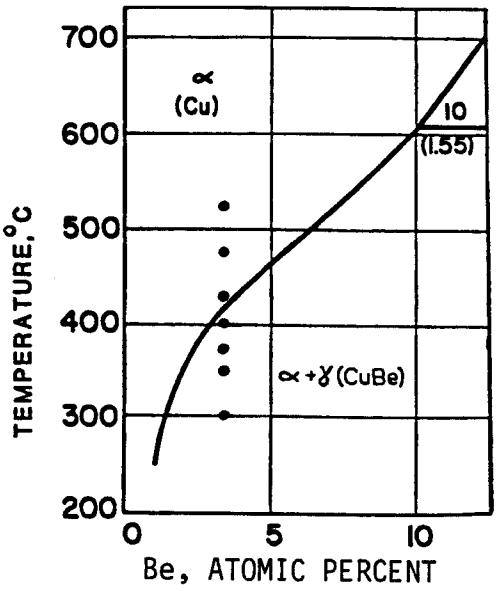

Figure VII.2. Copper-rich end of the Cu-Be equilibrium phase diagram, redrawn from Hanson(3). The black dots indicate the temperatures at which Cu-3.4 at% Be alloy specimens were irradiated.

fringes exhibited by the precipitates under certain imaging conditions indicate that the platelet faces are semi-coherent with the matrix. In all irradiated specimens, the precipitation was continuous, i.e. distributed uniformly throughout the matrix. (The apparent spatial nonuniformity of precipitation at 300°C in Fig. VII-3 results from spatial variations in the diffraction contrast of the foil.) Close examination of specimens irradiated below 400°C, however, revealed that precipitates often formed in clusters of 2 or 3, with each precipitate lying on a different habit plane. Discontinuous or cellular precipitation, which nucleates at grain boundaries in the aged Cu-13 at% Be[5,6] alloy, for instance, was never observed in the irradiated Cu-3.4 at% Be alloy. Precipitate-free zones 100 ~ 200 nm wide were occasionally observed on one or both sides of grain

boundaries, but often the continuous precipitation formed adjacent to grain boundaries also.

The microstructural detail of specimens irradiated at 300°C-400°C is shown in Fig. VII-5. Other than the precipitation, the matrix is quite free of radiation damage. The (350°C, 2 dpa) specimen contains blackspots smaller than 10 nm, which may be either precipitate nuclei or point-defect clusters. The precipitate density (and strain contrast) in the 300°C specimen is so great that other detail is obscured. In the (375°C, 1 dpa) and (400°C, 0.5 dpa) specimens, some blackspots, but few dislocation loops or tangles, are present in the matrix. In higher-dose specimens irradiated at 400°C, blackspot-type damage was visible in dark-field images from matrix reflections. Irradiation did not produce voids in any of the Cu-3.4 at% Be specimens.

While precipitation formed readily during irradiation of the supersaturated alloy, no precipitation of any kind was observed in regions of the specimens masked from the heavy-ion beam. Examples of the microstructure of the unirradiated alloy, which experienced the same temperature history as the irradiated alloy, are shown in Fig. VII-6. Later in this chapter, it is demonstrated that the morphology of the equilibrium precipitation that forms during prolonged aging of the Cu-3.4 at% Be alloy is very different than the morphology of the radiation-induced precipitation.

Radiation induced CuBe precipitation, qualitatively similar to that in the supersaturated alloys, was observed in all undersaturated

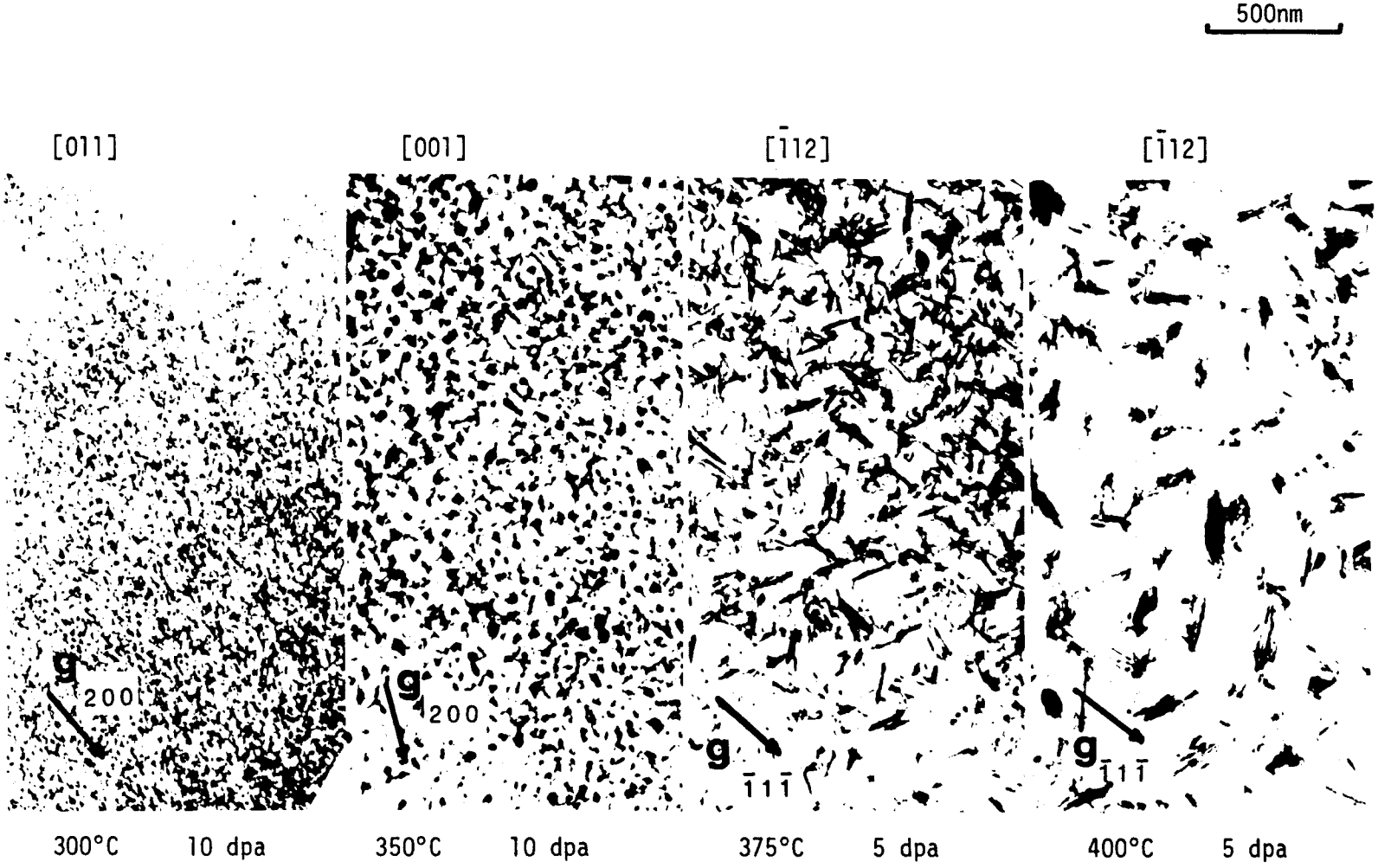

Figure VII. 3. Irradiation induced precipitation in supersaturated Cu-3.4 at.% Be irradiated at four different temperatures.

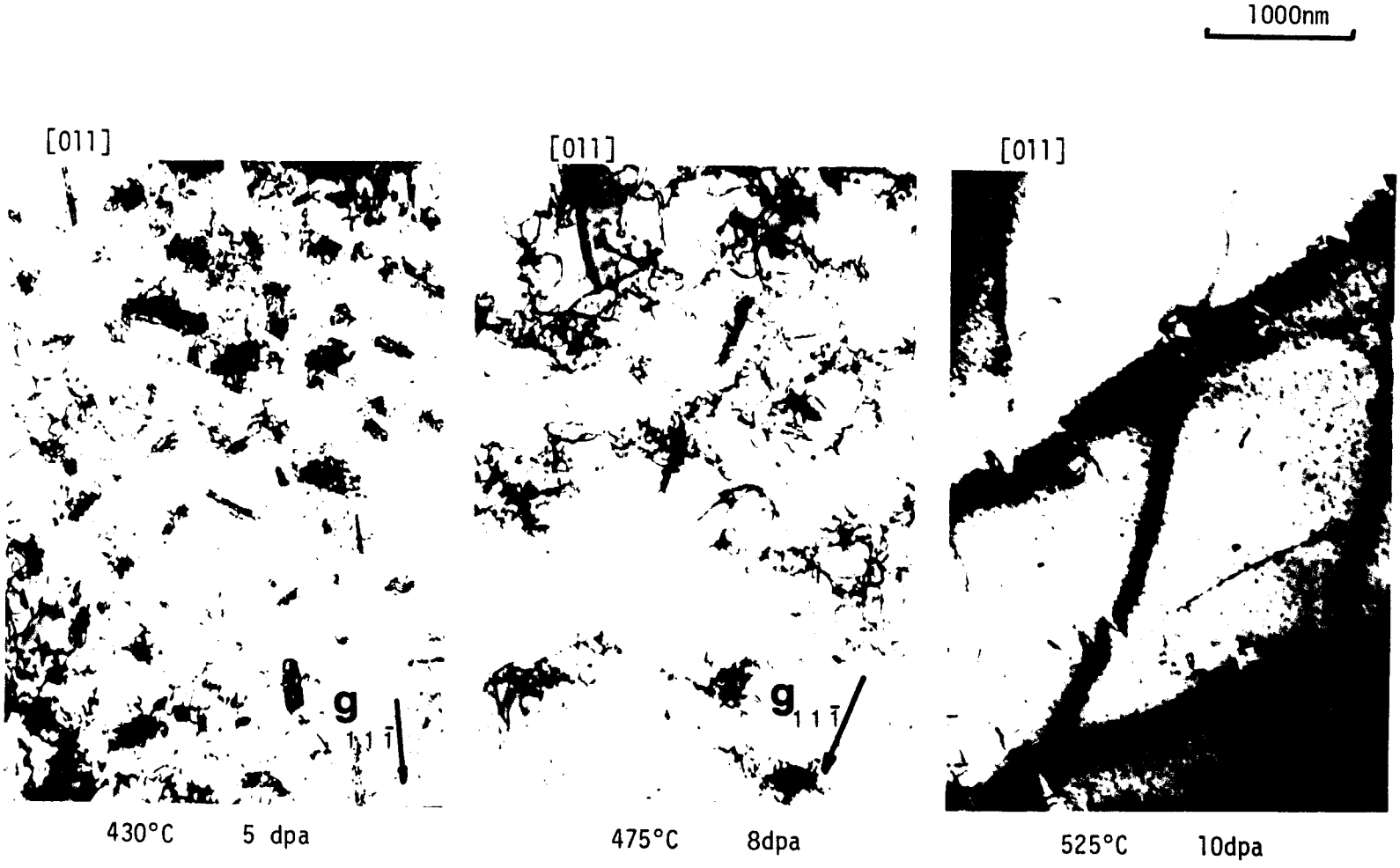

Figure VII. 4. Microstructure of undersaturated Cu-3.4% Be following irradiation at three different temperatures. Nonequilibrium CuBe precipitates form at 430°C and at 475°C.

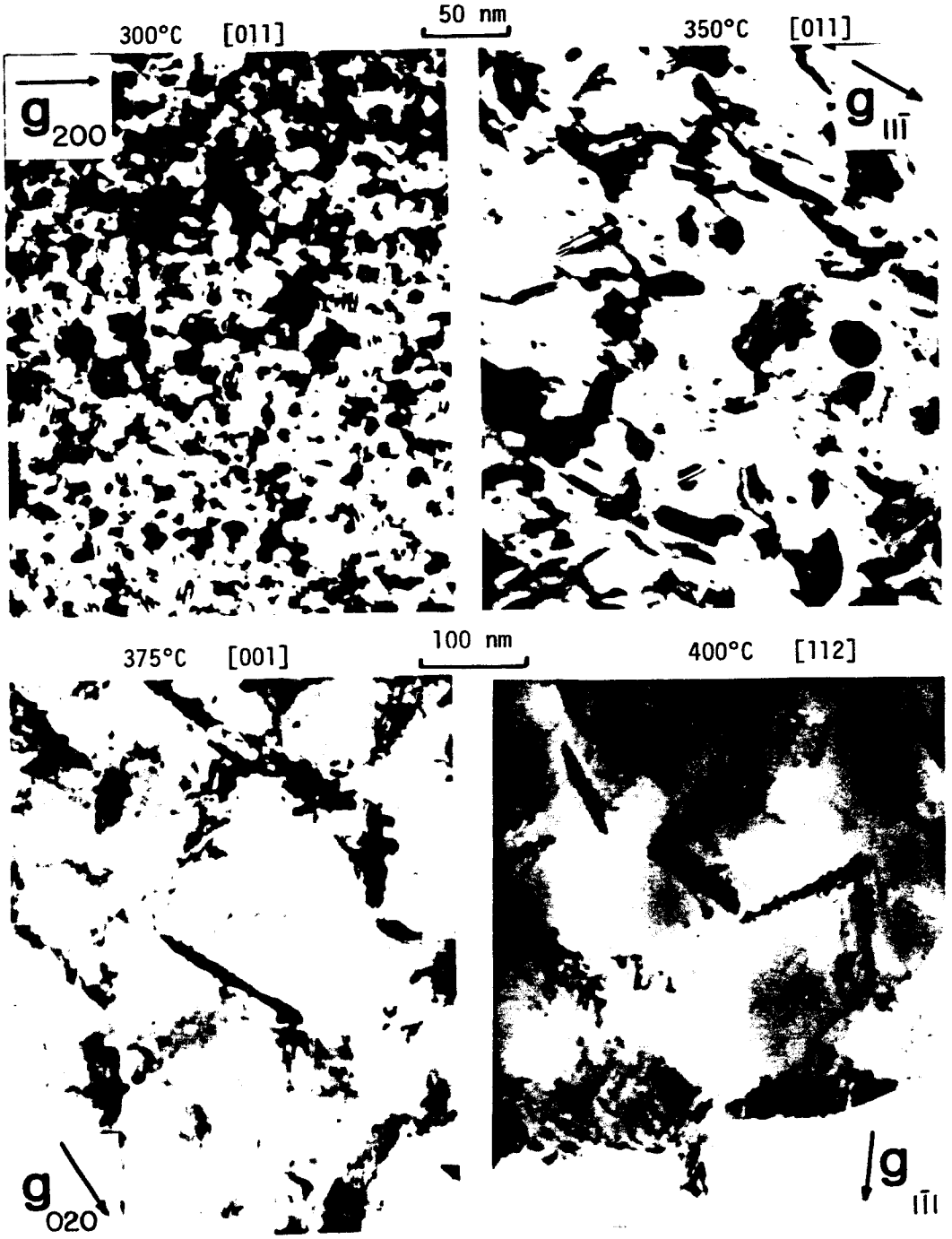

Figure VII.5. Microstructural detail in supersaturated Cu-3.4 at.% Be alloy irradiated to doses of 0.5 to 2 dpa at the temperatures indicated. Zone axis is also indicated above each micrograph.

UNIRRADIATED Cu-3.4 at.% Be CONTROL SPECIMENS

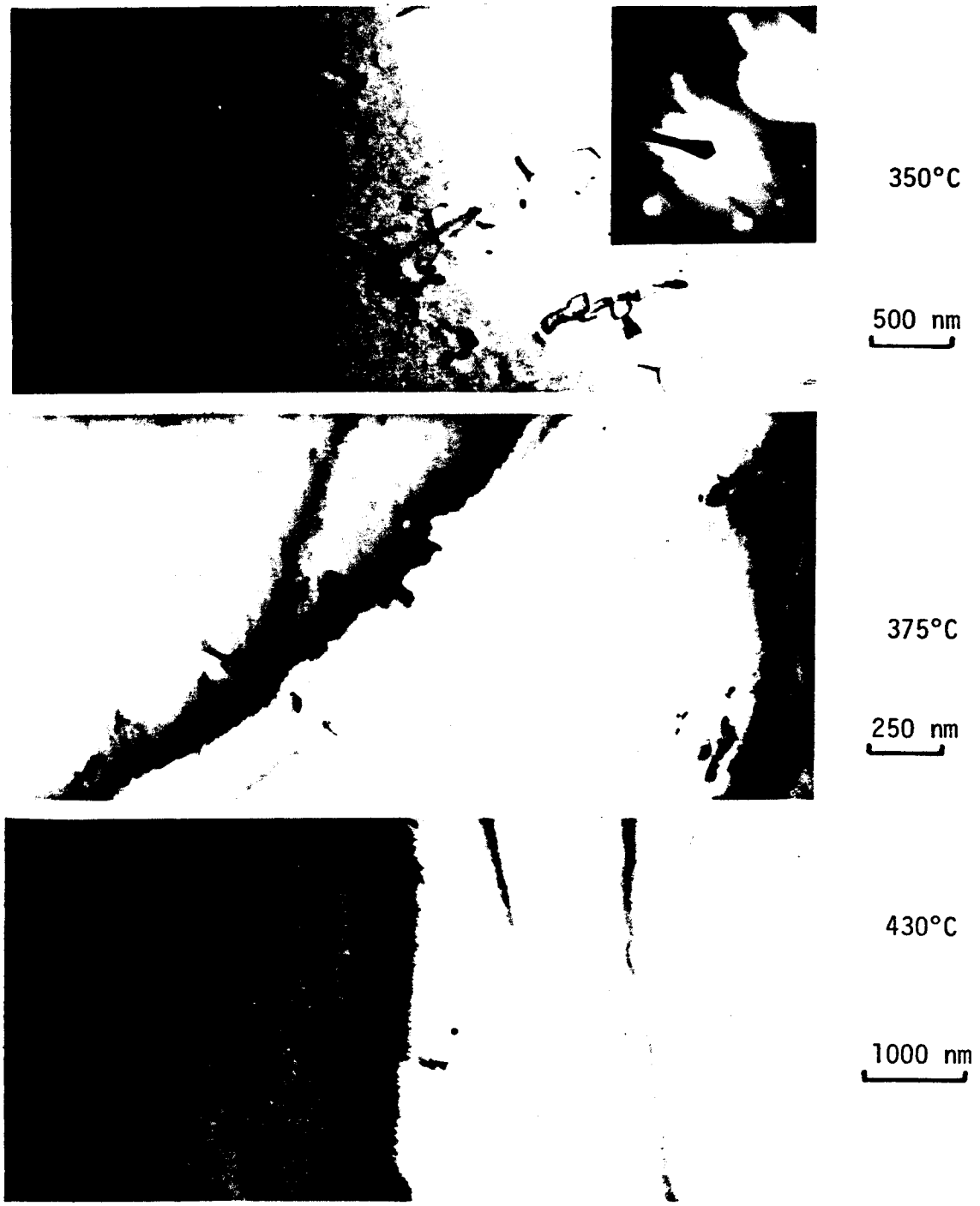

Figure VII.6. Examples of the microstructure of control samples. Shown here are unirradiated regions of specimens #8, #15, and #3, respectively, masked from the heavy ion beam. No precipitation formed in these areas. Zone axis is near [011].

Cu-3.4 at% Be specimens irradiated at 430°C, as shown in Fig. VII-4. At 475°C, lath-like CuBe precipitates were observed in foils irradiated to 5-8 dpa, but were not observed at lower doses. The damage structure at this temperature consisted almost entirely of dislocation tangles entwined with the precipitates. At irradiation temperatures of 430°C and 475°C, the precipitation appeared to be uniformly distributed on a large scale (e.g., several μm^2), but there were localized nonuniformities in the spatial distribution of the precipitates. Among the precipitates and dislocation tangles, there were regions (~ 1/4 μm^2) free of precipitates and damage. The general characteristics of the precipitation at 430°C and 475°C, however, are the same as in the supersaturated alloy. At 525°C, the solid solution did not decompose at doses up to 10 dpa, and no radiation effects were observed. The blackspot background on the 525°C specimen in Fig. VII-4 resulted from micropits on the electropolished surface of the thin foil.

Examination of Figs. VII-3 and VII-4 shows that precipitate size increases and precipitate number density decreases dramatically with increasing irradiation temperature. Precipitate sizes and number densities were measured in the high dose specimens shown in Figs. VII-3 and VII-4, and also in the low dose specimens irradiated to 1/2-1 dpa. These results are presented in Figs. VII-7 to VII-9. Particle sizes were measured on bright field or dark field micrographs by fitting an illuminated circle to the maximum precipitate

dimension.* Size and number density measurements** were obtained from specimens backthinned to a depth of ~ 1000 nm, and also from specimens thinned in cross section. In the latter case, only regions situated at depths between 500-1500 nm were selected, to avoid distortions due to surface or end-of-range effects.

The thickness of the precipitate platelets also increased as irradiation temperature and dose increased. With respect to temperature, the growth in the platelet thickness was proportionately slower than the edgewise growth; however, with respect to dose, the reverse was true. At 300°C, the platelet thickness increased from ~ 4 nm at 2 dpa to 9 nm at 10 dpa. At 430°C, thickness increased from 6 nm at 0.5 dpa, to 35 nm at 5 dpa.

The precipitate size distributions in high dose specimens irradiated at 300°C to 475°C are plotted as histograms in Fig. VII-7. On each histogram, the mean particle size ($\bar{d}$), and the standard deviation in the mean (σ) are indicated. Each histogram in Fig. VII-7 was generated by measuring the size of approximately 500 particles. An exception is the histogram of the 400°C specimen, which is based

*Because of the inherent variation in the precipitate orientations, the measured mean of the projected length of rectangular platelets is somewhat smaller than the actual mean length.

**Precipitate density, Np (particles/cm^3), was calculated as Np = n/At, where n is the particle count from a given micrograph, A is the actual area represented by the micrograph, and t is the measured foil thickness in the region where the count was made. Errors in Np result from uncertainties in foil thickness, from undercounts due to out-of-contrast precipitates, and from overcounts due to precipitates that are not wholly contained within the foil.

on the measurement of ~ 1500 particles. In Fig. VII-8, the mean precipitate size vs. irradiation temperature is plotted for both the high dose and low dose specimens. Finally, the precipitate number densities in the high and low dose specimens are plotted as a function of irradiation temperature in Fig. VII-9.

The behavior, with respect to irradiation temperature, of the mean precipitate size ($\bar{d}$), the precipitate number density (Np), and the shape of the precipitate size distributions for the high dose specimens can be summarized as follows:

(a) $\bar{d}$ increases relatively slowly with temperature between 300°C and 350°C, but increases rapidly at higher temperature. Above 375°C, $\bar{d}$ increases almost linearly with temperature. Over the temperature range studied, $\bar{d}$ increases from 19 nm at 300°C to 296 nm at 475°C.

(b) Np decreases exponentially with temperature, within the limits of experimental uncertainty. Np decreases from about $5.5 \times 10^{15}/cm^3$ at 300°C to $3 \times 10^{13}/cm^3$ at 475°C.

(c) The relative dispersion in the size distribution increases with increasing temperature. At 300°C the size distribution is clustered closely about the mean, and the relative dispersion is $\sigma/\bar{d} = 0.25$. At 475°C the relative dispersion increases to 0.45.

(d) The size distribution even at 300°C is skewed toward larger particle sizes. This asymmetry becomes somewhat more pronounced at higher temepratures.

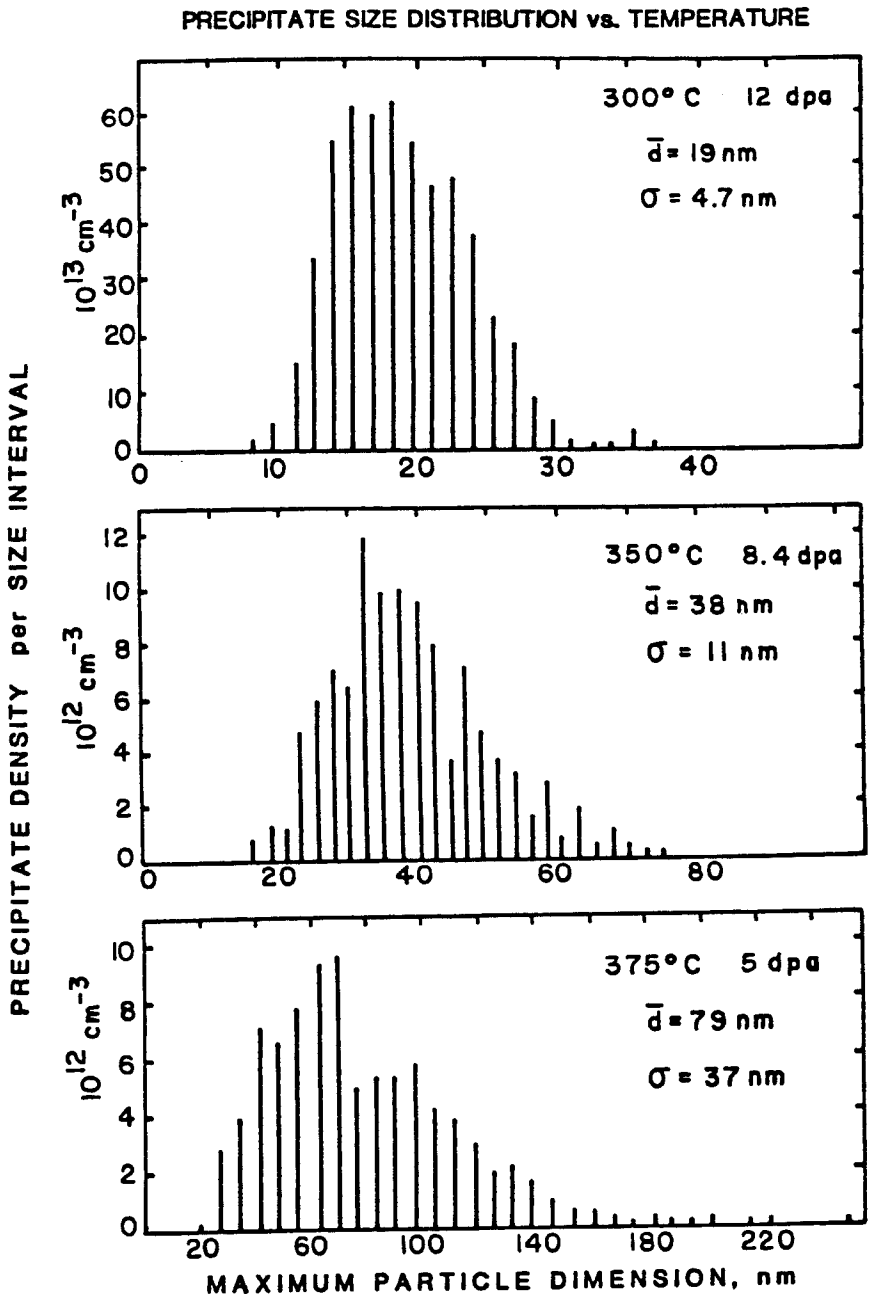

Figure VII.7. Precipitate size distributions in Cu-3.4 at % Be alloy irradiated at 300, 350, and 375°C, to doses ranging from 5-12 dpa. Precipitate size is defined as the length of the maximum precipitate dimension.

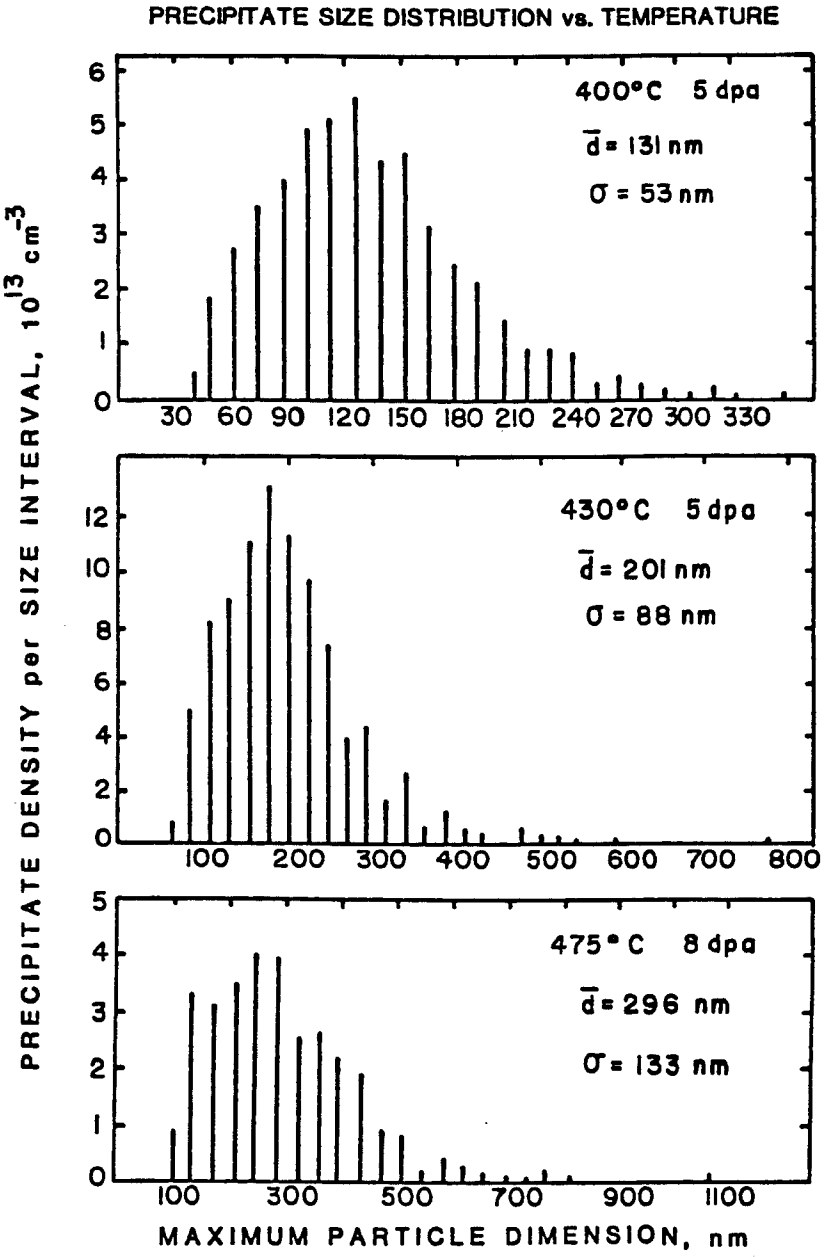

Figure VII.7. (cont.) Precipitate size distributions in Cu-3.4 at% Be alloy irradiated at 400°C, 430°C and 475°C to doses of 5-8 dpa.

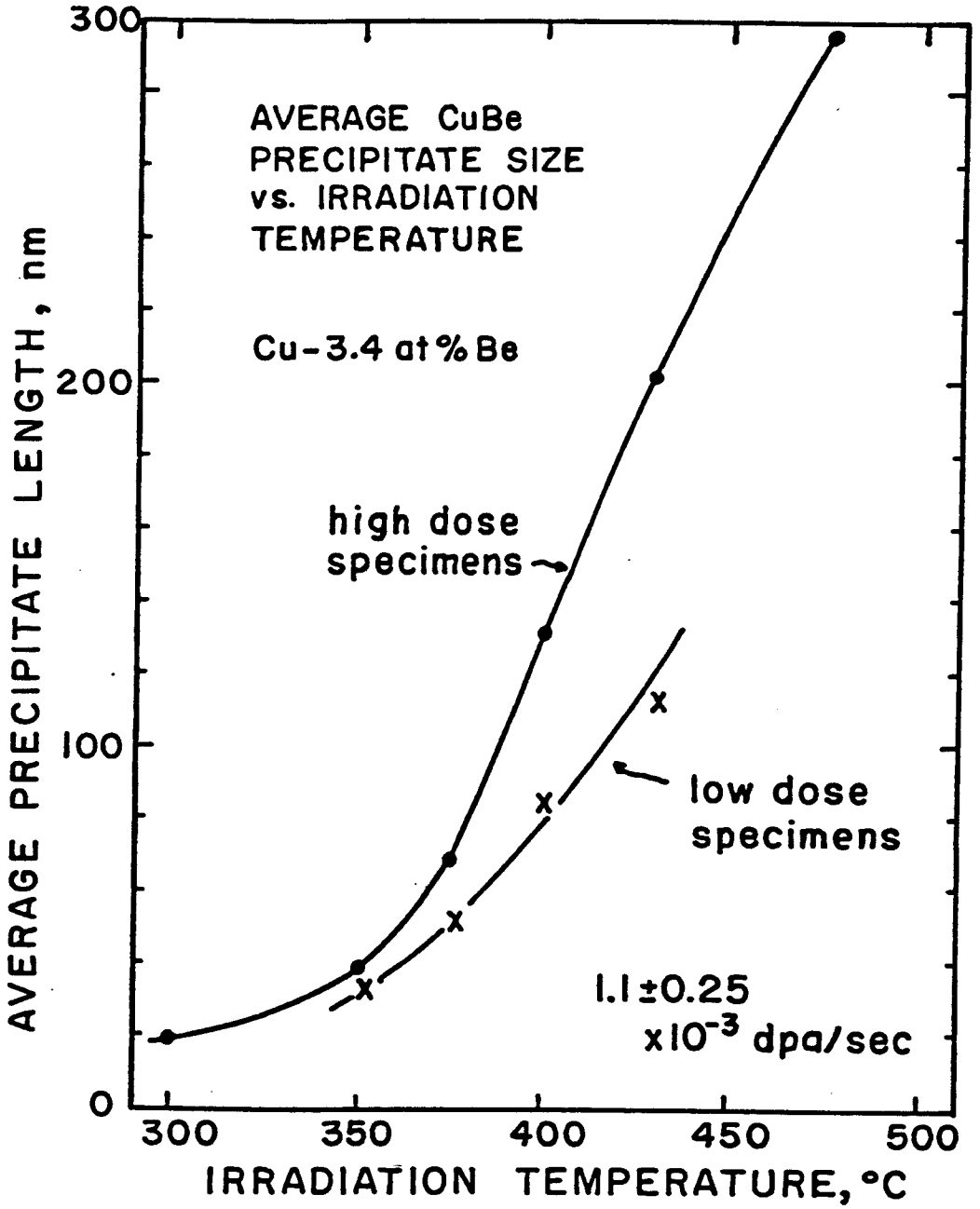

Figure VII.8. Variation in the average precipitate size, with temperature, in Cu-3.4 at.% Be specimens irradiated at similar dose-rates. Low dose and high dose specimens experienced doses in the range of 0.5 to 1 dpa, and 5 to 10 dpa, respectively.

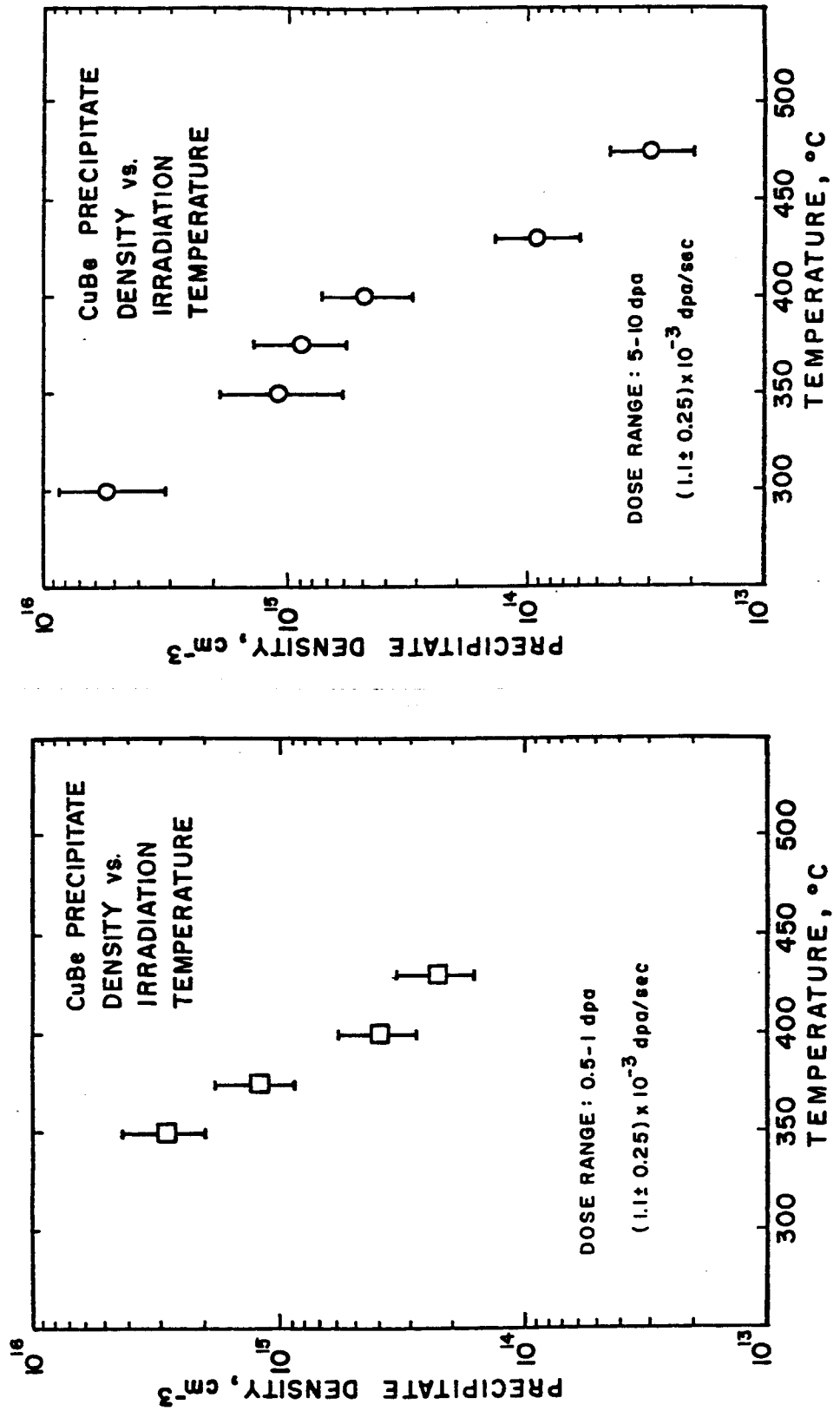

Figure VII.9. The dependence of the precipitate number density on irradiation temperature, in low dose specimens (left) and high dose specimens (right).

In the low dose specimens, irradiated at 0.5-1 dpa, the dependence of $\bar{d}$ and Np on temperature was similar in form to that in the high dose specimens.

A-2. Depth Dependence of the Precipitation

In cross sectioned specimens, the CuBe precipitation was studied as a function of depth from the surface, in a plane parallel to the path of the incident 14 MeV Cu ions. Since the displacement damage varies with depth (Fig. VII-1), each individual cross sectioned specimen provided a spectrum of radiation damage data, where the dpa rate and dpa level were directly coupled. The depth dependence of the precipitate size and number density in each cross sectioned specimen was measured. By comparing the data from several different specimens irradiated to different fluence levels, it was possible to isolate some effects due only to changes in the displacement rate, and some effects due only to cumulative displacement damage. An attempt was also made to correlate the observed depth dependence of the precipitation with the calculated dpa vs. depth curve.

Cross Sectioned Specimens

The characteristics of CuBe precipitation along the path of the 14 MeV Cu ions, during irradiation at 350°C to relatively high fluence levels, are illustrated in cross sectioned specimens in Figs. VII-10 and VII-11.* The band of precipitation in the specimen in Fig. VII-10 was produced during irradiation at 350°C to a fluence

*All specimens discussed in this chapter were irradiated with approximately the same ion flux.

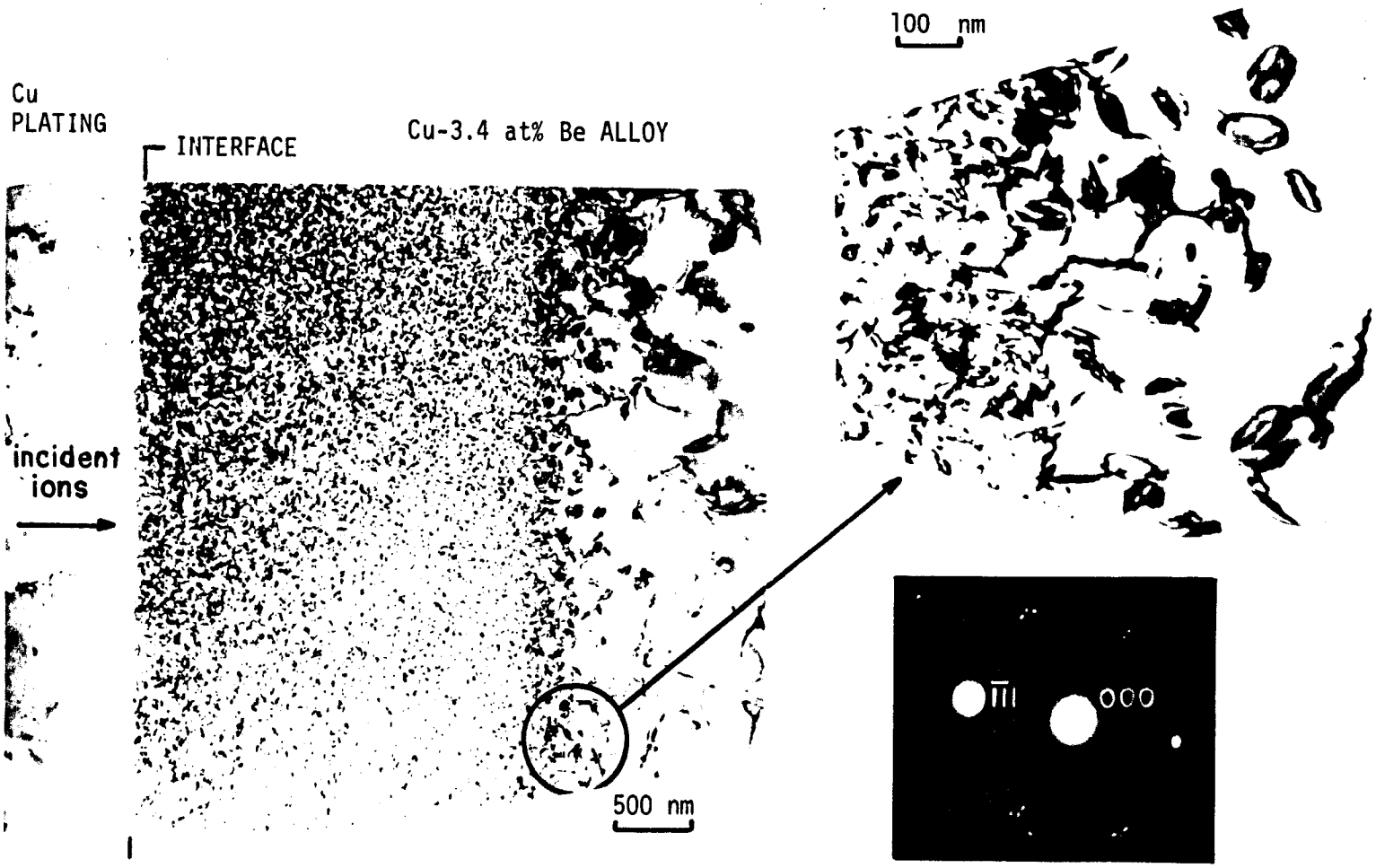

Figure VII.10. Precipitation in Cu-3.4 at% Be irradiated at 350°C with 7×10^{15} ions/cm^2, then thinned in cross section. Enlarged area shows the increase in precipitate size near the end of range of the incident ions. Zone axis is near [011].

level of 7 x $10^{15}/cm^2$ (2 dpa at a depth of 1000 nm). The interface between the Cu plating and the Cu-3.4 at% Be alloy is actually located at a depth of ~ 100 nm from the original specimen surface. Material was removed from the original surface both by sputter-etching during the AES analysis (Section VII.B), and by a brief electropolish to assure adherence of the Cu plating (Chapter VI). Between the interface and a depth of ~ 2700 nm, the CuBe precipitates are uniformly distributed, although their size decreases and number density increases somewhat with depth. At a depth of approximately 2700 nm, the precipitation coarsens and becomes more nonuniformly distributed. This region of the damage zone is enlarged in Fig. VII-10. Scattered precipitates and dislocations are present at depths up to 3300 nm, which is just beyond the tail end of the calculated dpa vs. depth curve. At greater depths, the microstructure is characteristic of annealed solid solution: no precipitates and few dislocations. Note that in the full-range micrograph in Fig. VII-10, the apparent variation in precipitate density in the direction parallel to the interface is due to a change in foil thickness and precipitate contrast.

The precipitation produced by irradiation at 350°C is shown in more detail in Fig. VII-11, in a specimen irradiated to a fluence level of 3.5 x $10^{16}/cm^2$ (10 dpa at a depth of 1000 nm). Here, the damage zone was divided into six depth intervals, and the precipitate characteristics were measured in each interval, using the same techniques described previously. (Foil thickness was measured in five

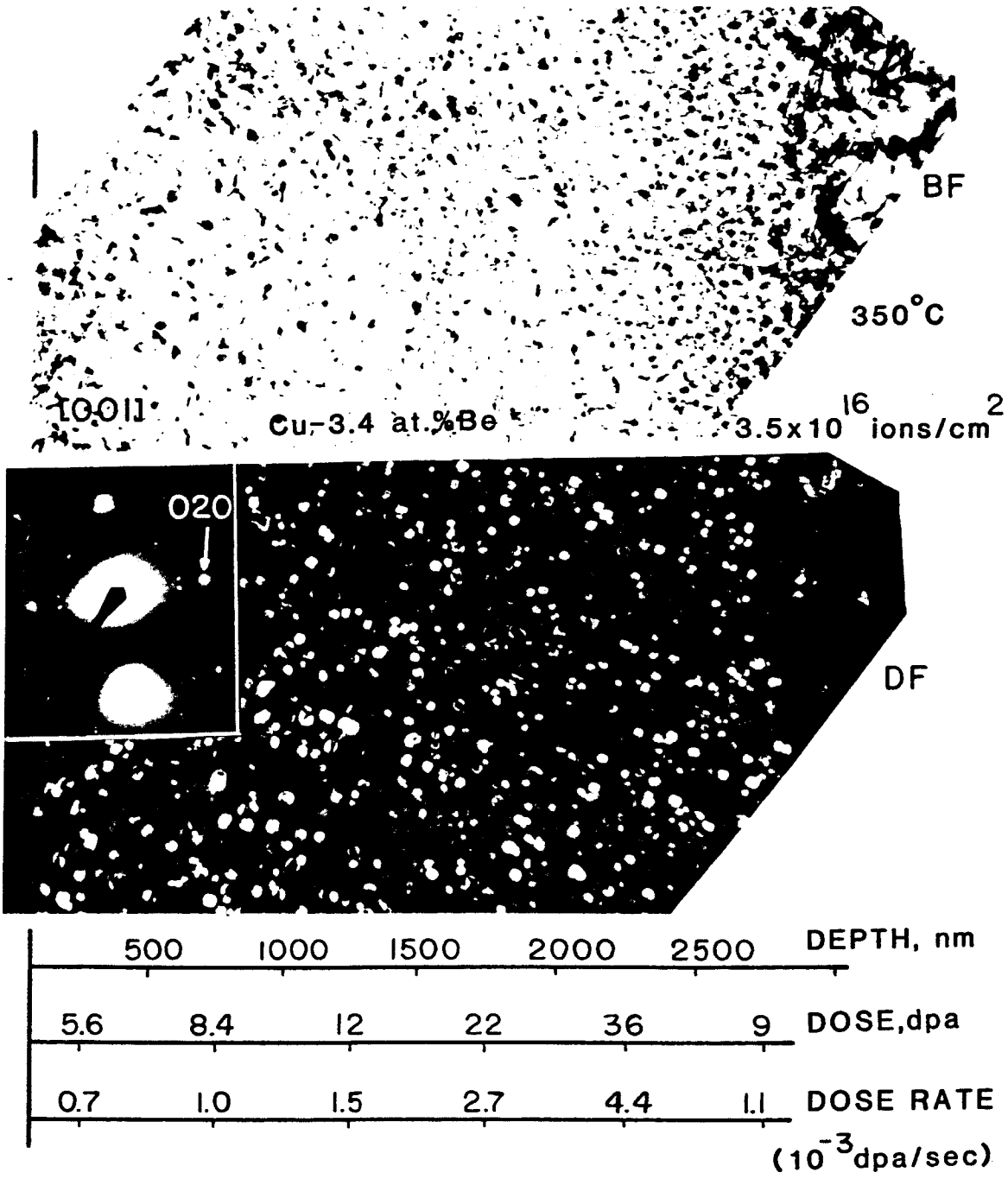

Figure VII. 11. CuBe precipitation in Cu-3.4 at.% Be irradiated at 350°C with 3.5×10^{16} ions/cm^2, and thinned in cross section. Dark field image was obtained using $(\bar{1}\bar{1}0)$ precipitate reflection, which coincides with (020) matrix reflection. Zone axis is near [001].

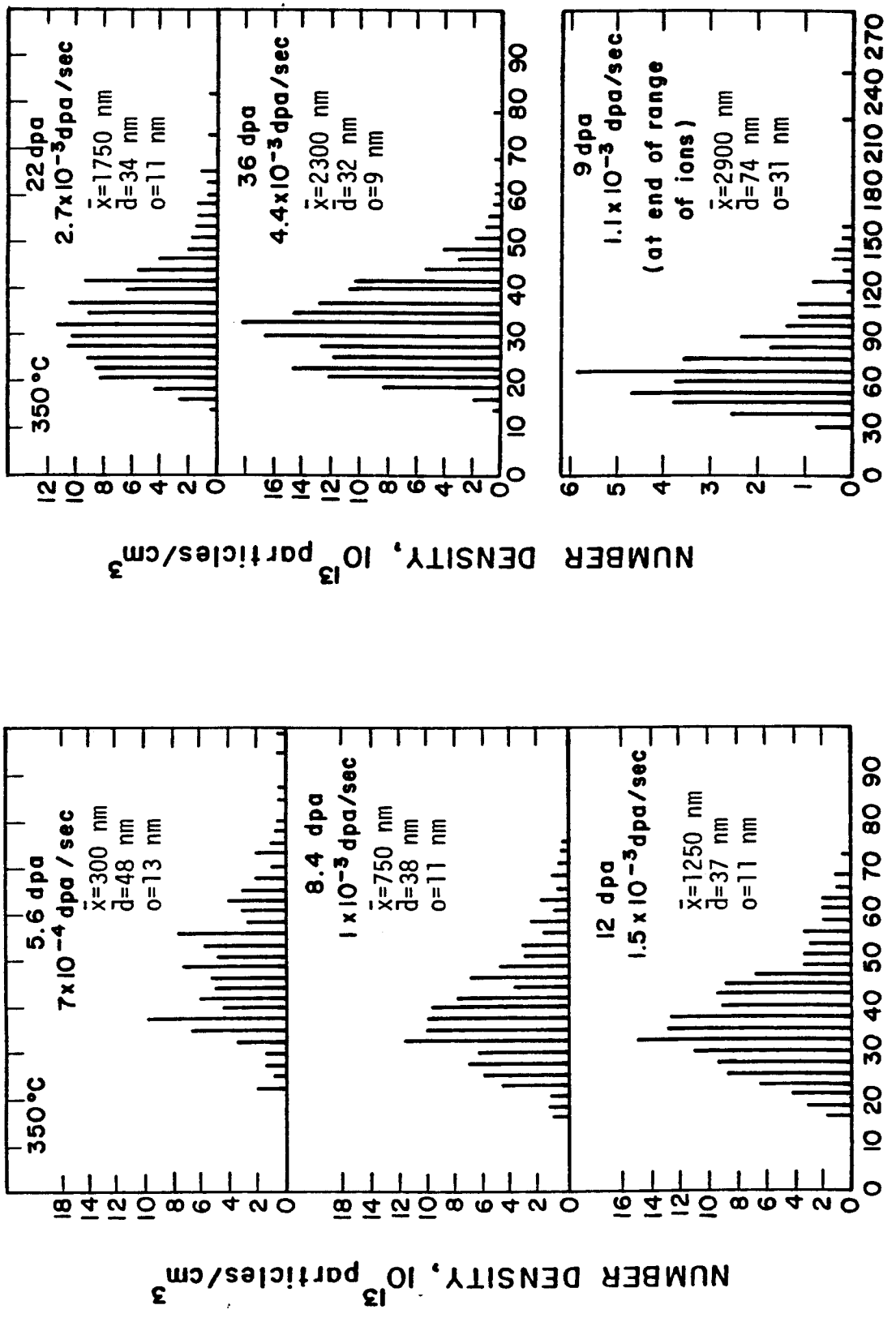

Figure VII.12. The depth dependence of the precipitate size distribution in Cu-3.4 at% Be irradiated at 350°C with 3.5×10^{16} ions/cm^2. On each histogram, the mean depth from the surface ($\bar{x}$), the mean precipitate size ($\bar{d}$), and the standard deviation in $\bar{d}$ are given.

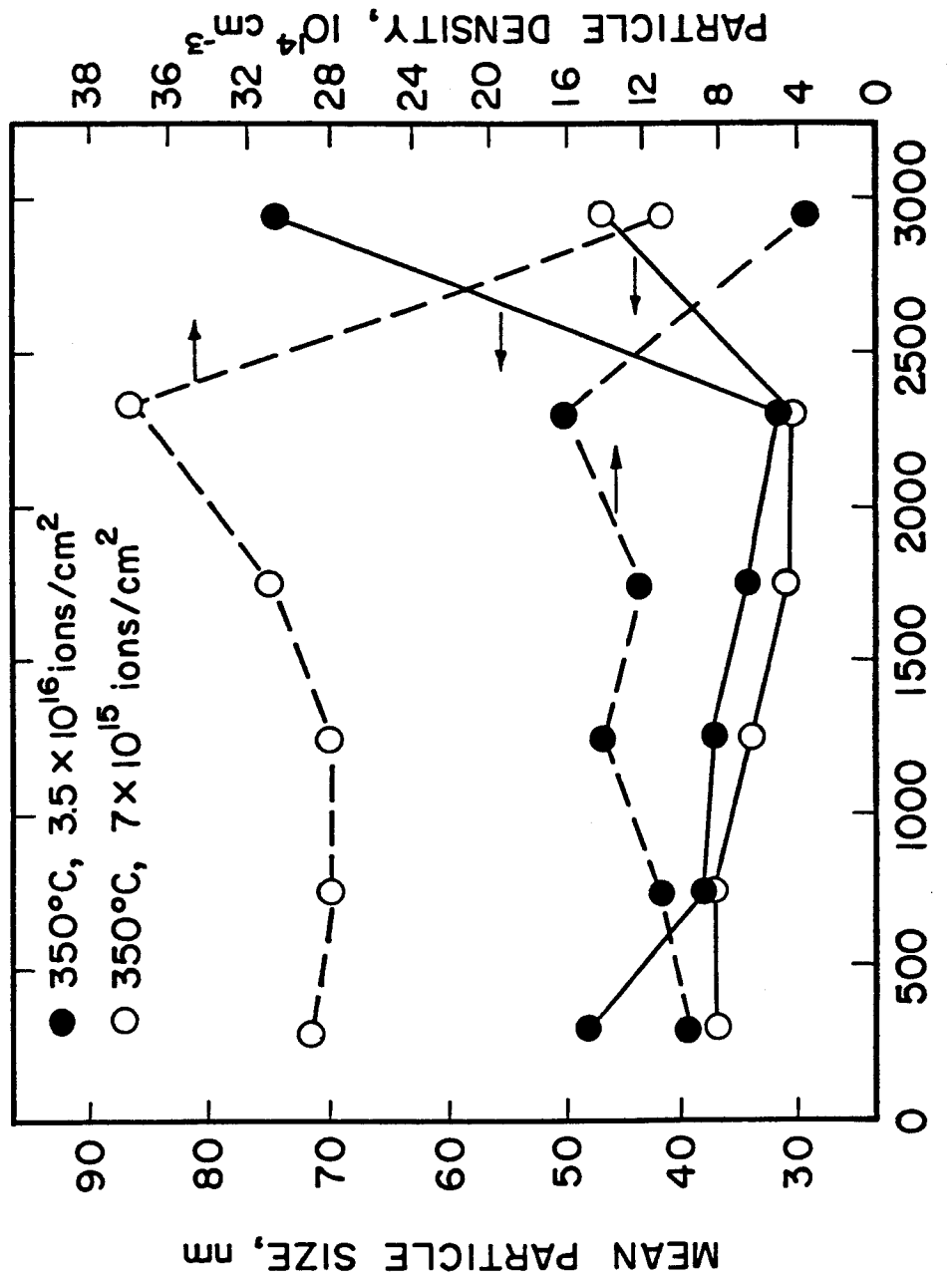

Figure VII. 13. The depth dependence of the mean precipitate size and number density in Cu-3.4 at% Be alloy irradiated with 14 MeV Cu ions at 350°C, to fluence levels of 3.5×10^{16}/cm^2 and 7×10^{15}/cm^2.

locations.) Below the micrograph in Fig. VII-11, the mean dose and dose rate in each depth interval are indicated at the midpoint of each interval. In Fig. VII-12, the precipitate size distributions for each depth interval are plotted. On each histogram is indicated 1) the mean depth of the interval within the damage zone, $\bar{x}$; 2) the mean projected length of the maximum precipitate dimension, $\bar{d}$; and 3) the standard deviation in the mean length, σ. Both the mean precipitate size and the precipitate density (N_p) are plotted vs. depth in Fig. VII-13. In the near-surface region, $\bar{d}$ = 48 nm, and N_p is approximately 1 x $10^{15}/cm^3$, at a mean displacement level and displacement rate of 5.6 dpa and 7 x 10^{-4} dpa/sec, respectively.** The mean displacement level and displacement rate then successively increase by a factor of 1.4 to 1.8 in each of the next four depth intervals, however, N_p and $\bar{d}$ do not change dramatically. While $\bar{d}$ decreases 25% between intervals 1 and 2, it decreases only 10% between interval 2 and 5, where the damage peak is located. At the same time, N_p increases by about 60% between the near-surface and the peak damage regions. Near the end-of-range (interval 6), mean precipitate size increases to 74 nm, and density decreases to 3.5 x $10^{14}/cm^3$. Although the average dpa level and dpa rate are comparable in intervals 2 and 6, the values of $\bar{d}$ and N_p differ by factors of 2 and 3, respectively, between the two regions. The precipitate

---

**The estimated uncertainty in the absolute value of N_p is ±30%; however the relative uncertainty in N_p is approximately ±15%, due to variations in precipitate contrast and foil thickness.

platelet thickness remains approximately constant throughout the damage zone, (~ 16 nm), and the precipitate volume fraction, V_p, is nearly constant in intervals 2-5.

In Fig. VII-13, the depth dependence of $\bar{d}$ and N_p in the specimen irradiated at 350°C with 7 x 10^{15} ions/cm^2 is also plotted, for comparison with the higher fluence specimen. The mean precipitate length ($\bar{d}$) in depth intervals 2 through 5 is similar in both specimens. In the near-surface and end-of-range regions of the lower fluence specimen, however, the increase in precipitate length is not as pronounced as in the higher fluence specimen. The principal difference between the two specimens is the precipitate density, which is twice as large in the lower fluence specimen. Since the precipitate thickness doubles (from ~ 4 nm to 8 nm) as the fluence increases from 7 x 10^{15}/cm^2 to 3.5 x 10^{16}/cm^2, however, the total volume fraction of precipitate is about the same in corresponding depth intervals of either specimen (excluding near-surface and end-of-range regions). This implies that under irradiation at 350°C to a fluence level of 7 x 10^{15}/cm^2, steady state has been achieved regarding the amount of Be transformed into precipitate. Also, coarsening of the precipitate particles is occurring during irradiation to the higher fluence level, since particle thickness increases while total particle volume is essentially constant. This behavior must be due solely to the increase in dose, since dose rate remains constant in a given depth interval. In the near-surface and end-of-range regions, there is a net increase in the precipitate volume

fraction, since both the particle thickness and length increase with dose.

Two Cu-3.4 at% Be specimens were also irradiated at 300°C to the same fluence levels as the 350°C specimens: $7 \times 10^{15}/cm^2$ and $3.5 \times 10^{16}/cm^2$. The foil thickness of the lower fluence specimen was too large throughout most of the damage zone to permit accurate counting and sizing of the precipitates, so a quantitative comparison between the two 300°C specimens could not be made. The depth dependence of the precipitation is qualitatively similar in the high fluence specimens irradiated at 300°C and 350°C. The main differences between these specimens are: (a) precipitate size is smaller but the density is greater at 300°C (e.g., see Figs. VII-8 and VII-9); and (b) precipitation at 300°C extends farther beyond the calculated end-of-range of the ions, as discussed later in this section.

Radiation-induced precipitation through the ion range, in a specimen irradiated at 375°C with 1.8×10^{16} ions/cm^2 (5 dpa at 1000 nm), is shown in Fig. VII-14. The mean precipitate size (projected length of maximum precipitate dimension) and precipitate density in five depth intervals within this damage zone are plotted in Fig. VII-15. The relative change in the size and density with depth is more pronounced at 375°C than at 350°C. Also, the average particle size within the near-surface region is larger than near the end-of-range. The size and density change in such a way, however, that the precipitate volume fraction remains relatively constant (variation of ±20%) throughout the damage zone. The precipitate platelet thickness is

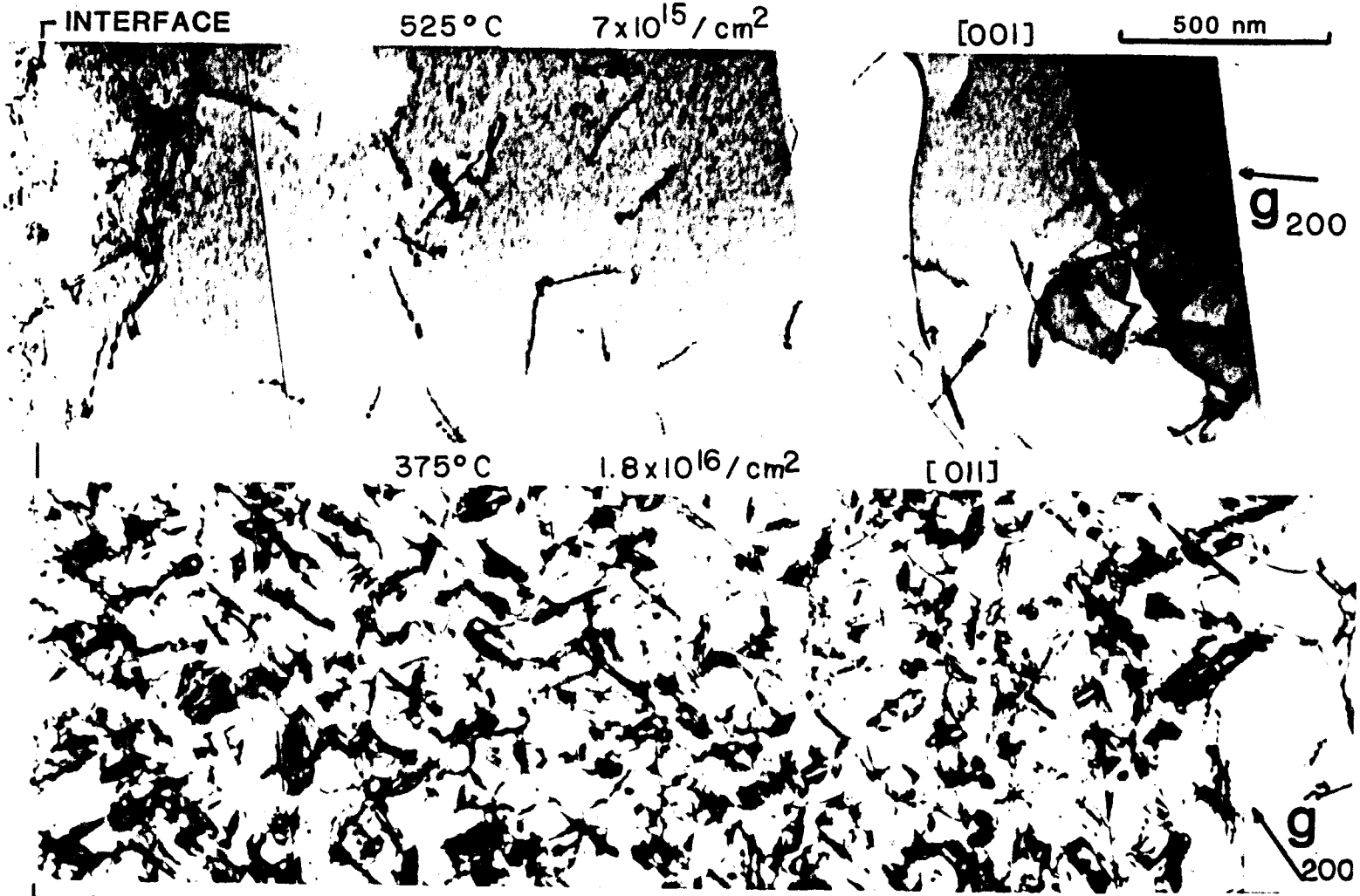

Figure VII.14. Cu-3.4 at.% Be irradiated with 14 Mev Cu ions at 525°C and at 375°C, then thinned in cross section. At the higher temperature no precipitation or damage is present, but at 375°C CuBe precipitates have nucleated along the path of the incident ions.

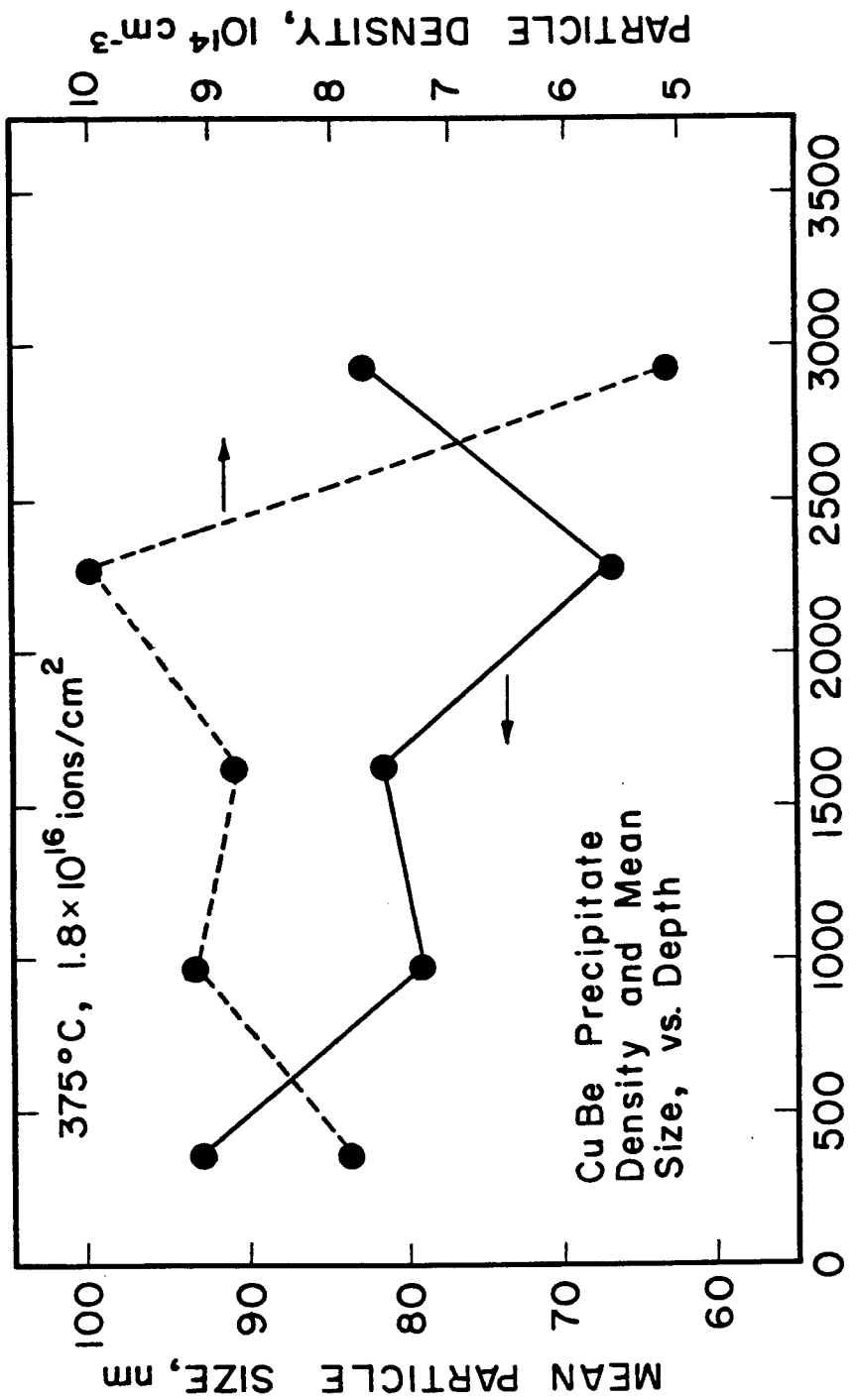

Figure VII.15. The depth dependence of the mean precipitate size and number density in Cu-3.4 at% Be alloy irradiated with 14 MeV Cu ions at 375°C, to a fluence level of 1.8×10^{16} ions/cm^2.

~ 14 nm in this specimen, and the thickness does not measurably vary with depth.

Figure VII-14 also contains a composite TEM micrograph of a specimen irradiated at 525°C to a fluence level of 7 x $10^{15}/cm^2$ (2 dpa at 1000 nm and 8.5 dpa at 2300 nm). Neither precipitation nor defect clusters are present in this specimen. The large dislocations visible in the micrograph are found throughout the specimen, and probably result from deformation of the thin specimen during electropolishing.

Figure VII-16 contains composite TEM micrographs of cross sectioned specimens, which were irradiated at 430°C and 400°C, respectively, to relatively low fluence levels of 8.8 x $10^{14}/cm^2$. These specimens are of interest because they show how rapidly precipitation forms under irradiation at these temperatures, and presumably at lower temperatures as well (the duration of each irradiation was only ~ 4 minutes). The displacement damage level is about 0.08 dpa, 0.25 dpa, and 1 dpa in the near-surface region, the 1000 nm region, and the peak damage region, respectively. The depth dependence of the displacement rate in these specimens is essentially the same as that shown for the 350°C specimen in Fig. VII-11. The depth dependence of the mean precipitate size and number density is plotted in Fig. VII-17. In the 400°C specimen, the precipitates exhibit two types of strain contrast. In the 100 ~ 700 nm depth region, most precipitate images are oval- or lens-shaped, and contain a line of no contrast, similar to planar dislocation loops. These particles are

16

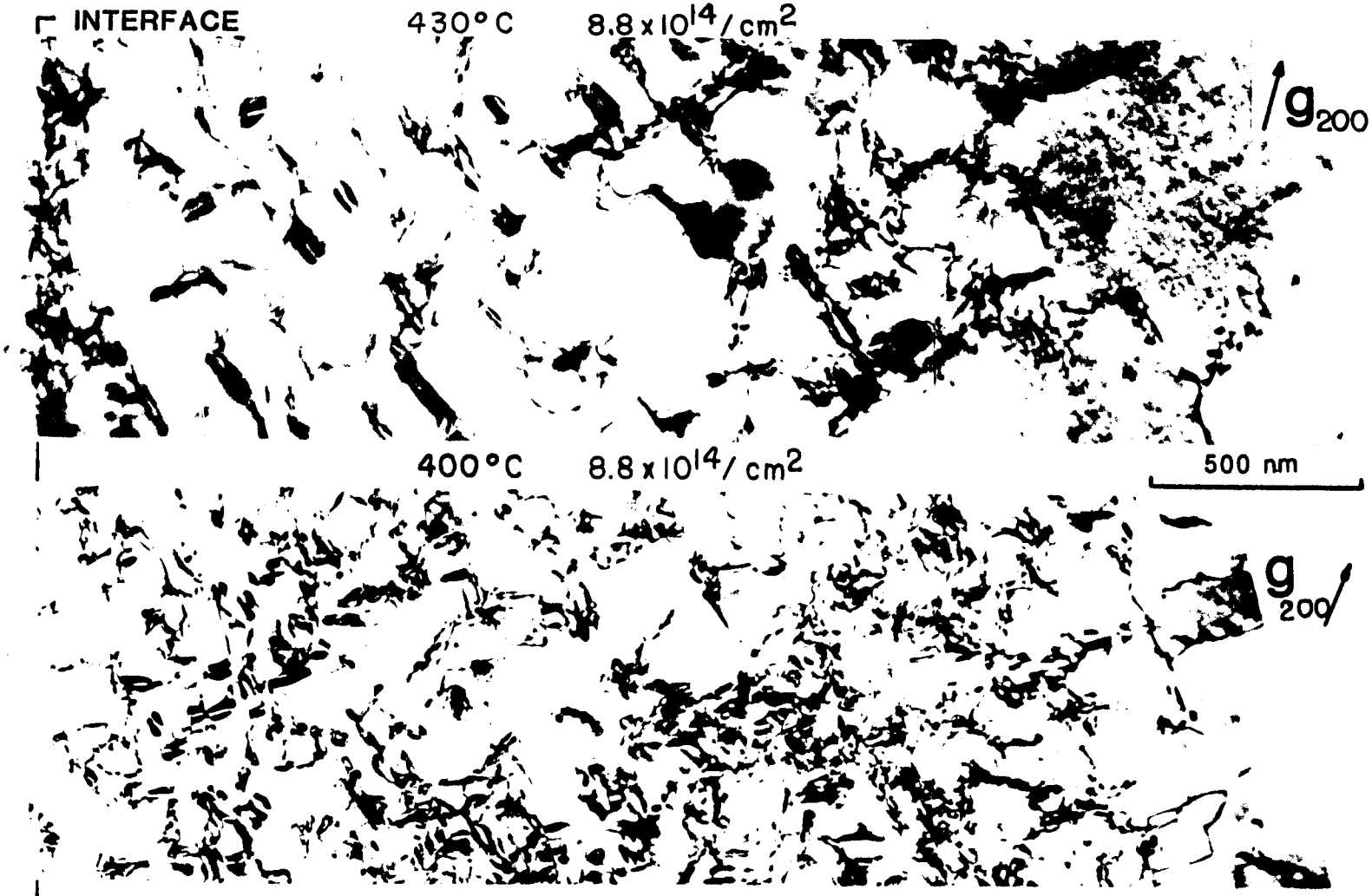

Figure VII. 16. Precipitation in Cu-3.4 at.% Be alloy irradiated with 14 MeV Cu ions at 430°C and 400°C, to a fluence of 8.8×10^{14} /cm^2. The specimens were thinned in cross section after electrodeposition of a thick Cu plating. Zone axis is close to [011].

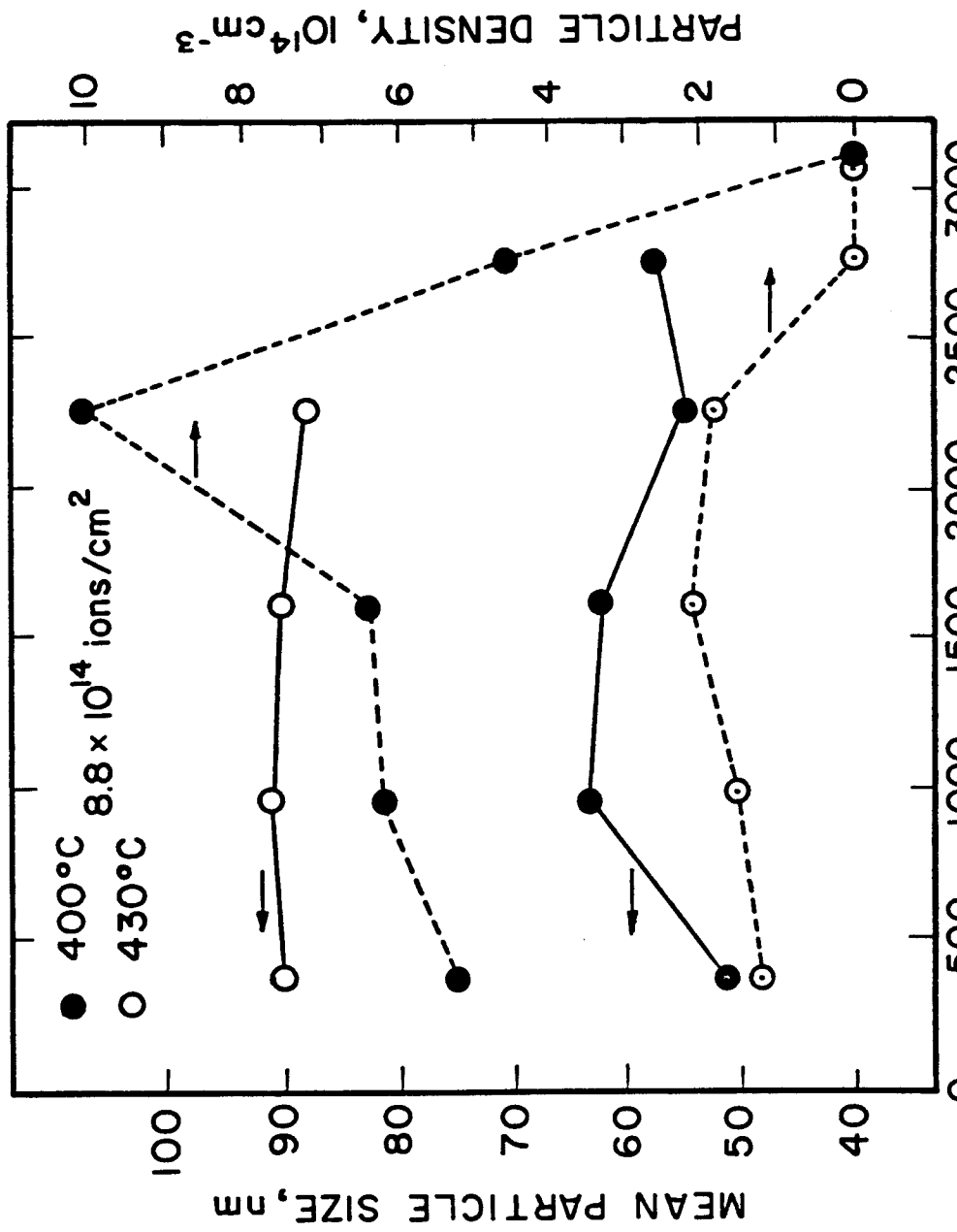

Figure VII.17. The depth dependence of the mean precipitate size and number density in Cu-3.4 at% Be alloy irradiated with 14 MeV Cu ions, at 400°C and 430°C, to a fluence level of $8.8 \times 10^{14}/cm^2$.

CuBe precipitates, however, since they produce extra reflections in the selected area diffraction pattern characteristic of the B2 structure with a = 0.27 nm. In higher dose regions, most precipitates are the usual rectangular platelets, and these precipitates have formed to a depth of ~ 2900 nm from the interface. Both the particle density and the precipitate volume fraction increase with depth to the peak damage region, after which they drop sharply.

After irradiation at 430°C with 8.8×10^{14} ions/cm^2, precipitates have formed in the region between the interface and a depth of ~ 2500 nm. Most of these particles exhibit the lens-shaped contrast, and the spatial distribution of the particles is nonuniform. The mean precipitate length and the precipitate thickness remain essentially constant with depth, and precipitate density increases slightly with depth. Interestingly, the precipitates are quite uniform in size, and few are smaller than 50 nm.

Dependence on Dpa-Level and Dpa-Rate

In a single cross sectioned sample, both the displacement rate and the cumulative displacement level vary in the same manner with depth, so the effects of either parameter on the precipitate characteristics cannot be isolated. Comparison of several cross sectioned or backthinned specimens irradiated to different fluence levels (at the same temperature), however, gives some indication of the dependence of particle size and density on dpa-rate and dpa-level. All available data are plotted in Figs. VII-18 to VII-22. Data from

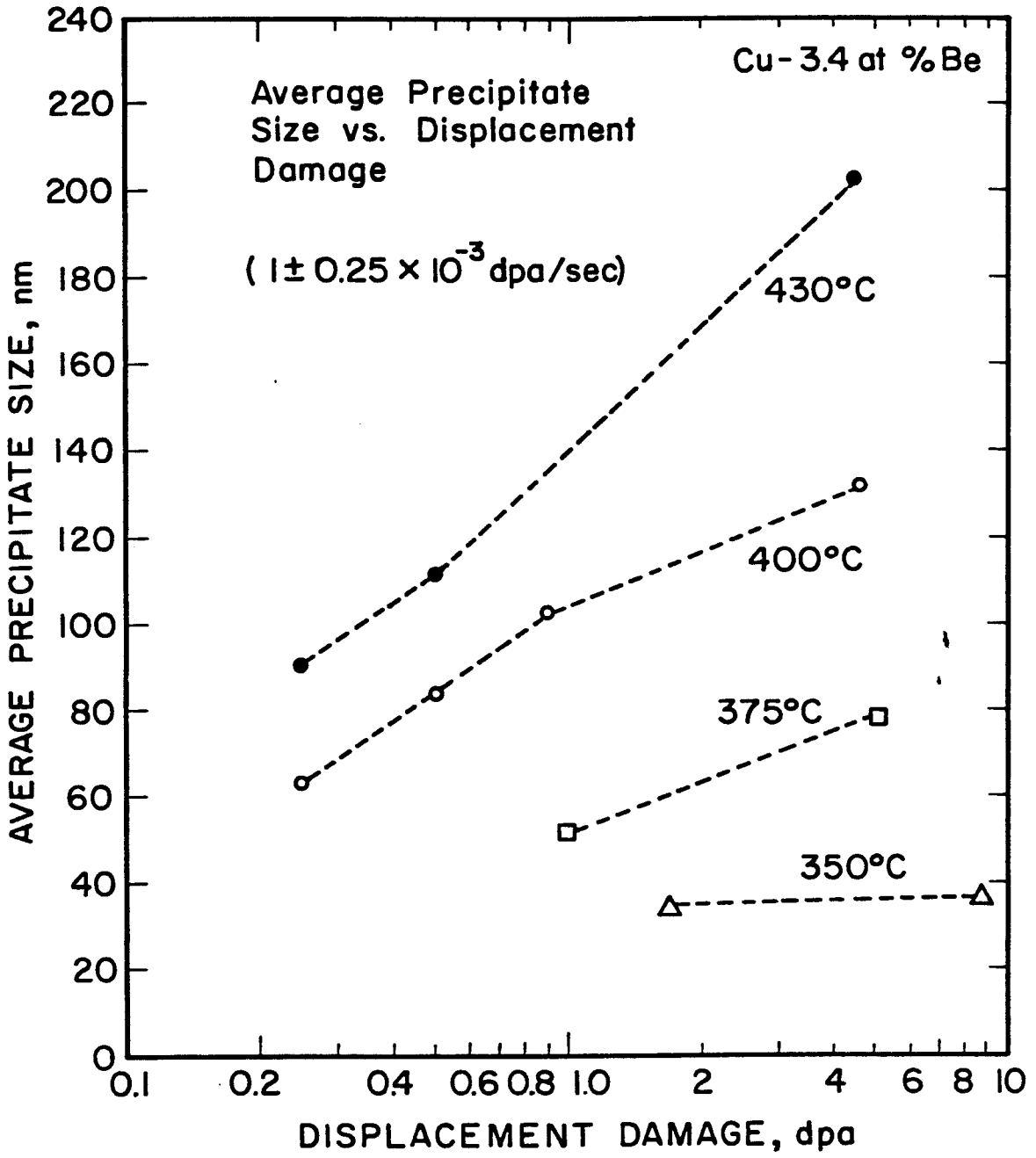

Figure VII.18. The dependence of the mean CuBe precipitate size on the displacement damage level in Cu-3.4 at% Be alloy irradiated with 14 MeV Cu ions. Precipitate size is defined as the length of the maximum precipitate dimension.

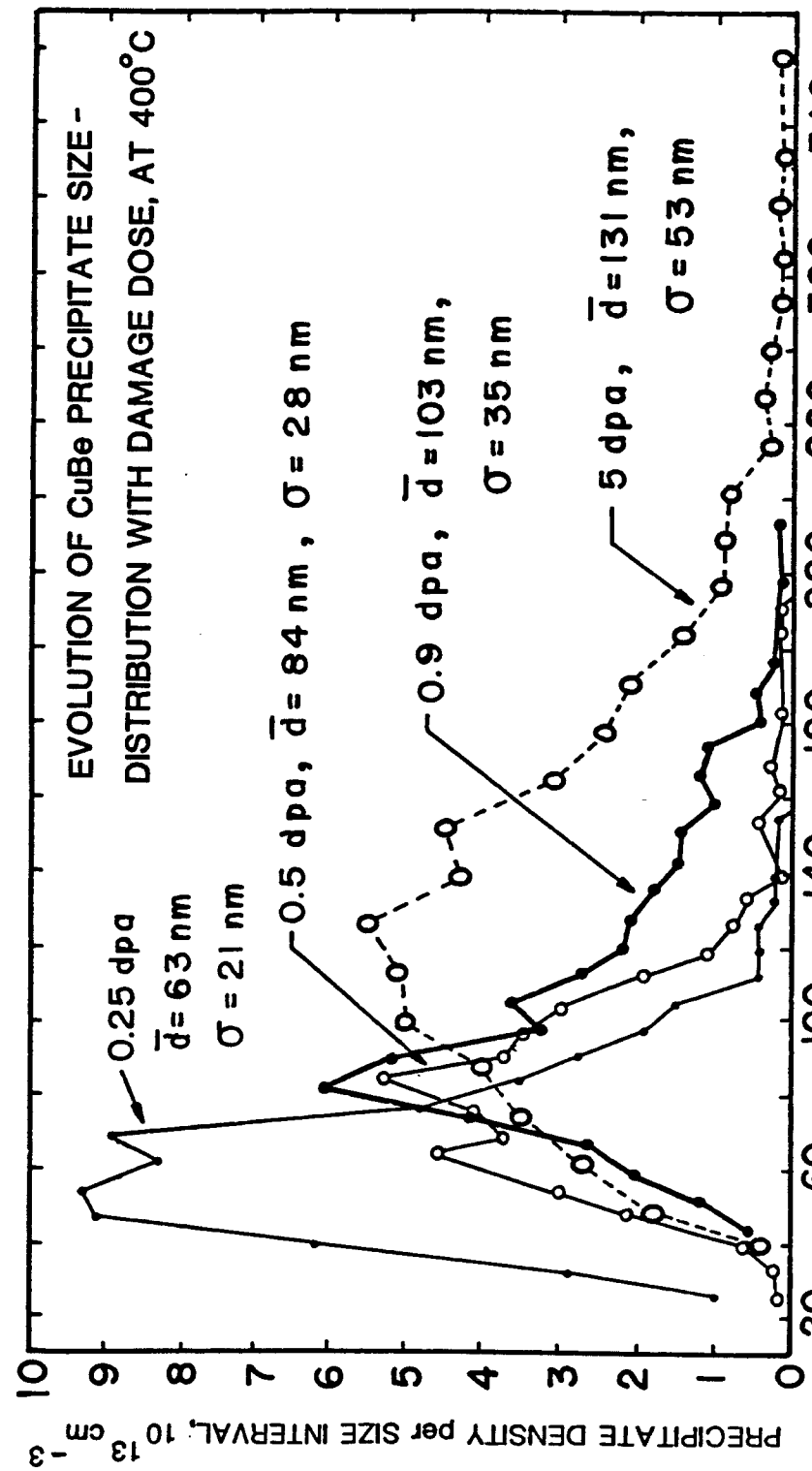

Figure VII.19. Evolution of the mean size ($\bar{d}$) and the standard deviation from the mean (σ) for CuBe precipitates in Cu-3.4 at% Be , irradiated at 400° C with doses ranging from 0.25 dpa to 5 dpa. In a given histogram, each point is plotted at the midpoint of the size interval. Lines connecting the points are to aid the eye.

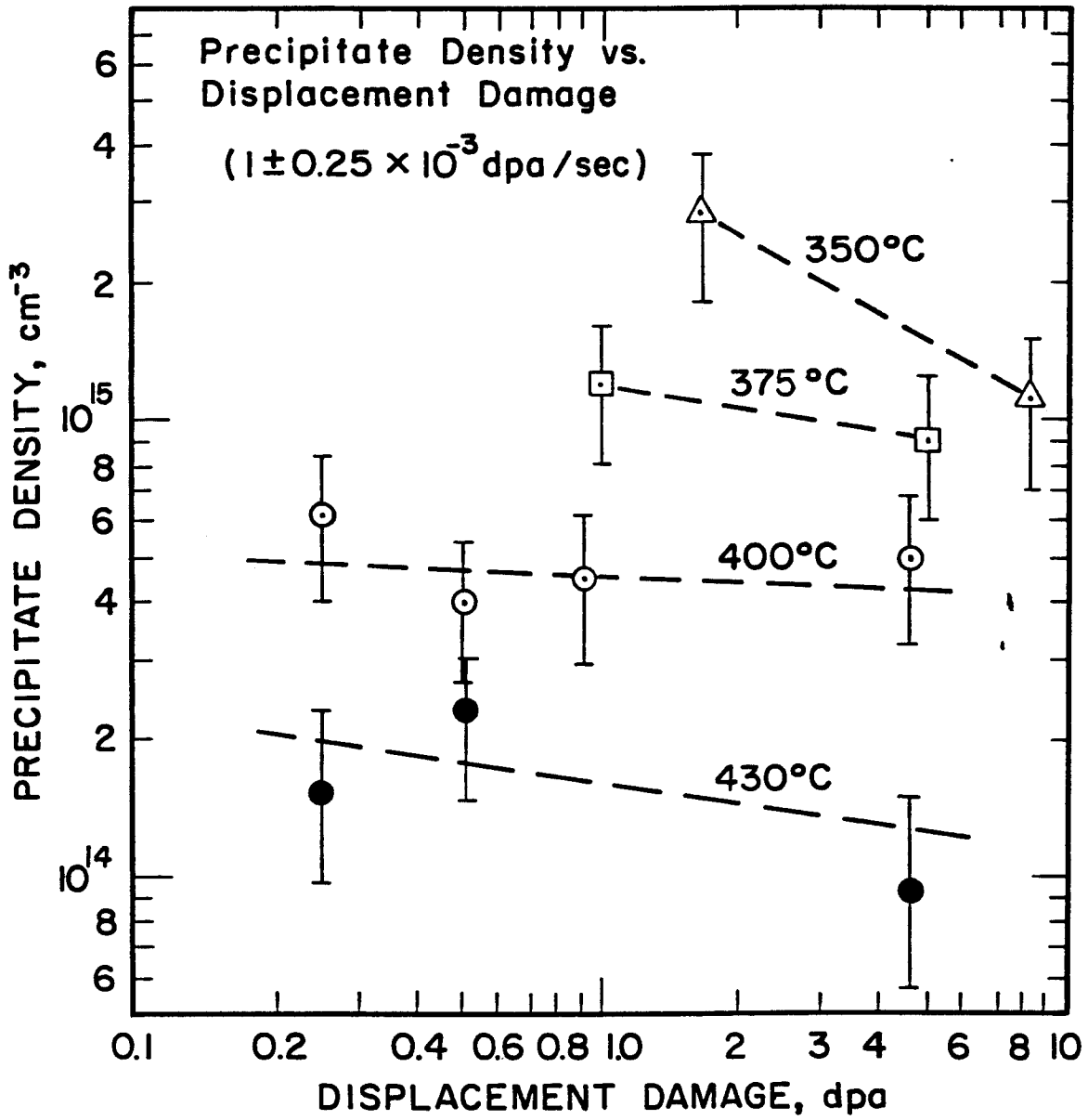

Figure VII.20. The dependence of CuBe precipitate number density on displacement damage level, in Cu-3.4 at% Be alloy irradiated with 14 MeV Cu ions.

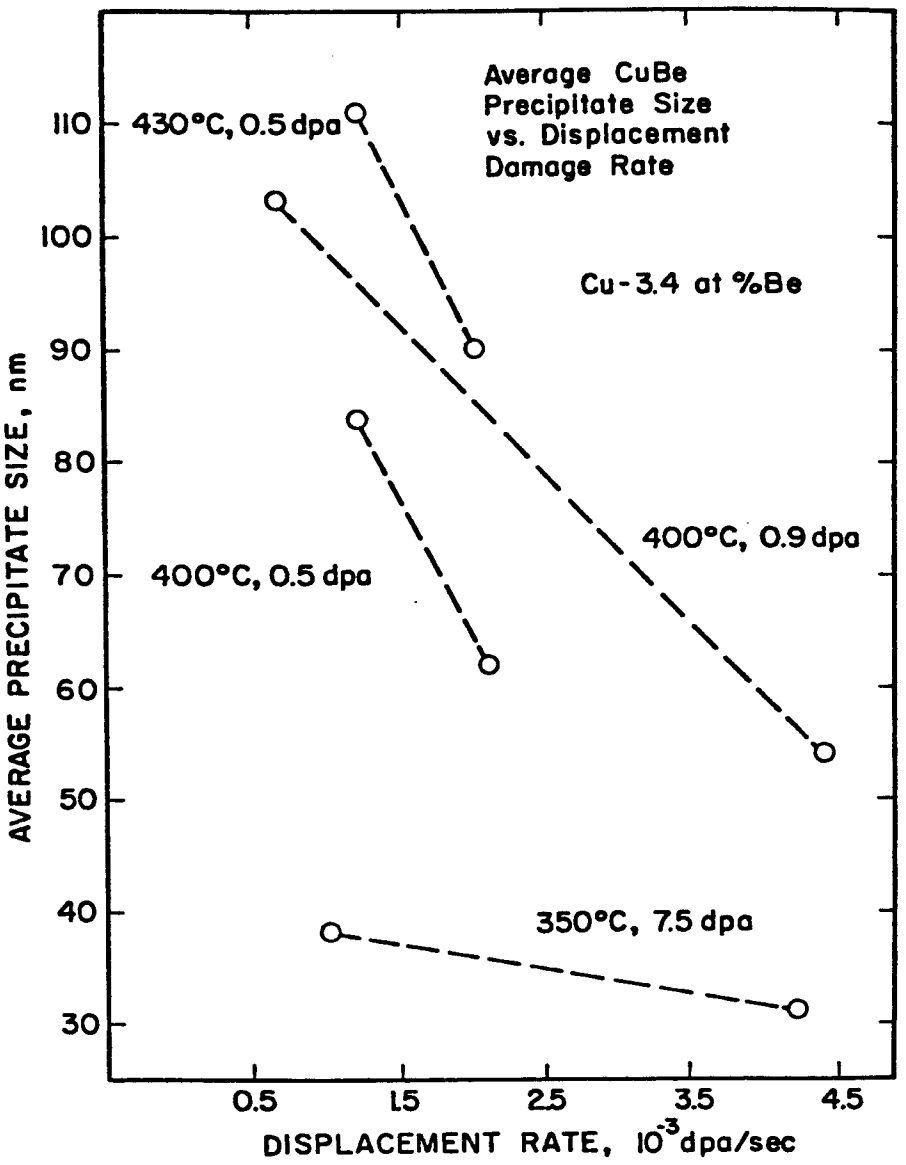

Figure VII.21. The dependence of the mean CuBe precipitate size on displacement rate, in Cu-3.4 at% Be alloy irradiated with 14 MeV Cu ions.

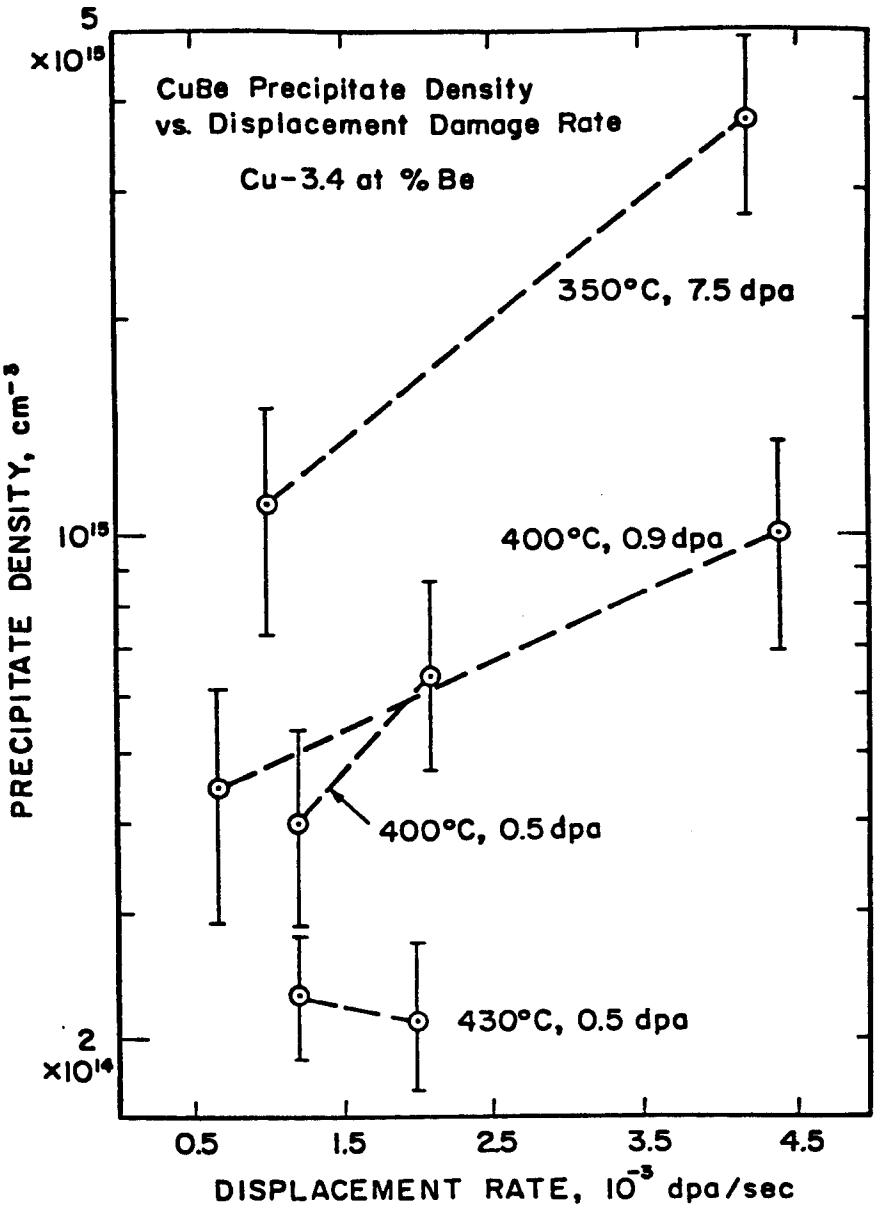

Figure VII.22. The dependence of CuBe precipitate number density on the displacement rate, in Cu-3.4 at% Be alloy irradiated with 14 MeV Cu ions.

cross sectioned specimens were obtained only from the interior of the damage zone, and not from the near-surface or end-of-range regions.

Figure VII-18 shows that at fixed temperature and dpa-rate, the mean precipitate size increases with increasing damage dose. This dose effect is more pronounced at the higher irradiation temperatures, and at lower dpa-levels (note the semi-log scale). Precipitate platelet thickness also increases with dose, as discussed in Section VII.A.1. Figure VII-19 illustrates the evolution of the precipitate size distribution with increasing dpa, at an irradiation temperature of 400°C. All of the distributions are skewed toward larger particle sizes, and the standard deviation from the mean size increases with increasing damage dose. Figure VII-20 indicates that precipitate number density either is unaffected or else decreases slightly with increasing dose. The dependence of precipitate size and density on displacement-rate is shown in Figs. VII-21 and VII-22. In general, irradiation at the higher displacement rate, to a fixed dpa-level, produces a finer precipitate size distribution than irradiation at the lower diplacement rate.

Comparison With the Calculated dpa vs. Depth Curve

In Figs. VII-23 and VII-24, the cross sectioned specimens discussed previously are compared with the calculated dpa vs. depth curve. To make as accurate of a comparison as possible, the micrographs in these figures were all taken at the same TEM magnification, and the enlargement of each print was adjusted to compensate for

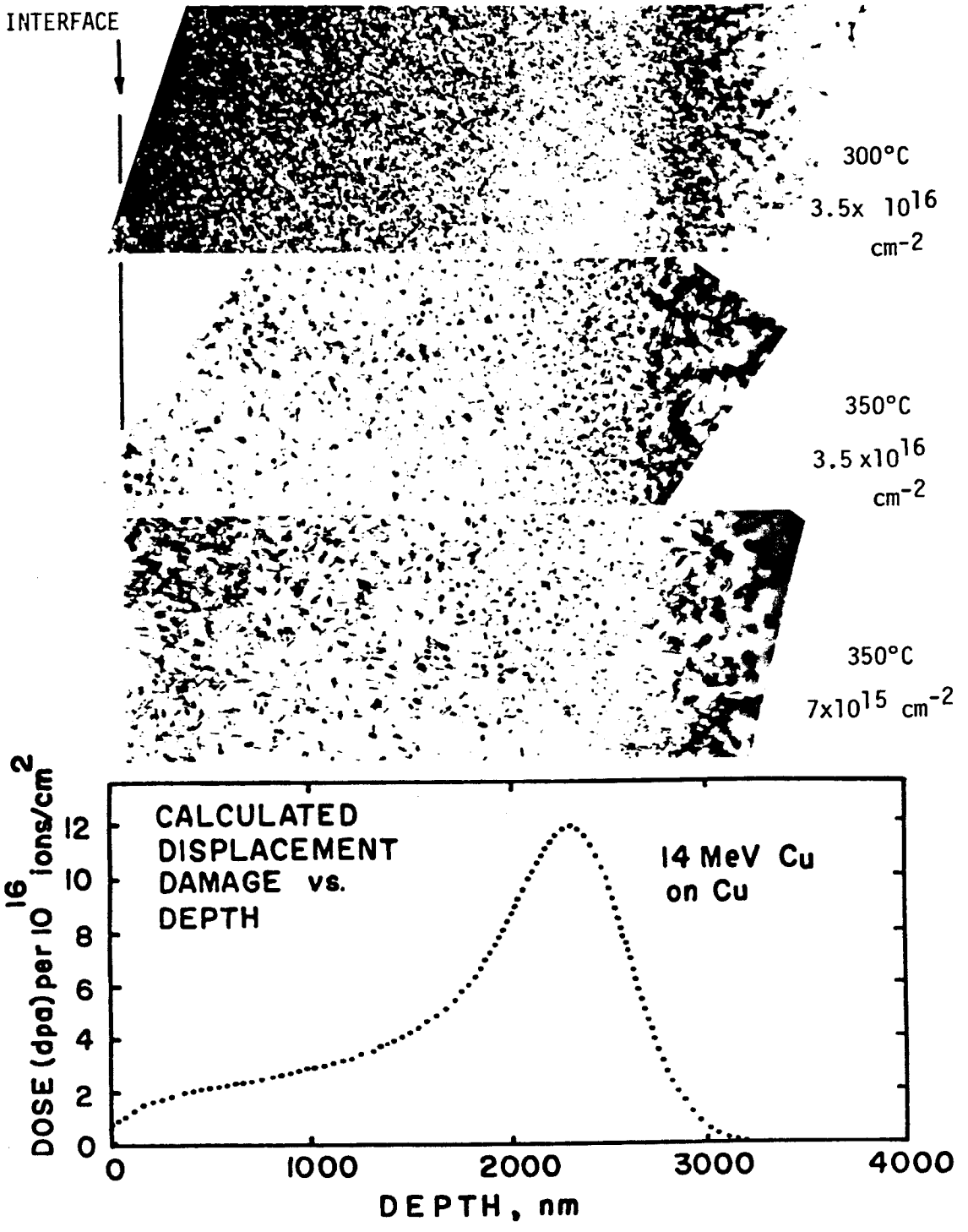

Figure VII.23. Comparison of observed microstructure in cross sectioned Cu-Be specimens with calculated dpa vs. depth curve.

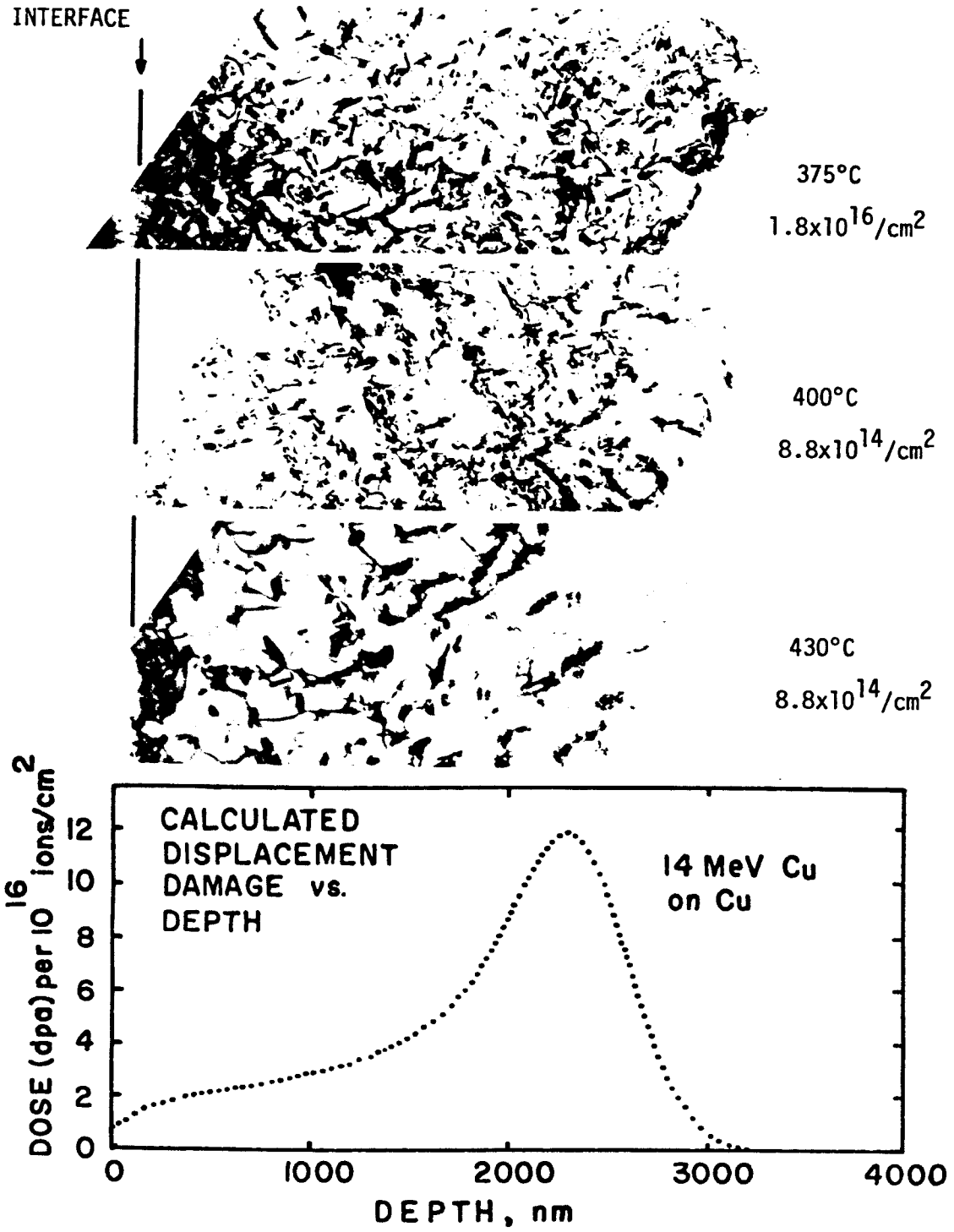

Figure VII. 24. Comparison of observed microstructure in cross sectioned Cu-Be specimens with calculated dpa vs. depth curve.

specimen tilt about the axis parallel to the interface.* The most obvious microstructural change in the low temperature specimens in Fig. VII-23 is the transition to the coarser precipitation, which begins at a depth of about 2700 nm, and extends beyond the tail of the dpa curve. In the 300°C specimen, some precipitation exists at a depth of 3600 ~ 3700 nm. In the 375°C specimen, precipitation extends to ~ 3300 nm, while at 400°C and 430°C (low fluence levels), precipitation ends before the calculated end-of-range. Precipitate distribution in another specimen (not shown here), irradiated at 400°C with 3×10^{15} ions/cm^2, was similar to that in the 375°C specimen. The above information shows that the depth distribution of the precipitation depends not only on the actual damage distribution, but also on the irradiation temperature and fluence. Therefore, an exact correlation between the observed microstructure and the damage distribution cannot be made.

Precipitation at the Specimen Surface

Because the free surface is a point defect sink, it is of interest whether precipitates nucleate at the surface, or whether a precipitate-free zone exists near the surface. Neither the back-thinned nor cross sectioned specimens provide information on the surface microstructure, since material was removed from the surface

*It was usually necessary to tilt the specimen during TEM examination to obtain the desired crystallographic orientation. Cross sectioned specimens were usually positioned within the specimen holder such that the Cu plating interface was parallel to the y-tilt axis of the goniometer, and tilt angles were routinely recorded.

during specimen preparation. One specimen, however, irradiated at 430°C with 10^{16} ions/cm^2, was backthinned directly to the surface, to study the BeO film that forms during irradiation (see Section VII.B, and Fig. VII-45). CuBe precipitates were present in the thinnest foil near the perforation, and precipitate platelets also adherred to the BeO film, indicating that the precipitates nucleated even at the surface. The precipitates were the same type as found within the damage zone, although their mean size (246 nm) was about 70% larger than predicted by the curve in Fig. VII-18, for irradiation at 430°C to a damage level of ~ 1 dpa; and their density (3×10^{13}/cm^3) was lower, by a factor of 5, than that predicted by the 430°C curve in Fig. VII-20.

A-3. Precipitate Structure and Crystallographic Orientation

The crystal structure of the radiation-induced precipitates was determined by analysis of the precipitate reflections in the electron diffraction patterns of the thinned specimens, using standard techniques.[4] The habit planes of the precipitates and the crystallographic orientation relationship between the matrix and precipitates were identified from the electron diffraction patterns and dark-field precipitate images, using stereographic projection techniques.[4,8] During electron microscopy of the irradiated specimens, it was routine practice to obtain electron diffraction patterns (DP) and dark-field (DF) images at several different matrix orientations. To aid in comparison of the TEM results from different specimens, the specimens were usually oriented in the microscope such that either a

[011], [001], or [$\bar{1}$12] matrix direction was parallel (or near parallel) to the electron beam.

The precipitate structure and orientations in every specimen were not analyzed in detail, because of the time-consuming nature of the task. Instead, the TEM micrographs and DP's of all specimens were surveyed, then a detailed analysis was performed on several representative specimens. The results of previous TEM studies of CuBe precipitation in the Cu-2 wt% Be alloy (Chapter IV) were particularly helpful in the interpretation of the TEM results in the experiment. The following generalizations can be made regarding the crystallography of the radiation-induced precipitation in the Cu-3.4 at% Be alloy:

(a) Precipitates in all specimens have the ordered-bcc structure (B2, or CsCl type) with a lattice parameter of a = 0.27 nm. This structure is characteristic of the mature γ' or the equilibrium γ CuBe precipitates.[5] There was no evidence of the tetragonal γ' precipitate, the γ'' precipitate, or G.P. zones that have been observed in the precipitation sequence of more concentrated Cu-Be alloys (see Chapter IV).

(b) The habit plane of the precipitate platelets varies between the {112} and {113} matrix planes. This same variance in habit planes has been reported for the metastable γ' CuBe precipitate in the aged Cu-2 wt% Be alloy.[5]

(c) The crystallographic orientation relation between the precipitate atomic planes and the matrix planes was difficult to

determine unambiguously. The DP's contained extra reflections due to 1) double diffraction; 2) the intersection of streaked reciprocal lattice points with the Ewald sphere; and 3) the splitting of some matrix and precipitate reflections.[4] Precipitate reflections were often quite weak, so higher order reflections were not visible on the negative, and the patterns were incomplete. Also, precipitate reflections were often located near, and were therefore masked by, the more intense matrix reflections. In most cases, however, the precipitate/matrix orientation could be described by the Bain orientation relationship, which is obtained by superimposing the [001] stereographic projection of the bcc precipitate on the [001] projection of the fcc matrix, such that $(\bar{1}10)_{fcc}$ is parallel to $(\bar{1}00)_{bcc}$.

(d) Diffraction patterns from specimens irradiated to doses $\gtrsim$ 1 dpa and containing a high density of precipitates, often contained more than one set of precipitate reflections, possibly because more variants of the {112}/{113} habit planes became occupied. Within the damage zone of cross sectioned specimens, the precipitate characteristics did not change with depth.

Examples of the crystallographic analysis of precipitates in a specimen irradiated at 430°C to 0.5 dpa are shown in Figs. VII-25 and VII-26. The first figure contains the DP near the $[001]_{\alpha}$ zone axis of the specimen (i.e. the diffraction pattern obtained with the (001) α-Cu matrix planes perpendicular to the electron beam direction).

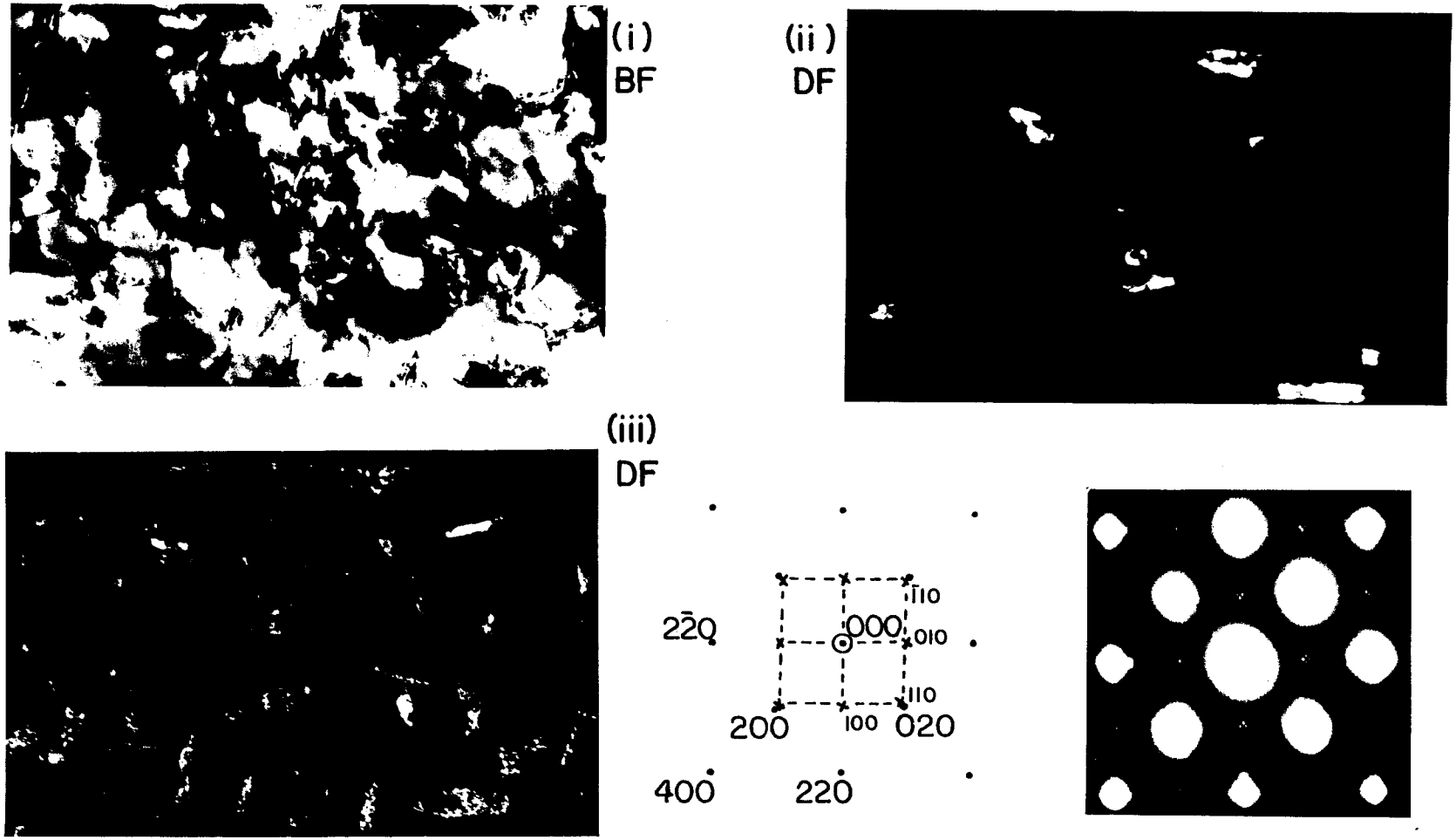

Figure VII.25. [001] diffraction pattern of matrix (intense spots) and precipitates in Cu-3.4 at% Be irradiated at 430°C to 0.5 dpa. The matrix and precipitate reflections are indexed in the schematic. Precipitate has B2 structure with lattice parameter= 0.27nm. Other micrographs are: (i) Bright field image of specimen. (ii) Dark-field image from (100) ppt. reflection. (iii) Dark field image from $(020)_{matrix}/(110)_{ppt.}$ reflections.

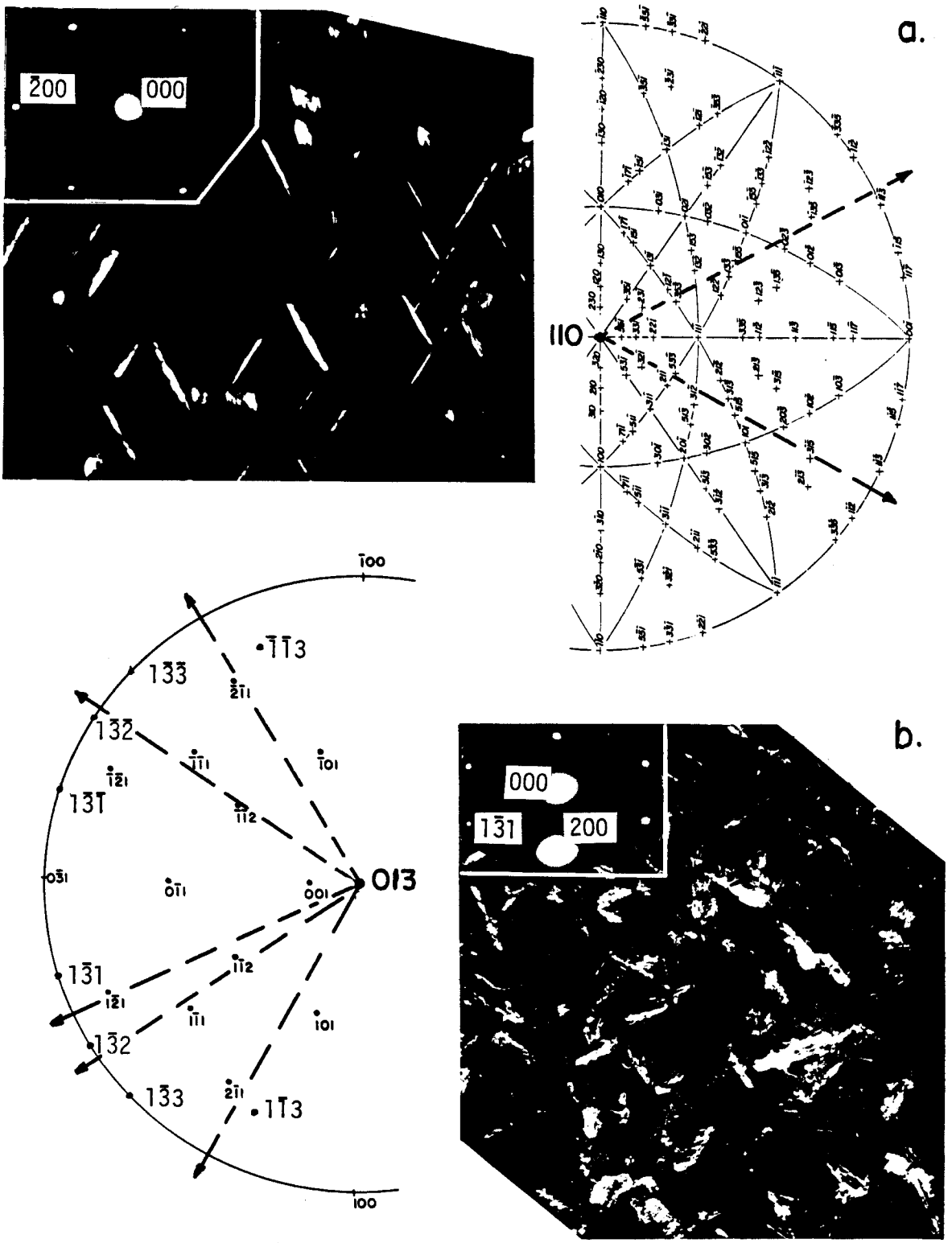

Figure VII.26. CuBe precipitate platelets imaged in dark-field, and viewed nearly edge-on. Zone axis is [110] in (a) and [013] in (b). The directions drawn on the corresponding stereographic projections are perpendicular to the habit planes of the platelets, therefore the habit plane is close to {112} and {113} planes. Specimen was irradiated at 430°C to 0.5 dpa.

The indexed schematic of the DP shows that the precipitate reflections correspond to the [001] diffraction pattern of an ordered bcc, B2-type lattice, with a lattice constant of 0.27 nm. The matrix/precipitate orientation relation is as follows:

$$[001]_{bcc} \parallel [001]_{fcc} \qquad \text{and} \qquad (\bar{1}10)_{bcc} \parallel (\bar{2}00)_{fcc} \ ,$$

which is the Bain relation.[4,5] The extra reflections clustered about the $(100)_{bcc}$ reflections result from double diffraction.[5] The DF (dark-field) images in Fig. VII-25 were obtained from the (100) and (110) precipitate reflections (the (110) precipitate reflection lies adjacent to the (020) matrix reflection and cannot be seen on the print of the diffraction pattern).

The information presented in Fig. VII-26 shows that the habit planes of the precipitate platelets lie near the {112} and {113} matrix planes. Figure VII-26(a) is a DF image from the (010) precipitate spot, where the matrix zone axis is near [011]. Two sets of platelets are viewed edge-on, and the directions normal to these platelets, drawn on a portion of a [110] stereographic projection, lie between the projections of the (113) and (112)-type planes. Figure VII-26(b) is a DF image from a (100) precipitate reflection, where the matrix zone axis is near $[013]_{\alpha}$, and several sets of platelets are viewed nearly edge-on. Again, the normals to these platelets, drawn on the [013] stereographic projection, show that the precipitate habit planes lie near the {112} and {113} planes.

Figure VII-27 shows diffraction patterns and dark-field micrographs from a Cu-3.4 at% Be specimen irradiated at 350°C to about 10 dpa, and is typical of the supersaturated specimens. The DP obtained near the $[001]_{\alpha}$ zone axis is indexed in Fig. VII-27(a). Extra reflections labeled B-E correspond to the $(\bar{1}00)$, $(\bar{2}00)$, $(\bar{1}10)$ and $(2\bar{2}0)$ planes of the CuBe precipitate (B2 structure), and they are oriented according to the Bain relation, as described previously. Precipitate reflections labeled A are from the CuBe (100) planes. These reflections, along with those labeled D and E, fit the orientation relation $[001]_{CuBe} \| [001]_{\alpha}$, with $(01\bar{1})_{CuBe}$ tilted ±6° from $(\bar{2}00)_{\alpha}$, which is compatible with the Bain relation. One interesting aspect of the diffraction pattern is that, for an unknown reason, the interplanar spacing of the (020) planes is ~ 5% larger than the (200) interplanar spacing, therefore the diffraction pattern is not symmetric.

Figure VII-27(b) shows the $[\bar{1}12]_{\alpha}$ DP, and DF images from the two precipitate reflections indicated. Extra reflections A and D are from the $(1\bar{1}1)$ and $(0\bar{2}1)$ planes of the CuBe precipitate, respectively, while reflection B is from the (100) CuBe plane. These reflections can be accounted for by the relations: $[112]_{CuBe} \| [\bar{1}12]_{\alpha}$ (approximately), and $[023]_{CuBe} \| [112]_{\alpha}$, with $(\bar{1}00)_{CuBe} \| (\bar{2}\bar{2}0)_{\alpha}$, which are compatible with the Bain relation. Figure VII-27(c) is a DF image from the $(100)_{CuBe}$ reflection, showing the precipitates edge-on. The habit planes of the precipitates are again near the {112} and {113} matrix planes, as indicated by the direction vectors.

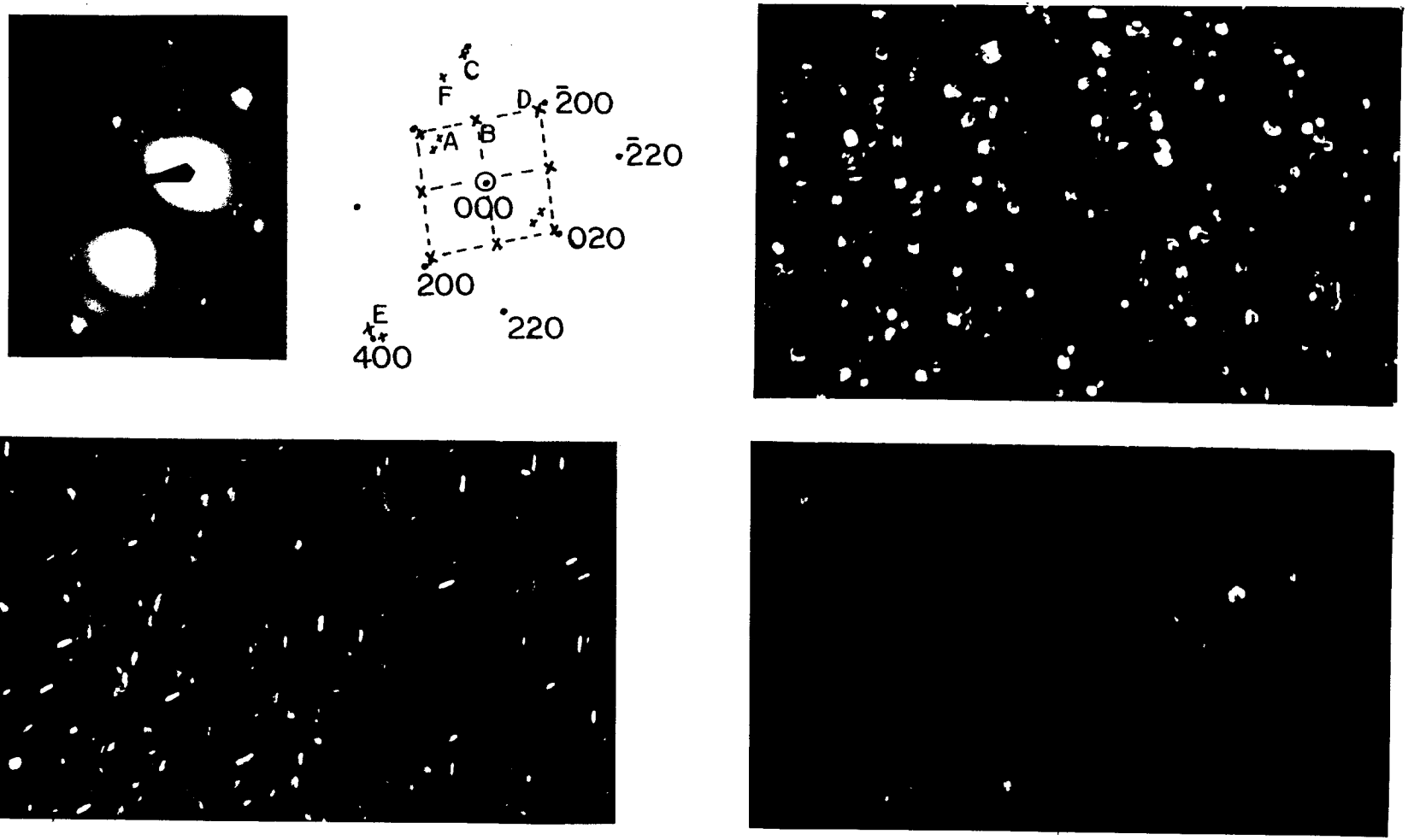

Figure VII.27(a) [001] difraction pattern from Cu-3.4 at% Be irradiated at 350°C to about 10 dpa. The matrix reflections(intense spots) and precipitate reflections are indexed in the schematic. Precipitate reflections labeled B-E correspond to the $(\bar{1}00)$,$(\bar{2}00)$,$(\bar{1}10)$ and$(2\bar{2}0)$ planes of CuBe, respectively. Reflections A and F are from (100) and (111)-type CuBe planes. DF image(i) is from (020) /$(110)_{ppt.}$ reflections, while (ii) and (iii) DF images are from ppt. reflections A and B respectively.

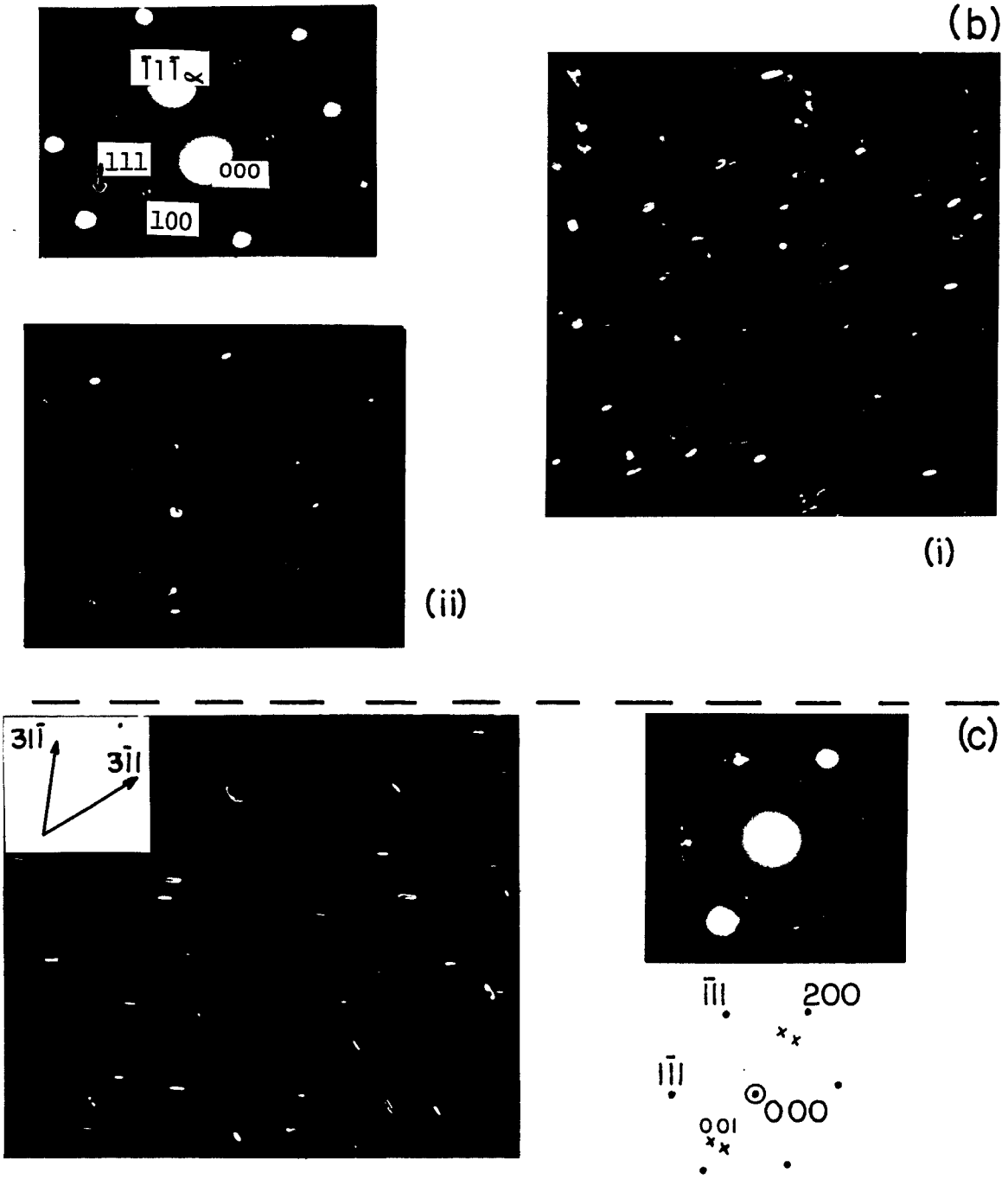

Figure VII.27(continued). (b) [$\bar{1}$12] matrix diffraction pattern(intense reflections),with CuBe reflections labeled. DF images (i) and (ii) are from (100) and (111) CuBe reflections, respectively. (c) [011] matrix DP containing precipitate reflections. DF image from (001) CuBe reflection indicates habit plane of precipitates is near {113} .

A-4. Effects of Post-Irradiation Heating

The nature of precipitates produced during irradiation can be elucidated through post irradiation aging or annealing studies. Precipitation that is stable only under high temperature irradiation, for instance, will dissolve, or will evolve to the equilibrium phase, if the irradiation is discontinued while the temperature is maintained. Some of the Cu-3.4 at% Be specimens irradiated in this study were aged or annealed after irradiation, and then were examined in the electron microscope. Specimens were heated *in situ* within the target chamber of the accelerator, or were heated in the high vacuum furnace either before or after thinning. In Table VII-2, a summary is given of the post-irradiation heating experiments. Some information on precipitate stability was also gained from specimens 1 through 8, which were irradiated in the linear specimen holder (Chapter VI) and were therefore subjected to high temperature following irradiation. To aid in the discussion of annealing effects on specimens 1-8, their temperature history during irradiation is plotted in Fig. VII-28.

The equilibrium phase diagram of the Cu-Be alloy system defines the temperature below which the two-phase (α_{Cu} + CuBe) mixture is stable, in the absence of irradiation. At equilibrium, the Cu-3.4 at% Be alloy is a solid solution above ~ 420°C. Therefore, the precipitation that forms during irradiation at 430°C and 475°C should dissolve when the ion beam is turned off and the irradiation temperature is maintained. This behavior was indeed observed following

TABLE VII .2. SUMMARY OF POST IRRADIATION HEATING EXPERIMENTS ON Cu-3.4 at.% Be SAMPLES

Cu-Be SPECIMEN NUMBER	IRRADIATION PARAMETERS		POST-IRRADIATION HEATING			AS-IRRADIATED MICROSTRUCTURE	EFFECT OF POST IRRADIATION HEATING
	T°C	dpa at 1 um	T°C	DURATION (sec)	METHOD		
51 00-1	475	9.2	*	*	I	CuBe ppts., dislocations	All precipitates dissolve.
" 2	475	0.9	*	*	I	Few or no precipitates.	" "
" 19	475	8	475	11,000	I	Radiation induced continuous CuBe precipitation, and dislocation tangles	" "
" 17	430	3	430	86,000	T		Precipitates dissolve.
" 3	430	4.6	*	*	I		No significant change.
" 4	430	0.9	*	*	I		No significant change.
" 11	430	0.25	400	80,000	U		Radiation induced continuous ppts. dissolve; some discontinuous precipitation forms.
"13(e)	400	0.25	400	80,000	U		Precipitates dissolve.
" 5	400	4.6	400	86,000	T		No significant change.
" 5	400	4.6	*	*	I		No significant change.
" 6	400	0.9	*	*	I		All ppts. dissolve but dislocation arrays remain.
" 24	400	5	500	7200	I		" " "
" 27	300	5	400	7200	I		

Method of Post Irradiation Heating

U: Heated in high vacuum furnace before TEM thinning.
T: Heated in high vacuum furnace after TEM thinning.
I: Heated insitu after irradiation, in target chamber.

* See Figure VII. 30 for temperature history of these specimens.

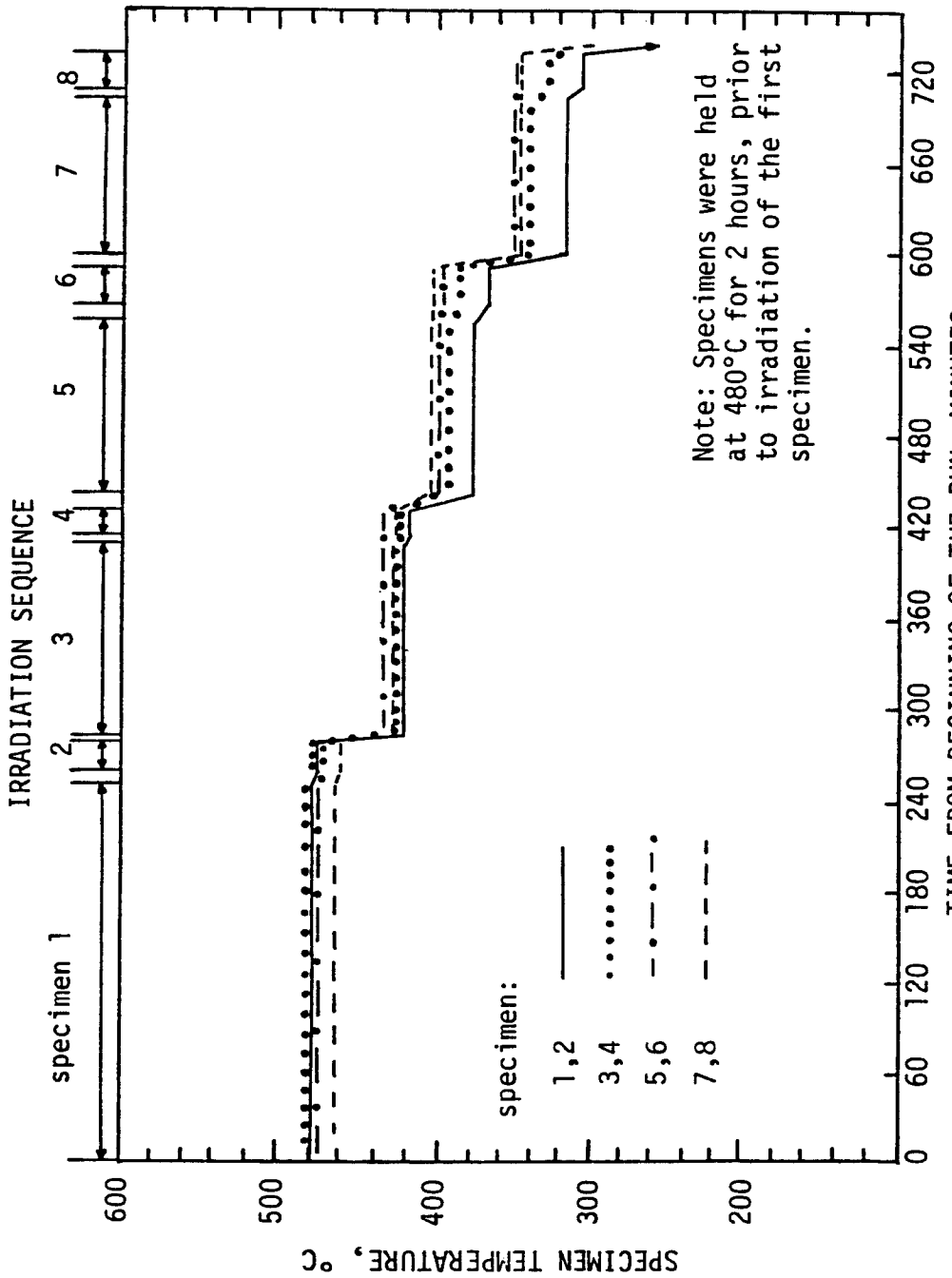

Figure VII.28. Temperature history of Cu-3.4 at.%Be specimens T51-00-1 through 00-8 during irradiation. These specimens were heated en masse rather than individually, in the linear (old) specimen holder, so all specimens were at elevated temperatures during the entire run. The upper abscissa indicates the irradiation sequence.

post-irradiation annealing of several specimens irradiated at 430°C or 475°C. Two specimens (#18 and #19) were irradiated identically at 475°C to a dose of 8 dpa at 1000 nm. Specimen #19 was then annealed at 475°C for 3 hours following irradiation, and both specimens were backthinned to a depth of 1000 nm for TEM examination. Copious precipitation was observed in the unannealed specimen (shown in Fig. VII-4); however, the precipitation had completely dissolved in the annealed specimen. Another example of precipitate dissolution was specimen #1, irradiated in the linear specimen holder at 475°C to 9.2 dpa at 1000 nm. As shown in Fig. VII-28, specimen #1 remained at 475°C for 31 minutes while specimen #2 was irradiated, and it was further annealed at 430°C for 143 minutes. Dislocation tangles but no precipitates were observed during examination of this sample in the TEM. Post-irradiation annealing of other specimens at 430°C caused some precipitate dissolution, but the kinetics were of course slower. There was no significant dissolution in specimen #3, post-irradiation annealed in situ at 430°C for about 30 minutes. However, most precipitates dissolved in specimen #17, annealed at 430°C for 24 hours after irradiation. These examples demonstrate the nonequilibrium nature of the CuBe precipitates that formed during irradiation at 430°C and 475°C.

While dissolution of the radiation induced precipitation at temperatures above 420°C was expected, a surprising discovery was that the continuous precipitation also dissolved after prolonged aging at 400°C. This was observed in specimens that were irradiated

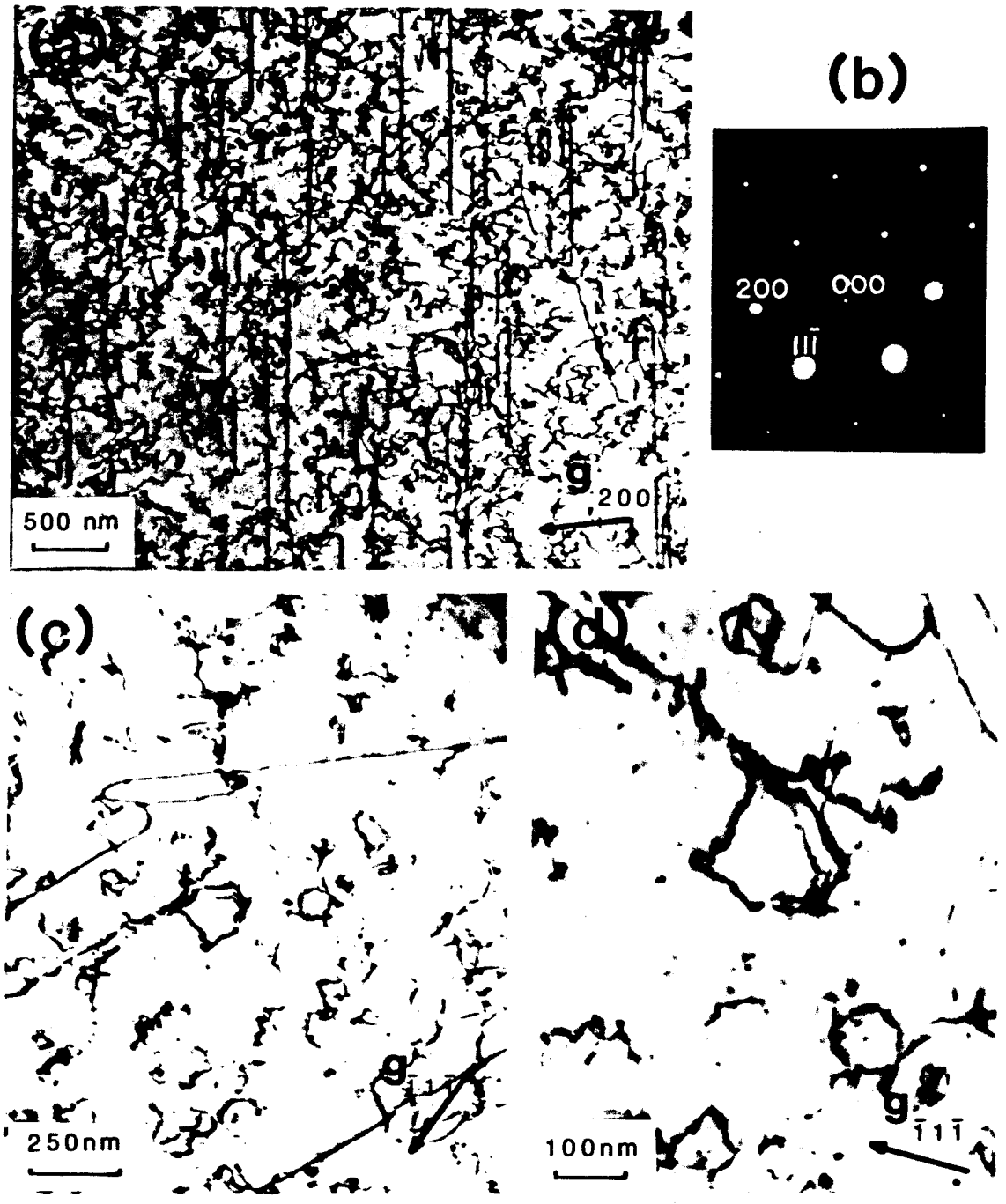

Figure VII. 29. Effect of post-irradiation aging at 400°C (2 hours) on Cu-3.4 at.% Be irradiated at 300°C to 5 dpa. (a) Dislocation structure in thick foil. Precipitates have dissolved. (b) SADP from (a). Note absence of precipitate reflections. (c) Thinner foil containing large dislocation loops but no precipitates. (d) Higher magnification view of (c) showing small dislocation loops.

at 300, 400, and 430°C, then were aged at 400°C in the unthinned condition. In the first case, specimen #27 was irradiated at 300°C to 5 dpa at 1000 nm, then was annealed in situ at 400°C for 2 hours. The microstructure of this specimen, shown in Fig. VII-29, contains no precipitates, and the diffraction pattern contains no precipitate reflections. This contrasts with specimens #26 and #28, which were irradiated at 300°C and contained precipitation throughout the damage zone. The dense dislocation structure produced by irradiation did not anneal out, however. The damage structure consists of large (~ 1000 nm) elongated loops aligned in the $\langle 02\bar{2} \rangle$ direction (micrograph-a), irregularly shaped loops approximately 250 nm in diameter (micrograph-c), and dislocation loops and blackspots smaller than 20 nm (micrograph-d).

To verify the precipitate dissolution at 400°C, unthinned, cross sectioned wafers from specimens #11 and #13, which contained continuous precipitation due to irradiation at 430°C and 400°C, respectively, were aged in the high vacuum furnace at 400°C for 22-1/2 hours, then were thinned in cross section for TEM examination. In Fig. VII-30, the microstructure of the alloy irradiated at 400°C and aged at 400°C following irradiation, is compared with the as-irradiated, unaged microstructure. The as-irradiated sample contains precipitation throughout the damage zone, as described in section A-2 of this chapter. In the specimen that was aged after irradiation, however, most of the precipitates have dissolved; in fact, no precipitates remain in the depth interval of 100 ~ 1000 nm, where dose and

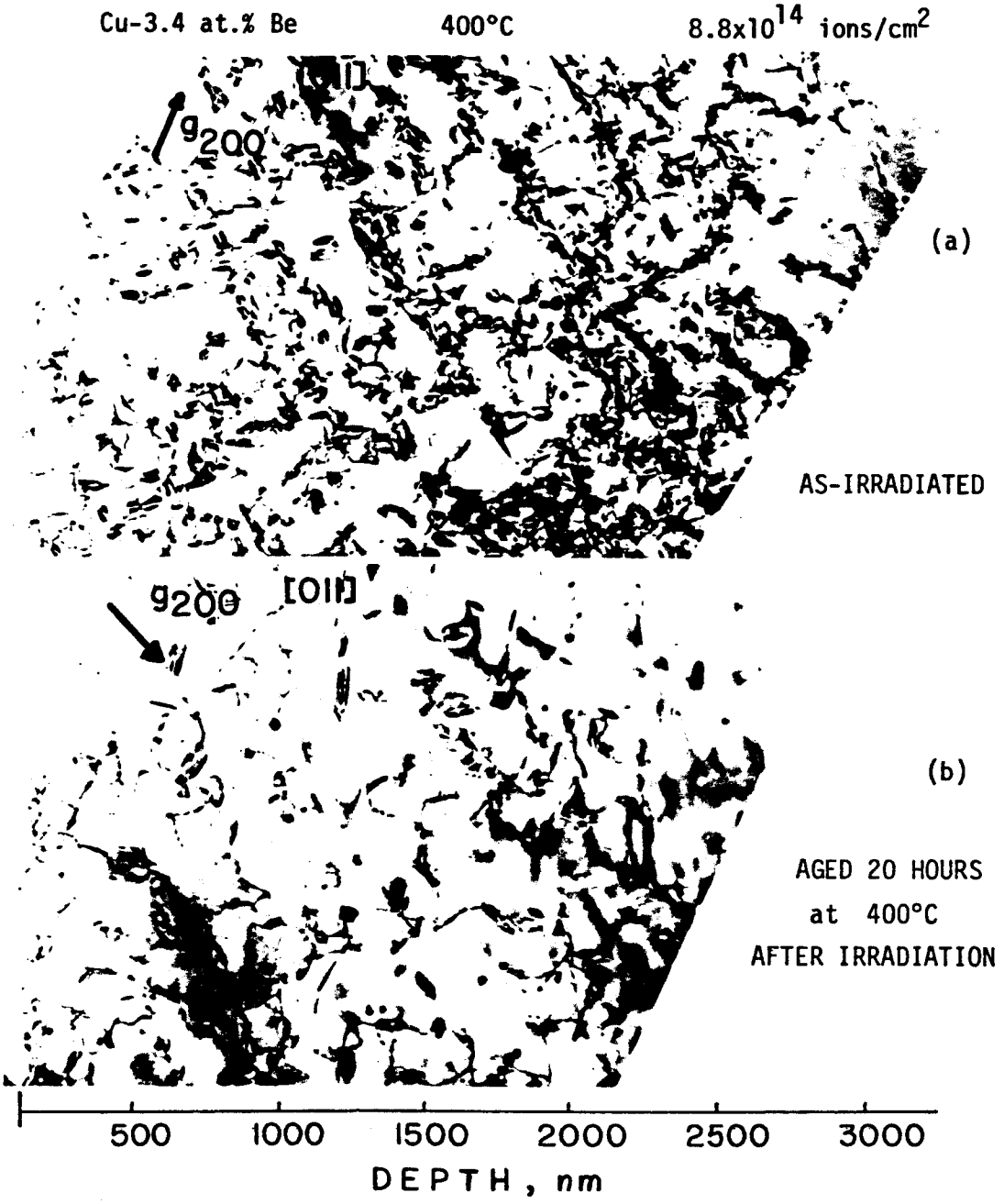

Figure VII. 30. Effect of post-irradiation aging on Cu-3.4 at.%Be irradiated at 400°C with 8.8×10^{14} ions/cm^2 (0.25 dpa @ 1 μm). (a) An as-irradiated specimen, containing irradiation-induced CuBe precipitation throughout the damage zone. (b) A specimen aged for 20 hours at 400°C after irradiation (specimen was thinned after the aging treatment). Most precipitates in the front and end-of-range regions of the damage zone have dissolved, although some precipitates in the central region remain.

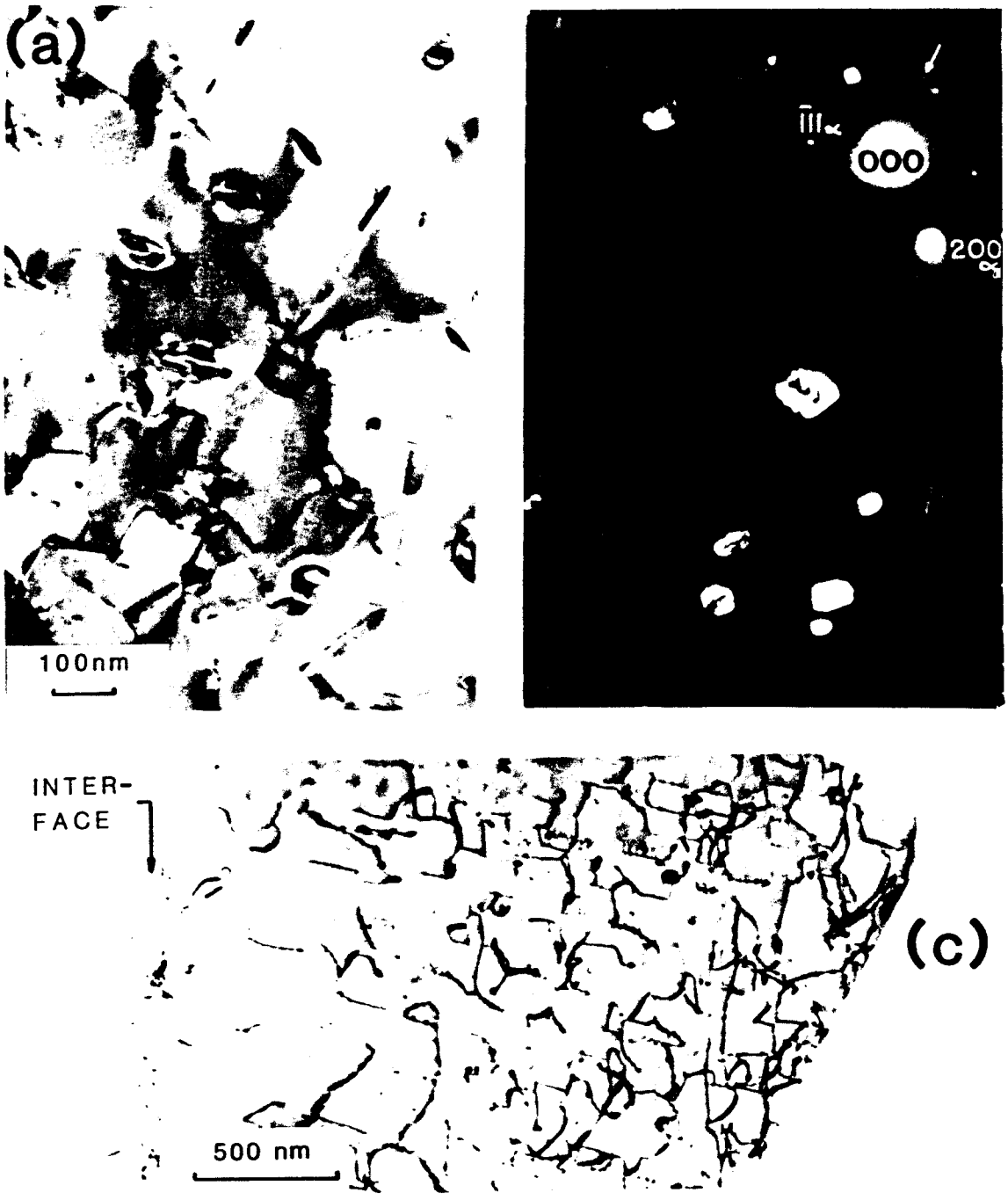

Figure VII. 31. (a) High magnification micrograph of precipitates in irradiated, aged specimen shown in the previous figure. (b) DF image from (a) using (011) precipitate reflection. Matrix zone axis is [011]. (c) Another region of the damage zone in the same specimen (in cross section) where almost all radiation induced precipitates have dissolved.

dose-rate were lowest. An enlarged micrograph from the center of the damage zone clearly shows precipitate shape, and the diffraction pattern indicates they have the usual B2 structure. In Fig. VII-31(c) a different region in the same aged specimen is shown, where all precipitates have dissolved even in the peak damage region.

A-5. Aging Studies on Unirradiated Cu-Be Alloys

The dissolution of continuous CuBe precipitation during aging at 400°C, as described in section A-3, proves that the continuous precipitate morphology is not the equilibrium morphology, even though the precipitate platelets themselves have the equilibrium B2-type crystal structure. The equilibrium phase diagram indicates that the Cu-3.4 at% Be alloy is two-phase at 400°C, however the diagram supplies no information regarding the phase structure. While the precipitation sequence and morphology in the aged Cu-2 wt% Be (12.6 at% Be) alloy has been well characterized by other researchers (see Chapter IV), no studies of precipitation in dilute Cu-Be alloys could be found in the literature for reference. Therefore, aging studies were performed on unirradiated Cu-3.4 at% Be alloy, to determine the morphology of the equilibrium precipitation. The principal result is that CuBe precipitates do nucleate and grow after prolonged aging at temperatures below about 420°C. Unlike the continuous precipitation produced by irradiation; however, precipitation produced by thermal aging is discontinuous, and nucleates as localized clusters of CuBe platelets at grain boundaries and within grains.

The Cu-3.4 at% Be specimens used in the aging experiments were initially solution-annealed and quenched, then were aged at high temperature in the high vacuum furnace. Aged specimens were mechanically polished and electropolished, then were etched in a $FeCl_3$-HCl solution (to reveal the two-phase regions), and were examined with an optical microscope. Three-millimeter discs were also punched from the aged samples, and were thinned for TEM analysis. Between the solution treatment and the high temperature aging, there was usually a time delay of at least several months, during which time specimens were stored at room temperature. The duration of the room temperature (R.T.) "aging" was found to be an important factor in the nucleation of precipitates in specimens studied here.

Unirradiated regions of specimens #1 through #28 provided initial evidence that the precipitation process in the Cu-3.4 at% Be alloy is very sluggish. Several of these specimens were aged at 350-400°C for up to 5 hours, yet no precipitation nor evidence of G.P. zones was detected. Further evidence of sluggish kinetics was provided by a specimen aged 8 months at R.T. and 50 hours at 380°C. Optical and TEM micrographs of this specimen are shown in Fig. VII-32. Several grains on the etched surface of the foil in the optical micrograph are twinned and contain etch pits, but no two-phase regions are visible. No precipitation was observed during TEM examination.

Figure VII-33 contains optical micrographs of a specimen aged 26 mo. at R.T. and 24 hours at 380°C. In this case, regions of the

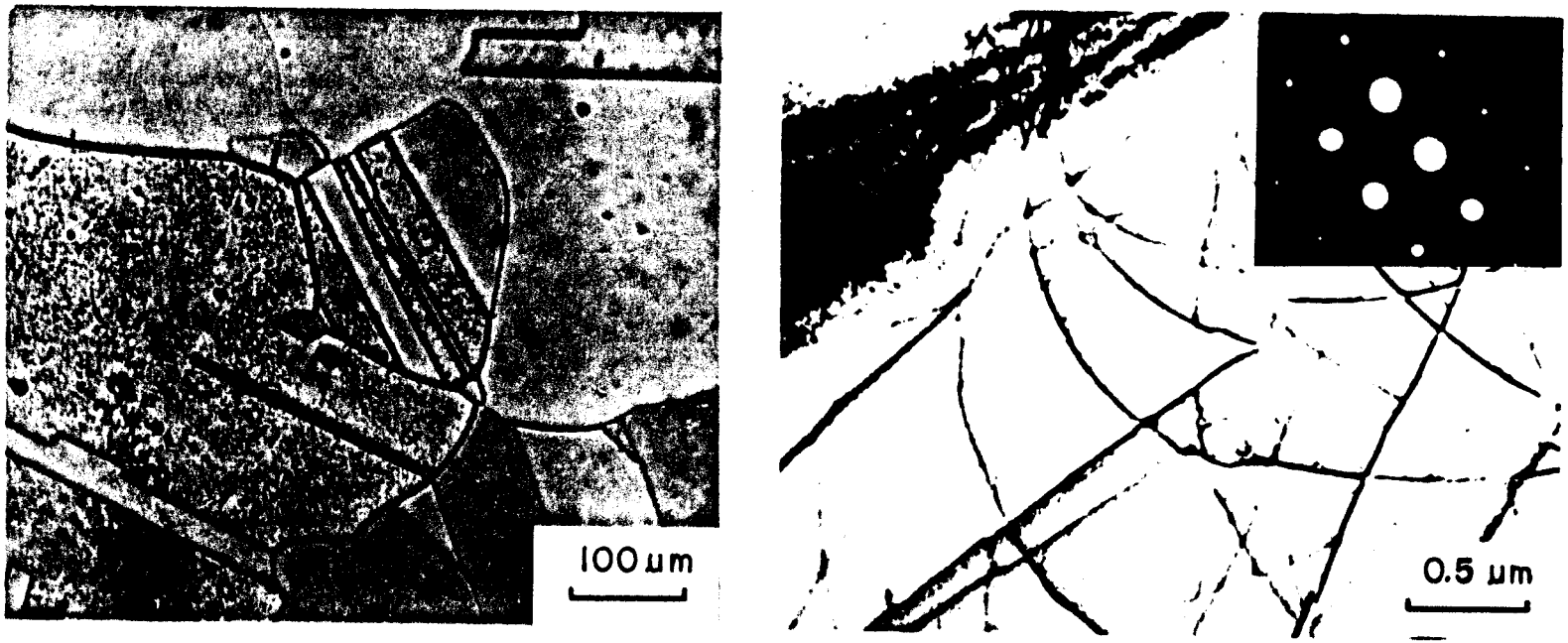

Figure VII. 32. Unirradiated Cu-3.4 at.% Be, solution annealed, then aged 8 months at room temperature and 50 hrs. at 380°C. No two-phase regions are evident in the polished, etched specimen (left). TEM micrograph (right) shows that supersaturated alloy did not decompose during this aging treatment. Zone axis is [001].

solid solution have decomposed. The two-phase regions appear as dark spots in the micrographs. The low magnification micrograph has a textured appearance because the two-phase regions are more resistant to electropolishing than the surrounding solid solution. This fact allowed the two-phase regions to be easily detected, however. The enlarged micrograph in Fig. VII-33 clearly shows the spatial distribution of these regions. Two-phase regions within the grains are spheres or ellipsoids, and they nucleate in an ordered array; at grain boundaries, these nodules tend to be elongated. The maximum dimension of the two-phase regions ranges from ~ 50 μm to less than 2 μm. Proof that the dark regions in the optical micrographs contain two phases was obtained by transmission electron microscopy, as shown in Fig. VII-34. Micrograph (a) in this figure was obtained from an area where the thin foil (at the edge of the perforation) intersected a grain-boundary and a dark nodule. The nodule contains a dense cluster of plate-like precipitates about 500 nm in length. The selected area diffraction pattern (SADP) from the precipitate cluster ([001] matrix orientation) contains extra reflections which correspond to interplanar spacings of 0.274 nm, 0.193 nm, and 0.133 nm; i.e. the (001), (011), and (002) planes of the ordered bcc CuBe precipitate, respectively. The crystallographic orientation relationship between the precipitates and the α-Cu matrix is:

$$[001]_{ppt.} \parallel [001]_{\alpha} \quad \text{and} \quad (\bar{1}\bar{1}0)_{ppt.} \parallel (\bar{1}00) \ .$$

This represents the Bain orientation relationship, which is the same

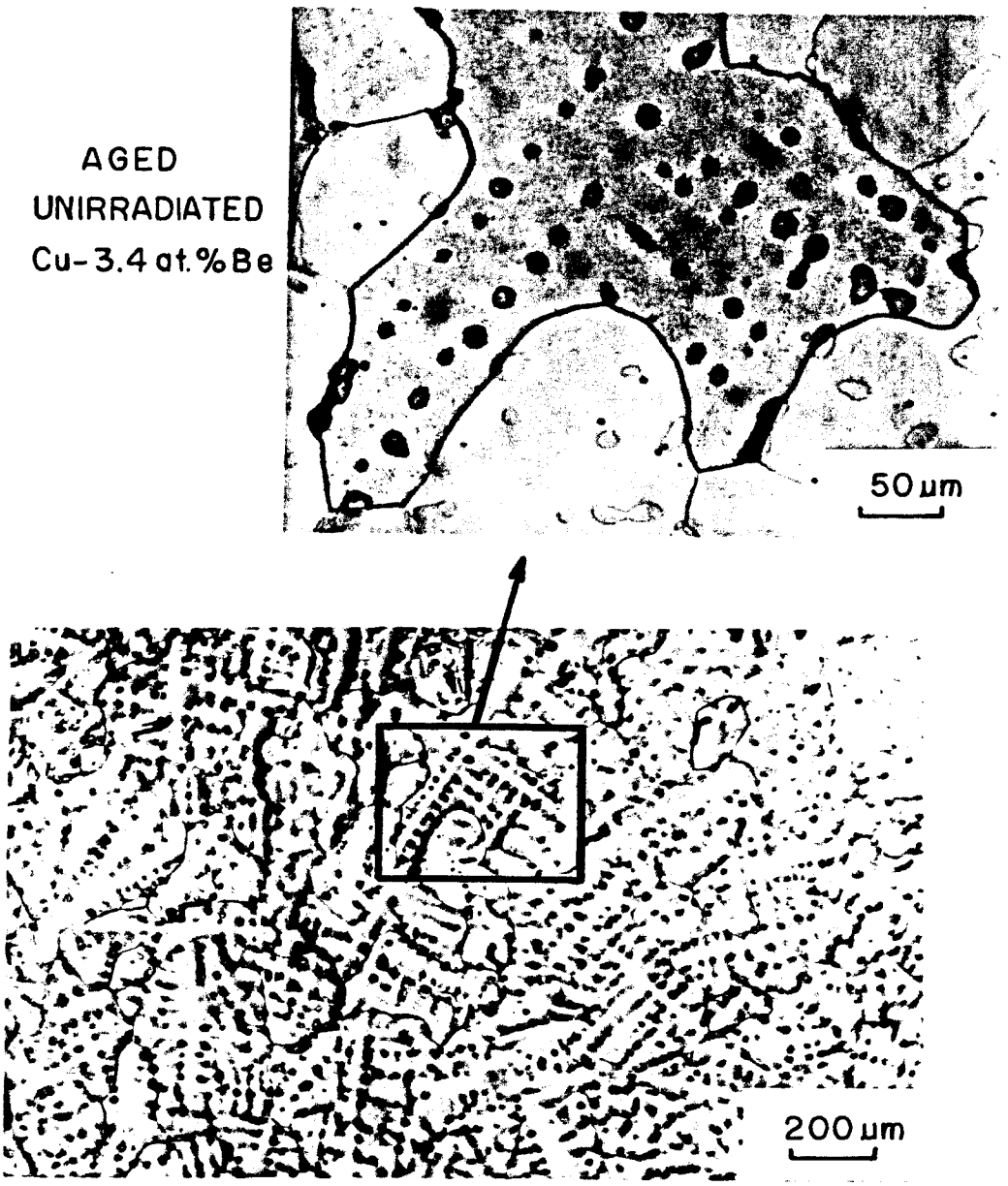

Figure VII. 33. Optical micrographs showing heterogeneous precipitation in unirradiated Cu-3.4 at.% Be aged 26 months at room temperature and 24 hours at 380°C, then etched in $FeCl_3$-HCl. Only the dark regions at grain boundaries and scattered throughout the grains contain CuBe precipitates.

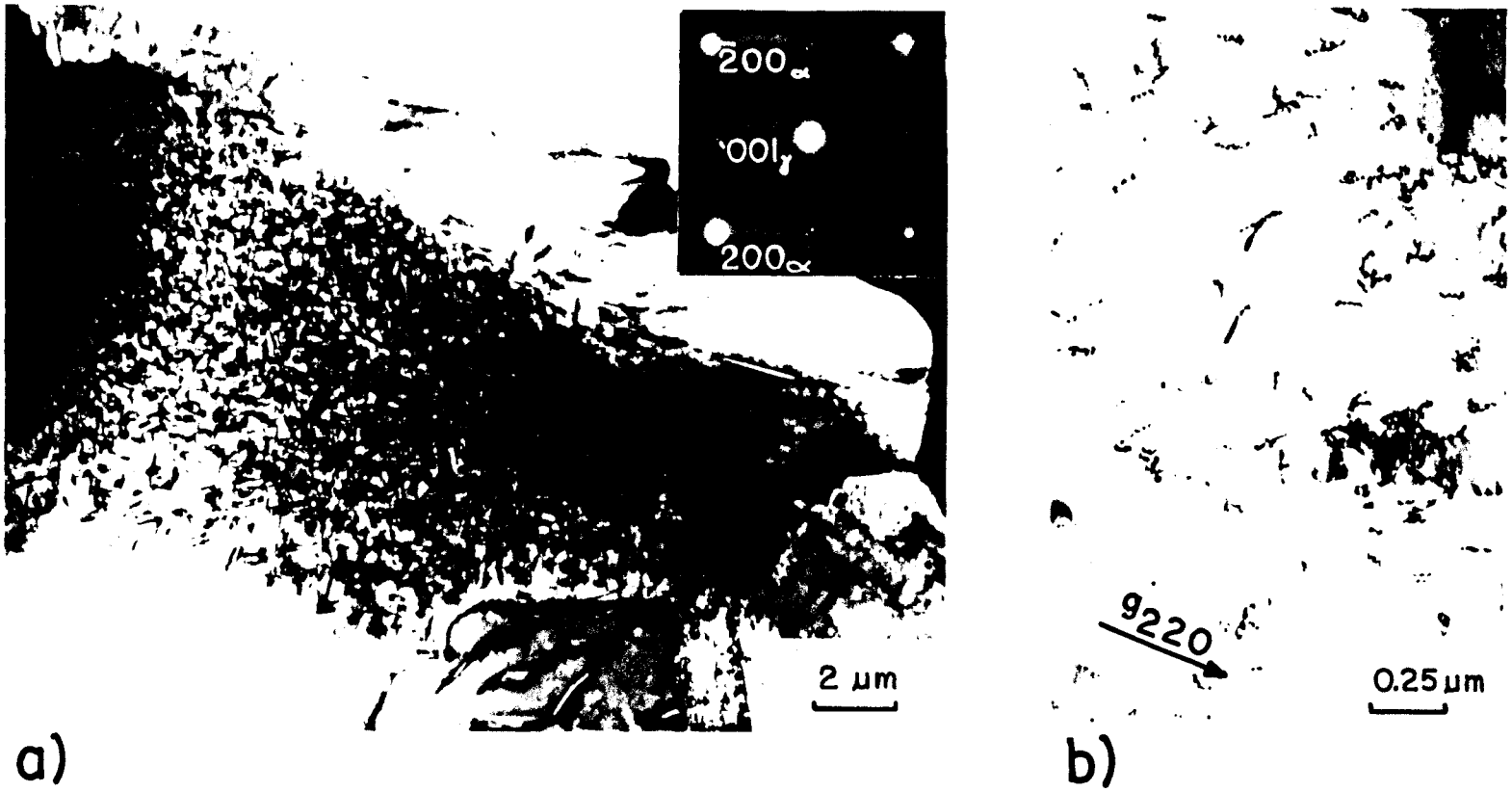

Figure VII. 34. Microstructure of unirradiated Cu-3.4 at.% Be aged 26 months at room temperature and 24 hours at 380°C. (a) Region near grain boundary containing CuBe platelets. Zone axis is [001]. (b) Typical region within the grain, free of precipitates.

as that reported by Rioja and Laughlin[5] for the equilibrium γ-CuBe precipitate in the Cu-12.6 at% Be alloy, in regions transformed by the grain boundary reaction. Whether or not the densely clustered precipitates observed here in the Cu-3.4 at% Be alloy are precisely the γ-CuBe precipitates cannot be stated, because a detailed TEM analysis of the precipitate habit planes was not performed. As discussed in Chapter V, both the γ and the mature γ' precipitates have the same structure (B2-type, with a = .27 nm) but lie on different habit planes, and have different crystallographic orientation relationships with the matrix.[5] Note also in micrograph (a) that adjacent to the precipitation described above, lie subgrains containing larger plates of discontinuous precipitation. The matrix between the two-phase regions was completely free of precipitates, as shown in micrograph (b) in Fig. VII-34. The features seen in this micrograph are dislocations about 100-150 nm in length.

When a Cu-3.4 at% Be specimen that had been aged at 380°C and which contained precipitates, as in Figs. VII-33 and VII-34, was again aged at 400°C for 24 hours, the two-phase regions grew somewhat, especially at grain boundaries. When the same specimen was aged at 435°C for 20 hours, most of the two-phase regions disappeared.

Another example of heterogeneous precipitation in aged Cu-3.4 at% Be is shown in Fig. VII-35. This specimen was cut from the Cu-3.4 at% Be billet, which had been stored at room temperature for the previous ~ 15 years,[7] and was aged for 100 hours at 380°C. In

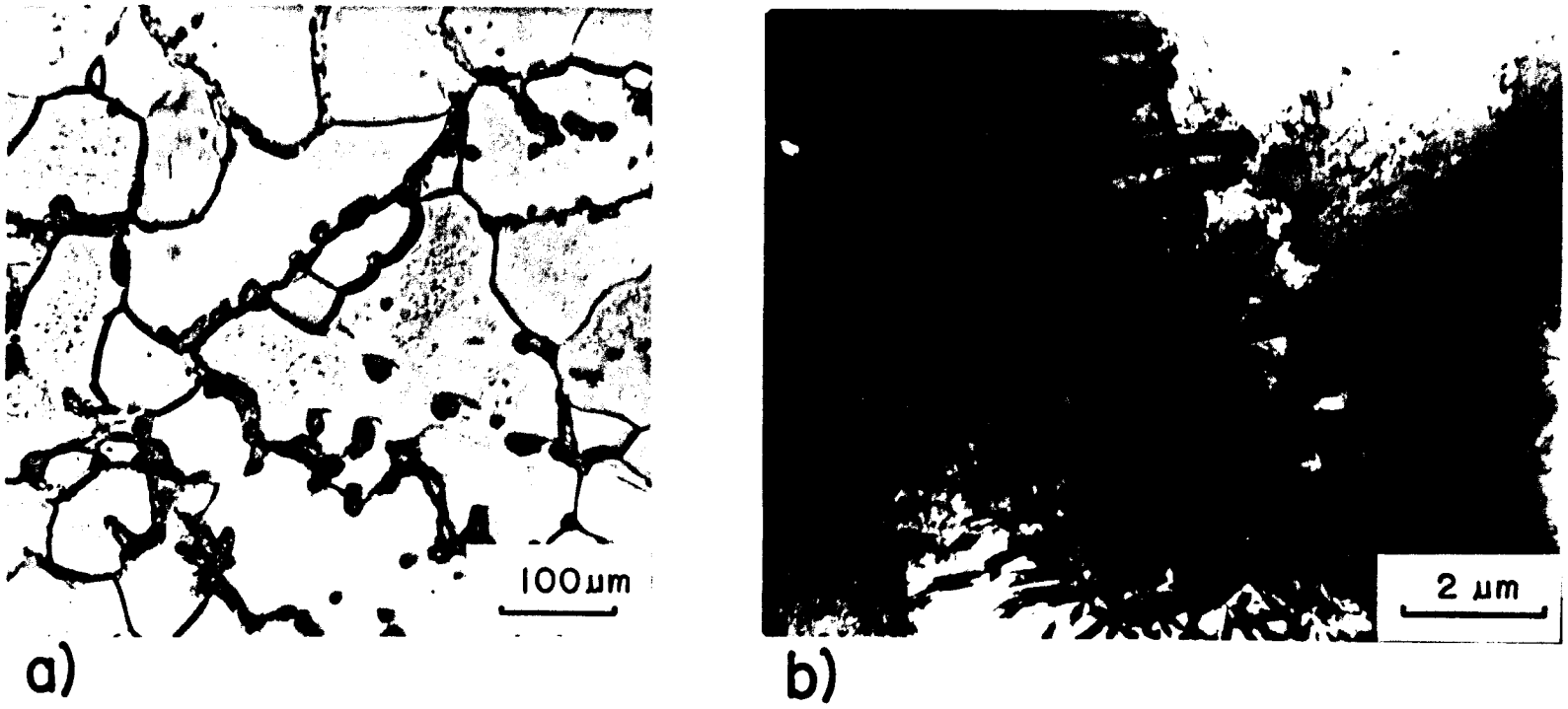

Figure VII. 35. Heterogeneous precipitation in Cu-3.4 at.% Be aged about 15 yrs. at room temperature, and 100 hrs. at 380°C. (a) Optical micrograph showing CuBe precipitation at grain boundaries and in isolated regions within the grains (darker areas). (b) TEM micrograph of a two-phase region as seen in (a), composed of densely clustered CuBe platelets. The surrounding matrix is completely free of precipitates.

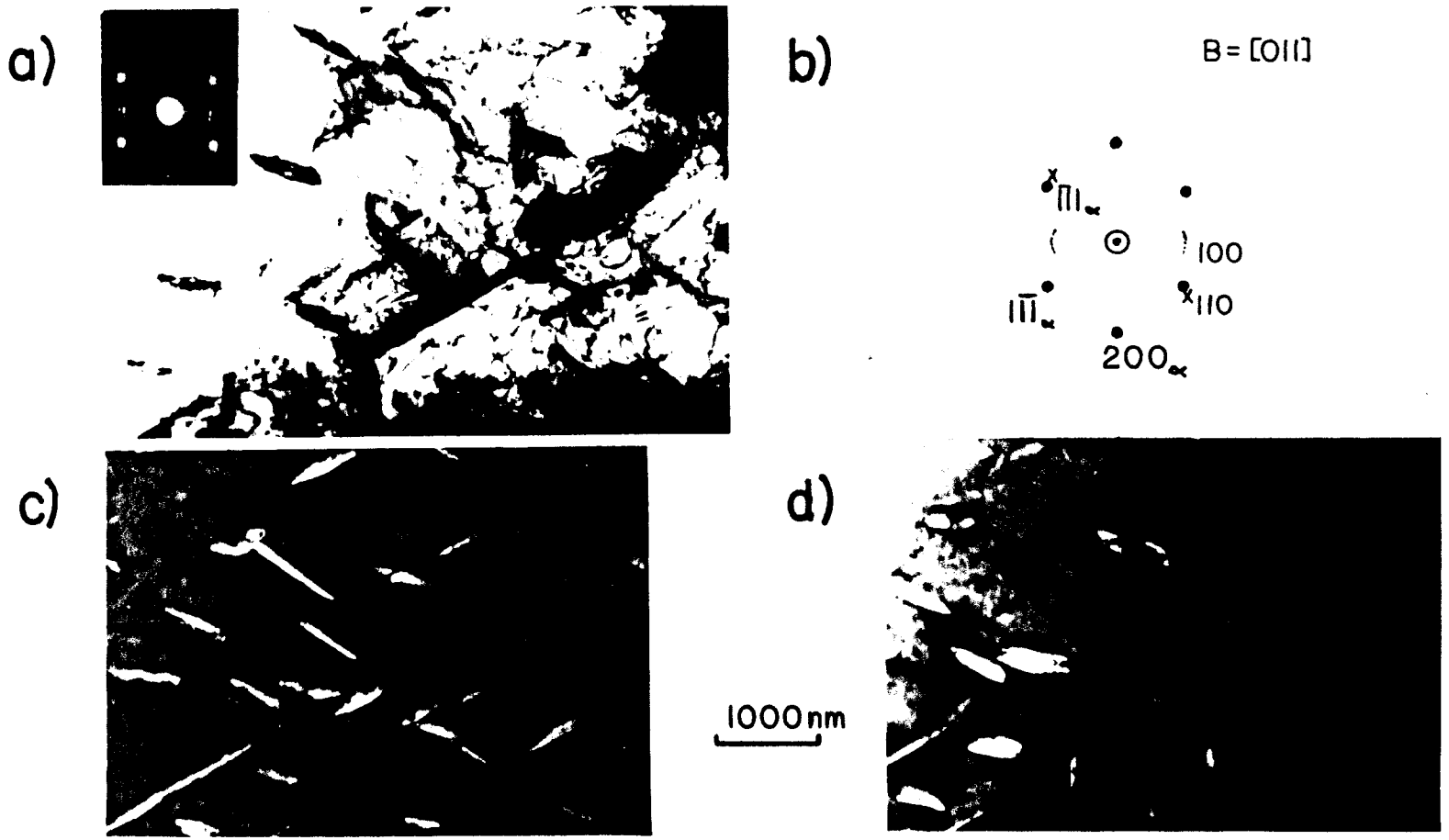

Figure VII.36. (a) An isolated cluster of γ-CuBe precipitates in Cu-3.4 at.% Be aged about 15 yrs. at room temperature and 100 hrs. at 380°C (unirradiated). (b) Schematic of the SADP from (a) with precipitate reflections (x) and matrix reflections (•) indexed. (c) DF image of (a) using ($\bar{1}00$) CuBe reflection. (d) DF image of (a) using (110) CuBe and ($1\bar{1}1$) matrix reflections. Zone axis is [011].

micrograph (a), two-phase nodules have formed along many of the grain boundaries, and also at various locations within the grains. Both the grain boundary and intragranular nodules appeared to have identical structures when examined in the TEM. The nodules are massive clusters of lathe-shaped precipitates, as shown in Fig. VII-35(b), and they are surrounded by matrix completely free of precipitation. Regions containing smaller CuBe platelets, as in Fig. VII-34(a), were not found in this specimen. Because of their resistance to electropolishing, the dense clusters were almost opaque to the electron beam. A less-dense cluster that yielded an incomplete electron diffraction pattern is shown in Fig. VII-36. Precipitate reflections in the SADP correspond to (100), (110) and (200) planes of the ordered bcc CuBe structure. The crystallographic orientation relation between the matrix and precipitate was not determined. Nevertheless, the spatial distribution of the precipitates, and the size of precipitates, are clearly different in the Cu-3.4 at% Be alloy aged at 380°C, compared to alloy irradiated at a similar temperature.

It is interesting that the morphology of the radiation induced precipitation in the Cu-3.4 at% Be alloy is similar to the morphology of continuous precipitation produced by thermal aging of the Cu-12.6 at% Be (2 wt% Be) alloy. An example of continuous precipitation in this alloy, which was solution annealed and quenched from 800°C, then stored at R.T. for 8 months and aged at 380°C for 100 hours, is shown in Fig. VII-37. The precipitate platelets are uniformly distributed throughout the matrix, they range in size to ~ 300 nm, and their

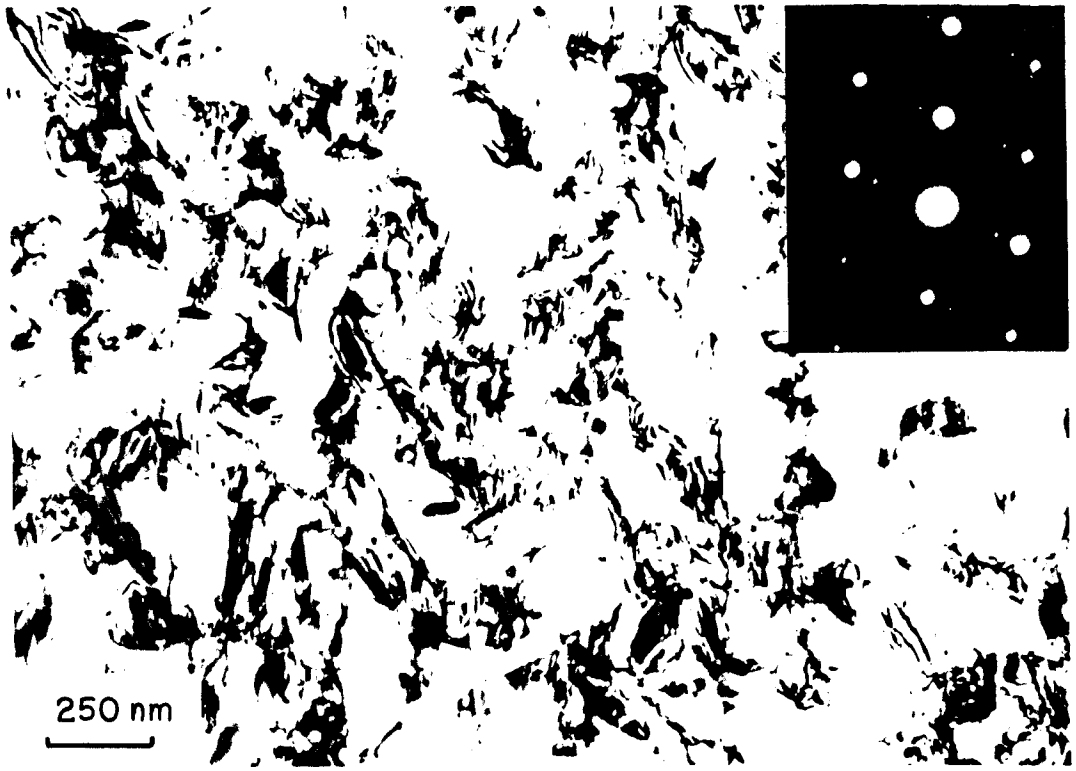

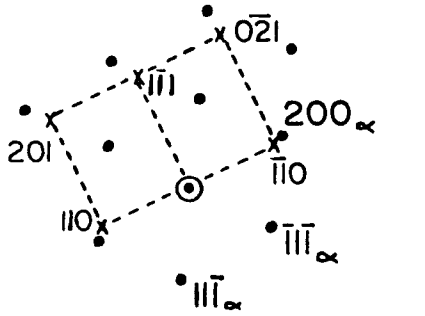

X = CuBe precipitate

Figure VII. 37. Continuous precipitation in Cu-12.6 at.% Be (2 wt.% Be) aged 8 months at room temperature and 100 hrs. at 380°C. The morphology of this precipitation is similar to that in irradiated Cu-3.4 at.% Be specimens. Precipitate reflections in the SADP, indexed at right, represent the ordered bcc (B2) structure with a= 0.27nm. Zone axis is [011].

structure is ordered bcc with a lattice constant of a = 0.27 nm. Both the continuous and discontinuous precipitation in the 12.6 at% Be alloy have been well characterized, as discussed in Chapter IV. The point to be made here is that under irradiation, the Cu-3.4 at% Be alloy behaves as if its solute concentration is much higher than 3.4 at% Be.

B. Beryllium Surface-Segregation Measurements

Before the Cu-3.4 at% Be specimens were prepared for electron microscopy, the depth dependence of the near-surface Be concentration was measured using Auger electron spectroscopy combined with sputter etching. The original intent of these measurements was to determine whether radiation-induced segregation of solute elements occurs at point-defect sinks in the Cu-Be alloy. Characterization of radiation-induced solute segregation at the external surface of the alloy (which is an unsaturable point defect sink) could provide insight on the segregation behavior at internal defect sinks, and thereby aid in the interpretation of phenomena such as radiation-induced precipitation.

Straightforward measurement of the near-surface Be concentration profiles was complicated by three factors:

(a) Heating the Cu-Be alloy, even in the absence of irradiation, causes surface segregation of Be. This effect was noted in previous surface studies of Cu-Be alloys using the Auger technique.[9,10]

(b) The principal Auger transition in Be occurs at an energy of 104 eV, which overlaps a secondary Cu Auger transition at 105 eV.[11]

(c) Be at the alloy surface is easily oxidized. Oxidation, however, shifts the energy of the Auger transition of Be from 104 eV to 96 eV.[10,12] At 96 eV there is no interference from other elements, so the amplitude of the Auger peak can be directly measured.

The problem of thermal segregation of Be was accommodated by profiling the Be concentration at both irradiated and unirradiated surfaces of each specimen, and using the unirradiated surface as a reference. Beryllium concentration vs. depth profiles obtained from the first set of irradiated Cu-Be specimens proved the following:

(a) Be enrichment was significantly greater at irradiated surfaces than at unirradiated surfaces, so Be segregation was enhanced by ion bombardment.

(b) The absolute quantity of Be near a surface was strongly dependent on the thermal history of the specimens.[13]

(c) All excess Be near the surface was completely oxidized; hence the effect of irradiation was to enhance the growth rate of BeO at the specimen surface. Based on these results, the effects of irradiation temperature and dose on the Be segregation were studied systematically, to try to determine the mechanism of the Be transport.

Typical Auger spectra from an irradiated Cu-3.4 at% Be specimen are shown in Fig. VII-38. (The instrument settings and the experimental method were described in Chapter VI.) These spectra were obtained from the center of the 3 mm dia. irradiated area of the specimen, and were recorded in the usual manner as $dN(E)/dE$ vs. E (where N(E) is the number of electrons collected at energy E). The Auger transitions are characterized by the energies of the negative peaks in the Auger spectrum[11]. The relative amplitudes of the peaks are related to the relative concentrations of elements within the first several atomic layers of the specimen surface. Spectrum "A" in Fig. VII-38 shows that the surface of the irradiated area is rich in oxygen and Be, and that the Be is fully oxidized, because the Be peak appears at 96 eV and not at 104 eV. Some of the surface oxygen is not bonded to the Be, but is adsorbed oxygen picked up during exposure to the atmosphere. This was tested by simultaneously sputter-etching and recording portions of the Auger spectrum, in which case the 508 eV oxygen peak immediately decreased to ~ 2/3 of its initial amplitude while the Be peak decreased only slightly (and remained at 96 eV). Spectrum "B" in Fig. VII-38, obtained after

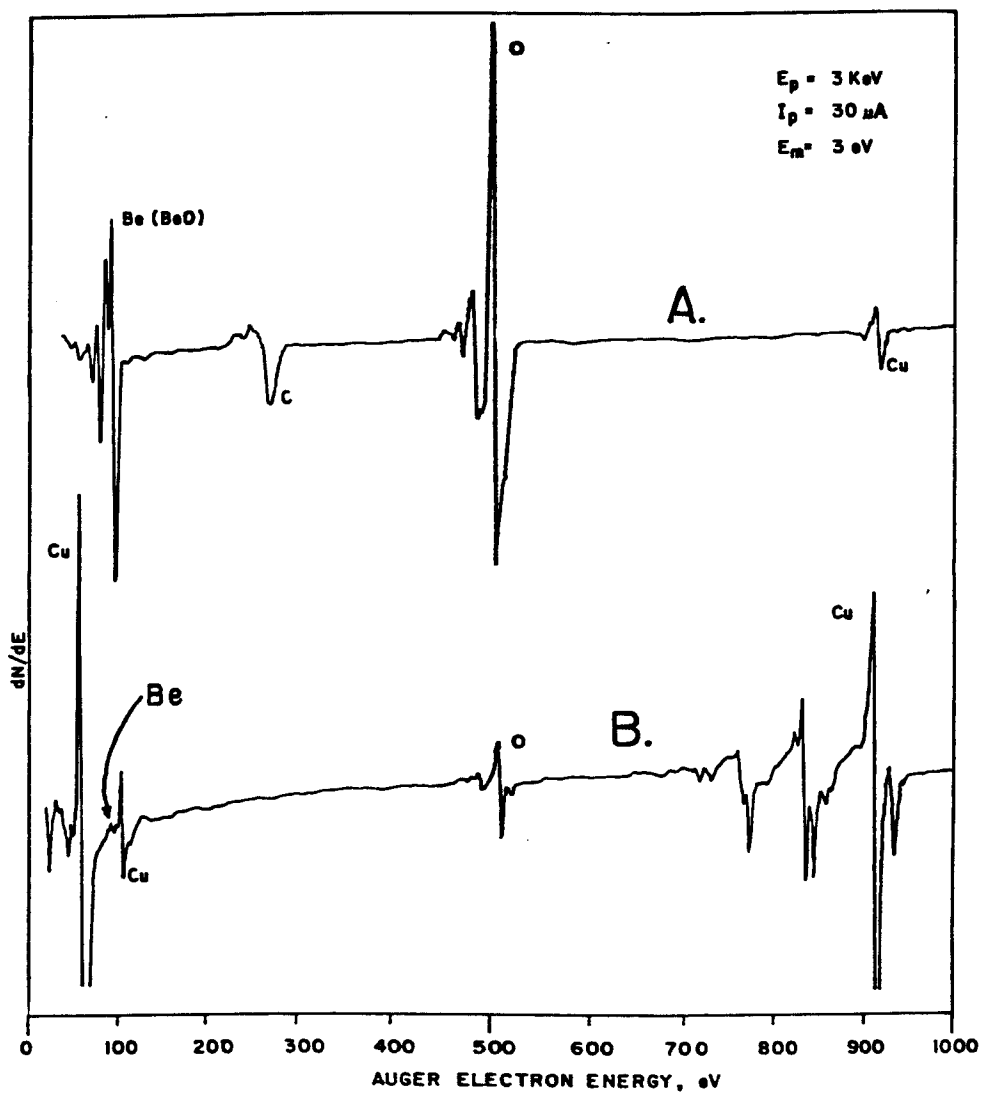

Figure VII.38. Typical Auger electron spectra from an ion bombarded Cu-3.4 at.% Be specimen. (a) At the irradiated surface, which is enriched in Be. The main Be Auger peak occurs at 96 eV rather than 104 eV, indicating the Be is fully oxidized. The large oxygen peak (508 eV) results from the BeO and from adsorbed oxygen. The carbon peak results from surface contamination. (b) At a depth of ~ 100 nm from the original surface, where the Be concentration has decreased to the bulk concentration. The 105 eV peak labeled Cu may contain a small contribution from unoxidized Be. Most of the oxygen present here is from residual O_2 within the vacuum chamber, which has adsorbed on the specimen surface.

sputtering to a depth of ~ 100 nm from the original surface, is representative of the bulk alloy composition. The spectrum is dominated by the Cu peaks, although small Be and oxygen peaks are still present. This oxygen peak results solely from residual oxygen picked up within the vacuum chamber of the instrument, and disappears completely during simultaneous sputtering.

Alloy composition vs. depth measurements were in most cases obtained from depths within 300 nm from the original surface. The relation between this depth interval and the range of the 14 MeV Cu ions is indicated on the dpa curve in Fig. VII-1.

Shown in Fig. VII-40 are depth profiles of the relative concentrations of Be, O, and Cu, in a Cu-3.4 at% Be specimen irradiated at 475°C with 1.8×10^{16} ions/cm^2 (corresponding to a dose of 1 dpa at the specimen surface). Both the Be and oxygen concentrations within 20 nm of the surface are ~ 8 times greater than their concentrations at depths beyond 100 nm. These profiles were generated by simultaneously sputtering and recording portions of the Auger spectrum, with the instrument in the multiplex mode. Occasionally, the sputtering was interrupted and the entire Auger spectrum was recorded, in order to verify that unoxidized Be was not present. Figure VII-40 shows that during high temperature irradiation, Be diffuses or is transported to the surface, accompanied by a build-up of oxygen within the same region. This observation, together with the shift in the energy of the Be Auger peak to ~ 56 eV and evidence obtained by electron microscopy (discussed below), suggest that the Be within the enriched

zone exists as BeO rather than as free Be. Because the bulk oxygen content of the Cu-Be alloy was low (approximately 10 ppm), the source of the excess oxygen must have been the residual oxygen within the target chamber of the accelerator.

In Fig. VII-40, the relative Be concentration (X_{Be}) is represented by the relative amplitude of the Be Auger peak. That is, $X_{Be} \propto I_{Be}/(I_{Be} + I_{Cu} + I_O)$, where I_{Be}, I_{Cu}, and I_O are the measured amplitudes of the Be, Cu and O peaks, occurring at ~ 96 eV, 920 eV, and 510 eV, respectively. The elemental concentrations were not calculated using the elemental sensitivity factors of Davis et al.,[11] because these factors were found to be inaccurate when applied to oxidized Be or Cu-Be alloys.

In an attempt to correlate X_{Be} with the true Be concentration, a calibration curve (Fig. VII-39) was constructed using measurements of X_{Be} from pure Be, and from Cu-Be alloys known to contain 3.4, 10, 12.6, and 23 at% Be in the bulk. Each of these specimens was sputter cleaned within the vacuum chamber, then the surface Be was allowed to oxidize fully (by introducing oxygen into the chamber) before the 96 eV Be (BeO) peak was measured. The shape of the calibration curve is interesting, because X_{Be} increases linearly with bulk Be concentration (C_{Be}) in the range $0 < C_{Be} \lesssim 25\%$. Unfortunately, Cu-Be alloys with higher Be concentrations were not available. Nevertheless, the curve must lie near the region indicated by the dashed line, in order to intersect the point representing pure, oxidized beryllium. Two possible explanations for the shape of this curve are:

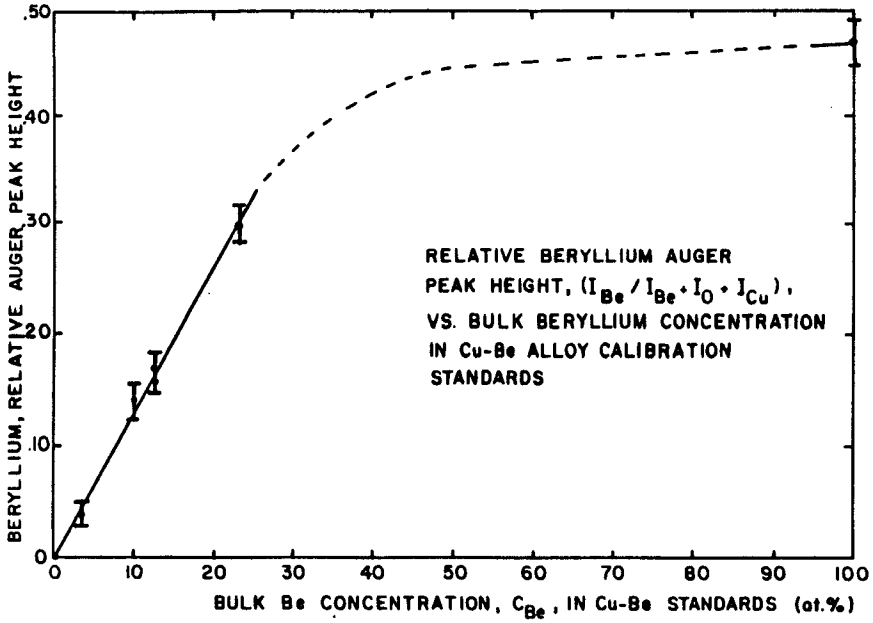

Figure VII. 39 Correlation between the relative height of the 96 eV peak of oxidized Be, and the actual Be concentration. AES measurements were performed on pure Be and on CU-Be alloys with various Be concentrations, C_{Be} . The surfaces of all samples were sputter cleaned, then the surface Be was allowed to oxidize. For alloys with $C_{Be} \lesssim 25\%$, the the surface Be concentration is enriched relative to the bulk concentration.

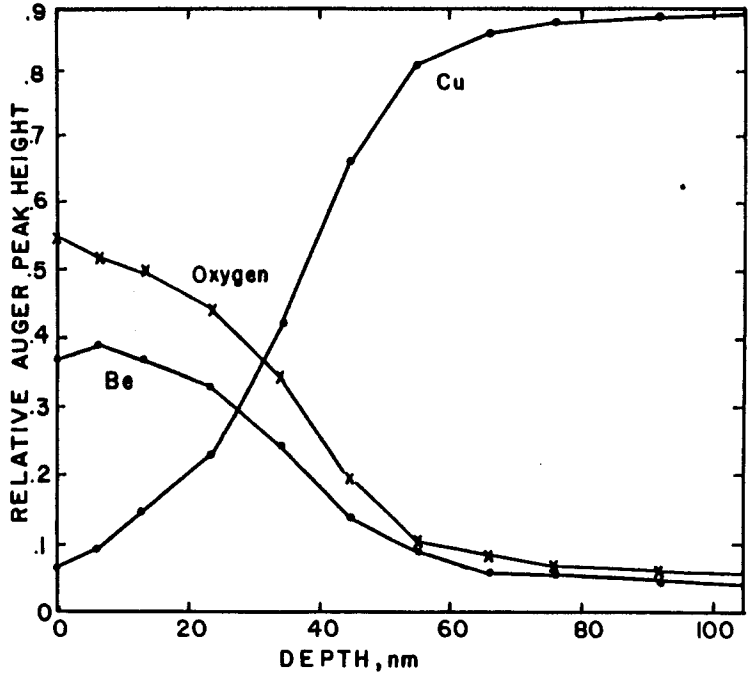

Figure VII.40 Relative concentration vs. depth profiles of Be, Cu, and oxygen in Cu-3.4 at.% Be irradiated with 1.8×10^{16} ions/cm^2 (1.3 dpa at the specimen surface) at 475°C. These profiles were generated from Auger electron spectroscopy data, and are first order approximations.

(a) the Auger electron yield is enhanced in the dilute Cu-Be alloys because of backscattering effects;[14] and,

(b) the surfaces of these alloys become enriched in Be, due to Be segregation occurring during sputter-cleaning of the surface.[15,16]

In Fig. VII-41, beryllium concentration vs. depth profiles are compared, for Cu-3.4 at% Be specimens irradiated to relatively high doses at temperatures of 350, 375, and 475°C. Concentration profiles from unirradiated areas of each foil are also plotted here. The irradiation temperature is the dominant variable governing the build-up of BeO, as suggested by the large difference between the 475°C and 375°C profiles. The effect of irradiation fluence is weaker; e.g., the Be profile of the 375°C specimen irradiated with $1.8 \times 10^{16}/cm^2$ is higher than the 350°C specimen irradiated with twice the fluence. This result might suggest that high temperature alone, not irradiation, caused the Be segregation. However, the Be profiles from unirradiated areas of the specimens were always smaller than those from the beamspot. This was found to be true whether or not the control area had been masked (by tantalum sheet) during heating within the target chamber.

Beryllium concentration profiles from specimens irradiated to low doses at 375-430°C (Figs. VII-42 and VII-43) illustrate how rapidly the BeO-enriched layer forms. After an ion fluence of $8.8 \times 10^{14}/cm^2$ (which was accumulated in less than 4 minutes of irradiation), the enriched layer is well established in the 400°C and 430°C

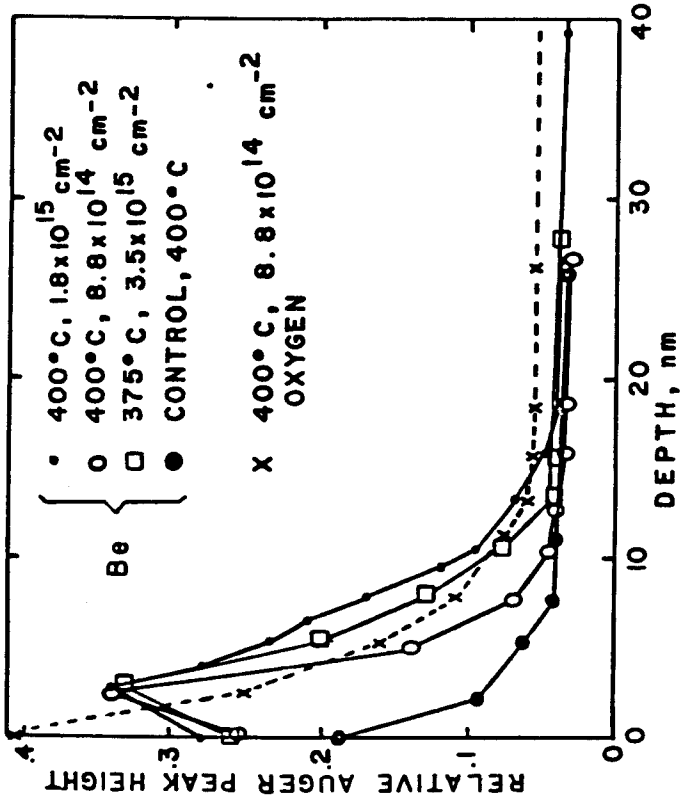

Figure VII.42. Concentration vs. depth profiles of Be and O in Cu-3.4 at.% Be irradiated at 400°C to relatively low doses (0.13 and 0.06 dpa at the surface), and at 375°C (0.25 surface dpa). The oxygen profile shown here is typical of these specimens.

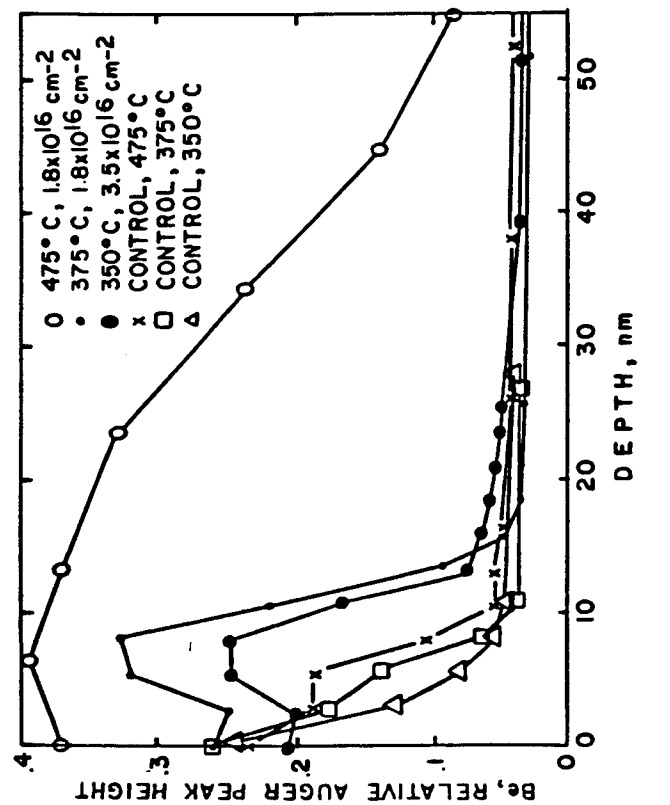

Figure VII. 41. Concentration vs. depth profiles of Be in Cu-3.4 at. % Be irradiated at 475°C (1.3 surface dpa), at 375°C (1.3 surface dpa), and at 350°C (2.6 surface dpa), generated from AES data. Control measurements were obtained from areas of the specimens masked from the Cu ion beam.

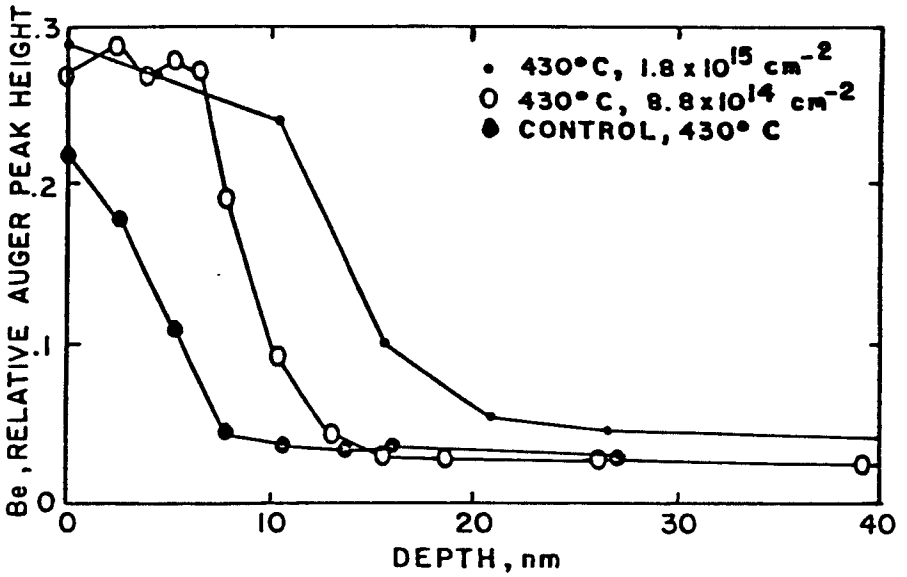

Figure VII.43. Beryllium concentration vs. depth profiles in Cu-3.4 at.%Be irradiated at 430°C to relatively low doses (0.13 dpa and 0.06 dpa at the surface).

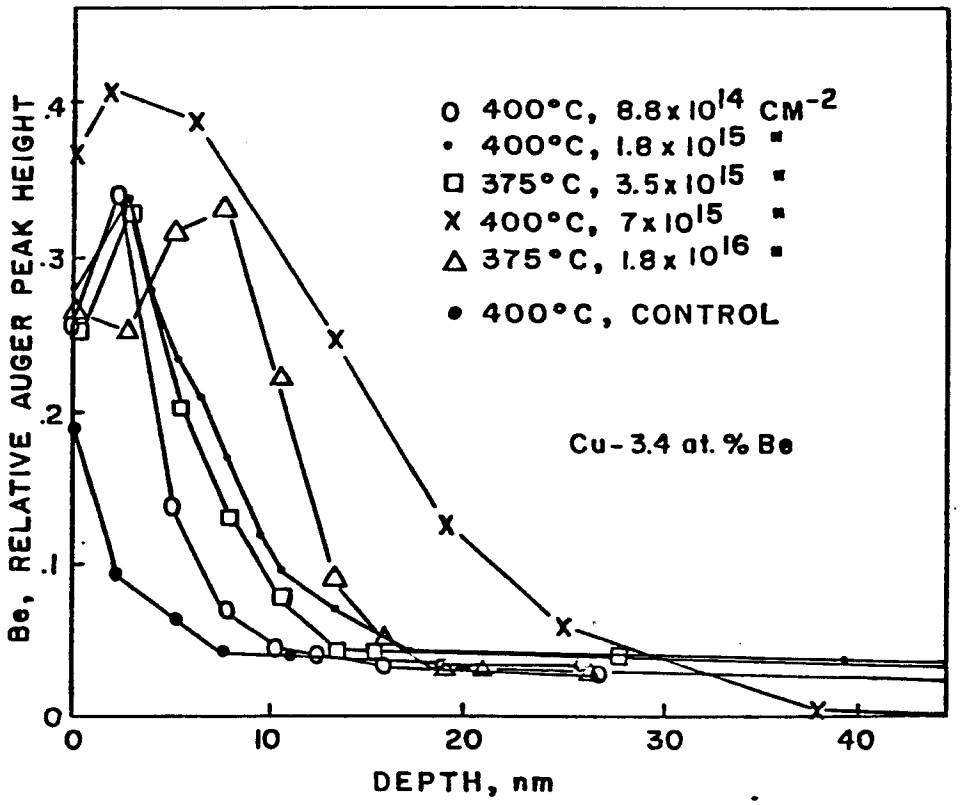

Figure VII. 44. The effect of irradiation dose on the near-surface Be enrichment of Cu-3.4 at.%Be specimens irradiated at 375-400°C. Doses ranged from 0.06 dpa to 1.3 dpa at the surface.

specimens. Doubling the fluence (at constant ion flux) increases the thickness of the enriched layer by about 40%. This same behavior is exhibited in Fig. VII-44, where the proflies from Fig. VII-42 are now compared with profiles from higher dose samples. At 400°C, the thickness of the BeO-enriched layer, W_B, increases at a rate proportional to $\sqrt{\phi t}$, where ϕ is ion flux and t is time. Since ϕ is approximately constant in this case, $W_B \propto \sqrt{t}$.

In studies such as this where sputtering is employed to erode an alloy surface, preferential sputtering[15] due to differences in the sputter yields of the alloying elements can produce apparent elemental concentration gradients. To illustrate that concentration profiles as in Figs. VII-41 to VII-44 are not the result of preferential sputtering, measurements were made in two annealed Cu-Be alloys whose surfaces were mechanically polished and electropolished (Fig. VII-46). The Be concentration profile from the 3.4 at% Be alloy reached steady-state after ~ 3 nm had been removed from the surface, while the 10 at% Be alloy reached steady-state at ~ 15 nm. If anything, these results show that the surface becomes slightly enriched in Be as a result of sputtering.

The structure of the near-surface region of one irradiated specimen was studied by transmission electron microscopy, as shown in Fig. VII-45. This specimen was bombarded with 10^{16} ions/cm^2 at 430°C, then was backthinned to the irradiated surface. At various locations along the edge of the perforation in the thinned specimen, fragments of a very thin, almost transparent film protruded beyond

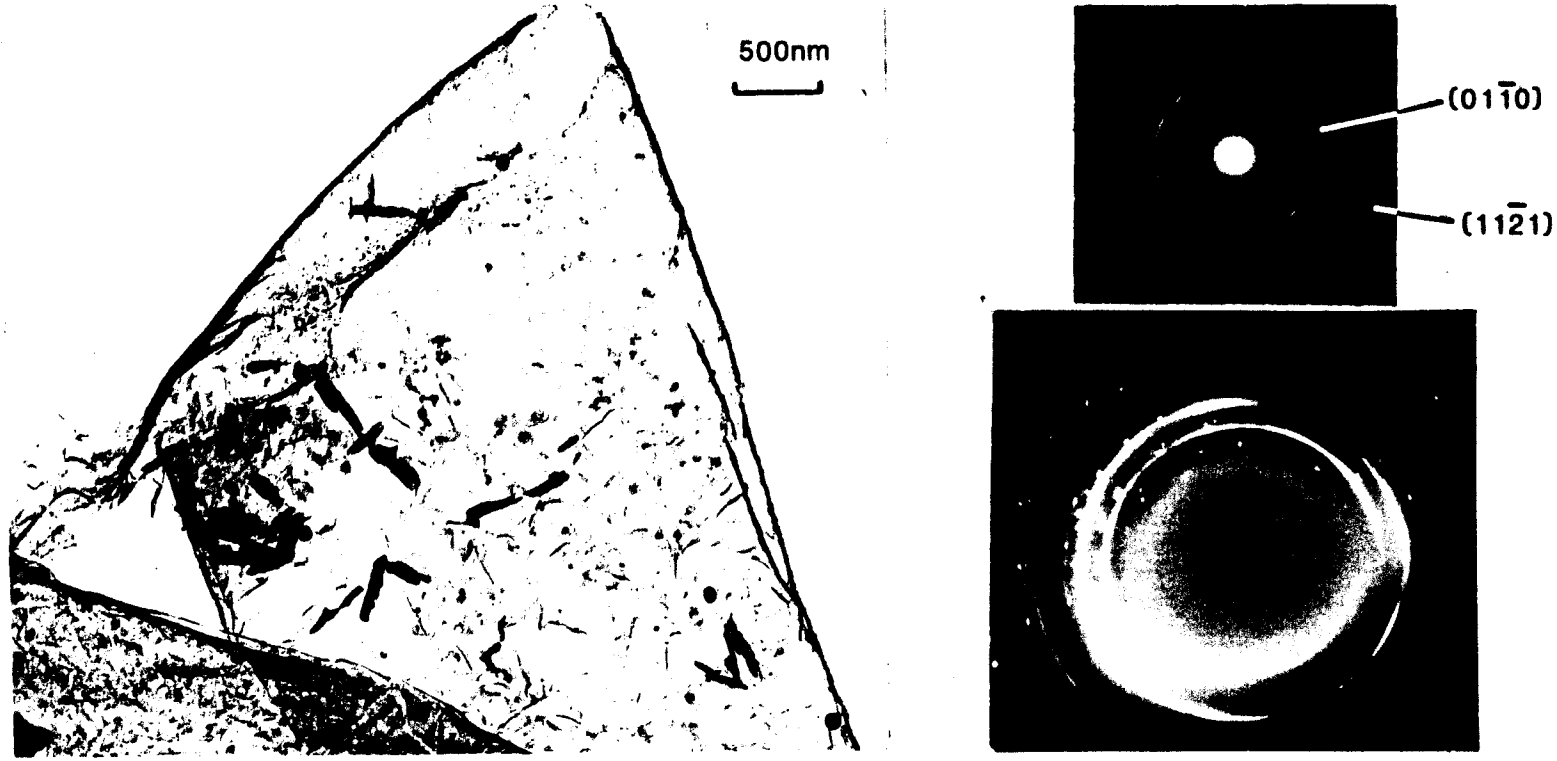

Figure VII. 45. TEM bright field micrograph (left) of the BeO film that formed on the surface of a Cu-3.4 at % Be specimen irradiated at 430°C with $1x10^{16}$ ions/cm^2. (The specimen was backthinned to the irradiated surface.) Such a film was not observed on the unirradiated surface of the same specimen. CuBe precipitate platelets on the film remained after the alloy matrix polished away. The electron diffraction ring-pattern from the film (right, underexposed and overexposed to show the lower and higher order rings) corresponds to an HCP BeO structure with a=0.27nm, c=0.44nm, with the c-axis perpendicular to the specimen surface. The CuBe precipitates produced the random diffraction spots on the overexposed pattern.

the edges of the specimen. Electron diffraction ring-patterns from the thin film correspond to the BeO hcp structure with a = 0.27 nm and c = 0.44 nm, thereby proving that a BeO layer formed on the irradiated surface. In the electron diffraction pattern, no reflections from the basal planes are observed, suggesting that the BeO film forms with the hcp basal planes parallel to the surface of the specimen. An unirradiated region of the specimen was backthinned and examined in the same manner, but no surface film was observed.

In a final experiment, an attempt was made to detect radiation-induced Be redistribution within and beyond the damage zone, which could occur if solute atoms are coupled to the point-defect currents produced by spatial variations in the displacement damage rate.[17] A Cu-3.4 at% Be specimen was irradiated at 400°C with 7×10^{15} ions/cm^2, then the Be concentration was profiled to a depth of ~ 3600 nm. At depths beyond ~ 800 nm, the measurements were performed with the instrument in the multiplex mode. However, the sputtering was periodically interrupted and the surface was allowed to oxidize, then the entire Auger spectrum was recorded to detect any concentrations of unoxidized Be. The resulting depth profile is shown in Fig. VII-47. Except for the usual surface segregation, the Be concentration profile is flat within the remainder of the damage zone, and beyond the end of range of the ions. Therefore, while Be atoms may segregate to microscopic sinks such as precipitates and dislocation loops, there is no measurable long range transport of Be from one depth interval to another.

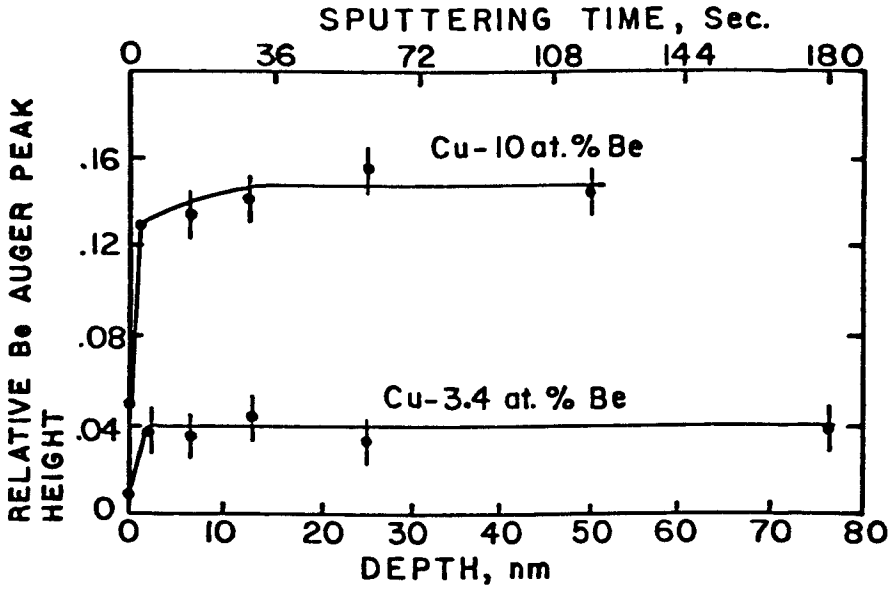

Figure VII. 46. Relative concentration vs. depth profiles of Be in two different Cu-Be alloys, demonstrating that preferential sputtering is insignificant. The alloys were solution annealed and quenched, then polished. The apparent deficiency of Be at the surface results from surface contamination.

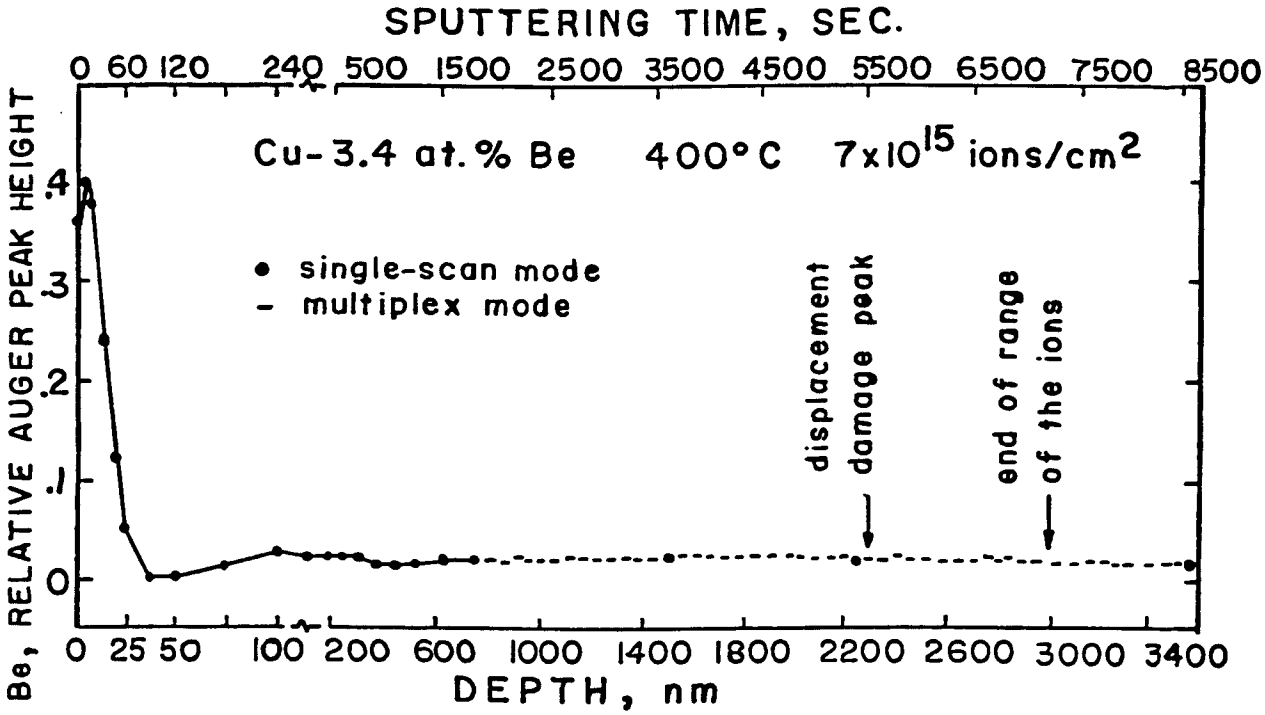

Figure VII. 47. Profile of the relative Be concentration through the depth of the entire damage zone in Cu-3.4 at.%Be irradiated at 400°C to 8.4 peak dpa. Surface segregation occurred as usual, otherwise no net Be redistribution was detected within or beyond the damage zone. (Note the break in the abscissa at 100 nm.)

References for Chapter VII

1. D. K. Brice, SAND 75-0622, Sandia National Laboratory, Albuquerque, NM, July 1977.

2. I. M. Torrens and M. T. Robinson, in Radiation Induced Voids in Metals, J. W. Corbett and L. C. Ianniello, eds., 739 (1972).

3. M. Hansen, Constitution of Binary Alloys, McGraw-Hill, London, 1958.

4. J. W. Edington, Electron Diffraction in the Electron Microscope, (Phillips Technical Library, 1974); P. B. Hirsch, A. Howie, R. B. Nicholson, D. W. Pashley, and M. J. Whelan, Electron Microscopy of This Crystals, (Butterworths, London, 1965); K. W. Andrews, D. J. Dyson, and S. R. Keown, Interpretation of Electron Diffraction Patterns, (Adam Hilger, Ltd., London, 1971).

5. R. J. Rioja and D. E. Laughlin, Acta Met. 28, 1301-1313 (1980).

6. W. Bonfield and B. C. Edwards, J. Mat. Sci. 9, 398-408 and 409-414 (1974).

7. P. Wilkes, Acta Met. 16, 153-158 (1968).

8. O. Johari and G. Thomas, The Stereographic Projection and Its Applications, Techniques of Metals Research, Volume II.A, (Interscience, New York, 1969).

9. T. Koshikawa and R. Shimizu, Phys. Letters 44A, No. 2, 112-114 (1973).

10. R. Buhl, W. K. Huber, and E. Löbach, Proc. 2nd Internl. Conf. on Solid Surfaces (1974), Japan J. Appl. Phys. Suppl. 2, Pt. 2, 807-810 (1974).

11. L. E. Davis, N. C. McDonald, P. W. Palmburg, G. E. Riach, and R. E. Weber, Handbook of Auger Electron Spectroscopy, Physical Electronic Industries, Eden Prairie, Minnesota, 1976.

12. M. Suleman and E. B. Pattinson, J. Physics F: Metal Physics 1, L24-L27 (1971); and 3, 497-504 (1973).

13. R. W. Knoll, P. Wilkes, and G. L. Kulcinski, "Solute Redistribution in Heavy-Ion Bombarded Copper Base Alloys," presented at Fall 1980 Cnference of the AIME, Radiation Phase Stability Session, Pittsburgh, PA, Oct. 1980.

14. T. E. Gallon, J. Phys. D: Applied Phys. 5, 822-832 (1972).

15. J. W. Coburn, J. Vac. Sci. Technol. 13, 1037-1044 (1976).

16. N. Q. Lam, G. K. Leaf, and H. Wiedersich, "Effects of Radiation-Induced Segregation and Preferential Sputtering on the Sputtering Rate of Alloys," presented at Fusion Reactor Materials Conference, Miami Beach, Florida, January 1979.

17. N. Q. Lam, P. R. Okamoto, and R. A. Johnson, J. Nucl. Mat. 78, 408-418 (1978).

CHAPTER VIII

RESULTS OF IRRADIATIONS OF Cu, Cu-1% Co, AND Cu-1% Fe

In this chapter, the results of irradiation experiments on Cu-1% Co and Cu-1% Fe alloys, and on high purity Cu are described. The irradiation parameters and methods of post-irradiation analysis pertaining to each specimen are given in Table VIII-1.

A. High Purity Copper

Six high purity Cu specimens were irradiated with 14 MeV Cu ions at temperatures of 400, 450, and 500°C. Following irradiation, the specimens were copper electroplated and were thinned in cross section for TEM analysis. The goal of this experiment was to study void formation in Cu along the path of the incident ions. Because of findings published by Glowinski et al.,[1] showing the importance of gas content on void formation in Cu, several specimens in this study were thoroughly outgassed before irradiation, while the remaining specimens were irradiated in the "nondegassed" condition. Initially, all specimens were annealed at 800°C and cooled to room temperature in an H_2 atmosphere, and were saturated with hydrogen. Specimens 1-4 were mounted in the target chamber in this condition, however specimens 5 and 6 were outgassed in the high vacuum furnace (2 hours at 600°C, 10^{-8} torr) before mounting. Because the specimens were irradiated and heated in the old (linear) specimen holder assembly, they experienced further annealing before irradiation (a minimum of 3 hours at 500°C) and after irradiation.

TABLE VIII.1. Irradiation Parameters and Post-Irradiation Analysis of Cu, Cu-Co, and Cu-Fe Samples.

	Material	Specimen Code Number	Pre-irradiation Heat Treatment (see code)	Irradiation Temperature °C	Nominal Dose, dpa @1μm	Nominal Fluence, 10^{16} ions/cm^2	Particle Flux, 10^{12} / cm^2 sec	TEM		Auger analysis
								back-thinned	cross sectional	
1	High Purity Cu	T50-00-1	A	500	2.1	0.75	4.5		x	
		T50-00-2	A	450	6.7	2.3	4.6		x	
		T50-00-3	A	450	2.3	0.80	4.4		x	
		T50-00-4	A	400	2.1	0.75	3.6		x	
		T50-00-5	B	450	2.1	0.75	4.1		x	
		T50-00-6	B	400	2.1	0.75	3.7		x	
3	Cu-1 at % Co	T55-00-1	C	475	4.6	1.6	2.5	x		x
		T55-00-2	C	475	0.92	0.32	2.6	x		x
		T55-00-3	D	475	4.6	1.6	2.8	x		
		T55-00-4	D	475	0.92	0.32	2.7		x	
		T55-00-5	C	400	4.6	1.6	2.8	x		
		T55-00-6	C	400	0.92	0.32	2.7		x	x
		T55-00-7	D	400	4.6	1.6	2.8	x		
		T55-00-8	D	400	0.92	0.32	2.9		x	
4	Cu-1 at % Fe	T56-00-1	E	500	3	1.1	4.7	x		x
		T56-00-2	F	500	3	1.1	3.2		x	x
		T56-00-3	E	450	3	1.1	3.5	x		
		T56-00-4	G	450	3	1.1	4.1	x		x
		T56-00-5	E	400	3	1.1	4.4		x	
		T56-00-6	F	400	3	1.1	4.3	x		x
		T56-00-7	E	350	3	1.1	4.9		x	
		T56-00-8	G	350	3	1.1	5.4		x	x

HEAT TREATMENT CODE:
(A) Annealed 1-1/2 hrs., 800°C, in H_2
(B) As in (A), also outgassed at 600°C, 10^{-8} torr.
(C) Solution annealed 1-1/2 hrs, 800°C in H_2; quenched.
(D) As in (C), also aged 48 hrs., 575°C.
(E) Solution annealed 840°C in H_2, quenched, aged 20 hrs., 680°C & 72 hrs., 600°C.
(F) Annealed, not aged.
(G) Furnace cooled 840→600°, quenched.

During examination in the transmission electron microscope, no voids were observed in any of the Cu specimens. Although one degassed specimen (T50-00-5) was lost due to poor adhesion of the Cu plating, there was no significant difference between the remaining degassed specimen and its nondegassed counterpart. At 500°C and 8×10^{15} ions/cm^2 (2 dpa at 1000 nm depth), there was no evidence of radiation damage within the range of the ions, see Fig. VIII-1(a). In the figure, the Cu plating interface runs vertically down the left side of the micrograph, and the entire ion range is shown. At 450°C, irradiation to fluences of 0.8 and 2.3×10^{16}/cm^2 produced dislocation tangles and loops in the depth range of ~ 1500 to 2800 nm, but there was little damage in the depth range of 0-1500 nm.

The microstructure of the nondegassed Cu irradiated at 400°C with 8×10^{15} ions/cm^2 is shown in cross section in Fig. VIII-1(b). Little damage is evident in the region between the surface and ~ 700 nm depth (0 to 1.7 dpa), but dislocation loops and tangles formed in the remainder of the damage zone. Close examination, however, revealed no voids in this region. The microstructure of the degassed specimen irradiated under the same conditions as the nondegassed specimen is shown in Fig. VIII-2. In the full-range view of the damage zone (left micrograph), a band of damage lies parallel to the interface, within the depth interval of ~ 2000-2800 nm (the nominal dose varies from 4.5 dpa at 1800 nm to 9 dpa at 2300 nm). Between depths of 100 to 900 nm there are scattered dislocation loops, and beyond 2800 nm the damage ends abruptly. The enlarged micrograph in

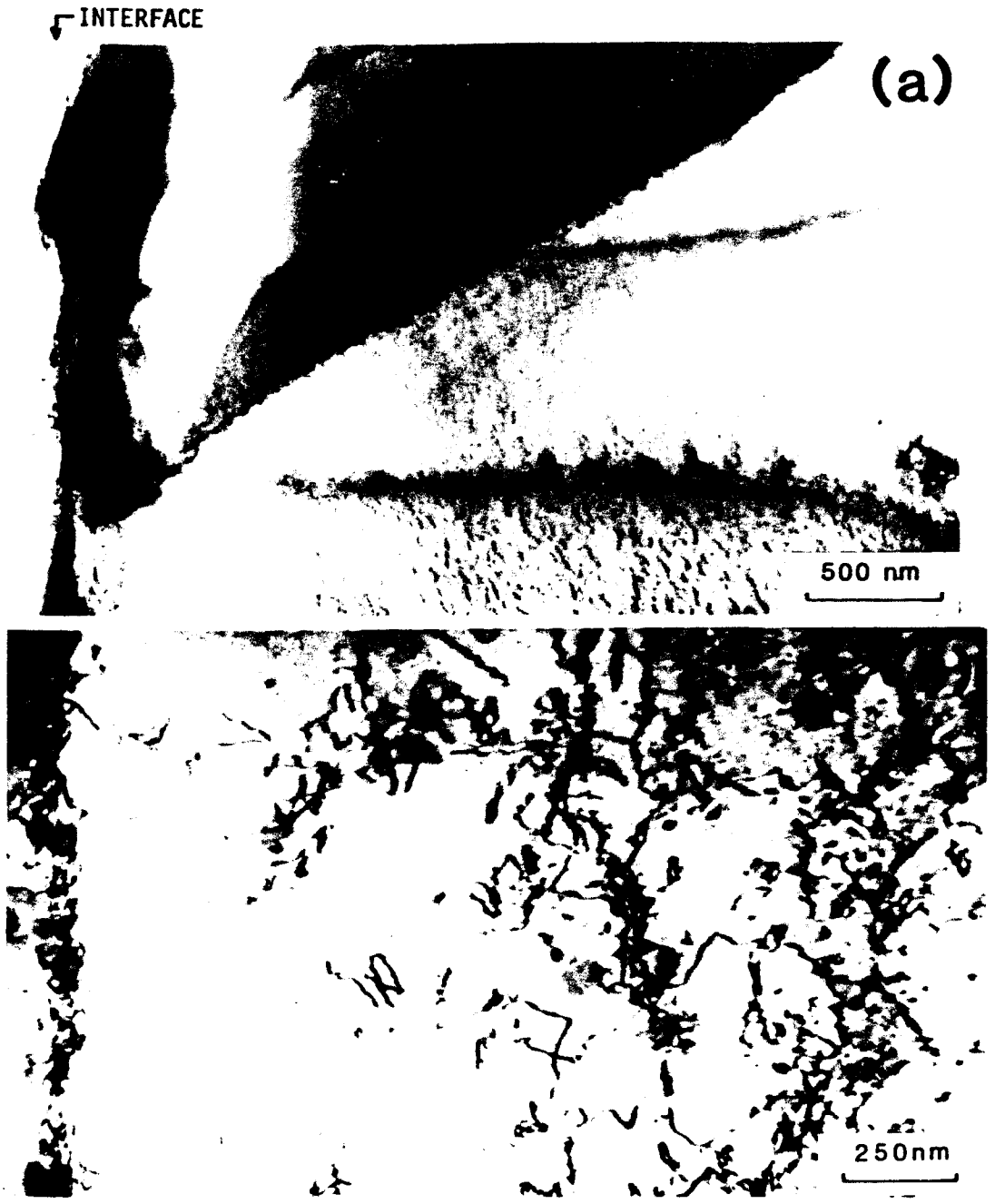

Figure VIII.1. High purity Cu specimens irradiated with 7.5×10^{15} ions/cm^2 (2 dpa @ 1000nm depth) and thinned in cross section. (a) Irradiated at 500°C. No damage is evident. (b) Irradiated at 400°C. Front 3/4 of the damage zone is shown here.

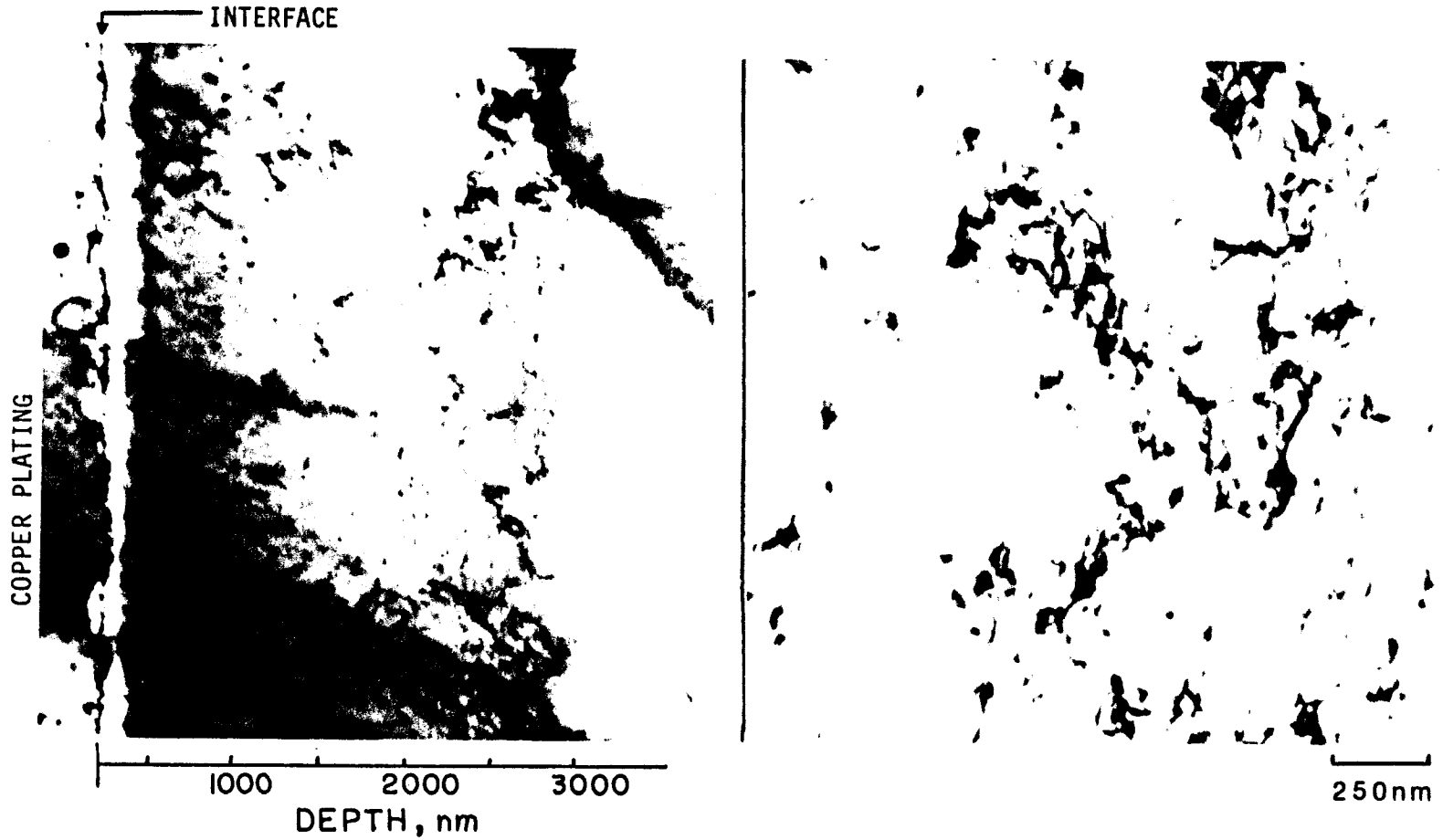

Figure VIII.2. Degassed Cu, irradiated at 400°C with 7.5×10^{15} ions/cm^2 and thinned in cross section. The microstructure of the entire damage zone and beyond is shown at left. At right is an enlarged micrograph of the peak damage region.

Fig. VIII-2 shows that the damage band consists of dislocation tangles, and dislocation loops approximately 30 nm in diameter.

B. Cu-1% Co

The effects of 14 MeV Cu-ion irradiation on the phase stability of the Cu-1% Co alloy at 400°C and 475°C were surveyed by irradiating a set of eight specimens (Table VIII-1). The specimens were divided into two groups with respect to their pre-irradiation heat treatment. Four of the specimens were solution annealed at 800°C in an H_2 atmosphere, then were quenched into H_2O. At the irradiation temperatures of 400°C and 475°C, these specimens were highly supersaturated solid solutions. The remaining specimens were similarly solution annealed and quenched, then were aged in the UHV furnace at 575°C for 48 hours to produce a uniform distribution of Co precipitates. As with the high purity Cu specimens, all Cu-Co specimens were irradiated in the linear specimen holder and were subjected to some pre-irradiation and post-irradiation heating. Specific goals of this experiment were to determine:

(a) whether irradiation enhanced the decomposition of the supersaturated solid solution;

(b) whether the size, distribution, or structure of the Co precipitates were altered by irradiation; and,

(c) whether radiation-induced solute segregation occurred near the irradiated surface of the specimen.

The precipitates that were produced during aging of the Cu-1% Co alloy at 575°C were typical of those observed in previous aging

experiments on dilute Cu-Co alloys[2-7]; i.e. spherical, coherent precipitates which nucleate homogeneously throughout the matrix.[7] According to the equilibrium phase diagram of the Cu-Co system[8], the composition of the precipitate is 90% Co and 10% Cu. In the transmission electron microscope, the strain contrast of the spherical coherent precipitate produces an elliptical image, split by a line of no contrast that is perpendicular to the reciprocal lattice vector of the diffracting planes[2] (see Fig. VIII-6(c)). The true diameter of the particle is approximately equal to the dimension of the minor axis of the elliptical image.[4] The mean diameter of the particles in the aged Cu-1% Co used in this experiment was ~ 22 nm, and the particle number density was ~ $10^{15}/cm^3$, yielding a precipitate volume fraction of about 0.0056.

Transmission electron micrographs of Cu-1% Co specimens irradiated in the as-quenched condition are shown in Figs. VIII-3, VIII-4, and VIII-5. There was a significant difference between specimens irradiated at the same temperature but at different doses. Irradiation at 475°C to a dose of 5 dpa produced scattered line dislocations and dislocation loops as well as a high density of small blackspots, as shown in Fig. VIII-3(a) and (b). An enlarged dark field micrograph of these spots, or particles, is shown in Fig. VIII-4. Most of the spots are smaller than 8 nm, so their structure cannot be resolved. No extra reflections were observed on electron diffraction patterns from the specimen, indicating that the crystal structure (if any) of these featrues is the same as that of the

Cu-1% Co Solution Treated and Quenched

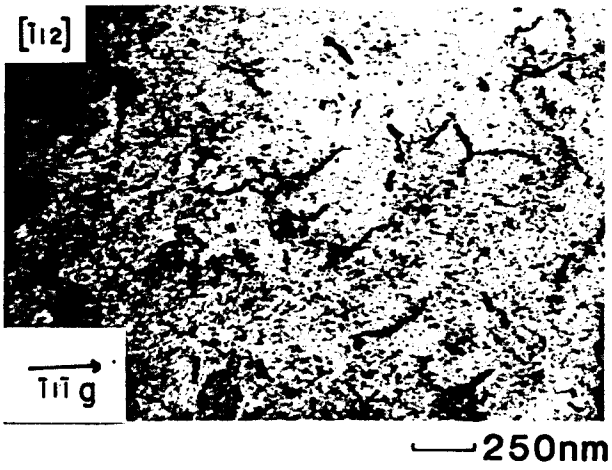

a)Irradiated to 5 dpa at 475°C

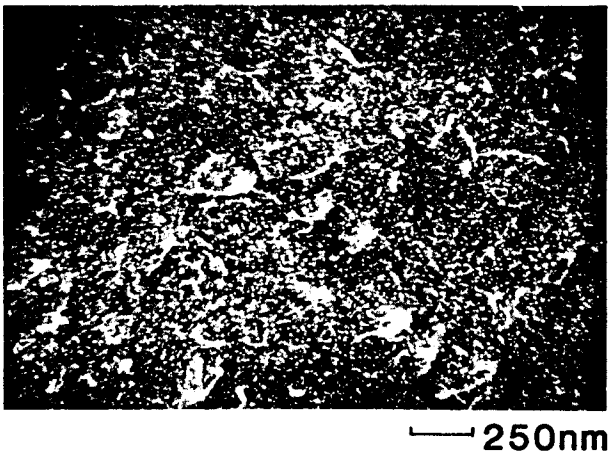

b)As above, dark field using matrix reflection

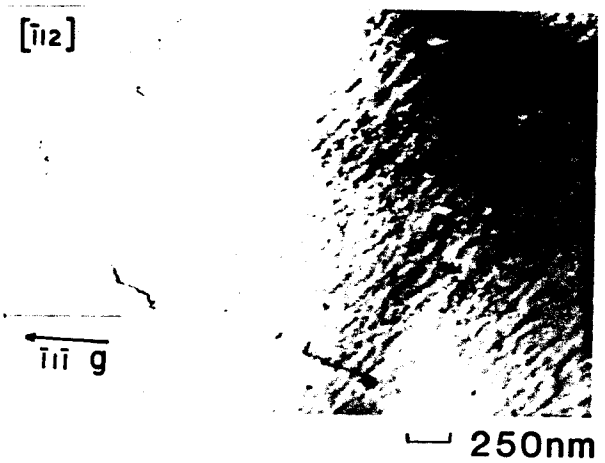

c)Non-irradiated (bright field)

Figure VIII.3.

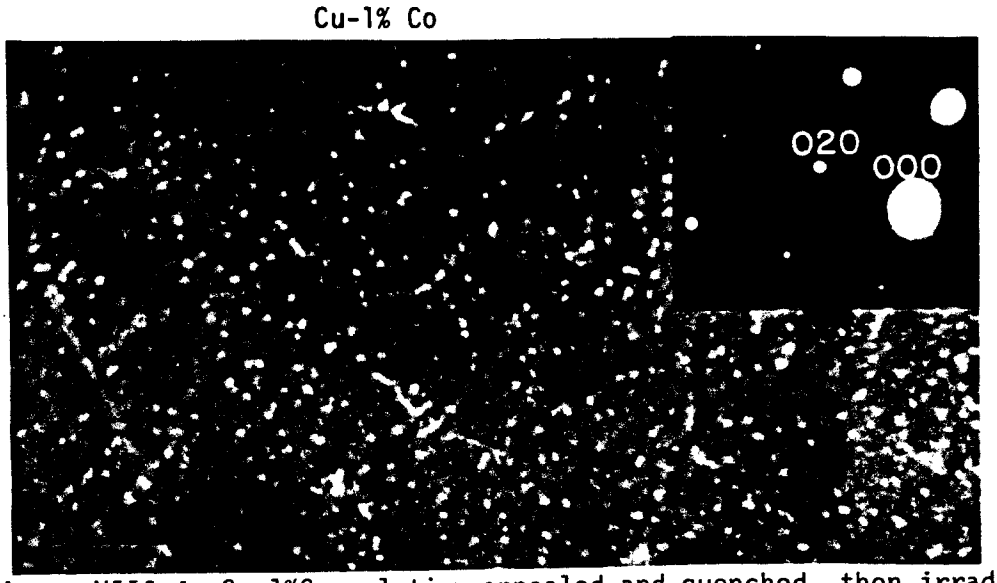

Figure VIII.4. Cu-1%Co solution annealed and quenched, then irradiated at 475°C to 5 dpa. Dark field image using (002) matrix reflection.

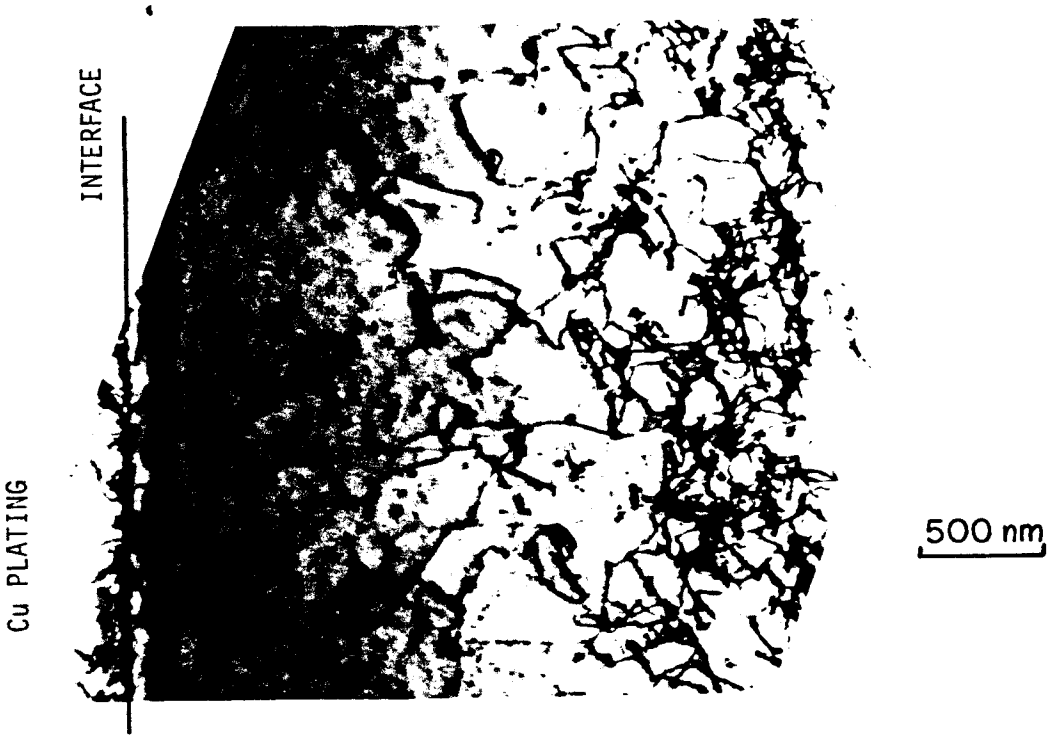

Figure VIII. 5. Cu-1%Co alloy irradiated at 400°C with 3.2×10^{15} ions/cm^2, thinned in cross section. The alloy was solution annealed and quenched prior to irradiation.

matrix. Close examination of the largest spots in Fig. VIII-4 reveals a line of no contrast through the center of the images, indicating they are small coherent spherical precipitates, or dislocation loops, that formed during irradiation. Blackspot images of this type were not observed in unirradiated regions of this same specimen (Fig. VIII-3(c)), therefore the spots are not due solely to thermal aging. The microstructure of the specimen irradiated at 400°C and 5 dpa was very similar to that of the 475°C specimen. No radiation-induced voids were observed in either of these specimens.

In the as-quenched specimens irradiated at 475°C and 400°C, but to a dose of only 0.9 dpa at 1000 nm, no blackspot damage was observed. The 475°C specimen (backthinned) contained scattered dislocation loops and line dislocations, but no other radiation effects. The 400°C specimen was thinned in cross section after irradiation and is shown in Fig. VIII-5. (100 nm was removed from the surface before electropolishing.) The damage structure of this specimen is similar to that of high purity Cu irradiated at 400°C. In the depth interval of 100 ~ 900 nm, where the dose ranges from 0.3 to 0.8 dpa, there are no defects except scattered line dislocations. At depths between 900 ~ 2000 nm (0.8-2.8 dpa) the line dislocation density increases to approximately $3 \times 10^9/cm^2$. The highest density of defects lies in the depth range of 2000 ~ 2900 nm, and consists of dislocation loops and line dislocations tangles at a density of about $4 \times 10^{10}/cm^2$. No voids or blackspots are found within this region, which received a maximum dose of about 4 dpa. A comparison can be made between the

depth of the observed damage peak in this specimen, and the depth of the calculated damage peak (Fig. VII-1). If the observed damage peak is assumed to lie at the center of the dislocation band (at ~ 2500 nm) in Fig. VIII-5, then the depth of the observed damage peak is slightly greater (~ 9%) than the depth of the calculated damage peak.

TEM micrographs of aged Cu-1% Co specimens irradiated at 400°C and 475°C, and backthinned to a depth of about 1000 nm (5 dpa), are shown in Figs. VIII-6 and VIII-7. Also presented in each figure is a micrograph of a typical unirradiated region from each specimen. The principal effect of irradiation was to transform most of the coherent precipitates to semi-coherent or incoherent structures. Dislocations produced by irradiation are entwined with the precipitates. No voids or prismatic dislocation loops are present. Examination of Fig. VIII-7(a) shows that after irradiation, most of the precipitate images contain several parallel lines of no contrast. This change in the strain contrast of the precipitate has been associated with a loss of coherency between the precipitate and matrix planes, due to the formation of dislocations at the precipitate/matrix interface.[2,5] The only difference between specimens irradiated at 400°C and 475°C was a higher dislocation density in the 400°C specimens. Irradiation did not significantly alter the precipitate size distribution or number density. Note that most of the small dark spots (10-20 nm in diameter) present in the micrograph of the 475°C specimen are surface defects or contamination resulting from electropolishing, and are not radiation effects. Unlike the blackspot

Cu-1%Co Aged at 575 °C for 48 Hrs.

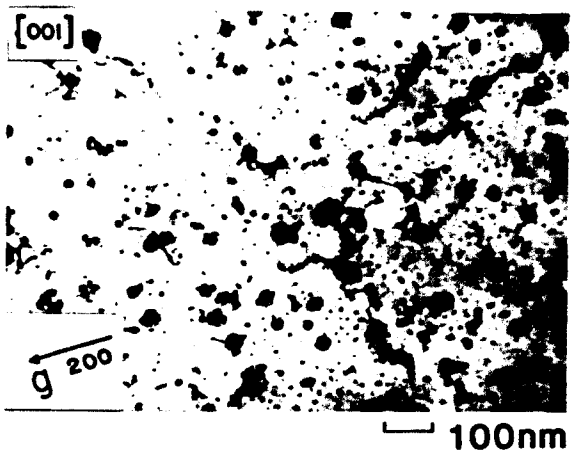

a)Irradiated to 5 dpa at 475°C

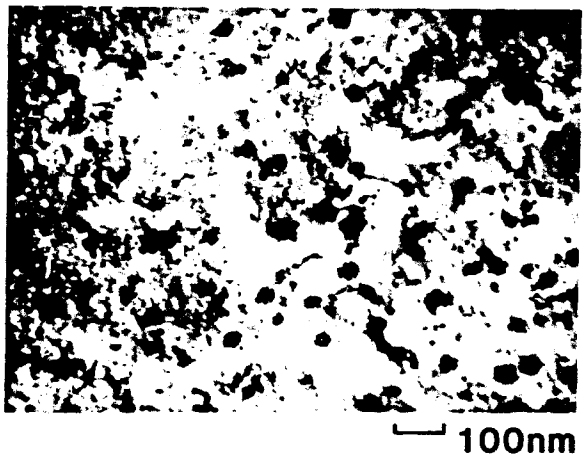

b)As above, dark field using matrix reflection

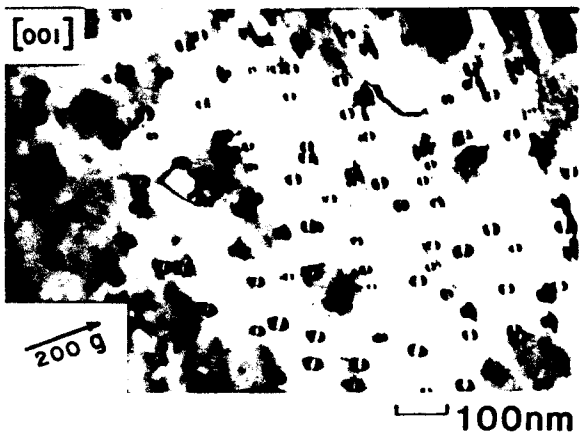

c)Non-irradiated (bright field)

Figure VIII.6.

Cu-1% Co Aged at 575°C for 48 Hrs.

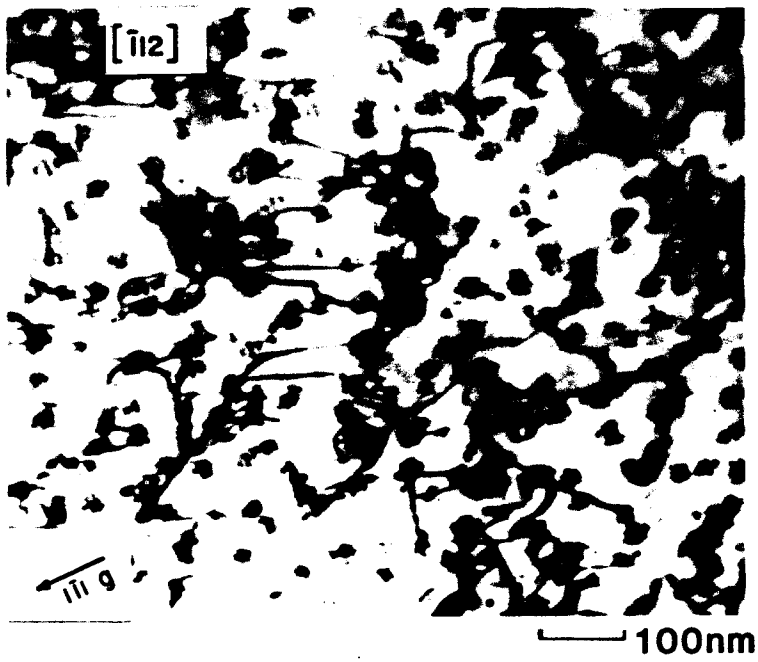

a) Irradiated to 5 dpa at 400°C

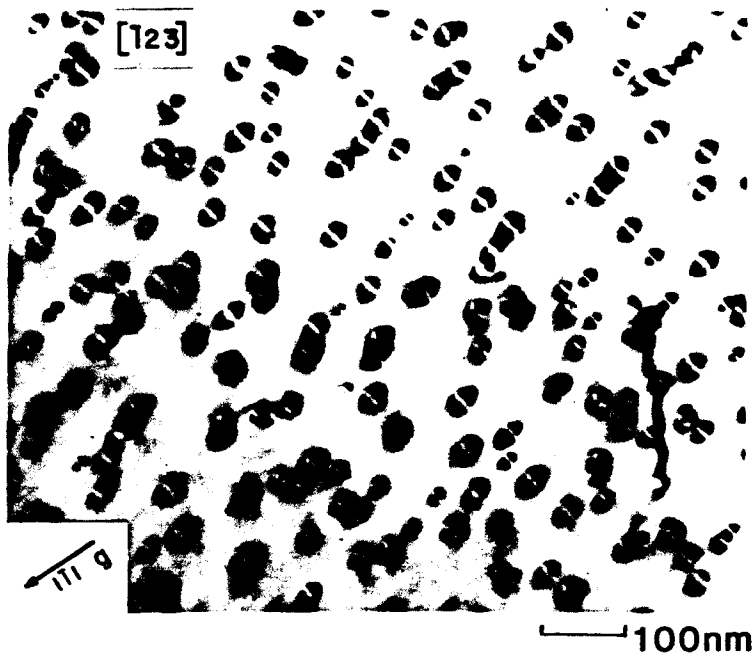

b) Non-irradiated

Figure VIII.7.

damage in the irradiated, as-quenched specimens, most of these spots do not exhibit diffraction contrast.

A full-range cross sectional view of the damage zone of aged Cu-1% Co, irradiated at 400°C with 3.2 x 10^{15} ions/cm^2, is shown in Fig. VIII-8. Enlarged micrographs detailing the microstructure at 4 different depths within and beyond the damage zone are shown below the full range micrograph. Precipitates have lost coherency even in the low dose region (~ 0.2 dpa) near the plating/alloy interface. Between depths of about 900 ~ 2800 nm, dislocation loops are associated with many of the incoherent precipitates. An interesting observation in this specimen is that precipitates in the depth range of ~ 3400-4300 nm have also lost coherency, even though the region is well beyond the calculated end-of-range of the incident ions (which occurs at ~ 3000 nm). Beyond a depth of about 4400 nm, all particles are coherent, as shown in the lower right micrograph of Fig. VIII-8.

The solute concentration near the irradiated surface of three Cu-1% Co specimens was profiled using Auger electron spectroscopy combined with sputter etching (as in section VII.B) to determine whether surface segregation of the Co solute occurred during irradiation. The results of measurements in low dose specimens irradiated at 400°C and 475°C, and in a high dose 475°C specimen, are shown in Fig. VIII-9. Data were obtained by recording the Auger spectrum with the sputter-ion beam off. In each profile, the relative Co concentration is represented by the ratio of the amplitudes of the 656 eV Co Auger peak to the 920 eV Cu peak. Larger Co peaks at 716 eV and

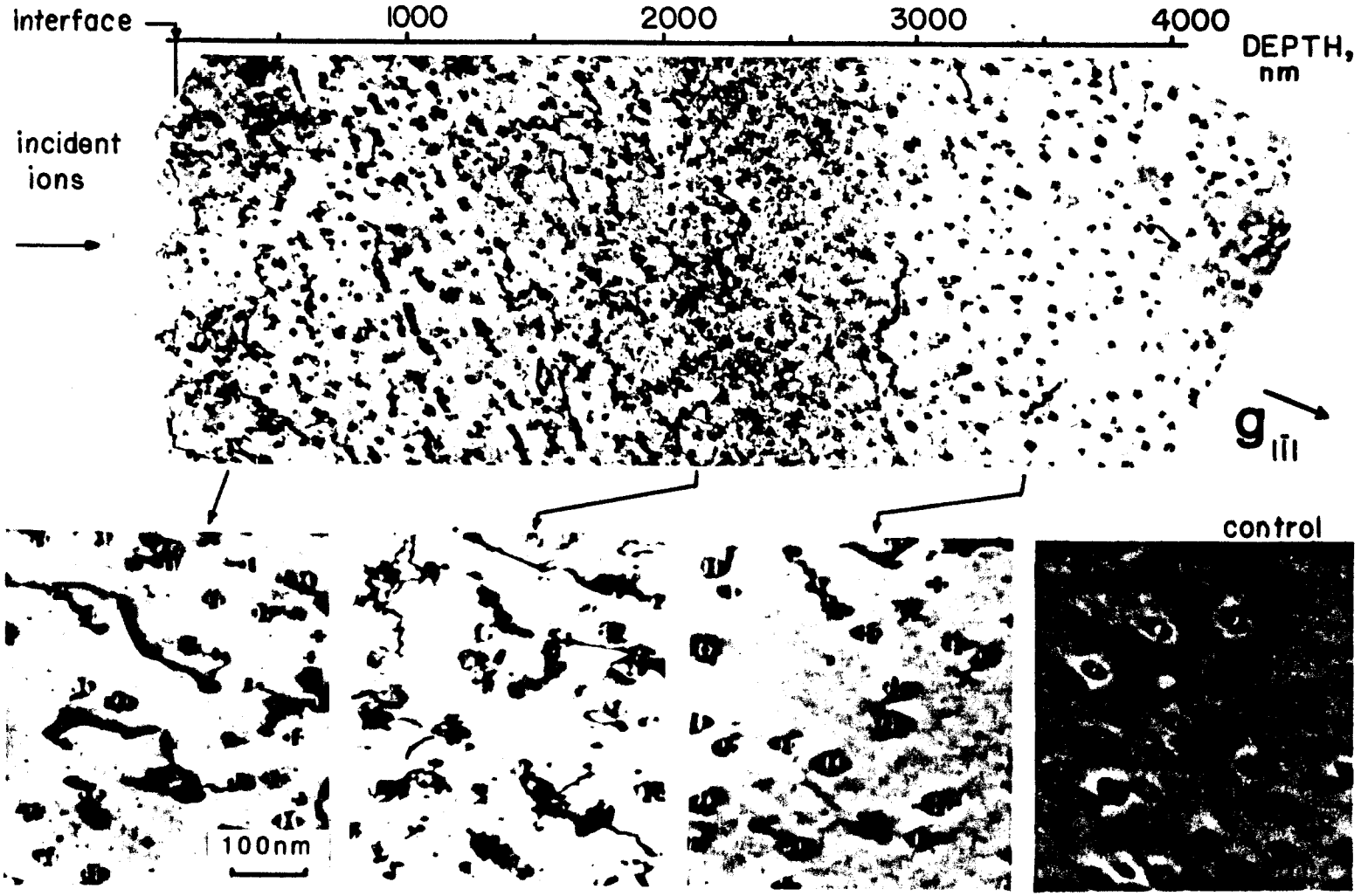

Figure VIII.8. Cu-1%Co alloy irradiated at 400°C with 3.2×10^{15} ions/cm^2, thinned in cross section. The alloy was aged 48 hrs. at 575°C prior to irradiation, to produce spherical coherent precipitates. Crystallographic zone axis is close to [112].

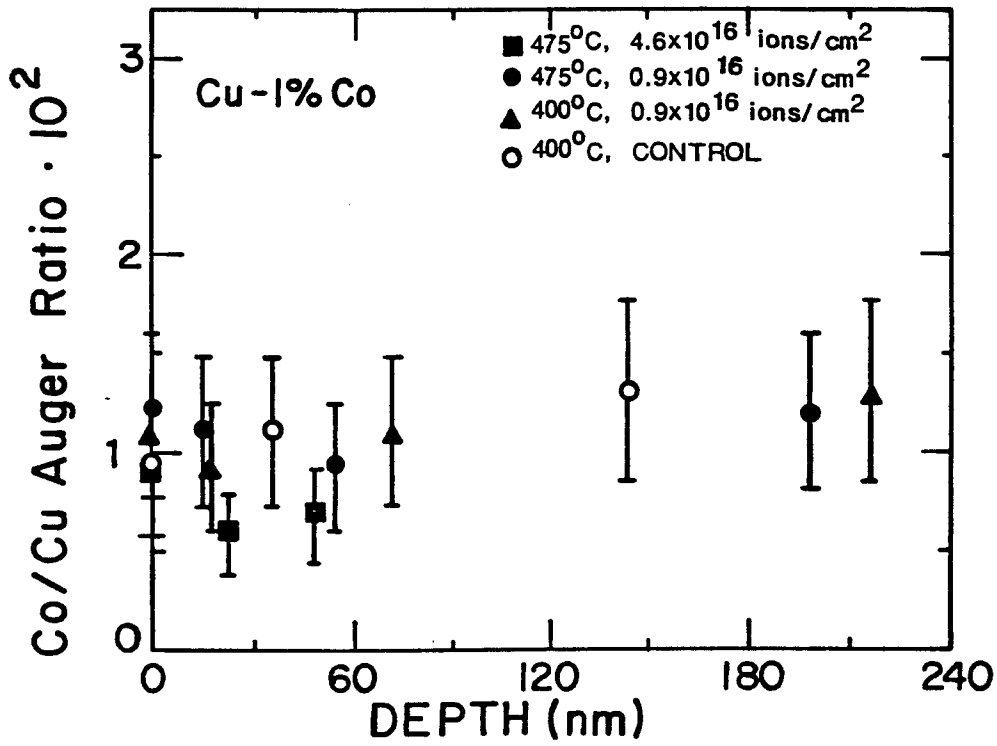

Figure 9. Relative concentration vs. depth profiles of Co in Cu-1% Co irradiated at 475°C (1.2 and .25 surface dpa) and 400°C (0.25 surface dpa), generated from AES data.

775 eV could not be used because of interference with Cu peaks near these energies. There was considerable measurement uncertainty (±30%), because the low Co concentration yielded a poor signal-to-noise ratio. Fig. VIII-9 shows, however, that no measurable radiation-induced Co segregation occured in these specimens.

C. Cu-1% Fe

The design of this experiment was similar to the design of the Cu-Co irradiation experiment. Specimens were irradiated at 350°C to 500°C to a fluence of $1.1 \times 10^{16}/cm^2$ (see Table VIII-1). Two of the specimens were irradiated in the solution annealed and quenched condition. Two specimens were solution treated, then were aged by slow cooling within the furnace to 600°C, followed by quenching. These specimens contained two types of continuous precipitation: blocky, incoherent Fe particles, ~ 160 nm in size, at a density of $\sim 2 \times 10^{12}/cm^3$; and, spherical, coherent Fe precipitates ~ 20 nm in diameter, at a density of $6 \times 10^{14}/cm^3$. The remaining four specimens were solution annealed, quenched, and aged (72 hours at 600°C and 20 hours at 680°C) to produce a uniform distribution of coherent spherical Fe precipitates ~ 33 nm in diameter, at a density of $2 \times 10^{14}/cm^3$. Grain boundary precipitates also formed in the aged specimens.

Examples of the irradiated microstructure of Cu-1% Fe specimens are shown in Figs. VIII-10, VIII-11, and VIII-12. The damage structure in the Cu-Fe is similar to that in the Cu-Co alloy. In one Cu-Fe specimen, however, radiation induced voids were observed. This

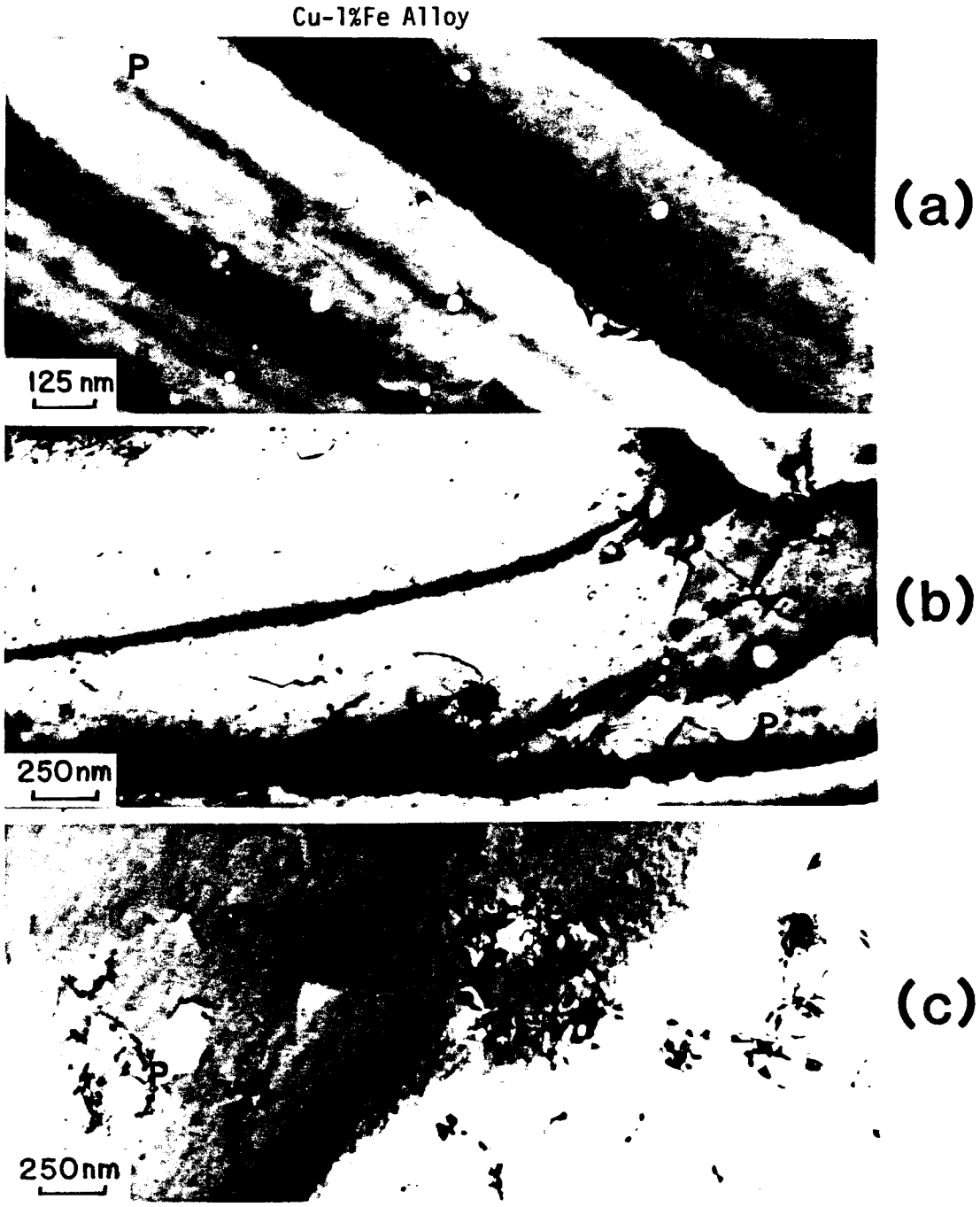

Figure VIII.10. (a) and (b): Cu-1%Fe alloy solution annealed, then irradiated at 400°C with 10^{16} ions/cm^2. Voids approximately 30 nm in diameter are produced by irradiation. Larger holes ~ 120 nm in diameter (labeled "P"), seen also in unirradiated foil (c), are from Fe precipitates that have electropolished from the foil.

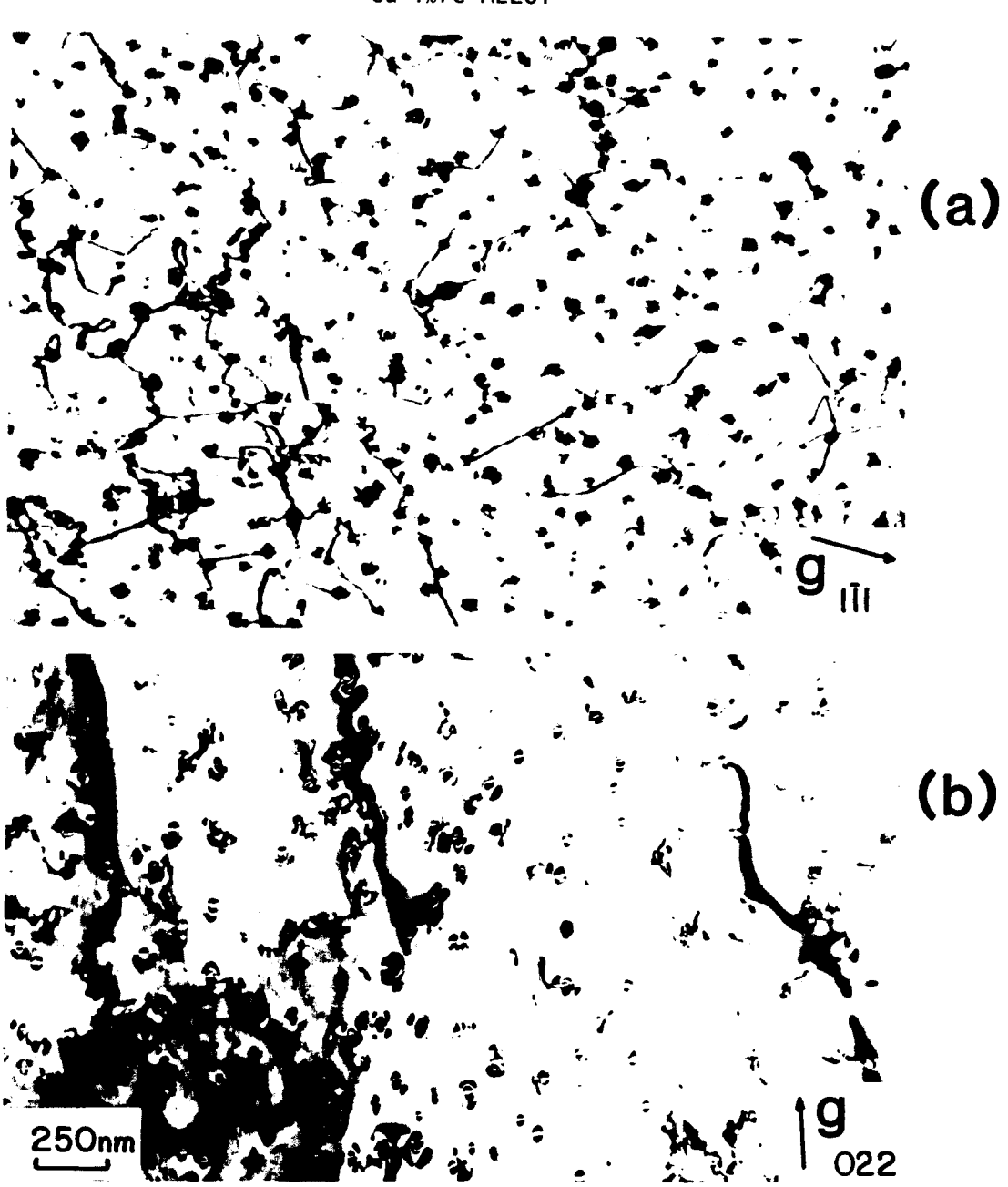

Figure VIII.11. (a) Incoherent precipitates in Cu-1%Fe alloy irradiated at 450°C to a dose of 3 dpa. (b) An unirradiated region from same specimen, where the precipitates remain coherent. Specimen was aged before irradiation to produce spherical coherent precipitates.

specimen, shown in Fig. VIII-10, was irradiated at 400°C in the as-quenched condition, and was backthinned such that the dose in the region examined by TEM was 3 dpa. The mean void size was 30 nm, at a density of 4 x $10^{13}/cm^3$, corresponding to a swelling of 0.06%. In micrographs (b) and (c) of the same figure, several large holes (~ 140 nm) are seen in both the irradiated and unirradiated specimens, which were left by incoherent Fe precipitates that fell from the thin foil during electropolishing. Because small Fe precipitates also tended to fall or dissolve out of thin foil, stereographic analysis was performed on this specimen to assure that the small holes were radiation-induced voids, and not surface holes left by fallen precipitates. The analysis showed that the voids are distributed throughout the foil volume, and therefore are an effect of irradiation.

Figure VIII-11 compares the irradiated and unirradiated microstructures of aged Cu-1% Fe that was backthinned to 1000 nm. The irradiation temperature was 450°C. Precipitates in the irradiated foil have lost coherency, and are often looped or interconnected by dislocations. The number density and size of the precipitates were not measurably altered by irradiation. An aged Cu-1% Fe specimen irradiated at 350°C and thinned in cross section is shown in Fig. VIII-12. The variation of the microstructure with depth in this specimen is very similar to that in the Cu-Co specimen shown in Fig. VIII-8. All precipitates within the ion-range, as well as precipitates located up to 500 nm beyond the calculated end of range have

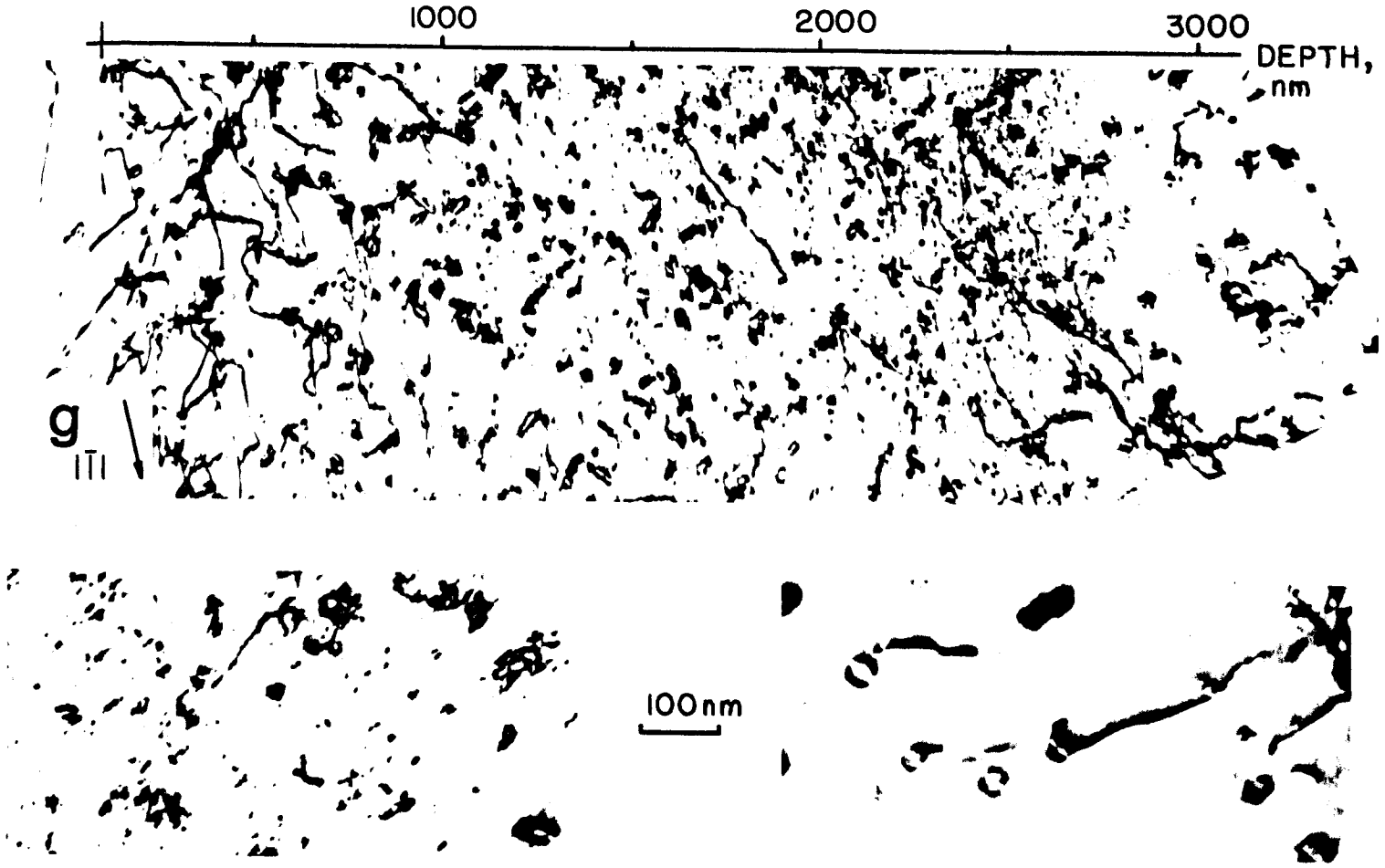

Figure VIII.12. Damage structure in Cu-1%Fe irradiated at 350°C with 10^{16} ions/cm^2, and thinned in cross section. At bottom left is an enlarged view of the peak damage microstructure. At right is an unirradiated section of the alloy, where the particles remain coherent. Some particles fell from the thin foil during electropolishing, leaving holes. Zone axis is near [112].

lost coherency. Line dislocations and loops ranging in size to 100 nm have formed throughout the damage zone. At depths of 1800 ~ 2800 nm (6 dpa to 12 dpa maximum) the foil is filled with dark spots smaller than 8 nm, whose structure cannot be resolved. These spots are seen more easily in the enlarged micrograph from the peak-damage region in the same figure. Whether these spots are defect clusters or tiny Fe precipitates could not be determined. Void formation was not observed in any of the aged Cu-1% Fe specimens.

Alloy composition vs. depth profiles near the irradiated surface of several Cu-1% Fe samples were measured using AES combined with sputtering (Figs. VIII-13 and VIII-14). The relative Fe concentration is represented by the ratio of the amplitudes of the Fe-651 eV/Cu-920 eV Auger peaks. As with the Cu-Co samples, there was a large measurement uncertainty due to the poor signal-to-noise ratio. In specimens irradiated at 350°C and 400°C (Fig. VIII-13), no measurable segregation of the Fe solute is evident. However, in a specimen irradiated at 450°C (#T-56-00-3), the apparent Fe concentration is depleted near the irradiated surface. Measurements in both of the 500°C specimens (Fig. VIII-14) exhibit the same behavior. However, in unirradiated areas of these specimens the Fe concentration is also depleted within ~ 100 nm of the surface, so the Fe depletion cannot be attributed to irradiation. A possible cause of the Fe depletion is preferential sputtering of Cu atoms, resulting in an apparent enrichment of Fe with depth. Alternatively, the near-surface region may have become enriched in Cu and depleted of Fe during heating in

the target chamber. Thermodynamic calculations have predicted, for example, that the free surface of a Fe-Cu solid solution should be enriched in Cu and depleted of Fe.[9]

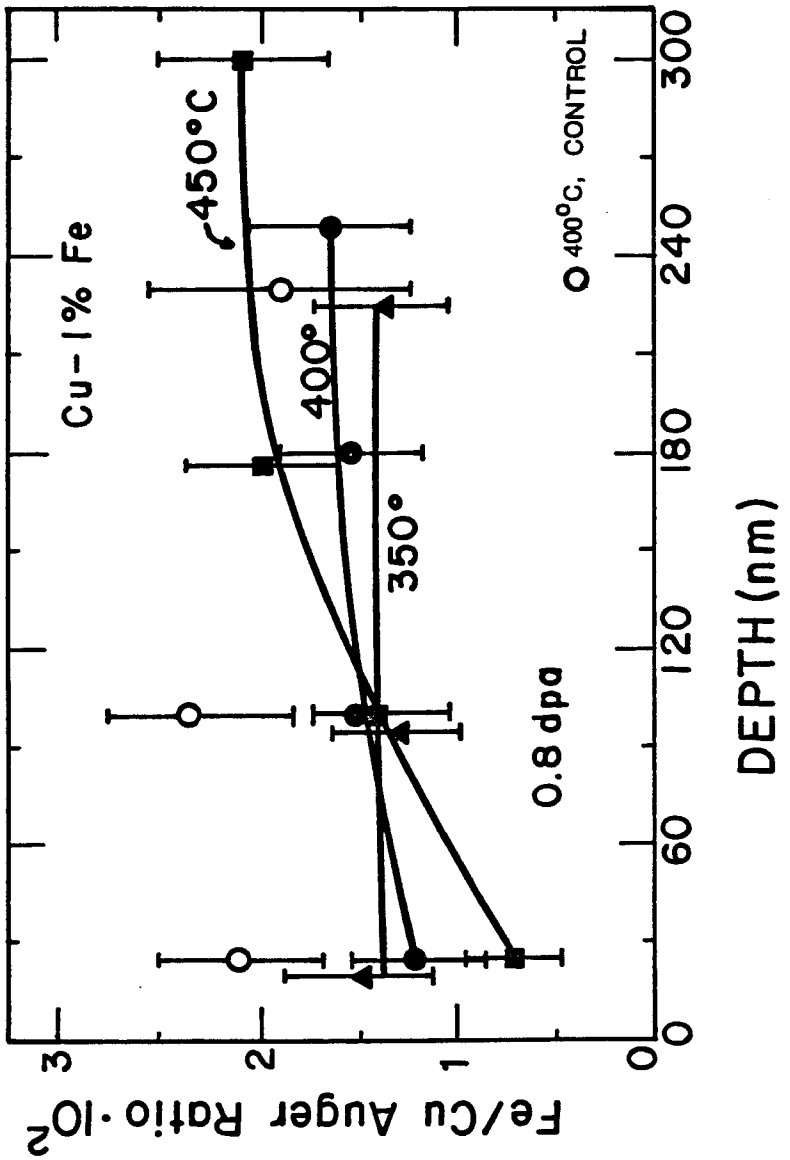

Figure VIII. 13. Relative concentration vs. depth profiles of Fe near the surfaces of Cu-1% Fe specimens irradiated at 350, 400 and 450°C. The profiles were generated from Auger electron spectroscopy data.

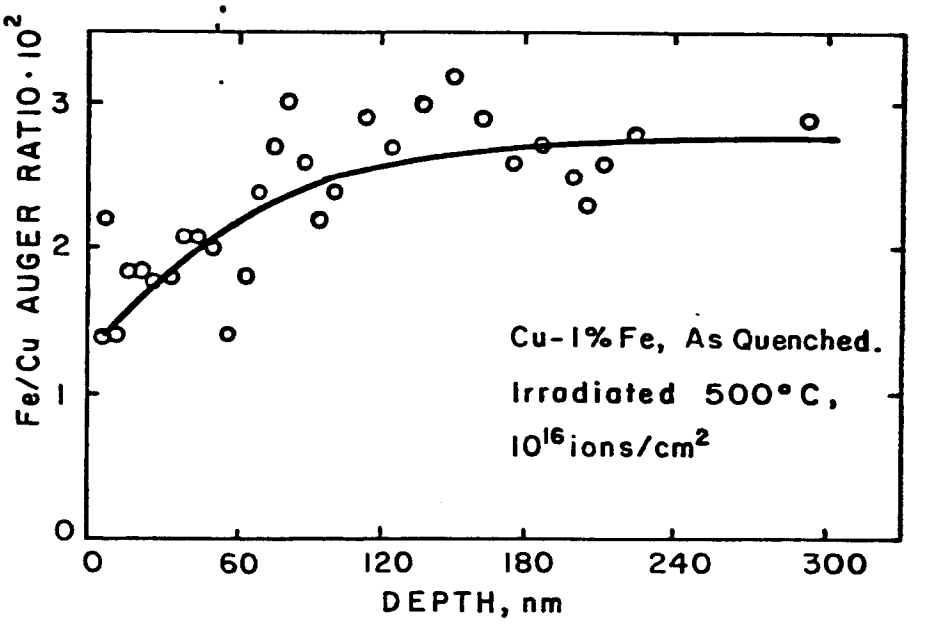

(a)

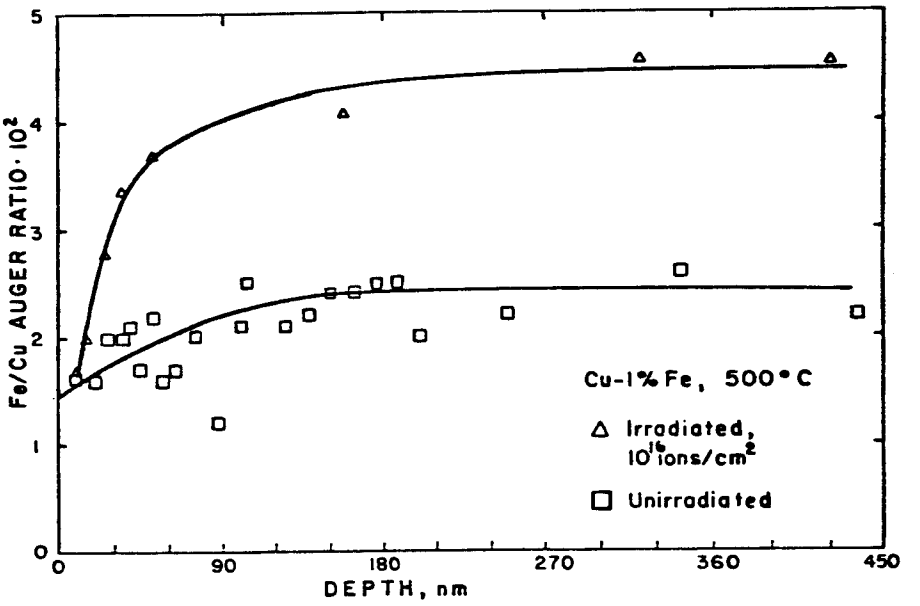

(b)

Figure VIII.14. Relative concentration vs. depth profiles of Fe in the Cu-1% Fe alloy irradiated at 500°C, to a dose of 1 dpa at the surface. (a) Concentration profile near the irradiated surface of an as-quenched specimen. (b) Near irradiated and unirradiated surfaces of an aged specimen.

References for Chapter VIII

1. L. D. Glowinski and C. Fiche, J. Nucl. Mat. 61, 22-28 and 29-40 (1976).

2. V. A. Phillips and J. D. Livingston, Phil. Mag. 7, 969 (1962).

3. M. F. Ashby and L. M. Brown, Phil. Mag. 8, No. 91, 1083 (1963).

4. V. A. Phillips, Trans. AIME 230, 967-976 (1964).

5. V. A. Phillips, Acta Met. 14, 271-278 (1966).

6. L. E. Tanner and I. Servi, Acta Met. 14, 231-234 (1966).

7. I. S. Servi and D. Turnbull, Acta Met. 14, 161 (1966).

8. M. Hansen, Constitution of Binary Alloys, McGraw-Hill, London, 1958.

9. J. L. Meijering, Acta Met. 14, 251-258 (1966).

CHAPTER IX

DISCUSSION AND INTERPRETATION OF RESULTS

A. Precipitation in the Cu-3.4 at% Be Alloy

In Chapter VII, the dependence of the CuBe precipitate morphology on the irradiation temperature, cumulative displacement damage level, displacement rate, and depth into the damage zone of the Cu-3.4 at% Be specimens were described. Qualitative comparison of the results of the irradiation experiments and the thermal-aging experiments demonstrated that under heavy-ion irradiation, the precipitation kinetics were greatly enhanced, and the precipitate morphology was quite different compared to that produced by thermal aging. Among the many previous investigations of alloy phase stability under irradiation (for example, Refs. 1-3), relatively few studies have systematically characterized the precipitate morphology as a function of irradiation parameters. However, a number of studies have dealt with radiation-induced precipitation[4-9] or segregation[12-26] of undersize solute elements. In several of these studies[4-11], radiation-induced precipitation in undersaturated solid solutions has been investigated. In this section, discussion of the data presented in Chapter VII will center on: a) determination of the mechanism(s) responsible for the radiation-induced nucleation and growth of the CuBe precipitates; b) interpretation of the nucleation and growth characteristics in terms of theory; and c) comparison of these characteristics with the results of previous studies. To aid in this discussion, the principal results of the

irradiation experiments on the Cu-3.4 at% Be alloy are summarized below:

(a) During irradiation at 300-400°C, the supersaturated Cu-3.4 at% Be solid solution decomposed into a mixture of α_{Cu} solid solution and continuously distributed CuBe precipitate platelets, even at very low damage doses (~ 0.1 dpa).

(b) The continuous CuBe precipitation was irradiation-stable but not thermally-stable. Post-irradiation annealing of several specimens at a temperature within the two-phase region on the Cu-Be equilibrium phase diagram (400°C), caused dissolution of the continuous, radiation-induced precipitation. However, some discontinuous clusters containing large CuBe platelets were observed in these specimens after the anneal.

(c) Precipitation in the supersaturated Cu-3.4 at% Be solid solution was very sluggish during thermal aging at 300-400°C, in the absence of irradiation. However, prolonged thermal aging produced discontinuous precipitation of large CuBe platelets, at grain boundaries and in clusters within the grains. The matrix between these clusters was completely free of precipitates.

(d) Irradiation of the undersaturated Cu-3.4 at% Be solid solution at temperatures above ~ 420°C also produced continuous CuBe precipitation, although the damage dose required to nucleate precipitates increased with temperature. No precipitates formed at 525°C even at high dose.

(e) In general, the structure of the radiation-induced CuBe precipitates was the same (ordered bcc, with a_o = 0.27nm) as the structure of the equilibrium γ or the mature γ' precipitate[27], which form during thermal aging of concentrated Cu-Be alloys (e.g., Cu-13 at% Be). The habit plane and spatial distribution of the radiation-induced precipitates were also similar to that of the γ' precipitates found in the more-concentrated Cu-Be alloys.

(f) The size (maximum radial dimension, and thickness) of the precipitate platelets increased with irradiation temperature (in the range of 300-475°C), while the precipitate number density decreased exponentially with temperature.

(g) The precipitate size and number density depended on damage dose and dose-rate as follows: At 350°C and presumably at 300°C, the precipitate distribution coarsened with increasing dose. At higher temperatures, preciptiate size and volume fraction increased with dose. Irradiation at a higher displacement rate produced a finer precipitate-size distribution.

(h) The precipitate-size distributions were skewed, with a tail toward larger particle sizes.

(i) In cross sectioned specimens, within the depth range of 500 ~ 2700 nm, the depth dependence of mean precipitate size and number density was rather mild, considering that damage dose and dose-rate varied by a factor of ~ 6 within this region. Near

the surface and the end-of-range, a coarser precipitate size distribution existed.

(j) Substantial Be enrichment was detected near the irradiated surface of each specimen, relative to unirradiated surfaces. The Be enrichment increased strongly with irradiation temperature and increased weakly with damage dose (or irradiation time). This near-surface Be was oxidized, and in fact a BeO film existed on the irradiated surface. At internal sinks, there was no evidence of Be segregation at grain boundaries, nor was there evidence that Be was transported out of the peak damage region, which might be expected according to solute segregation theory.

A.1 Precipitate Nucleation and Growth

The data presented in Chapter VII does not reveal with certainty the mechanism responsible for the nucleation and growth of the CuBe precipitates during irradiation of the Cu-3.4 at% Be alloy. However, we can speculate on the precipitation mechanism by considering current theory, and by comparing the results of this experiment with the results of previous experiments. In view of points (a)-(d) provided in the above summary, the precipitation mechanism must account for the (spatially) continuous nucleation of the CuBe platelets and for their subsequent growth, in both the supersaturated and undersaturated solid solutions. Because of the nonequilibrium nature of the continuous precipitation, the decomposition of the solid solution during irradiation must have been radiation-induced rather than just

radiation-enhanced. If the precipitation kinetics had only been accelerated by irradiation (through an enhanced diffusion mechanism), then an equilibrium precipitate morphology should have formed, and the undersaturated solid solution would not have decomposed.[28]

A.1.a. Precipitate Nucleation

Nucleation Rate

Some characteristics of the precipitate nucleation rate, as a function of temperature, time (dose), and displacement rate, can be extracted from the data presented in sections VII-1 and VII-2. The plot of precipitate number density vs. displacement damage at 400-430°C in Fig. VII-20 shows that the precipitate density did not increase after a displacement damage level of 0.25 dpa was attained. In fact, examination of Fig. VII-17 indicates that the precipitate number density saturated at a damage dose less than 0.15 dpa. At temperatures below 400°C, there is less data on the dose dependence of the precipitate number density. However, Figs. VII-13, VII-15, and VII-20 suggest that at temperatures below 400°C, the precipitate number density did reach a maximum at doses much less than 1 dpa, then the density decreased due to coarsening.

The precipitate number density at the end of the nucleation stage, N_p, represents the time integral of the nucleation rate, i.e.

$$N_p = \int_t J(t)\, dt \qquad (9.1)$$

where J(t) is the time dependent nucleation rate at a fixed temperature and dpa rate. Therefore, at irradiation temperatures $\lesssim$ 430°C, and at a dose rate of about 10^{-3} dpa/sec, it appears that the precipitate nucleation stage commenced soon after the startup of irradiation, then ceased before a damage level of ~ 0.2 dpa had been attained. Further irradiation produced growth of the precipitates, although coarsening of the precipitation occurred at the lower temperatures. At 475°C, precipitate nucleation apparently required an incubation dose of several dpa. However, there was not much difference between the precipitate densities of specimens irradiated with fluences of 1.8E16/cm^2 and 2.8E16/cm^2, hence the duration of the nucleation stage in these samples must have been brief also. With regard to temperature and dose rate effects, Fig. VII-9 shows that the integrated nucleation rate decreased exponentially with irradiation temperature, while Fig. VII-22 shows that the nucleation rate increased somewhat with dpa rate.

Although several mechanisms have been postulated in the literature that can generally account for radiation-induced precipitation (see below), there is no detailed theory that can be applied quantitatively to precipitate nucleation in the Cu-Be alloy. Nevertheless, the dependence of the CuBe precipitate nucleation rate on irradiation temperatures, dose, and dose rate can be explained qualitatively using the principles of classical nucleation theory[35,36], and using ideas from the theory of the nucleation of defect clusters under irradiation (see Chapter II). In addition, Russell et al.[37-39] have

developed a theory of vacancy-assisted precipitate nucleation under irradiation, which applies mainly to the formation of incoherent precipitates having a positive misfit with the matrix (see section III-B), but which supplies ideas that are generally applicable. From these theories, the radiation-induced precipitate nucleation rate is expected to depend strongly on the concentration or supersaturation of solute atoms and radiation-induced point defects. Therefore, the cessation of nucleation at low dose levels can be explained by the decrease in the solute concentration and in the reducton of the point-defect supersaturation that occurred after precipitates formed. The defect supersaturation decreased because the precipitate/matrix interfaces acted as traps for migrating point-defects. The nucleation rate increased with decreasing temperature (provided the solute remained mobile) because the solute supersaturation increased. Finally, the nucleation rate increased with displacement rate, G, because both the point-defect supersaturation and the flux of defects to sinks increased as G increased.

Nucleation Mechanisms

Both the solute-drag model of Okamoto, Wiedersich, and their co-workers[29-31], and the homogeneous precipitation model proposed by Cauvin and Martin[10] provide mechanisms that could explain radiation-induced precipitation in the Cu-3.4 at% Be alloy. The former model has been more extensively developed than the latter, and was described in some detail in section III.A.2. Specifically, the solute-drag model of Okamoto et al., assumes that undersize solute

atoms interact preferentially with self-interstitial atoms, and undergo long-range migration by forming <100> mixed dumbbells with interstitial atoms.[30] The undersize solute atoms therefore migrate with the interstitial flux and are deposited at defect sinks such as dislocation loops, free surfaces, or grain boundaries. When the local solute concentration surpasses the equilibrium solubility limit in an undersaturated solution, precipitates nucleate heterogeneously at the sinks. Precipitate growth is supported by the continuing transport of solute to the sinks. Like the above model, the Cauvin-Martin[10] model also assumes the solute is coupled to the defect flux, however defect-sinks need not be present for precipitates to nucleate. Instead, homogeneous precipitation can occur via a spinodal-like decomposition, as explained in section III.A.2.

Previously, radiation-induced precipitation similar in morphology to that observed in this study has been reported in the following binary solid solutions containing an undersize solute: 1) HVEM irradiated, undersaturated and supersaturated Cu-Be [Kinoshita and Mitchell[8,9]]; 2) Ni^+ ion irradiated, undersaturated Ni-Be [Okamoto et al.[4,31]]; 3) HVEM, ion, and neutron irradiated undersaturated Ni-Si [Barbu, Silvestre and co-workers[5-7]]; and, 4) HVEM irradiated, undersaturated Al-1.9% Zn [Cauvin and Martin[10]].

In the Al-Zn alloy irradiated under various conditions, both interstitial loops and Zn precipitates were observed to form under irradiation. However, the precipitates were clearly not associated with the loops, therefore the authors proposed the homogeneous

precipitation model. In the Ni-Be solid solutions, there was indirect evidence that the NiBe precipitates were associated with Frank loops, thus, the precipitation was attributed to solute segregation to the loops. In the Ni-Si alloys, however, there was direct evidence that γ' (Ni_3Si) precipitates nucleated on interstitial loops during irradiation of undersaturated solid solutions. In particular, the γ' formed in the loop interior, near the dislocation line. Barbu and Ardell[5] postulated that the interstitial loops formed as usual, then became enriched in Si due to the solute segregation mechanism. It is energetically favorable for the undersize Si to preferentially populate the compressive side (interior) of the loops.

In Cu-Be alloys, there is evidence from previous experiments that the Be solute interacts strongly with interstitial defects, and that Be interstitials segregate to point-defect sinks. First, Blewitt[32] and Dworschak et al.[33] have shown that the Be solute in copper significantly affects the low temperature annealing kinetics. For instance, interstitials are trapped up through Stage III annealing. Secondly, Lensa, Bartels, and coworkers[12,13] detected a decrease in the bulk solute concentration in very dilute Cu-Be alloys following irradiation with 3 MeV electrons at 7-137°C. They attributed this decrease to the segregation of Be interstitials at defect sinks, and their analysis indicated that the mechanism of segregation was the diffusion of tightly bound mixed-dumbbell, solute-interstitial complexes. The strong interaction of Be solute atoms with substitutional interstitial atoms is due to the small size of the Be

atom relative to the copper matrix (the volumetric misfit is -27%). According to the theory of Okamoto and Wiedersich[29], Be solute atoms are therefore expected to segregate to defect sinks during irradiation.

In the present study it could not be directly determined whether the radiation-induced CuBe precipitates had evolved from defect sinks (e.g., defect clusters of interstitial loops), or whether they nucleated homogeneously in the matrix. Many of the precipitate platelets have the superficial appearance of Frank loops, but even in the very low dose specimens (~ 0.1 dpa, see Fig. VII-16) irradiated at 400°C and 430°C, the entire platelets could be imaged in dark field with CuBe superlattice reflections. This fact does not eliminate the possibility of heterogenous CuBe nucleation on loops, since Rehn et al.[20] have shown that pronounced solute segregation to a surface (in Ni-Si) can occur even at a dose of ~ 0.05 dpa. Also, in the TEM diffraction patterns of many Cu-3.4 at% Be samples, streaking of matrix spots was observed, which may indicate the presence of faulted Frank loops[34].

However, there is some reason to believe that the precipitates nucleated homogeneously in the matrix. First, Kinoshita and Mitchell[8,9] reported that CuBe precipitates appeared to have nucleated homogeneously during irradiation of Cu-Be solid solutions in a high voltage electron microscope. They observed that early in the irradiation, existing dislocations were preferred sites for precipitate nucleation. Later, however, precipitates began to form in the

matrix, which were not associated with defect sinks. Secondly, in the present study, CuBe precipitates were present with a number density greater than $10^{14}/cm^3$, after irradiation to a dose of less than 0.2 dpa at temperatures of 400-430°C (see Fig. VII-20). If these precipitates nucleated heterogeneously on defect sinks such as dislocation loops, then a sink density of $\sim 10^{14}/cm^3$ was required. However, examination of the microstructure of the high purity Cu specimens and the Cu-Co and Cu-Fe solid-solutions, irradiated at $\sim$ 400°C and thinned in cross section (discussed later in this chapter) indicated that the density of visible sinks was much less than $10^{14}/cm^3$ even after irradiation to a dose of 1 dpa. In comparison, it is doubtful that such a high density of uniformily distributed interstitial dislocation loops had formed in the Cu-Be alloy after a dose of only $\sim$ 0.2 dpa. This argument, along with the observations of Kinoshita and Mitchell, favors the conclusion that the CuBe precipitates either nucleated homogeneously in the matrix, or else nucleated on very small, invisible defect clusters.

In a final comment regarding the nucleation of CuBe precipitates, there was evidence that individual precipitates acted as nucleation sites for additional precipitate platelets. This would reduce the initial number of sites required for heterogeneous nucleation. The first piece of evidence is that at irradiation temperatures lower than 400°C (see Section VII-A-1), close examination showed that the precipitate platelets formed in clusters of 2 or 3, with each platelet

on a different variant of the habit plane. Secondly, Kinoshita and Mitchell reported that the CuBe platelets were clustered into pyramid-like shapes, with an {001} base and {112}/{113} sides. Thirdly, in Section VII.A.5 it was shown that the precipitates formed in very large clusters during prolonged thermal aging. This behavior may be explained by a reduction in ΔG^* (the activation free energy for nucleation of precipitates) when an existing precipitate platelet acts as a nucleation site for a new precipitate. The reduction in ΔG^* may be due to a decrease in the surface energy or in the volume strain energy[35,36] when the nucleation site is an existing precipitate.

A.1.b. Precipitate Growth

In speculating upon the mechanism responsible for growth of the CuBe precipitates during irradiation, it should be noted that several factors governed the precipitation process during irradiation. One way of viewing radiation-induced precipitation is to assume that even though irradiation perturbs the conditions set forth by equilibrium thermodynamics[50], the basic precipitation process and the observed precipitate characteristics are still, to a large extent, defined by the equilibrium phase diagram of the alloy system. In other words, the physical properties of the alloy are not fundamentally changed by irradiation. Using this framework, one major factor that governed the precipitation process (e.g., the temperature dependence of precipitation) was the inherent solubility of beryllium in copper, as defined by the equilibrium phase diagram (Fig. IV-1). A second

factor was the radiation-induced mechanism that caused Be atoms to precipitate out of solution. A third factor was related to the non-equilibrium nature of the radiation-induced precipitate morphology; i.e., the instability of the continuous precipitation during thermal aging (at 400°C) in the absence of irradiation proved there was a natural driving force for dissolution of the continuous precipitation. Therefore, this driving force competed against the growth mechansim during irradiation. Finally, there is some evidence that a radiation-induced precipitate-dissolution mechanism also competed against precipitate growth, as discussed later in this section. Because the observed characteristics of the CuBe precipitation were the result of the simultaneous operation of several mechanisms, it is difficult to correlate the data with theory, except in a qualitative manner. Nevertheless, the main point of this section is to argue that the most likely mechanism of precipitate growth during irradiation was the solute-drag mechanism.

Because of the non-equilibrium nature of the precipitate morphology, the continued growth of the CuBe platelets during irradiation required a radiation-induced rather than a radiation-enhanced mechanism. Radiation-enhancement of normal diffusion mechanisms probably contributed to precipitate growth by increasing the solute mobility. However, enhanced diffusion alone could not produce the non-equilibrium precipitate morphology observed in the irradiated specimens. There are only two theories in the literature of radiation effects that could explain the growth of the non-equilibrium

precipitates: one theory is due to Russellet al.[37-39] (discussed in section III.B), while the other is the solute-drag concept of Okamoto et al.[29-31] As mentioned earlier, Russell's theory applies mainly to incoherent precipitates, which are unbiased point-defect sinks. His theory predicts that precipitates with a positive misfit (where the precipitate lattice parameter is larger than that of the matrix) will grow during irradiation, while precipitates with a negative misfit will dissolve. It is not clear how applicable Russell's theory is to the γ or γ' CuBe precipitates, first because these precipitates are semi-coherent with the matrix, and secondly because these precipitates have both negative and positive misfits, depending on the crystallographic plane that is considered. Overall, the γ or γ' CuBe precipitates are undersize with respect to the matrix, because the average volume occupied by a precipitate atom is 9.8×10^{-24} cm^3/atom compared with 1.18×10^{-23} cm^3/atom for the α matrix. Due to the crystallographic orientation of the γ or γ' precipitate with respect to the matrix planes, however, the lattice misfit is negative around the periphery of the precipitate platelets, and the misfit is positive on the habit plane faces. Hence, it is unlikely that the vacancy-assisted nucleation mechanism was responsible for growth of the CuBe precipitates.

On the other hand, the solute-drag concept could explain the radiation-induced growth of the CuBe precipitates. First, the interface between the undersize precipitate and the matrix serves as a sink for migrating interstitials, so the interface would become

enriched in Be solute atoms transported by the interstitial flux. Secondly, the temperature range of the CuBe precipitation is consistent with the temperature range over which the solute-drag mechanism has been predicted or observed to operate. Calculations by Johnson and Lam[40] have indicated that segregation occurs in the approximate range of temperature $0.2\ T_m < T < 0.6\ T_m$ (0°C to 540°C for Cu-base alloys) and that the temperature dependence of segregation is similar to that of void swelling. The results of recent experiments (measurements of surface segregation in Ni-Si alloys, by Rehn et al.[18]) have generally agreed with these calculations, although the temperature range over which segregation occurred was narrower than predicted. Rehn et al. also found that the greatest amount of solute segregation occurred at about one-half the melting point of the alloy ($1/2\ T_m$).

In the present study, it was found that the fraction of Be solute that precipitated out of solution under near-steady-state conditions was greatest in the temperature range of ~ 390°C to 430°C, which is ~ $1/2\ T_m$ for the Cu-3.4 at% Be alloy. This is consistent with the reported temperature dependence of the solute-drag mechanism, and provides evidence that this mechanism was responsible for the precipitation. In Fig. IX-1, the approximate atom fraction of Be remaining in solution (the unprecipitated solute) is plotted as a function of irradiation temperature, for Cu-3.4 at% Be alloy irradiated to a dose of ~ 5 dpa at a displacement rate of 7×10^{-4} to 1.3×10^{-3} dpa/sec. The atom fractions of Be in solution, f_{Be}^{α}, is

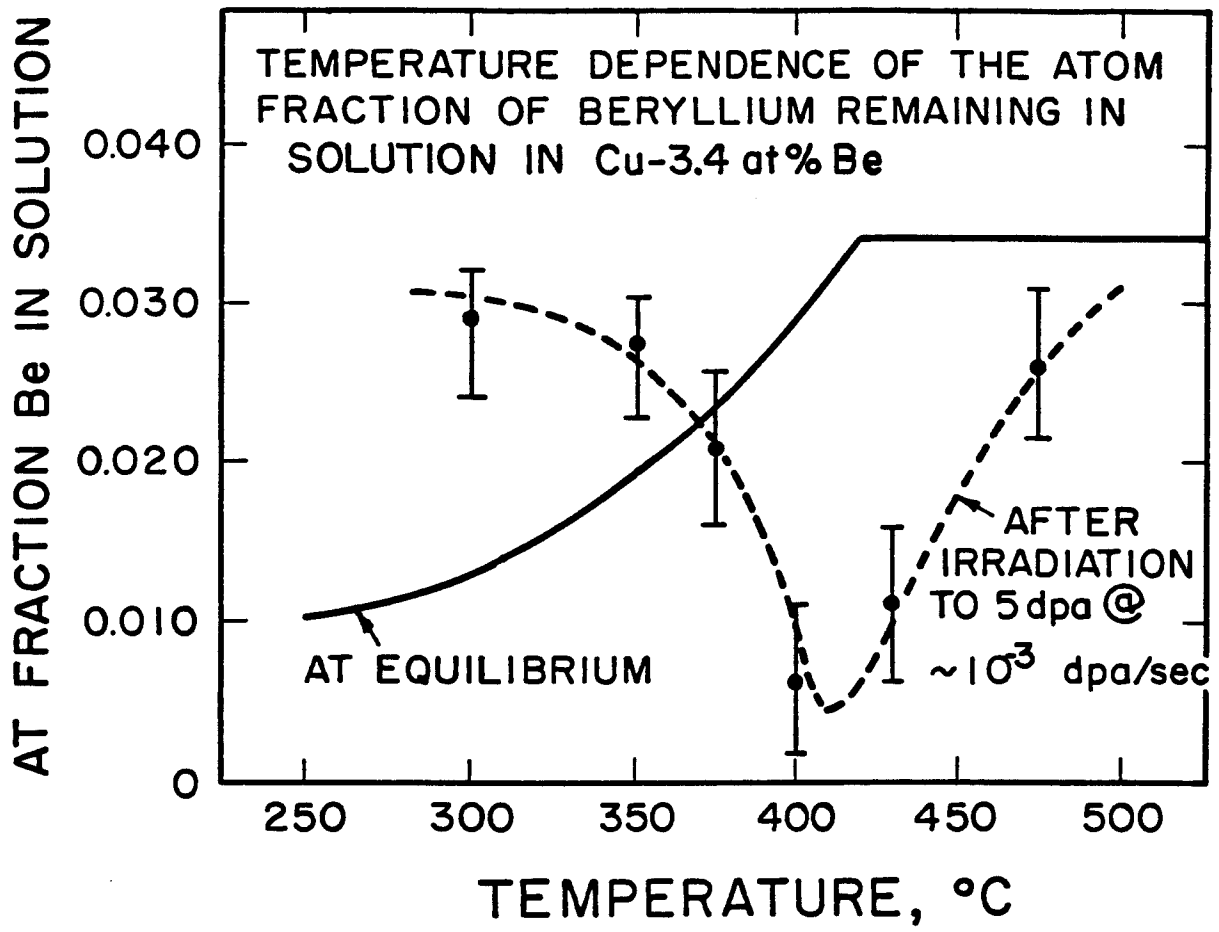

Figure IX.1. The dashed curve shows the temperature dependence of the atomic fraction of beryllium remaining in solution in the Cu-3.4 at% Be alloy, after irradiation to a dose of ~5 dpa @ ~10^{-3} dpa/sec. The microstructure had evolved to near steady-state under these irradiation conditions, as further irradiation did not significantly change the unprecipitated fraction of Be solute. For comparison, the solid curve shows the atomic fraction of Be in solution at equilibrium, as calculated from the Cu-Be equilibrium phase diagram. At equilibrium, all Be is in solution at temperatures above about 420°C.

given by:

$$f_{Be}^{\alpha} = 0.034 - f_{Be}^{p} \tag{9.2}$$

where f_{Be}^{p} is the atom fraction of Be that had precipitated out of solution, and the constant "0.034" is the overall atom fraction of Be in the alloy. The atom fraction of Be contained in the precipitates was calculated from the measured precipitate characteristics (Chapter VII), as is given by:

$$f_{Be}^{p} = \bar{V}_p N_p n_p / 2n_a \tag{9.3}$$

where

$$\bar{V}_p = t_p R \bar{d}^2 \quad . \tag{9.4}$$

In these equations, N_p is the measured precipitate number density (see Fig. VIII-9), n_p is the atomic density of the CuBe precipitate, which is calculated as $1.02 \times 10^{23}/cm^3$ (assuming the precipitate has the B2-type structure with $a_o = 0.27$ nm), and n_a is the overall atomic density of the alloy ($\sim 8.5 \times 10^{22}/cm^3$). The factor 2 in the denominator arises because Be atoms constitute one-half of the CuBe unit cell. Also, $\bar{V}_p$ is the mean volume of a precipitate, t_p is the measured mean precipitate thickness, and $\bar{d}$ is the mean of the maximum precipitate dimension (see Fig. VII-8). Finally, R is the mean

aspect ratio of the precipitate platelets, such that $(R\bar{d})\ \bar{d}$ is the mean area of the habit-plane face of a precipitate (the precipitates are assumed to be rectangular platelets). The precipitate thicknesses were measured from dark-field TEM micrographs, and ranged from an average of 6 nm at 300°C, to 14 nm at 375°C, and 30 nm at 475°C. For these same temperatures, the average aspect ratios were 0.8, 0.4 and 0.17, respectively.

Also plotted in Fig. IX-1, for comparison with the irradiated alloy, is the temperature dependence of the atom fraction of Be in solution at equilibrium. The curve was calculated from the CuBe equilibrium phase diagram using the lever law as usual. At equilibrium, the amount of Be dissolved in the α_{Cu} solution increases exponentially with temperature as usual until the solvus temperature is reached at ~ 420°C (conversely, the amount of Be existing as precipitation decreases). Above this temperature, all Be is dissolved in solution. Figure IX-1 shows that the behaivor of the alloy under irradiation contrasts sharply with the behavior expected near equilibrium. Under irradiation, the amount of Be remaining in solution decreases rapidly as the solvus temperature is approached. In the temperature range of 390 ~ 430°C, most of the Be contained in the alloy has precipitated out of solution. This curve suggests that the segregation mechanism was most efficient near a temperature of ~ 400°C, which is ~ 1/2 T_m for the Cu-3.4 at% Be alloy.

It might be argued that the shape of the low temperature portion of the curve representing the irradiated alloy in Fig. IX-1 resulted

because steady state conditions had not yet been achieved. On the contrary, analysis of the specimens showed that at irradiation temperatures below about 375°C, the precipitate volume fraction had reached steady state before doses of 5 dpa were attained. For instance, at 350°C the precipitate volume fraction did not change significantly with dose in the range of 2 dpa to 10 dpa, at a dose rate of 1.1×10^{-3} dpa/sec. (Refer to discussion in section VII.A.2 pertaining to Fig. VII-13. Although the precipitate number density decreased with dose at 350°C, the particle thickness increased to keep $\bar{V}_p N_p$ approximately constant.) The shape of the low temperature portion of the curve cannot be explained by classical theory and by the solute-drag mechanism alone. According to classical nucleation and growth theory (in the absence of irradiation) the driving force for precipitation increases as the solute supersaturation increases at temperatures below T_{solvus}.[35,36] Therefore, in the Cu-3.4 at% Be alloy, the driving force for precipitation is greater at 300-350°C than at 400-420°C, although the solute mobility is reduced at lower temperatures. Qualitatively, the radiation-induced precipitation mechanism (presumably the solute drag mechanism) would be expected to co-operate with the natural driving force for precipitation to produce more precipitation at ~ 350°C than is indicated in Fig. IX-1. A possible explanation for this behavior is that radiation-induced precipitate dissolution occurred simultaneously with growth, and that this mechanism was more efficient at limiting the precipitate volume fraction at lower temperatures than at higher temperatures. Since

the CuBe precipitates have an ordered structure, the disorder-dissolution mechanism proposed by Nelson et al.[50] could compete against precipitate growth. The disorder-dissolution rate is proportional to the displacement rate, G, and should be temperature dependent because reordering would be more sluggish at lower temperatures. It should be noted here that a precipitate dissolution mechanism that is dependent on G can help explain the weak depth dependence of the precipitate volume fraction in cross sectioned specimens. Within the depth range of ~ 500 nm to 2700 nm, the dose varies by a factor of ~ 6, but the precipitate volume fraction varies by only ~ 25%. Because the peak damage region also experiences the highest displacement rate, the precipitate volume fraction in this region may be limited by a dissolution mechanism that is dependent on dpa rate.

At irradiation temperatures of 400°C and 430°C, the steady state precipitate volume fraction had not yet been attained. As indicated in Fig. VII-18, precipitate size was still increasing with dose at 5 dpa. Because the fraction of Be in solution was still decreasing at 5 dpa, the dip in the curve at ~ 400°C in Fig. IX-1 would be even more pronounced at steady state. At 475°C, there was not much difference in the precipitate volume fraction of specimens irradiated to 5 dpa and to 8 dpa, so it is believed that steady state was nearly achieved at 5 dpa. The rapid increase in the fraction of Be dissolved in solution at temperatures greater than ~ 420°C can be explained by several factors. First, the solubility of Be in copper continues to increase rapidly with temperature (Fig. IV-1), so

radiation-induced precipitation was hindered by the natural driving force for precipitate dissolution. Secondly, the radiation-induced precipitation mechanism became less efficient at higher temperatures. In the case of the solute-drag mechanism, the solute/interstitial interaction weakens above temperatures of ~ 1/2 T_m. Also, as the solute diffusivity increases with temperature, the solute concentration gradient becomes more difficult to maintain.

In conclusion, the growth characteristics of the CuBe precipitates are consistent with the reported dose and temperature dependence of the solute-drag mechanism, however it cannot be proved that this mechanism was responsible for the precipitation. In view of current theory regarding radiation-induced precipitation, the solute drag mechanism provides the most satisfactory explanation for radiation-induced precipitation in the Cu-3.4 at% Be alloy.

A.2. Measurements and Observations Pertaining to Beryllium Segregation

The most interesting results of the Auger electron spectroscopy (AES) measurements were the enhanced rate of BeO formation at the irradiated surface, and the absence of Be transport out of the peak-damage region. In addition, transmission electron microscopy (TEM) showed no particular evidence of Be segregation at grain boundaries. These results are discussed in this section.

Surface Segregation

The suspected role of the solute-drag mechanism as a cause of the radiation-induced CuBe precipitation was the primary motivation

for performing the AES measurements described in section VII.B. The justification for using surface segregation data to obtain information on the solute-drag mechanism has been discussed previously in sections III.A.2, V.C, and VII.B. Also, previous investigations of radiation-induced solute segregation in binary alloys were reviewed in section V.C. Some of the difficulties that were encountered in the present study (described in section VII.B.), had been experienced previously by other investigators. Indeed, in their study of electron irradiated Cu-Be alloys, Bartels et al.[13] reported that their attempts to measure radiation-induced Be surface segregation were "considerably hindered" by the Be enrichment and oxidation even at unirradiated surfaces, and their results were not published. Rehn et al.[18] noted that AES measurements of Be surface enrichment in a Ni-1% Be alloy (analogous to Cu-Be) could not be obtained because of serious overlap of Auger transition lines of Be and Ni.

The complications that were encountered early-on in the present study were outlined in section VII.B. It was shown that despite these complications, Be concentration vs. depth profiles could be measured, because oxidation of the Be shifted the principal Be Auger transition line down to ~ 96 eV, where there was no interference from the 104 eV Cu transition. Further investigation proved that the excess Be beyond the immediate surface was oxidized, and that oxidation could only have occurred during heating in the target chamber. Apparently, oxygen diffused into the alloy and reacted with Be solute, trapping the solute by formation of immobile BeO. Because

the BeO-enriched layer was thicker and the shape of the Be profile was different at the irradiated surface compared to control surfaces, (this was true whether or not the control area was covered by the tantalum mask), AES measurements were performed on subsequent specimens to try to determine if the solute-drag mechanism was responsible for transporting Be from the interior of the specimen to the surface. There was also some fundamental interest in these measurements; i.e., to the author's knowledge, radiation-enhanced oxidation of an active solute has not been reported previously in the literature.

A thorough analysis of the enhanced-oxidation phenomenon is out of the scope of this thesis, primarily because this would require an anlysis of the effects of irradiation on the kinetics of the Be + O oxidation reaction and on the rate of diffusion of oxygen into the alloy. Although this phenomenon warrants further investigation, the intent here is to argue that the solute-drag mechanism did not play an important role in the radiation-induced Be enrichment. Instead, the time and temperature dependence of the data in Figs. VII-40 to VII-44 suggest that a thermal diffusion mechanism (probably enhanced by irradiation) was responsible for the radiation-enhanced enrichment of Be and the formation of BeO near the irradiated surface.

A general idea of the temperature dependence of the solute-drag mechanism can be obtained from Rehn's [18] study of surface segregation in an ion-bombarded Ni-1 at% Si solid solution, where Si is an undersize solute. The near-surface Ni enrichment was measured using AES, and no complications due to oxidation of the Si were

reported. Their results showed that the thickness and the magnitude of the Si-enriched layer varied strongly with irradiation tempera-. ture. At low temperature (385°C), solute segregation was minimal. As temperature increased, the Si surface concentration increased until a Ni_3Si film nucleated; the thickness of this film increased to a maximum vlaue at ~ 560°C, then diminished at higher temperatures. The maximum segregation therefore occurred at about one-half the melting point (1/2 T_m) of the alloy, and the general temperature dependence was similar to that observed for void swelling in Ni. The reason for the decrease in surface segregation at high temperature is that the solute-interstitial binding becomes ineffective at high temperature and back-diffusion occurs more readily, as discussed in section III.A.2.

By comparison with the Ni-Si results of Rehn et al., the Be surface-segregation should have been greatest at about 400°C (~ 1/2 T_m for Cu) if the solute-drag mechanism was responsible for transporting Be to the surface. Examination of Figs. VII-41 and VII-44 shows that the maximum BeO concentration, and the thickness of the BeO-enriched layer, increased greatly with temperature in the range 400°C to 475°C. Other AES measurements not presented in section VII.B (specimens 21 and 22, see Table VII.1) showed that the near-surface BeO enrichment was even greater at an irradiation temperature of 525°C. This behavior is not characteristic of the solute-drag mechanism, but is characteristic of thermal diffusion, where the diffusion coefficient increases exponentially with

temperature.[35,41] Futhermore, as mentioned in section VII.B, the thickness of the BeO-enriched layer in Cu-3.4 at% Be specimens irradiated at 400°C (Fig. VII-44) grew at a rate proportional to $\sqrt{\phi t}$ (fluence), where t is the irradiation time and ϕ is the ion flux (ϕ remained approximately constant during irradiation). The $\sqrt{t}$ dependence of the growth rate of the BeO layer is characteristic of a thermal-diffusion-controlled reaction.[41] In contrast, the work of Rehn et al.[20] shows that the buildup of an enriched layer by the solute drag mechanism does not have a $\sqrt{t}$ dependence.

If radiation-enhanced diffusion was responsible for the accelerated growth rate of the BeO layer, then the growth rate should have been dependent on the displacement rate, G.[43] At temperatures where there is a large vacancy supersaturation due to irradiaton, the diffusion coefficient should be either directly proportional to G, or else proportional to $\sqrt{G}$, depending on the mechanism of vacancy annihilation. In the present experiment, the displacement rate was nearly constant. To determine the role of enhanced diffusion in the formation of the BeO layer, further irradiation experiments conducted at various ion flux levels are required.

Beryllium Segregation Within the Damage Zone

Figure VII-47 in section VII.B shows that the Be solute concentration did not vary as a funcion of depth either within the damage zone (except near the surface), or beyond the end-of-range of the incident Cu ions in a speciment irradiated at 400°C to a peak dose of 8.4 dpa. At first glance, this result appears to conflict with

previous calculations[42] and experiments[17,21] pertaining to ion-bombarded alloys, which showed that undersize solutes are transported out of the peak damage region, and are deposited beyond the end-of-range by the solute drag mechanism, provided the sink density within the damage zone is low. Lam et al.[42] used a kinetic model to calculate the effects of depth dependent damage on solute segregation in a 3 MeV Ni ion bombarded, dilute Ni-Si alloy. Their calculations showed that at a temperature of about 1/2 T_m and a peak dose of 10 dpa, most of the undersize Si solute was transported out of the peak damage region by the out-flowing interstitial flux. This effect was observed experimentally by Piller and Marwick[17,21], who measured depth profiles of Si in dilute Ni-Si solid solutions that were ion-bombarded at 500°C. The main difference between the present study and previous work is that the sink density was high in the irradiated Cu-3.4 at% Be alloy (because of the precipitation), but sink density was low in the calculations of Lam et al. and in the Ni-Si alloy irradiated by Piller and Marwick. The copious CuBe precipitation apparently prevented Be solute from being transported far. (The alternative explanation is that the solute-drag mechanism did not operate in the Cu-Be alloy.) At an irradiation temperature of 400°C, the CuBe precipitate density was ~ 5 x $10^{14}/cm^3$ and the equivalent platelet radius was about 55 nm, therefore the average spacing between precipitates was less than 125 nm. The closely spaced CuBe precipitates served as point-defect sinks that prevented the long-range migration of interstitial atoms. This fact is tied to the

growth of the precipitates by solute segregation, as discussed previously. In addition to the precipitates, the matrix dislocations also acted as point defect sinks.

The effectiveness of the CuBe precipitates in trapping point defects and in reducing long-range defect migration cannot be determined without the aid of a detailed numerical model. However, an analogy can be made with the work of Carpenter and Yoo[26], who showed that semicoherent θ' precipitate platelets (in Al-Cu alloys) could significantly reduce the vacancy and interstitial concentrations by point defect trapping at the precipitate/matrix interface. The total interface area of the θ' precipitates in their work was similar to that of the CuBe precipitates in this study. The reduction in the point defect concentrations was estimated by numerically solving a set of differential equations governing the conservation of free and trapped point defects and the growth of defect clusters. There were two principal unknown parameters that governed defect trapping at the precipitates: 1) σ_t, the surface density of trapping sites on the semichoerent precipitate/matrix interface, and 2) $E_{v,i}$, the binding energy of vacancies and interstitials to the trapping sites. By using physically reasonable values for σ_t and $E_{v,i}$, however, Carpenter and Yoo found that the semicoherent precipitates could reduce the point-defect concentrations.

Another interesting observation in the present study was the absence of strong segregation effects at grain boundaries. Although

Be enrichment would be expected at these sinks,[20] precipitate-free zones were occasionally observed on one or both sides of grain boundaries during TEM analysis. A precipitate structure was never observed on the boundary itself. It could not be determined whether the Be concentration was enriched at grain boundaries and precipitates did not nucleate, or whether Be enrichment at grain boundaries was prevented because solute was tied up in the matrix precipitates. Clearly, further investigation of solute redistribution is required in alloys where precipitation occurs or where the matrix sink density is large.

B. Phase Stability of the Cu-Co and Cu-Fe Alloys

The principal effect of irradiation on the aged Cu-1% Co and Cu-1% Fe alloys was loss of precipitate coherency, which is discussed below in detail. Irradiation at 400°C and 475°C did not measurably change the size or number density of the spherical Co-rich and Fe-rich precipitates, nor did it appear to affect the blocky, incoherent Fe precipitates. In contrast, several previous irradiation studies on Cu-Co and Cu-Fe alloys[44-49] (reviewed in section V.B.) conducted at temperatures below 210°C reported precipitate dissolution, although measurement techniques more indirect than electron microscopy were used to analyze the specimens. According to the theory of Nelson, Hudson, and Mazey[50], however precipitate shrinkage due to recoil dissolution should have been negligible in the present study: Eq. 3.2 predicts that at a displacement rate of 10^{-3} dpa/sec, a

precipitate of radius 12 nm would lose only ~ 0.1% of its volume during irradiation to a damage dose of 3 dpa.

The results of the Auger electron spectroscopy measurements in Chapter VIII showed that no measurable radiation-induced enrichment or depletion of solute occurred at the surface, indicating a weak interaction between point defects and the Co or Fe solutes.[29] This result is compatible with the small size-difference between the solute and solvent atoms in these alloys; i.e. the strain field near the solute atom is small. The lack of a strong defect/solute interaction (and subsequent solute transport mechanism) may have been a factor in the near-absence of radiation-induced precipitation in the Cu-Fe and Cu-Co solid solutions, even though the solutions were highly supersaturated at 400-475°C. Thermal diffusion data[51] indicates the Co and Fe solutes are rather immobile even at 475°C. During a typical irradiation period of 3600 seconds at 475°C, the thermal diffusion lengths of Co and Fe solutes in Cu are, respectively: $\sqrt{D_{Co}t}$ = 10 nm and $\sqrt{D_{Fe}t}$ = 21 nm. The experimental results in the irradiated solid solutions indicate either that a) irradiation does not significantly enhance the solute diffusivity, or b) recoil-dissolution[50] may prevent the growth of precipitates by redissolving the tiny precipitate nuclei.

Loss of Coherency

If the lattice parameter of a coherent precipitate is different from that of the matrix, the misfit strain increases with particle growth, and at some point the particle loses coherency by nucleation

of interfacial dislocations. In the case of the Cu-Co and Cu-Fe alloys, the lattice parameter of the precipitate is smaller than that of the matrix by about 1%, and the coherency strain is accommodated by formation of one or more interstitial dislocation loops. Through the use of elasticity theory and strain energy considerations, Brown et al.[53] calculated that above a critical radius of ~ 6 nm, the incoherent precipitate is more stable than the coherent one in the Cu-Co alloy. In practice, however, the spherical precipitate grows much larger than the critical size before coherency is lost, because of the barrier to nucleation of the dislocation loop. During prolonged thermal aging, the Co precipitate has been observed to grow beyond diameters of 50 ~ 60 nm before coherency is lost.[55,56] Deformation of the alloy can cause smaller particles to lose coherency; e.g., Phillips[56] reported that stretching the alloy ~ 5% caused particles ~ 25 nm in diameter to lose coherency. Under irradiation, coherency loss occurs much more readily (Co or Fe particles 5 ~ 20 nm dia. become incoherent[52-54]) because of mechanisms that enhance the formation of interstitial dislocation loops at the precipitate/matrix interface. Careful examination of coherency loss in Cu-Co or Cu-Fe alloys during irradiation in the high voltage electron microscope, and following reactor-irradiation, lead to the identification of two probable radiation-induced mechanisms for the formation of interstitial loops to relieve coherence strain[54]:

(1) Interstitial loops move by glide and conservative climb to equilibrium positions where they act directly as interfacial loops.

(2) Free interstitials are trapped within the precipitates due to the high attractive interaction energy and subsequently agglomerate into strain-relieving interstitial dislocation loops.

In the aged Cu-1% Co and Cu-1% Fe alloys irradiated in this study, essentially all visible precipitates lost coherency as a result of irradiation. The greatest amount of information can be obtained from the cross sectioned Cu-Co specimen irradiated at 400°C to a total fluence of $3.2 \times 10^{15}/cm^2$ (Fig. VIII-8), and the cross sectioned Cu-Fe specimen irradiated at 350°C to $10^{16}/cm^2$ (Fig. VIII-12). In both specimens, precipitates within the damage zone (at depths $\lesssim$ 3000 nm) have lost coherency, even in the low dose ($\sim$ .3 dpa) near-surface region of the Cu-Co. Visible dislocation loops are associated with some incoherent precipitates, however there are no loops in the matrix between the precipitates. The mechanism responsible for the loss of coherency must have been the absorption of free interstitials (mechanism #2, above), since few dislocation loops and line dislocations are visible in the micrographs. Continued growth of some initial loops, by interstitial absorption, may be the reason some large loops are seen in Figs. VIII-8 and VIII-12.

It is interesting that most precipitates situated up to 1300 nm beyond the end-of-range in the Cu-Co specimen, and up to 500 nm beyond range in the Cu-Fe specimen, have also lost coherency. Since few dislocations of any kind are present beyond the end-of-range in either Fig. VIII-8 or VIII-12, coherency loss must have resulted from the migration of free interstitials well beyond the damage zone. The

migration energy of Cu, Co or Fe interstitials is very low (~ 0.2 eV); therefore, interstitials could have easily migrated to these depths, because the sink density is low, and the solute atom/defect interaction is apparently weak in these alloys.

An alternative to the mechanisms described above is that precipitate coherency was lost due to strains introduced by the electroplating, or by the ion-implantation itself. The electroplating strain is ruled out because coherency loss was observed in back-thinned specimens also. Significant strain due to ion implantation is unlikely, since 10^{16} implanted ions/cm^2, distributed over a depth range of ~ 1000 nm, represents an excess volume of only about 0.1%.

C. Absence of Void Formation

In this study, radiation-induced voids did not form in the high-purity Cu, nor in the Cu-base alloys, with the exception of the as-quenched Cu-1% Fe irradiated at 400°C. In the high purity Cu, little damage was evident except in the peak damage region, indicating that most radiation-produced defects were removed by mutual recombination. Comparison with the results of Glowinski et al.[59-61] suggests that the absence of void formation in the high-purity Cu was probably due to a lack of gaseous impurities, which can serve as void nucleating agents (section V-A). Glowinski did not observe void swelling in thoroughly outgassed, self-ion bombarded Cu, even if the Cu was pre-injected with hydrogen. If the Cu was pre-injected with O or He ions, these impurities apparently stabilized the void nuclei, and swelling did occur. The Cu used in the present study initially

contained very little oxygen (Table VI.1), and the pre-irradiation heating at 500°C in the target chamber probably outgassed the samples further. A simple diffusion calculation shows that, in the absence of trapping, any hydrogen left in the specimens, from the high temperature anneal in the H_2 atmoshpere, diffused out during the pre-irradiation heating. The possibility that voids annealed out during the in situ post-irradiation heating (~ 400°C for at least several hours, depending on the specimen) was also investigated by solving Eq. 2.19, to estimate the void shrinkage rate, dr_v/dt. The calculation indicated that voids larger than ~ 3 nm in diameter would not have been affected by the anneal.

A lack of nucleating agents could also explain the absence of void formation during irradiation of the Cu-1% Co and Cu-1% Fe specimens. As discussed in the theoretical background in section II-C, several other mechanisms can suppress the nucleation and growth of voids in alloys. In the Cu-Co and Cu-Fe alloys, several possible void suppression mechanisms are point-defect trapping near solute atoms in the matrix,[62,63] and defect trapping near the coherent precipitate/matrix interfaces.[64,65] Direct experimental evidence for defect trapping of Co or Fe solutes Cu was not found in the literature. The AES measurements in this study, showing the absence of radiation-induced solute segregation, are evidence that defects do not interact strongly with the Co and Fe solutes. Also, the similarity in atomic size (small strain field) and electronic structure between Cu and the Co or Fe solutes may rule out trapping by the

solute atoms. In the aged Cu-Co and Cu-Fe alloys, however, the loss-of-coherency of the spherical precipitates during irradiation clearly indicates these particles acted as defect sinks or traps. This enhanced the recombination of vacancies and interstitials and reduced the vacancy supersaturation necessary for void formation.

It is interesting that the results of heavy-ion irradiations of the Cu-1% Fe alloy in this study contrast sharply with results of HVEM irradiations of a Cu-1.5% Fe alloy by Takeyama et al.[66] These workers irradiated both as-quenched specimens and aged specimens (which contained coherent or incoherent Fe precipitates) at 250°C to doses up to 10 dpa. They observed void formation in all specimens, although swelling was least in the as-quenched specimens and greatest in specimens aged the longest, which contained incoherent precipitates. Voids often formed at precipitates, particularly at the interface of coherent particles, which otherwise did not lose coherency during irradiation. However, one factor contributing to the void formation in these thin, HVEM-irradiated foils may have been a significant loss of the fast-diffusing interstitials to the foil surfaces, thereby enhancing the vacancy supersaturation within the foil.

The absence of void nucleation in the Cu-3.4 at% Be specimen can be explained by two factors in addition to the possible absence of nucleating agents. First, there is experimental evidence that Be solute atoms interact strongly with interstitial defects produced by irradiation as discussed earlier in this chapter. Therefore

interstitial diffusion is hindered, and the probability of recombination with vacancies is increased.[12,13,32,33] Secondly, in the temperature range where voids might be expected to nucleate, the CuBe precipitates form very quickly after irradiation commences. The semi-coherent matrix/precipitate interface can act as a defect trap or sink; and because of the platelet geometry, the interface area presented by the precipitates is relatively large. Other studies of void swelling in Cu and Ni have also shown that the Be solute effectively suppresses void formation.[67]

References for Chapter IX

1. Radiation Effects in Breeder Reactor Structural Materials, M. L. Bleiberg and J. W. Bennett, eds., AIME, 1977.

2. "Solute Segregation and Phase Stability During Irradiation," J. Nucl. Mat. 83, (1979).

3. Irradiation Effects on Phase Stability, Fall 1980 Meeting of AIME, Pittsburgh, PA, October 1980.

4. P. R. Okamoto, A. Taylor, and H. Wiedersich, Fund. Aspects of Rad. Damage in Metals, CONF 751006-P2, 1188-1195 (1975). These authors also quote work by T.D. Ryan, Ph.D. Thesis, University of Michigan, 1975.

5. A. Barbu and A. J. Ardell, Scripta Met. 9, 1233-1237 (1975).

6. G. Silvestre, A. Silvent, C. Regnard, and G. Sainfort, J. Nucl. Mat. 57, 125-135 (1975).

7. A. Barbu and G. Martin, Scripta Met. 11, 771-775 (1977).

8. C. Kinoshita and T. E. Mitchell, 38th Annual Proc. Electron Microscopy Soc. America, G. W. Bailey, ed., San Francisco, CA, 148-149 (1980).

9. C. Kinoshita and T. E. Mitchell, Elec. Microscopy 1980 4, 236-239 (1980).

10. R. Cauvin and G. Martin, Workshop on Solute Segregation and Phase Stability During Irradiation, Gatlinburg, TN (1978), J. Nucl. Mat. 83, 67-78 (1979); and G. Martin, Fund. Aspects of Rad. Dam. in Metals, CONF. 751006-P1, 1084-91 (1975).

11. V. K. Sikka and J. Moteff, Met. Trans. 5, 1514-1517 (1974).

12. W. Lensa, A. Bartels, F. Dworschak and H. Wollenberger, J. Nucl. Mat. 71, 78-81 (1977).

13. H. Bartels, F. Dworschak, H. Meurer, C. Abromeit, H. Wollenberger, J. Nucl. Mat. 83, 24-39 (1979).

14. E. A. Kenik, Scripta Met. 10, 733-738 (1976).

15. D. I. Potter, L. E. Rehn, P. R. Okamoto, and H. Wiedersich, Scripta Met. 11, 1095-1099 (1977).

16. A. D. Marwick and R. C. Piller, Rad. Effects 33, 245-250 (1977).

17. R. C. Piller and A. D. Marwick, J. Nucl. Mat. 71, 309-313 (1978).

18. L. E. Rehn, P. R. Okamoto, D. I. Potter, and H. Wiedersich, J. Nucl. Mat. 74, 242-251 (1978).

19. P. P. Pronko, P. R. Okamoto, and H. Wiedersich, Nucl. Inst. and Methods 149, 77-82 (1978).

20. L. E. Rehn, P. R. Okamato, and H. Wiedersich, J. Nucl. Mat. 80, 172-179 (1979).

21. A. D. Marwick, R. C. Piller, and P. M. Sivell, J. Nucl. Mat. 83, 35-41 (1979).

22. R. C. Piller and A. D. Marwick, J. Nucl. Mat. 83, 42-47 (1979).

23. K. Farrell, J. Bentley, D. N. Braski, Scripta Met. 11, 243-248 (1977).

24. R. A. Erck, D. I. Potter, and H. Wiedersich, J. Nucl. Mat. 80, 120-125 (1979).

25. T. Takeyama, S. Ohnuki, and H. Takehashi, Electron Microscopy 1980 4, 208-211 (1980).

26. R. W. Carpenter and M. H. Yoo, Met. Trans. A 9A, 1739-1747 (1978).

27. R. J. Rioja and D. E. Laughlin, Acta Met. 28, 1301-1313 (1980).

28. P. Wilkes, J. Nucl. Mat. 83, 166-175 (1979).

29. P. R. Okamoto and H. Wiedersich, J. Nucl. Mat. 53, 336-345 (1974).

30. R. A. Johnson and N. Q. Lam, Phys. Rev. B 15, No. 4, 1794-1800 (1977).

31. N. Q. Lam, P. R. Okamoto, H. Wiedersich, and A. Taylor, Met. Trans. A 9A, 1707-1714 (1978).

32. T. H. Blewitt, in Radiation Damage in Solids, D. S. Billington (ed.), 630-716 (1962).

33. F. Dworschak, R. Lennartz, and H. Wollenberger, J. Phys. F., Metal Phys. 5, 400-418 (1975).

34. C. W. Allen and P. R. Okamoto, Phys. Stat. Sol. (a) 36, 107 (1976).

35. J. W. Christian, The Theory of Transformations in Metals and Alloys, Part I, 2nd Ed. (Pergamon Press, 1975).

36. J. D. Verhoeven, Fundamentals in Physical Metallurgy, (John Wiley, 1975).

37. S. I. Maydet and K. C. Russell, J. Nucl. Mat. 64, 101-114 (1977).

38. K. C. Russell, Scripta Met. 3, 313 (1969).

39. M. R. Mruzik and K. C. Russell, J. Nucl. Mat. 78, 343-353 (1978).

40. R. A. Johnson and N. Q. Lam, J. Nucl. Mat. 69 & 70, 424-433 (1978).

41. P. G. Shewmon, Transformation in Metals, Chapter 9, (McGraw-Hill, New York, 1969).

42. N. Q. Lam, P. R. Okamoto, and R. A. Johnson, J. Nucl. Mat. 78, 408-418 (1978).

43. G. J. Dienes and A. C. Damask, J. Appl. Phys. 29, No. 12, 1713-1721 (1958).

44. J. M. Denney, Phys. Rev. 94, No. 5, 1417-18 (1954).

45. A. Boltax, ASTM Special Tech. Pub. 208, Rad. Effects on Materials, Vol. 1, 183-190 (1956).

46. A. Boltax, Nucl. Appl. 1, 337-347 (1965).

47. T. H. Gould and D. H. Vincent, J. de Physique C6, No. 12, 315-319 (1974).

48. G. R. Piercy, J. Phys. Chem. Solids 23, 361-365 (1962).

49. A. Blaise, J. de Physique 26, 361-365 (1965).

50. R. S. Nelson, J. A. Hudson, and D. J. Mazey, J. Nucl. Mat. 44, 318-330 (1972).

51. D. B. Butrymowicz, J. R. Manning, and M. E. Read, J. Phys. Chem. Ref. Data 4, No. 1, 110-111 and 118-119 (1975).

52. G. R. Woolhouse, Nature 220, 573-574 (1968).

53. L. M. Brown, G. R. Woolhouse and U. Valdre, Phil. Mag. 17, 781-789 (1968).

54. G. R. Woolhouse and M. Ipohorski, Proc. R. Soc. London A324, 415-431 (1971).

55. V. A. Phillips and J. D. Livingston, Phil. Mag. 7, 969 (1962).

56. V. A. Phillips, Trans. AIME 230, 967-976 (1964).

57. L. E. Tanner and I. S. Servi, Acta Met. 14, 231-234 (1966).

58. L. M. Brown and G. R. Woolhouse, Phil. Mag. 21, 329-345 (1970).

59. L. Glowinski, C. Fiche, and M. Lott, J. Nucl. Mat. 47, 295-310 (1973).

60. L. D. Glowinski and C. Fiche, J. Nucl. Mat. 61, 22-28 (1976).

61. L. D. Glowinski and C. Fiche, J. Nucl. Mat. 61, 29-40 (1976).

62. S. D. Harkness and C. Y. Li, in Radiation Induced Voids in metals, J. W. Corbett and L. C. Ianniello, eds., 798-824 (1972).

63. W. Schilling and K. Schroeder, AERE-R7934.

64. A. D. Brailsford, J. Nuc. Mat. 78, 354-361 (1978).

65. R. Bullough and R. C. Perrin, Voids Formed by Irradiation of Reactor Materials, S. F. Pugh, ed., BNES, 79 (1971).

66. T. Takeyama, S. Ohnuki and H. T. Takehashi, J. Nuc. Mat. 89, 253-262 (1980).

67. M. J. Makin, in Voids Formed by Irrad. of Reactor Materials, S. F. Pugh, ed., BNES, 269-274 (1971).

CHAPTER X

CONCLUSIONS

The most important observations that emerged from this study, regarding the irradiation experiments on the Cu-3.4 at% Be, Cu-1% Co, and Cu-1% Fe alloys, and on the high purity Cu, are listed below. Several comments are also made regarding the experimental methods used to obtain the data. Finally, suggestions are given regarding further work in this area.

Cu-3.4 at% Be Alloy

(a) Irradiation of supersaturated and undersaturated Cu-3.4 at% Be solid solutions with 14 MeV Cu ions, at temperatures ranging from 300-475°C, induced copious precipitation of CuBe platelets in the region traversed by the ions. The precipitates nucleated rapidly after the start-up of irradiation, and they were distributed uniformly throughout the matrix. In contrast, thermal aging studies showed that nucleation and growth of CuBe precipitates in the Cu-3.4 at% Be alloy was very sluggish in the absence of irradiation. Prolonged thermal aging produced equilibrium, discontinuous precipitation at grain boundaries and in discrete clusters within the grains.

(b) Post-irradiation annealing of the undersaturated specimens caused complete dissolution of all precipitation, as expected. However, post-irradiation aging of supersaturated specimens also caused dissolution of the continuous, radiation-induced precipitate morphology, and some discontinuous CuBe precipitation

formed instead. This proved that the precipitation was radiation-induced rather than simply radiation-enhanced.

(c) This study provides further evidence that undersize substitutional solute elements interact strongly with irradiation-produced defects. Previously, radiation-induced continuous precipitation has been reported in a number of other types of solid solutions containing undersize solute elements.

(d) The mechanism of radiation-induced precipitate nucleation could not be determined, because it was not possible to prove whether precipitates nucleated homogeneoulsy on dislocation loops or on other defect clusters. However, there was evidence that the precipitates did not nucleate on visible defect clusters.

(e) Among the mechanisms that have been proposed in the literature to explain the growth of precipitates under irradiation, the only one that satisfactorily explains the continued growth of the CuBe precipitates is the solute-drag mechanism, whereby Be solute atoms preferentially segregate to the precipitates via the interstitial flux. Experimental evidence that supported this conclusion was that the fraction of Be solute precipitated from solution (at near-steady-state conditions) was greatest at a temperature of $\sim 1/2\ T_m$, which is approximately the same temperature where the solute-drag mechanism is reported to be most efficient.

(f) Measurements of the mean precipitate size and number density as a function of irradiation temperature and (to a more limited

extent) dose and dose-rate were presented. The dependence of the precipitate characteristics on these variables was qualitatively consistent with current theories of precipitate and defect-cluster nucleation and growth under irradiation.

(g) Measurement of the precipitate size and number density as a function of depth into the damage zone were also presented. These measurements were taken from specimens that were prepared for TEM analysis using a cross sectional thinning technique. Precipitate size, density and volume fraction typically varied less than 25% throughout the damage zone (excluding near-surface and end-of-range regions) even though the dpa level and dpa rate varied by about 600%. However, the dpa rate was highest in the regions experiencing the highest dpa level, and it was postulated that a precipitate dissolution mechanism (which was dependent on dpa rate and which competed against precipitate growth) tended to limit the precipitate volume fraction in these regions.

(h) Measured elemental concentration vs. depth profiles from near-surface regions of specimens showed that enhanced Be segregation occurred at irradiated surfaces. However, this segregation was attributed to radiation-enhanced diffusion and to oxidation of the Be, and not to the solute-drag mechanism. Within the damage zone, solute was not transported out of the peak damage region (at 400°C), nor was there apparent Be enrichment at grain boundaries. This behavior was attributed to the copious

precipitation of CuBe platelets within the matrix, which served as sinks for the migrating interstitials, and which subsequently grew due to Be segregation via the solute-drag mechanism. The presence of the precipitate sinks prevented the long-range migration of the interstitials.

(i) The Cu-3.4 at% Be alloy did not support the formation of voids under irradiation, presumably because the Be solute atoms trapped interstitial atoms and enhanced recombination, and because CuBe precipitates that formed quickly under irradiation acted as defect sinks

Cu-1% Co and Cu-1% Fe Alloys

(a) The principal effect of irradiation at 350-500°C on aged Cu-Co and Cu-Fe alloys was loss of precipitate coherency, due to absorption of free interstitials to relieve the coherence strain. Loss of coherency was observed well beyond the end-of-range of the incident ions, and this was attributed to long range migration of free interstitials originating within the damage zone.

(b) Void formation was not observed in any specimen except a solution-treated CuFe sample irradiated at 400°C. The absence of void formation was attributed to a lack of void nucleating

agents, and also to point-defect trapping at the interface of coherent precipitates.

High Purity Copper

Voids did not form in the high purity Cu at irradiation temperatures of 400-500°C, because of a lack of void nucleating agents, i.e., gaseous impurities.

Experimental Methods

(a) The carrousel specimen holder assembly, which was designed and built as a part of this thesis project, worked well with regard to heating individual specimens only during their irradiation, while not heating the other specimens in the holder. Comparison of the microstructure of Cu-Be specimens irradiated under similar conditions in the carrousel holder and in the linear holder (which heated all specimens en masse) showed that those heated in the linear holder suffered significant effects from post-irradiation annealing. For alloy specimens, therefore, care should be taken to prevent any extraneous heating.

(b) The cross sectional method of thinning specimens for TEM analysis was found to be a very useful tool for surveying the effects of ion-bombardment on the phase stability of alloys. By comparing the data from several cross sectioned specimens irradiated at the same temperature but to different fluence levels, a good idea of dose and dose-rate effects at that temperature could be obtained. The principal difficulty with this technique was thinning the specimen uniformly throughout the damage zone.

Suggestions for Further Work

Careful reading of Chapters VII-IX reveals many areas that deserve more detailed investigation. There are several areas in particular that could be explored further.

(a) The effects of displacement rate on the precipitate characteristics could be studied in much more detail, especially at lower dose rates. Figures VII-21 and VII-22 suggest that precipitate size and density depend strongly on displacement rate, and it would be interesting to determine whether, at much lower rates, the precipitate morphology approaches that produced by thermal aging alone. Dose rate studies are of general importance because of the desire to compare ion-bombardment and neutron-bombardment data.

(b) Dilute Cu-Be alloys containing various Be concentrations could be irradiated to determine the shift in the Be solubility, as a function of temperature and dose rate. This type of study, i.e. determining the phase diagram under irradiation, would be similar to that performed on Ni-Si alloys by Martin et al. [J. Nucl. Mat. 83, 67 (1979)].

(c) Attempts could be made to mathematically model the results.

(d) The cross sectioning technique in Cu could be utilized to further study the correlation between the observed and calculated distributions of the deposited ions. An ion that is very insoluble and immobile in copper, such as carbon or oxygen, could be injected at a sufficiently high fluence and temperature

such that the elements would precipitate in the matrix. The resulting visible precipitate distribution might accurately reflect the injected ion distribution.